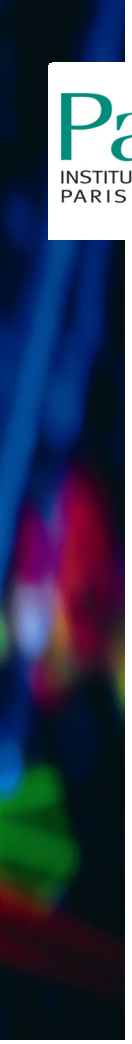

ParisTech
INSTITUT DES SCIENCES ET TECHNOLOGIES
PARIS INSTITUTE OF TECHNOLOGY

MINES ParisTech

Ecole doctorale n° 432 : SMI-Sciences des métiers de l'ingénieur

Doctorat ParisTech

T H È S E

pour obtenir le grade de docteur délivré par

l'École Nationale Supérieure des Mines de Paris

Spécialité « Informatique temps réel – Robotique – Automatique »

présentée et soutenue publiquement par

M. Keerthi NARAYANA K.S

le 24 Mai 2011

Solutions de localisation des Systèmes Mobiles de Cartographie en environnements structurés

***

Solutions for the localization of Mobile Mapping Systems in structured environments

Directeur de thèse : **M. François GOULETTE**
Co-encadrement de la thèse : **M. Bruno STEUX**

Jury

M. Saïd Mammar	**Professeur à l'Université d'Evry, HDR**	**Rapporteur**
M. Juha Hyyppä	**Professeur Associé à l'Université Aalto (Finlande)**	**Rapporteur**
M. Laurent Trassoudaine	**Professeur à l'Université Blaise-Pascal, HDR**	**Président du jury**
M. François Goulette	**Enseignant Chercheur, MINES ParisTech, HDR**	**Examinateur**
M. Bruno Steux	**Enseignant Chercheur, MINES ParisTech**	**Examinateur**

T H E S E

MINES ParisTech
Centre de robotique
60 Boulevard Saint Michel 75006 Paris

SOLUTIONS FOR THE LOCALIZATION OF MOBILE MAPPING SYSTEMS IN STRUCTURED ENVIRONMENTS

ABSTRACT: Automated localization or in other words, the functionality to determine the position and orientation (pose) has several applications, such as autonomous navigation, search and rescue, and mobile mapping. This thesis focuses on proposing complimentary solutions to the current localization methods (performed using GPS receivers and Inertial Measurement Units (IMU)) of Mobile Mapping Systems (MMS), which are designed to generate 3D maps of the environments.

First, the obvious errors in the already generated trajectory of the mapping platform are corrected using our smoothing-based post-mission processing. This approach is sufficient to correct the 3D maps to make them visually realistic. However, for precise localization this approach is still insufficient, especially when the input sensors have significant errors such as: GPS signal degradation or outage (due to the presence of obstacles to the satellite signal reception), and uncorrected IMU measurement biases (results as drifts in the estimated pose). These situations rise often in manmade environments, particularly in urban and indoor scenarios.

The thesis therefore, proposes an alternative localization method using a set 2D laser scanners, which are normally used for perception/mapping in MMS. Our approach is comparable with the Simultaneous Localization and Mapping (SLAM) technique, used in indoor robotic navigation. However, the category of laser odometry is suitable, since the relative 3D transformation between two sets of landmarks is computed without using a map, but exploiting the time invariant properties of the extracted features from perception. Planar surfaces are one of the most recurring geometrical features available in manmade structured environments, and using their properties 3D transformation resolution is proposed.

In order to achieve this objective, first, a novel method to extract the planar landmarks using a synchronized pair of 2D laser scanners is proposed, to ensure a quick data extraction to retain the landmark's time invariant properties intact, even while scanning from a vehicle in motion. Then we propose a Divide & Conquer (D&C) approach to simplify the transformation and landmark matching (Data Association) processes by splitting both the operations in two. The critical factor, in this approach is, the ability to obtain the minimal set of associations from a larger set, containing potential ambiguities and outliers, occurring due to the compensation in association, for unknown transformation. The new algorithm, Optimal Candidate Selection by Consensus (OCSC), and its weighted variant (WOCSC) handles not only this, but also computes the optimal transformation itself. The algorithm performs significantly better with noisy data, compared to the standard mean-based approach. Finally, prior concluding, we propose our designed method called "Delayed Map Update", to address the common problem of drift errors, affecting all odometry or SLAM approaches, while converting the computed noisy relative transformation to an absolute pose, by integration.

KEY WORDS: Localization, Mobile Mapping Systems (MMS), SLAM, GPS receivers, Inertial Measurement Units (IMU), Laser scanners, Post-Mission processing, Laser odometry, Planar landmarks, Data association.

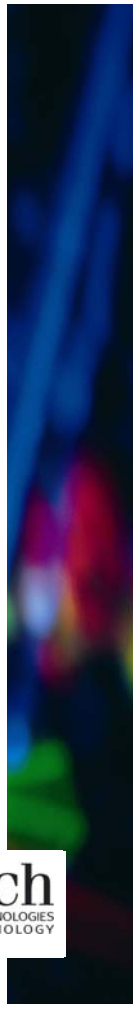

MINES ParisTech

ParisTech
INSTITUT DES SCIENCES ET TECHNOLOGIES
PARIS INSTITUTE OF TECHNOLOGY

SOLUTIONS DE LOCALISATION DES SYSTEMES MOBILES DE CARTOGRAPHIE EN ENVIRONNEMENTS STRUCTURES

RESUMÉ: La localisation automatique, autrement dit la possibilité de déterminer la position et l'orientation (*pose*) d'un système mobile, trouve de nombreuses applications dans la navigation autonome, la recherche et le sauvetage ou la cartographie mobile. La présente thèse a pour objectif de compléter les méthodes employées jusqu'ici, pour assurer la localisation de systèmes de cartographie mobiles (*MMS*) (récepteurs GPS et centrales à inertie – *IMU* – le plus classiquement). Ces systèmes sont conçus pour générer des cartes en trois dimensions (3D) de leur environnement.

Dans un premier temps un post-traitement, par lissage des données, permet de corriger certaines erreurs manifestes, dans les données d'une trajectoire enregistrée. Cette approche est acceptable pour redonner un aspect visuel réaliste à des cartes en 3D. Une telle approche n'est évidemment pas applicable quand une localisation précise est demandée, bien que certains capteurs fournissent des données erronées. Citons à titre d'exemples courants la dégradation ou la disparition momentanée du signal GPS (dues à la présence d'obstacles), les dérives des centrales à inertie. De telles situations sont fréquentes dans les environnements structurés par l'Homme : les sites urbains ou les intérieurs de bâtiments.

La présente thèse se propose d'utiliser, comme outil complémentaire de localisation, un ensemble de scanners à lasers 2D, ceux là mêmes qui sont employés comme capteurs dimensionnels dans les systèmes de cartographie mobile. Notre approche est voisine de la technique employée pour assurer la navigation des robots en espaces intérieurs : la localisation et la cartographie simultanées (*SLAM*). Il est justifié d'employer l'expression d'odométrie par laser, puisque le déplacement apparent de points de repères est calculé, en 3 dimensions, sans avoir besoin de carte, en utilisant des propriétés invariantes de l'environnement reconstruit. Les environnements artificiels sont souvent riches en portions de surfaces planes, il est donc proposé ici d'en exploiter leurs propriétés, pour déterminer un mouvement en 3D.

Dans une première étape, nous proposons une nouvelle méthode qui permet de caractériser rapidement les repères plans, ainsi que leurs propriétés invariantes, même à partir d'un véhicule en mouvement. Nous utilisons pour ce faire une paire de scanners à lasers 2D, synchronisés entre eux.

Nous proposons ensuite une approche par “division pour régner” (*divide and conquer*, D&C) qui simplifie les tâches d'association des repères et de reconstruction du mouvement (*data association*, DA) :chacune de ces tâches est elle-même divisée en deux. L'élément critique de cette approche consiste à extraire l'ensemble minimum d'associations, qui permettent de reconstruire le mouvement inconnu, à partir d'un ensemble beaucoup plus vaste d'associations apparemment plausibles, comportant des ambiguïtés, voire des cas aberrants. Un nouvel algorithme de sélection des candidats optimaux par consensus (OCSC), et sa variante pondérée (WOCSC), permettent cette extraction. Ces mêmes algorithmes permettent, de plus, de calculer la transformation la plus probable. Cet ensemble d'algorithmes présente une meilleure résistance, face à des données bruitées, que ceux qui font appel aux classiques approches statistiques.

Finalement, avant de conclure, nous proposons notre méthode, appelée “mise à jour différée d'une carte”, pour résoudre le problème bien connu des dérives. Ces erreurs concernent toutes les techniques fondées sur l'odométrie ou les SLAM, elles prennent leur source dans le passage, par intégration, de la mesure bruitée de transformations relatives, en une position absolue.

MOTS CLÉS : Localisation, Systèmes de cartographie mobiles (MMS), SLAM, Récepteurs GPS, Centrales à inertie (IMU), Scanners laser, Post-traitement, Odométrie laser, Repères plans, Association de données.

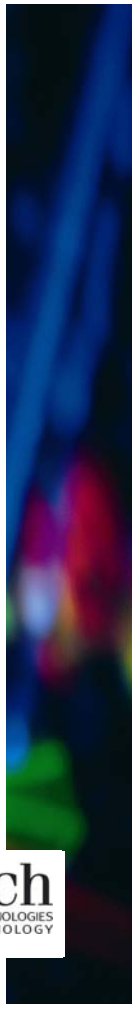

MINES ParisTech

ParisTech
INSTITUT DES SCIENCES ET TECHNOLOGIES
PARIS INSTITUTE OF TECHNOLOGY

PANORAMA DE LA THÈSE

Chapitre 2 : Ce chapitre fournit un panorama général des systèmes de cartographie mobiles (MMS), il souligne également l'importance de la localisation de ces systèmes. Pratiquement tous les systèmes MMS connus font appel, pour assurer leur localisation, à des récepteurs GPS et à des centrales à inertie. Nous examinons rapidement les propriétés de ces capteurs, afin de mettre en évidence l'impact de leurs lacunes sur le fonctionnement d'un MMS.

Chapitre 3 : Ce chapitre présente une méthode de post-traitement par lissage des données ; une telle méthode permet de corriger certaines erreurs évidentes provoquées par les limitations des capteurs de position. Le traitement est complètement automatique, il corrige, au moyen d'un lissage par des splines, les sauts d'altitude et les anomalies d'azimut (*yaw*) d'une trajectoire enregistrée. Nous montrons les résultats obtenus par cette approche sur des cartes 3D issues de la plate-forme LARA-3D. Nous mettons en évidence l'efficacité du procédé, qui corrige des erreurs manifestes, visibles sur des nuages de points, en 3D.

Chapitre 4 : Le post-traitement décrit précédemment, au chapitre 3, ne corrige que des erreurs évidentes. Il est insuffisant pour obtenir une localisation précise, notamment quand le signal GPS présente des lacunes. C'est pour cette raison que nous explorons la possibilité d'utiliser les capteurs perceptifs (comme les scanners à laser, dans notre cas) pour assurer la localisation ; de tels capteurs font de toute façon partie intégrante de tout système de cartographie mobile, ils sont utilisés pour la construction des cartes. Ce chapitre introduit rapidement ce concept de localisation par des capteurs perceptifs ; cette technique est utilisée dans les systèmes de localisation et cartographie simultanées (SLAM). Cette approche justifie le thème principal de notre travail : « odométrie par laser au moyen de repères plans ».

Chapitre 5 : Ce chapitre couvre la première étape, primordiale, de l'odométrie par laser introduite au chapitre 4. La détection et la caractérisation de motifs plans au moyen de deux scanners par laser, dans un arrangement particulier, sont expliquées. Les détails d'organisation sont décrits, ainsi que les algorithmes développés et les résultats obtenus.

Chapitre 6 : Ce chapitre décrit notre approche de « diviser pour régner » (*divide and conquer*, D&C), qui permet de résoudre le problème complexe de localisation en 3D, au moyen des repères plans extraits comme expliqué au chapitre 4. Nous donnons les détails des algorithmes qui permettent d'associer les données observées à deux époques différentes (*lenient data association*, LDA et *strict data association*, SDA). Les calculs de la transformation associée utilisent des propriétés géométriques invariantes des plans-repères utilisés. L'algorithme de sélection des candidats optimaux par consensus (OCSC), et sa variante pondérée (WOCSC), est expliqué ; ces algorithmes permettent également le calcul de la transformation.

Chapitre 7 : Ce chapitre présente les détails des algorithmes, et des méthodes présentées au chapitre précédent, appliqués à des exemples concrets. Les dispositifs expérimentaux sont expliqués, les résultats obtenus par différentes variantes des algorithmes sont présentés et critiqués. Les résultats obtenus nous permettent de proposer notre méthode, appelée “mise à jour différée d'une carte”, pour résoudre le problème bien connu des dérives. Ces erreurs concernent toutes les techniques fondées sur l'odométrie ou les SLAM, elles prennent leur source dans le passage, par intégration, de la mesure bruitée de transformations relatives, en une position absolue.

Chapitre 8 : Ce chapitre conclut le travail de thèse, et met en évidence les extensions possibles de ce travail.

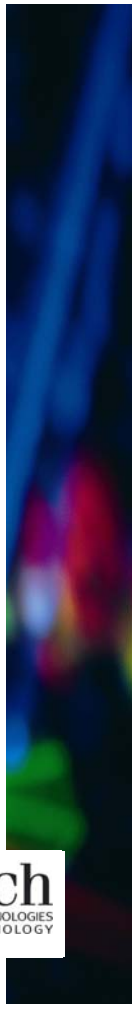

"Two roads diverged in a wood, and I, I took the one less traveled by, and that has made all the difference."- R. Frost

To my father, to my son
&
to my family in India and in France

ACKNOWLEDGEMENTS

I would like to thank Ecole des Mines de Paris (Mines ParisTech), laboratory of robotics (CAOR) and my thesis advisors for giving me an opportunity to realize my valuable academic aspiration.

My deepest gratitude to my family, friends and well wishers who supported in the last three years of challenging and interesting path I have travelled.

I sincerely thank Mr. Bruno Steux, for his continuous support, encouragement and guidance. His sincere cooperation, availability, thorough understanding of the subject and valuable discussions deserve everlasting remembrance and appreciation. I am also grateful to Mr. Jöel Senpauroca, Mr. Fawzi Nashashibi for their motivating advices, assistance, and encouragement.

I thank the invaluable efforts of Professor Saïd Mammar, Director of the laboratory IBISC, from University of Evry and Professor Juha Hyyappä, Head of the department of Remote Sensing and Photogrammetry at the Finnish Geodetic Institute, associated to University of Aalto, Finland, in reviewing, analyzing and validating my work in an efficient time period. Special thanks to Professor Laurent Trassoudaine, from the laboratory of LASMEA, associated with University of Blaise Pascal for presiding the jury of my defense, and providing his precious inputs.

A thesis is like life with highs and lows. The people really counts are the ones who trusts, appreciates, supports and motivates you during the low phases. For me, this thesis started with an end and ended with a start. My beloved father, from whom I drew my academic inspirations, passed away in the early stages of this thesis. However, life brings always new hopes, and my son born at the end of the thesis, brought a bundle of joy to my life. The thesis retained its due course due to the continuous understanding and encouragement from my wife Adèle, her parents, Jacques and Josée, and her grandmother. I owe a ton of sincere thanks to all of them, for all the support they have given. I thank also my mother, brothers and sister who sent their well wishes from far away.

I am lucky to meet some wonderful people as colleagues, who were always present for me, when it mattered the most. My deepest thanks to Raoul, Fatin, Taha, Anne-Sophie, Jackey, Hyun-Jae, JE, Omar, Jeff & Benjamin for their unconditional time, advices, suggestions and discussions, which made the thesis even more a worthy experience.

Finally, I like to thank the projects, Terra Numerica, VIZIR and DIVAS for partially funding this research.

Contents

List of Figures

List of Tables

Table 1: Abbreviations

Acronyms	**Expansion**
ABA	Adaptive Breakpoint Algorithm
ABS	Anti-lock Breaking System
AR	Auto Regression
C/A	Coarse Acquisition
CCDA	Combined Constraint Data Association
Cog	Center of gravity
DA	Data Association
D&C	Divide and Conquer
DGPS	Differential GPS
DMU	Dynamic Measurement Unit
DOD	Department of Defense
DOF	Degrees of Freedom
DOP	Dilution Of Precision
DR	Dead Reckoning
DSM	Digital Surface Model
DTMO	Detection and Tracking of Moving Objects
ECEF	Earth Centered Earth Fixed
EGNOS	European Geo Stationary Navigation Overlay Service
EKF	Extended Kalman Filter
EM	Expectation Maximization
ENU	East, North, Up
ESOC	European Space Operations Center
FOF	First Order Filter
FRF	Fixed Reference Frame
GBAS	Ground Based Augmentation Systems
GNSS	Global Navigation Satellite System
GPS	Global Positioning System
HISS	Hybrid Inertial Survey System
HMM	Hidden Markov Model
ICC	Instantaneous Center of Curvature
IDC	Iterative Dual Correspondence
ICP	Iterative Closest Point
ICR	Instantaneous center of rotation
IEPF	Iterative End Point Fit
IGS	International GPS Service
IMU	Inertial Measurement Unit
INS	Inertial Navigation System
ISA	Inertial Sensor Assembly

Continued on Next Page...

Table 1 – continued from previous page

Acronyms	Expansion
LASER	Light Amplification by Stimulated Emission of Radiation
LDA	Lenient Data Association
LIDAR	Light Detection And Ranging
LRF	Laser Reference Frame
LTP	Local Tangent Plane
MEMS	Micro Electro Mechanical Systems
MEO	Medium Earth Orbit
MHT	Multiple Hypothesis Tracking
MMS	Mobile Mapping System
MRF	Moving (Mapping) Reference Frame
NED	North, East Down
NIS	Normalized Innovation Squared
OCSC	Optimal Candidate Selection by Consensus
ORF	Object Reference Frame
POS	Position and Orientation System
POS/LV	Position and Orientation System for Land Vehicles
PRN	Pseudo Random Noise
RANSAC	RANdom SAmple Consensus
RLG	Ring Laser Gyroscope
RTK	Real Time Kinematic
SA	Selective Availability
SBAS	Space Based Augmentation Systems
SDA	Strict Data Association
SHT	Single Hypothesis Tracking
SLAM	Simultaneous Localization and Mapping
SLAMMOT	Simultaneous Localization, Mapping and Moving Object Tracking
UKF	Unscented Kalman Filter
ULEE	User Local Environment Errors
VRF	Vehicle Reference Frame
VRS	Virtual Reference Station
WGS84	World Geodetic System
WOCSC	Weighted Optimal Candidate Selection by Consensus

Chapitre 1

Introduction

Ce chapitre présente le contexte de la thèse, son domaine d'applications, ses objectifs et les contraintes associées ; il comporte également un bref aperçu de l'ensemble de l'étude. Ce chapitre présente l'ensemble des contributions scientifiques originales de cette thèse. Cette recherche est menée avec la collaboration de l'équipe dédiée au système de cartographie mobile (Mobile Mapping System - MMS) dans le laboratoire de robotique (CAOR) de l'École des Mines de Paris.

Le contexte de la recherche est de fournir des outils complémentaires pour la localisation d'un système MMS terrestre. Tous ces systèmes utilisent des récepteurs GPS et des centrales à inertie (Inertial Measurement Units - IMU), pour déterminer la position et l'orientation (pose) de la plateforme mobile dans l'espace à 3 dimensions. Les limitations actuelles des MMS sont dues aux insuffisances de ces capteurs : Les récepteurs GPS peuvent subir une dégradation de la qualité du signal reçu, dans un environnement qui masque une partie du ciel ; les informations fournies par les centrales à inertie présentent souvent des décalages non corrigés, ces décalages se traduisent par des dérives dans la position estimée (une centrale de bonne qualité est très couteuse, de l'ordre d'une centaine de milliers d'euros).

La thèse porte sur deux aspects : d'une part, une technique de post-traitement (lissage des résultats) permet de corriger certaines erreurs triviales liées aux limitations des capteurs ; d'autre part, les scanners à laser, qui sont utilisés pour créer les données cartographiques, permettent également d'aider à la localisation du véhicule.

Le chapitre 2 présente l'état de l'art des MMS. Le chapitre 3 illustre les limitations des MMS et présente une approche de post-traitement. La méthode qui utilise les scanners à laser dans la localisation est décrite en détail dans les chapitres 4 à 7. Le chapitre 8 conclut cette thèse.

Chapter 1

Introduction

Contents

1.1 Context

This research is done in collaboration with the dedicated Mobile Mapping Systems (MMS) team in the Robotics lab (CAOR) of Ecole des Mines de Paris. The MMS team is involved in projects: VIZIR/DIVAS (under the program SARI) and TERRA Numerica (under the program Cap Digital). The *LARA-3D*, a land-based MMS prototype platform being developed by the MMS team is used for providing the digitalized 3D terrestrial maps for these projects. The maps are created using a laser scanner and represented in the form of 3D point clouds. At some instants, the quality of the maps degrades, when the mobile mapping platform (a land-based vehicle) faces difficulties to localize itself with respect to the mapping reference frame. This is the most common problem for many MMS around the world. The thesis, therefore, focuses on improving the localization ability of a land-based laser MMS.

Localization is the process that unambiguously defines one's position and orientation (i.e. pose) in space with respect to a reference, at a given time. Self localization is needed in several fields such as autonomous navigation, search and rescue, and mobile mapping, the domain of focus in this thesis. Mobile Mapping Systems (MMS) requires continuous pose estimation of the moving mapping platform, during the data acquisition phase.

MMS reduce the incurred cost and acquisition time compared to the conventional mapping methods. The technology dates back to the early 1990s, where the first MMS GPSVan is designed and implemented at Ohio State University, USA [Grejner-Brzezinska 02].

The map quality generated through this technique is however very sensitive to the localization accuracy. Any error in the computed pose, transforms into errors in the map. Therefore, this study focuses on improving the localization functionality of a mapping system.

1.2 Scope

The localization functionality has three principal components shown in figure 1.1: *input sensors* which directly or indirectly measure the pose components, *data fusion*, also called as *sensor integration schemes*, consisting of algorithms to combine one or more independent sensor measurements to estimate the optimal pose, and the *post mission processing*, consisting of any additional off-line algorithms applied to improve the obtained results. Among these, input sensors are the most critical component for the localization.

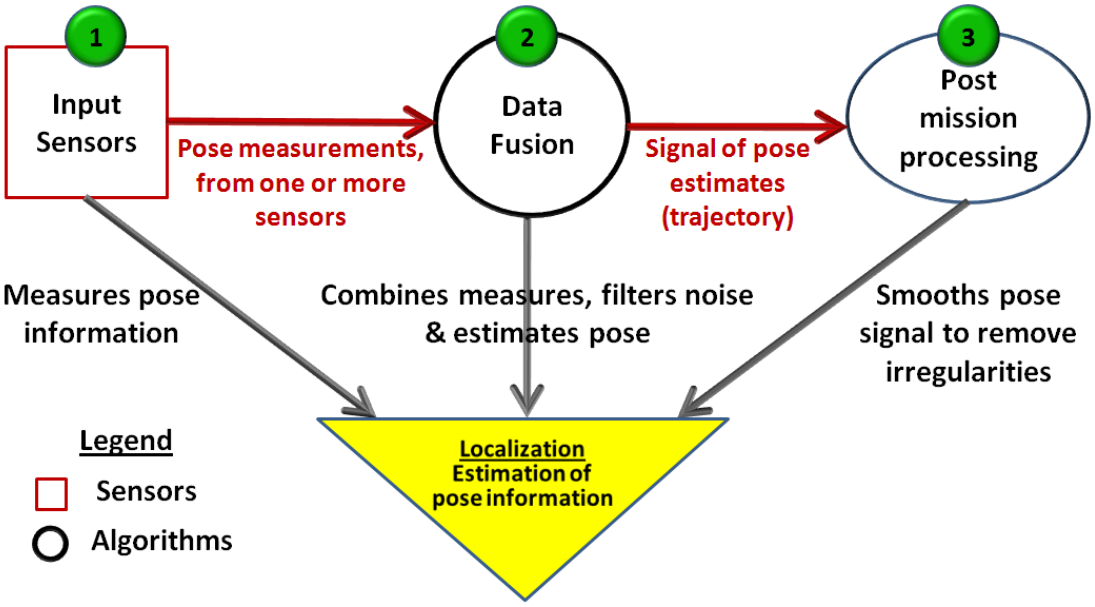

Figure 1.1: Three functional levels in localization: the data flow is sequential and shown in red, where each of the three blocks can contribute to the pose estimation

In MMS, satellite signal-based positioning by Global Navigation Satellite System

(GNSS) receivers (in most context it is just the GPS), and inertial navigation using an Inertial Measuring Units (IMU), are used as the common input sensors. Although each of these technologies can, in principle, determine both position and orientation, they are usually integrated in such a way that the GPS receiver is the main position sensor, while the IMU is the main orientation sensor [Schwarz 04]. However, dependency on GPS receivers, which require satellite signal for positioning, limits the MMS to outdoor mapping applications. Most of the existing MMS suffer when the GPS-based positioning accuracy degrades. This problem arises often in the most frequently mapped urban areas, due to the presence of tall manmade structures, masking the clear view to the sky. Due to drift errors in the computed pose and the high cost versus quality ratio of the IMU, an alternative method for localization is desirable for many mapping applications.

In the context of this thesis, multiple sensors (**items 1**) and data fusion (**items 2**) of figure 1.1, were the focus of an earlier research done in the MMS team [Abuhadrous 05], and several other works [El-Sheimy 96], [Skaloud 99], [Manandhar 00], [Schultz 06], [Chiang 05], [Shi 08]. All these works focus on combining multi-sensor data, to better estimate the pose. The multi-sensors (**items 1**) are often limited to GPS, IMU (both 3D pose), odometer and compasses (2D or 1D pose). This thesis focuses on improving localization of a mobile mapping system by an alternative way to compute 3D pose and a set of algorithms (*items 1* and *item 3*).

Our research addresses the shortcomings of 3D pose sensors (GPS and IMU), by proposing solutions adhering to two main objectives:

- **Pose information in 3D space** - Solution capable of computing 3D pose.
- **Complementary to current 3D localization** - Solution to overcome the limitations of the two commonly used 3D pose sensors. i.e. to minimize the effects of degraded GPS signal and IMU measurement drifts, on the computed pose of the mobile mapping platform.

Additionally, we apply a cost constraint, which limits the selection of the improvement axis to methods, incurring only a marginal increase to the cost. Therefore, solutions such as a good quality IMU (navigation grade), which costs more than a hundred thousand Euros are not considered.

1.3 Main contributions

The thesis proposes two solutions. First, an improvement of the current localization technique based on GPS&IMU, and, the second, developing a new localization method, independent of these localization sensors.

After analyzing the effect of GPS signal quality on the pose of an MMS, a post mission processing method is proposed to correct these errors in the trajectory. *This is achieved by an automated smoothing approach, which we designed and implemented to correct the slowly varying altitude errors caused by the inaccurate GPS signal.* Combining this method with a spline-based trajectory smoothing, most of the apparent errors in the trajectory is corrected. This approach however needs further improvements to tackle slowly varying sensor errors.

Perception sensors such as laser scanners and cameras, are integral part of MMS, but used mainly for mapping. We propose a novel geometrical localization approach, based on laser scanner measurements. For the perception to work, mapping environment must contain objects and obstacles, as opposed to the GPS receivers, whose solutions degrade in such situations. Additionally, this approach can contribute to the reduction in the cost of the MMS, since the localization and the mapping can be achieved by the same set of sensors.

Perception sensor-based localization is presently used with the technology of Simultaneous Localization and Mapping (SLAM). SLAM approaches are mainly used for the navigation of robots in the indoor environments, where GPS positioning (GPS fix) is unavailable. The feature-based SLAM, detects and localizes the landmarks on a map, while simultaneously estimating the pose of the robot, from where the landmarks are observed [Durrant-Whyte 06], [Bailey 06]. Most of the existing SLAM approaches resolve robot pose in 2D space.

In this thesis, we use planar features as landmarks, not only because, they occur frequently in manmade environments and easier to extract, but also, their geometrical properties can help determine the 3D pose information. We choose dead reckoning, the method used in odometry, to compute the relative pose between two set of observed planar landmarks. Therefore, this approach can be called as a *laser odometry*. This approach, helps reduce the landmark association (called as Data Association or DA: association of new observation of landmarks with the already observed ones) failures typically observed in most SLAM approaches). These are caused by the growing uncertainties in the mapped landmark locations due to the uncertainties in the robot pose.

For a laser odometry to function, a set of landmarks need to be extracted in such a short time that the deformation due to movement of the robot remains insignificant. To compute an independent pose from other sensors, the features need to be extracted from raw scans, rather than the one's referred in a map (georeferencing). This way of planar extraction is not seen in any literature before. *Therefore, we propose a new system design and the chain of algorithms, tailor made to extract the planar features from a given pose of the vehicle, using a 2D laser scanner arrangement.*

The 3D pose problem (transformation computation) has 6 degrees of freedom (6DOF), which is complex to resolve due to the additional load of unknown Data Associ-

ation. Optimization techniques and regression models are applied to solve this problem, however, they treat it as a single problem (transformation and DA) to solve. *We propose a method to simplify this process, by applying a unique Divide and Conquer approach (D&C), which separates the Data Association and transformation computation in two, and further splits the two process in two. The sequential processes are: a Lenient Data Association or LDA, rotation resolution, a Strict Data Association or SDA (optional), and translation computation.*

As the name suggests, LDA, is performed using a relaxed set of constraints, to compensate for all the unknowns related to transformation and DA. This implies, the resulting associations can be ambiguous. Therefore, a mean-based or least square-based methods unfit to resolve transformation from these associations, since the final result gets biased by the erroneous input associations. *We propose a new Optimal Candidate Selection with Consensus (OCSC) algorithm, and its weighted variant (WOCSC), which selects an optimal minimal set of association to compute the transformation. We demonstrate that, the algorithm effectively eliminates outliers, deals with noisy candidates, and resolves ambiguities. The transformation is estimated using the geometrical properties of planar landmarks by applying only WOCSC, or alternatively, at this stage, translation alone can be computed using a mean-based method with SDA.*

Finally, we also propose our designed solution, termed as "delyed map update", to tackle drift errors (another common SLAM and odometry problem) in the integrated pose.

1.4 Overview of the dissertation

Figure 1.2 gives the overall flow of this thesis.

Chapter 2: Overall view of the MMS, and the importance of localization for such systems is given here. Almost all MMS around the world, depend on GPS receivers and inertial sensors, for localization. We therefore, briefly look at their functionalities and limitations to understand the impact of their shortcomings on MMS.

Chapter 3: This chapter presents a post mission processing approach to correct the apparent errors in the trajectory, occurring due to the localization sensor limitations. This fully automated method corrects altitude jumps, and azimuth (yaw) anomalies in the trajectory. We present the results of this approach, using the 3D maps generated from the *LARA-3D* platform.

Chapter 4: The post mission processing described in chapter 3 can be improve appearance of 3D maps, but insufficient for precise localizations, especially when the GPS signals are not available. Therefore, we explore the possibility of using the integrated mapping or perception sensors (e.g. laser scanners) of MMS for localization. This chapter briefly introduces the concept of perception-based localization, and the technique of Simultaneous Localization and Mapping (SLAM). This leads to the motivation to our

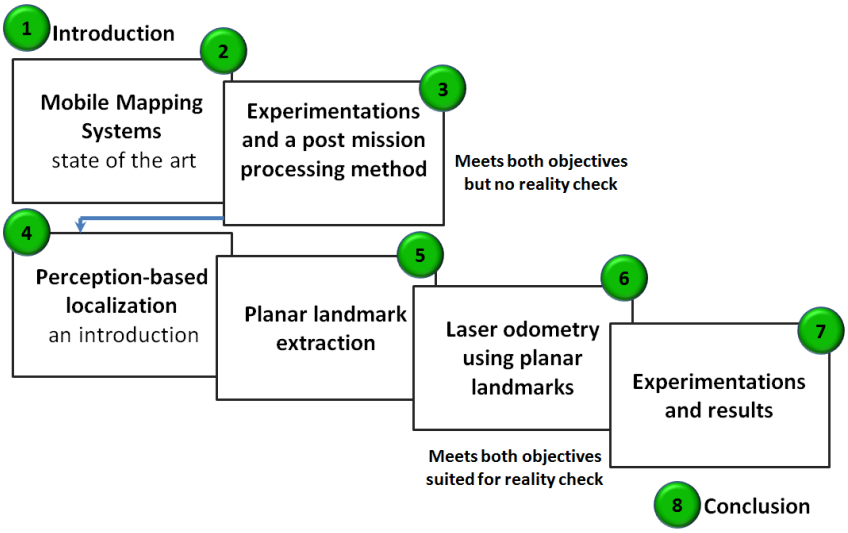

Figure 1.2: Overview of the thesis dissertation.

work on "laser odometry using planar landmarks".

Chapter 5: This chapter covers the first and important step of the laser odometry introduced in chapter 4. Quick acquisition of planar feature information is a key to extract the landmarks properties, without deforming them due to the motion of the sensor platform. Planar landmark extraction using a specific arrangement of 2D laser scanners are detailed in this chapter. We present the system design, algorithms, and the obtained results.

Chapter 6: This chapter describes our D&C approach, to resolve the complex 3D localization, using planar landmarks, possibly extracted using the process explained in chapter 4. The method of Data Association (both LDA and SDA), and transformation computation using time invariant geometrical properties of the landmarks is explained. Theories of the OCSC and WOCSC are given, with their application to transformation computation.

Chapter 7: This covers the implementation details of the algorithms and the methods presented in chapter 6. Following that, the experimentation setups along with the algorithm validation results and analysis are presented. These results lead us to present a novel delayed map update method, which addresses the drift errors in the integrated pose, observed in most SLAM approaches.

Chapter 8: This chapter concludes the thesis, highlighting the possible extensions to this work.

Chapitre 2

Les systèmes de cartographie mobiles

Ce chapitre présente l'état de l'art des systèmes de cartographie mobiles (MMS). Un MMS comporte une plateforme mobile, équipée de capteurs qui assurent sa localisation et permettent la cartographie de son environnement.

Les cartes numériques sont générées à partir des propriétés de l'environnement, propriétés mises en relation avec la position courante du véhicule, position qui est estimée par le sous système de localisation. Ce processus de mise en relation est appelé géoréférencement. Toute erreur de localisation se traduit par une erreur dans les cartes numériques générées.

La plupart des MMS sont utilisés en extérieur, une estimation correcte de la position 3D de la plateforme (6 degrés de liberté) est donc essentielle.Notre analyse de près d'une quarantaine de MMS a mis en évidence que localisation et cartographie sont le plus souvent effectuées séparément, par des capteurs dédiés. Tous ces systèmes utilisent des récepteurs GPS et des centrales à inertie pour estimer leur position 3D.

Ces deux catégories de capteurs de localisation sont à l'origine de la principale limitation des systèmes mobiles de cartographie actuels. Les récepteurs GPS perdent de leur précision dans un environnement où une partie de l'espace est masqué par des obstacles tels que les constructions, la végétation, etc. Ces obstacles provoquent de plus des réflexions multiples du signal radio, qui accentuant encore la dégradation de la précision de l'estimation de position. Les centrales à inertie sont principalement utilisées pour calculer l'orientation d'un mobile ; elles permettent également de compenser une dégradation du signal GPS sur de courtes périodes. La position calculée à partir des données d'une centrale à inertie est sujette à des dérives, et une centrale de bonne qualité a un cout élevé.

Ces limitations des capteurs limitent l'usage des MMS à des applications en extérieur, à l'exclusion des situations en intérieurs ou en sous-sols. Ces systèmes posent également problème dans les environnements urbains où les immeubles peuvent créer des couloirs étroits.

Chapter 2

Outdoor and Indoor Mapping Systems

Contents

2.1 Introduction

This chapter intends to give an overall view of the Mobile Mapping Systems (MMS), and their current limitations. We identified nearly forty MMS, developed both academically and commercially, around the world.

MMS have two main functionalities: localization and georeferencing (or mapping), performed by the dedicated set of sensors. Localization estimates the pose of the mobile vehicle using which the georeferencing creates the maps from the perception sensor measurements.

Unless specified, in this thesis, MMS means the land-based MMS, with a sensor equipped land vehicle or robot, as the mobile mapping platform.

The flow of this chapter is organized as follows:

Sections 2.2, 2.3 and 2.4, presents the Mobile Mapping Systems (MMS), their applications and typical results. The list of nearly 40 MMS that are studied is given in section 2.5 with their sensor configurations. The functional structure of MMS is given in section 2.6, and the importance of localization under section 2.7. Then an overview of the most commonly used localization sensors, their functionalities and the limitations are listed in section 2.8. Section 2.9 concludes the chapter.

2.2 Mobile Mapping Systems (MMS)

In comparison to the traditional mapping techniques, Mobile Mapping Systems (MMS) provide a time efficient mean to digitize the surrounding environments. The complete definition of such a system is:

"A Mobile Mapping System can be defined as a moving platform, upon which multiple sensor/measurement systems have been integrated to provide, three-dimensional, near-continuous positioning of both the platform and simultaneously collected geospatial data, with no or limited ground control using single or multiple GPS base stations" [Grejner-Brzezinska 02].

The development of such systems become possible, as the USA government made the GPS signal available to the civilian community [Manandhar 00].

Four different MMS platform configurations are shown in figure 2.1.

2.3 Applications

The latest developments in surveying and mobile mapping technologies open new avenues for acquisition, update, fast and near real time online data processing [Zhang 03]. With the continuous growth of urban centers on world-wide scale, the demand of city planners for up-to-date information is increasing at a rapid rate. Along with these developments, comes the need of improving the infrastructures as well. This has led to the

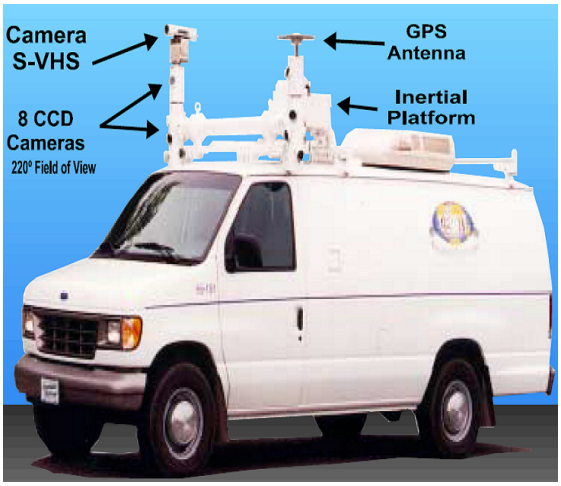

(a) VISAT van - land-based [El-Sheimy 96]

(b) Quadbike, Street mapper - land-based [Hunter 06]

(c) HELIMAP - airborne [Skaloud 05]

(d) Google Trike - land-based [Google. 10]

Figure 2.1: Different mobile mapping platforms used in MMS

establishment of spatially-referenced Geographic Information Systems (GIS) for a variety of applications [El-Sheimy 96]. Due to the growth and rapid changes in the cities, it is essential to rapidly update the GIS at a reasonable cost. Therefore, mobile mapping technology becomes an essential method for acquiring and characterizing information for vital infrastructure management.

The accurate 3D terrain models contribute to a number of applications such as mapping, planning, organizing, and for various other studies. Due to the increasing popularity of this technology, a number of industrial solutions have emerged along with a vast number of research projects undertaken around the world. Improved solutions and reduced operating cost has helped in identifying several new applications for the MMS which are exhaustively presented below:

- **City modeling** - 3D realistic modeling of the urban environment helps studies of architecture and infrastructure and provides a tool for city planning. This application is described in [Grinstead 05] and [Hunter 06].

- **Feature extraction** - The resulting 3D models are used for extracting objects of interest and features from the mapped scene, triggering several automated studies and analysis [Manandhar 01]. Each element can be tagged individually as a building, a monument, or a street, helping to construct a 3D GIS. GIS contribute to the growth of applications like Location Based Services (LBS) [Hwang 03].

- **Analysis and improvement of road infrastructure** - Applications that require generated 3D models include surveillance and road infrastructure analysis tools, geometric studies (infrastructure) of the road to determine the visibility etc. These studies can help validate the speed limits and identify the need of new sign boards. The feature extraction techniques are used to automate the analysis of road signage and delineation [McLoughlin 08]. These applications are mentioned in several articles [Gilliéron 01], [Ooishi 04], [Grinstead 05], [Yu 07].

- **Automatic productive operations** - Highway asset measurements, indivisible abnormal load route planning, or recording accident scenes - to shorten the time before the road can be cleared [Hunter 06].

- **Precision agriculture** - This term refers to within-field management of crops using an information and technology-based system. "It basically means adding the right amount of treatment, at the right time and the right location, within a field-that's the precision part". [Shaikh 03].

- **Virtual reality** - The 3D map-based realistic models are used in virtual reality applications, including driving simulators, robotic path planning, terrain-fire interactions etc. [Grinstead 05], [Hwang 03] or a mere entertaining way such as virtual tourism, and video games etc. [Goulette 06].

A real time map generation is desirable for most of these applications but its not a necessity. Only a few mapping applications such as military and emergency response systems require real time performances [Li 97]. For all the others, only the data acquisition requires time critical performance, where the sensor measurements needs to be precisely timestamped for further processing.

Due to the limitations of GPS receivers, all these applications rely on outdoor acquisitions. *The availability of a reliable GPS independent pose information can open up a new set of applications for MMS, in GPS signal denied environments such as indoors.*

2.4 Generated 3D maps

The 3D maps generated depends on the type of the moving mapping platform and the mapping (or perception) sensors.

The moving mapping platform can be of three principle types: land-based, aerial and marine, however, the first two are the most frequently used. This thesis focuses only on a land-based MMS. This type of MMS is potentially more efficient in data capturing, for numerical modeling and/or visualization in support of decision making, and also for filling the void between static terrestrial and mobile airborne laser scanning [Barber 08].

The obtained results using typical MMS are demonstrated in figure 2.2, where a comparison is drawn between the 3D models of the same urban scene, constructed using a land-based and an aerial MMS. The figure shows *Rue Boulevard Saint Michel in Paris*, highlighting *Ecole des Mines de Paris (Mines ParisTech)*.

In this figure, the land-based MMS *LARA-3D* uses a laser scanner as the perception sensor, whereas the airborne MMS uses digital camera. The terrestrial model has more realistic information about the architecture and fine details compared to the airborne system, which is constructed by mathematical models using 2D orthophotos and altitude information.

2.5 Existing Mobile Mapping Systems

At present, there are at least 40 different land-based MMS solutions available around the world, with USA having 9, Japan with 4 and France, Germany Italy and Canada all with at least 3 each. MMS solutions are now even being developed commercially as turnkey projects in different countries.

An MMS is equipped with two classes of sensors: localization (or navigation) sen-

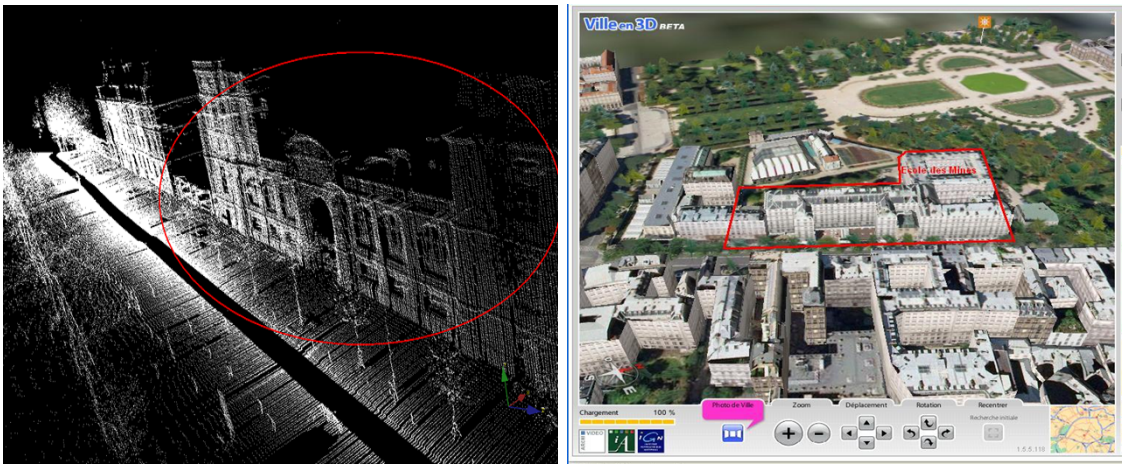

(a) Result of a land-based MMS (*LARA-3D*) (b) Processed aerial MMS (Bati-3D, IGN)

Figure 2.2: Comparison of results of a land-based (a) and an aerial MMS (b), both highlighting Ecole des Mines de Paris (Mines ParisTech), in red

sors, which aid in the trajectory estimation of the mapping platform, and mapping (or perception) sensors, used for digitizing the environment. In most MMS, they contribute only to their dedicated functionality, i.e. a localization sensor is not used for mapping, and vice versa. The mapping platform embed these sensors. These two types of sensor information is combined together by the georeferencing, to produce the maps of the environment.

In table 2.1, an attempt is made to list and categorize most of the presently available MMS systems. Several sources of inputs ([Barber 08], [Ellum 02] and individual articles of the developers of MMS) are taken to accumulate this information. At times different sources had different information such as number of sensors, type of used sensors and the name of the MMS etc. We believe this is because, the MMS are evolved over a period of time and used in different configurations for various tests. The field "year" is just an indicative, mostly taken from the published article dates.

Table 2.1: Existing Mobile Mapping Systems

N	Name of the system	Country	Approx Year	University or Company	POS - Sensors	Perception Sensors
1	GPS-VanTM	USA	1991	Center for Mapping Ohio State University	Kinematic Differential Carrier phase Range data (GPS RTK) and a Dead Reckoning System (DRS). DRS included Three axis reference system (TRS-Gyros) and wheel sensors (odometer)	CCD Cameras (Stereo PULNiX), VHS Cameras
2	GIM	USA	1994	Navsys	GPS, Low cost IMU	CCD Camera, VHS Camera
3	Kinematic Survey System (KiSS)	Germany	1995	Integrierte Kinematische Vermessung (IKV), University of Munich	GPS (Novatel 95 1R), IMU (Litton LN-83), Odometer(Datron Dls-1), Barometer(Setra 470), Inclinometer(HL-Planar), Compass	Multiple CCD Cameras (Stereo PULNiX TM 9700), VHS Cameras (1Sony VX 1E VHS)
4	Car-Driven Survey System (CDSS)	Germany	1998	Geodatisches Institut Aachen	C/A Code GPS (Trimble 4000 Ssi),Odometer, Barometer (SESTRA 470)	2 CCD Cameras (PULNix), 2 Umatik VHS

Continued on Next Page...

Table 2.1 – continued from previous page

N	Name of the system	Country	Approx Year	University or Company	POS - Sensors	Perception Sensors
5	WUMMS	China	1999	Wuhan University	Pseudorange measurement GPS	3 monochrome CCD Camera, Laser Range Finder
6	Mobile Road Mapping System or (Mobiles Straßen Erfassungs System) (MoSES)	Germany	2001	Integrierte Kinematische Vermessung (IKV), University of Munich	GPS - Navigation grade IMU,(APPLANIX POS/LV), Odometer(Datron Dls-1), Barometer(Setra 470), Inclinometer(HL-Planar)	Multiple CCD Cameras (Stereo PULNiX TM 9700), VHS Cameras (1Sony VX 1E VHS) (possible laser scanners)
7	NAIST	Japan	2002	Advanced Intelligence Laboratory NARA Institute of Science and Technology	GPS, IMU	CCD Camera and Laser Scanner (Riegl LMS-Z360)
8	LD2000-R	China	2005	Leador Corp Started in 1999	Dual Frequency Carrier phase measurements (GPS RTK), INS, Compass	Not Disclosed

Continued on Next Page...

Table 2.1 – continued from previous page

N	Name of the system	Country	Approx Year	University or Company	POS - Sensors	Perception Sensors
9	INSA Strasbourg	France	2005	Laboratory of MAP PAGE (MAP Photogrammetrie Architecturale et GEomatique)(National Institute of Applied Sciences of Strasbourg) INSA Strasbourg	GPS, INS	4 monochrome CCD Camera, 1 Color VHS camera, Trimble Laser (GX DR 200+)
10	Stanley – Automated Vehicle (not MMS)	USA	2005	Stanford University Stanford Artificial Intelligence Laboratory	Stanley's GPS L1/L2/Omnistar HP, two GPS for compass, IMU, ABS	5 SICK laser range finders
11	4S-Van	Korea	2006	Electronics and Telecommunications Research Institute (ETRI)	GPS, IMU and DMI	IMPERX CCD Cameras VGA-120, 2M30C, 4M15C SICK Laser scanner LMS 291
12	LARA 3D	France	2004-05	Ecole des Mines Paris	GPS (Trimble AG 132), IMU (Crossbow VG600)	Lidar (IBEO), CCD Cameras

Continued on Next Page...

Table 2.1 – continued from previous page

N	Name of the system	Country	Approx Year	University or Company	POS - Sensors	Perception Sensors
13	NoName	Japan	2006	Waseda University, Tokyo	Trimble BD950 and ANTARIS ubox (GPS), Mitsubishi Electric (odometer), CROSSBOW AHRS400CC-100 INS, Japan Aviation Gyro Electronics JG-35FD (Gyro)	Lidar and Fish Eye Camera
14	StreetMapper	England	2006	StreetMapper is a joint venture between *3D Laser Mapping* and the engineering company *IGI* They work with University of NewCastle upon Tyne	GPS, IMU (TerraControl - IGI product)	5 Riegl LMS-Q120 laser range finders
15	NoName	Malaysia	2006	Universiti Teknologi Malaysia	Trimble 4800 and Leica GPS System 500 (RTK)	CCD Cameras

Continued on Next Page...

Table 2.1 – continued from previous page

N	Name of the system	Country	Approx Year	University or Company	POS - Sensors	Perception Sensors
16	ON-SIGHT	USA	2006	Adaptive Machine Technologies (AMT) Started in 1984	GPS, Navigation Grade IMU	Kodak DC290 and Canon S400
17	CityGRID	Austria	2007	GeoData	GPS and others (not disclosed)	CCD Cameras, Laser range finders
18	Stereopolis	France	2007	IGN	Applanix	Lidar, CCD Cameras
19	Automatic Road Analyzer (ARAN)	Canada	2000-2008	Fugro-Roadware Roadware group acquired by Fugro Intl (2008)	ARAN® GPS and INS (SmartGeometrics) or Applanix POS LV	CCD Camera and Laser Scanner
20	Video images, INS system, GPS Satellite system (VISAT-Van)	Canada	1993-94 1999	Geomatics Engineering Department University Calgary	Dual Frequency GPS (Ashtech 12), Navigation Grade IMU (Litton LTN 90-100), ABS, Digital magnetic compass/Inclinometer	Stereo CCD 37 Ultra sound

Continued on Next Page...

Table 2.1 – continued from previous page

N	Name of the system	Country	Approx Year	University or Company	POS - Sensors	Perception Sensors
21	TruckMapTM (FLI Map)	USA	1995 1996	John Chance Land Surveys/FUGRO	DGPS or OTF-Kinematic (Lecia MX 8614 Magellan Systems' ProMARK X-CP), Digital Altitude Sensor	8 COCHU 4980 CCD Cameras, 4 Super VHS Cameras
22	GPSVision	USA	1996 2006	Lamda Tech	Geodetic Quality Dual Frequency GPS (Trimble 7400), Navigation Grade IMU (Litton LN-200), Linear Distance Measuring Unit	Laser Range Finder
23	Unidade Móvel de Mapeamento Digital (UUMD)	Brazil	1999-2005	São Paulo State University (UNESP)	Two GPS receivers, and a image frame synchronisation system	2 or 4 High Speed CCD Cameras
24	VLMS - Vehicle-Borne Laser Mapping System (VLMS)	Japan	2000-04	University of Tokyo	Hybrid Inertial Survey System (HISS) (DGPS INS, Electronic Odometer)	Three IBEO digital video cameras (Sony DSR 200A)

Continued on Next Page...

Table 2.1 – continued from previous page

N	Name of the system	Country	Approx Year	University or Company	POS - Sensors	Perception Sensors
25	Tele Atlas Mobile Mapping System	Belgium	2007	Tele Atlas	GPS, INS, Odometer	Laser Scanners - 4 Line Cameras (CCD) - Fisheye lens from Sigma fl 8mm
26	Geosoft Video Survey (GVS)	Italy	2006	GeoSoft	NMEA compatibile (GPS), CROSSBOW (INS) ABS	4 Sony dfw V500 (CCD/VHS)
27	ScanVan	Netherlands		DelftTech	Not disclosed	Cyrax 2500 scanner
28	Data Acquisition Vehicle with Inertial and DGPS Equipment (DAVIDE)	Italy		GIOVE Srl	GPS (Trimble) INS (Systron Donner) Odometer	Nikon E2 Stereo 5 VHS

Continued on Next Page...

Table 2.1 – continued from previous page

N	Name of the system	Country	Approx Year	University or Company	POS - Sensors	Perception Sensors
29	Precise Inertial System for Land Use with GNSS Real Time Integrated Multipurpose (PILGRIM) also GIGI	Italy		University of Triest GEOLAB	Applanix GPS - Novatel Millenium + DARC/DGPS real time system or EGNOS INS - Litton Italia (with LITEF, Germany)	Stereo CCD
30	GEOMOBIL (GEOVAN)	Spain		Catolunya Institute of Cartographie	GPS, IMU	CCD Cameras, Lidar
31	VISIMIND	Sweden		VISIMIND AB	GPS (TRIMBLE 7400), Odometer, (Modulo SOM misura assetto : Italian)	Cameras

Continued on Next Page...

Table 2.1 – continued from previous page

N	Name of the system	Country	Approx Year	University or Company	POS - Sensors	Perception Sensors
32	Photobus	Switzerland		Geodetic Engineering Laboratory Swiss Federal Institute of Technology EPFL	2 GPS RTK	CCD Camera
33	Road Measurement Data Acquisition System (ROMDAS)	New Zealand	2000	ROMDASS	GPS, Gyroscope, Single or Duel Bump Detectors, Distance Speed Sensor	Laser, Videos
34	NoName	USA	2005	University of Tenessee	Differential RTK GPS, IMU, Pose from Video (PfV)	High resolution video cameras, laser range finders
35	Segway Robotic Mobility Platform (Segway RMP)	USA		University of Southern California	GPS (Garmin), IMU MicroStrain	Laser range-finders (in both vertical and horizontal planes)

Continued on Next Page...

Table 2.1 – continued from previous page

N	Name of the system	Country	Approx Year	University or Company	POS - Sensors	Perception Sensors
36	LYNX Mobile Mapper M1	Canada	2010	Optech	Applanix POSLV 420	1-4 lasers (Optech, Lynx or ILRIS-3D) and 2 passive CCD camera
37	FGI ROAMER	Finland	2007	Finnish Geodetic Institute	NovAtel SPAN^{TM} positioning system with NovAtel DL-4 plus GPS reciever Honeywell HG1700 AG58 IMU	FARO Photon^{TM} 120 terrestrial laser scanner
38	FGI Sensei	Finland	2010	Finnish Geodetic Institute	NovAtel SPAN-CPT consists of tightly couple GPS/INS receiver with fiber optic gyros and accelerometers	Ibeo lux and SICK LMS151 laser scanners, AVT Pike F-421C CCD camera, Specim Spectral camera, Flir Photon 320 thermal camera

2.6 Functional blocks

Although all MMS share the same concept and functionalities, the diversity among different MMS, is in the types and grades of sensors depending on the application, mapping platform, integration scheme, and the required accuracy [El-Sheimy 07]. Figure 2.3, summarizes the different categories and components of MMS. An MMS can be built by using one or more objects from each of these categories [El-Sheimy 04].

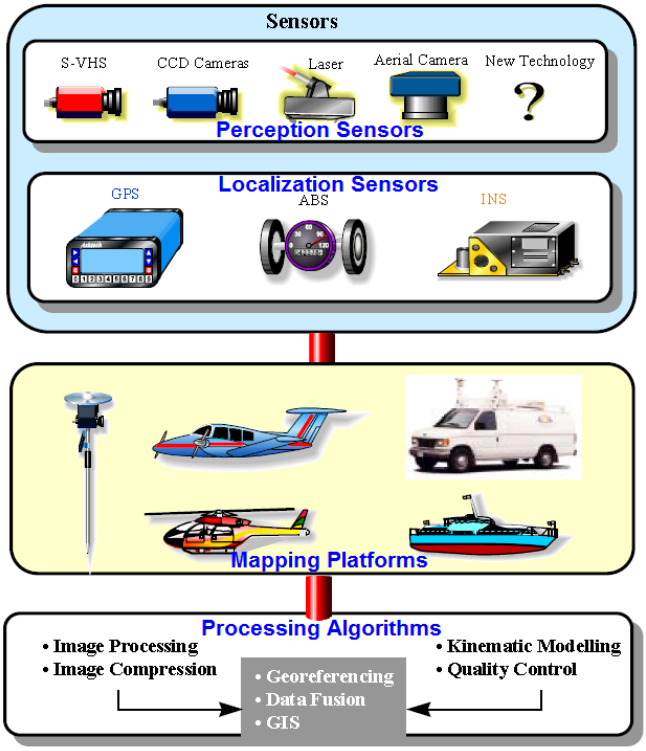

Figure 2.3: Elements of a mobile mapping system (modified version of [El-Sheimy 96])

The overall functionalities of an MMS can be summed up using figure 2.4. The two primary processes are: localization and georeferencing.

2.6.1 Localization process

As defined earlier, the process of determining the position and orientation of the moving mapping platform from the acquired sensor measurements is termed as localization. The pose computation has to be performed between short time spans to estimate the true trajectory traversed by the mapping platform [Abuhadrous 03b], [Goulette 06]. In the

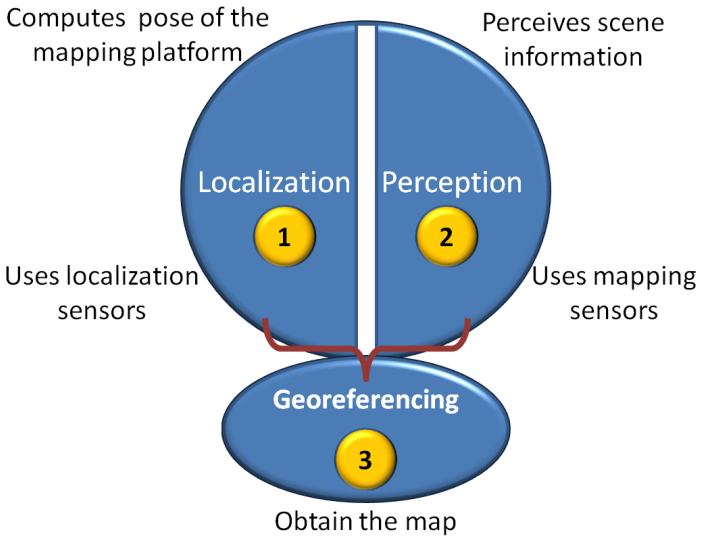

Figure 2.4: Primary functionalities of MMS

MMS literature, this process is also termed as Position and Orientation System (POS) functionality ([Hutton 97] [Scherzinger 00] [Graefe 01] and [Sever 04]).

The process is shown using figure 2.5, where the Moving Reference Frame (MRF) is first estimated using the sensor measurements, which are then mapped to a fixed coordinate system using the transformation matrix R_b^{map}.

Since there is no single sensor which can accurately estimate the complete position and orientation of the moving mapping platform, with respect to a fixed reference coordinate, it is normally estimated by the data fusion of a GPS receiver and an Inertial Measurement Unit (IMU). Although each technology can in principle determine both position and orientation, they are usually integrated in such a way that the GPS receiver is the main position sensor, while the IMU is the main orientation sensor [Schwarz 07]. In MMS, IMU is widely used because it can compute the pose information in 3D space at a higher data rate. However, due to the high drift rates in their pose estimation, they are often limited to fill the gaps in the GPS positioning for short periods of time. Additionally sensors such as odometers, are used for aiding the localization functionality.

The most common way to combine the measurements of different sensors and to estimate the pose is to use the data fusion approach like different flavors of Kalman filters. Among these, an Extended Kalman Filter (EKF) is widely used for modeling the nonlinear motion of the moving platform, with a loosely coupled integration scheme where the GPS position and velocity solutions are directly combined with the Inertial Navigation System (INS, an integrator of IMU signal) position, velocity and attitude information [Abuhadrous 03a], [Moon 99]. IMU is used in the prediction step of the EKF

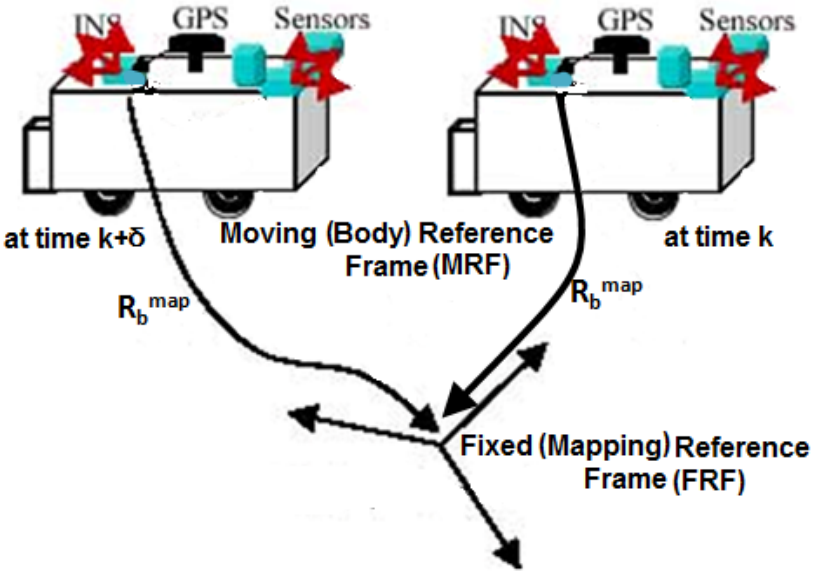

Figure 2.5: In the localization process the pose of the mobile platform is determined in Moving Reference Frame (MRF) at each instant of time, using the input sensor measurements and then mapped to a Fixed Reference Frame (FRF)

to determine the state transitions, because of the higher data rate and the differential nature of its measurements. GPS measurements with lower data rate are used for correcting the predicted estimate of the system state (pose and its derivate information). This setup is commonly known as GPS/INS integration filter.

To overcome the limitations of EKF, some studies used Unscented Kalman Filters (UKF) ([Julier 97], [El-Sheimy 06]) and others applied artificial intelligence techniques like neural networks [Chiang 05]. These techniques are employed for better estimation of the nonlinear motion of the land vehicle, which in EKF is treated as a sequence of short term linear steps.

In addition, in the presence of obstacles to the satellite signals, GPS receivers face outages (minimum of four satellites need to be visible to compute a 3D pose). The tightly coupled scheme, over comes this problem, by adding supplementary measures derived from the IMU measurements([Scherzinger 00], [Giebner 03], [Sever 04], [Wendel 04]). As stated in [Weiss 95], under good satellite geometry, both the loosely coupled and tightly coupled schemes behave identically. However, under degraded satellite signal conditions a tightly coupled scheme is more appropriate. The need to have a high quality IMU, and the implementation complexities (average implementation time of 3 years [Knight 02]) of the tightly coupled scheme are the limiting factors, in comparison to the simple structure and easy implementation of the loosely coupled system [Abuhadrous 03a].

In addition to these, there is an additional choice, to use a calibration technique: an open loop (feed forward), where the Kalman filter estimates the pose information, and the closed loop (feedback), where the INS provides the pose information which is corrected by the Kalman filter [Abuhadrous 05]. In the later case, Kalman filter estimates the residual between the predicted pose estimate (using INS rate measures), and the observed GPS pose solution. Most MMS, prefer closed loop solution because the system output (pose) rate is same as the output rate of the INS (INS output is accurate within short span of time), which is generally a magnitude higher than the open loop technique, limited by the output rate of GPS receivers.

Several MMS including the commercial MMS solutions like Applanix and StreetMapper have tried out most of the feasible combinations of the integration schemes. Some MMS identify the localization functionality as individual subsystem; e.g. Hybrid Inertial Survey System (HISS) ([Manandhar 00], [Manandhar 03]), Position and Orientation System for Land Vehicles (POS/LV) ([Scherzinger 00], [Graefe 01] and [Sever 04]) and IGI TERRAControl GPS/INS system for StreetMapper [Hunter 06] etc.

2.6.2 Direct georeferencing

The georeferencing identifies the spatial position of the objects scanned by the perception sensors (laser or camera), at any time while the vehicle is moving, with respect to a common coordinate system, as shown in figure 2.6 [Manandhar 00]. In MMS, this technique is often referred as *direct georeferencing*.

This is fundamentally different from traditional *indirect georeferencing*, where the position and orientation of the platform are determined using measurements made to control points. The establishment of these points are done by field surveys (e.g. by using total stations) prior to the data acquisition. This operation is expensive and time-consuming. Also, for many terrestrial surveys, the establishment of sufficient control points is virtually impossible [Shi 08], [Reshetyuk 09]. On the contrary, direct georeferencing, localizes the perception sensor measurements on the map, by using the estimated pose of the vehicle at the instant of perception. For this reason, the localization is a key step for MMS, in order to compute the pose of the mapping platform with respect to a fixed coordinate system.

The entire process of georeferencing can be expressed by the formula in equation 2.1, where a point $\mathbf{p}$ is localized on a map at $\overrightarrow{X_p^{map}}$, referenced in FRF. The specified equation is for a laser MMS.

$$\overrightarrow{X_p^{map}} = \overrightarrow{X_{gps}^{map}} + \mathbf{R_b^{map}} \left[\mathbf{R_{laser}^{b}} [\overrightarrow{X_{laser}}] + \mathbf{T_{laser}^{b}} \right] \tag{2.1}$$

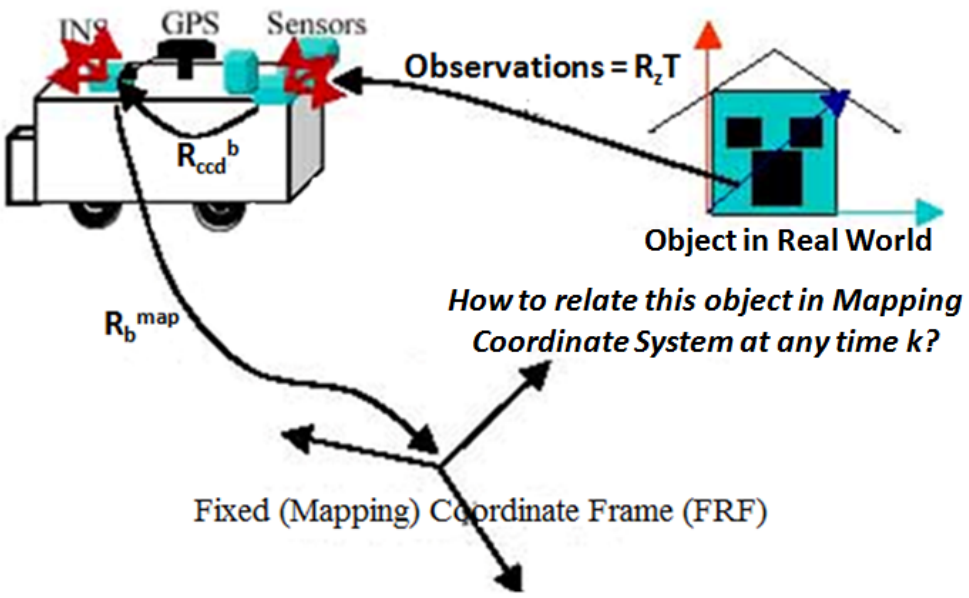

Figure 2.6: Georeferencing (modified version, original from [Manandhar 00])

In equation 2.1, $\overrightarrow{X_{gps}^{map}}$ and $\mathbf{R_b^{map}}$ are the results of localization functionality. $\overrightarrow{X_{laser}}$ is the laser measurement given in laser coordinate (LRF). $\overrightarrow{X_{laser}}$ is first transformed to the body coordinate (or MRF) of the vehicle, by using rotation $\mathbf{R_{laser}^b}$ and translation $\mathbf{T_{laser}^b}$ components, measured by calibration. This is then transferred to the FRF using the localization results to obtain $\overrightarrow{X_p^{map}}$.

2.7 Importance of localization for a Mobile Mapping System

The accuracy of an MMS generated map mainly depends on the accuracy of the pose estimates of the moving platform. As uncertainties in the laser scanner and photogrammetry measurements are relatively low, their influence on the accuracy of the map is insignificant compared to lolalization errors.

Apart from the accuracy, the continuity of the pose information is also an important aspect. A good MMS can therefore operate without interruption in areas where a discontinuity in the data from one or more of the navigation sensors is expected [Hassan 07], meaning typically overcoming the GPS outages. Discontinuity in the localization causes discontinuity in the map.

An alternative is to use more sensors complementary to each other. However, apart from GPS receivers and the IMUs, no other sensor addresses the pose in 3D space. Additionally, solutions to use high-quality sensors such as a navigation grade IMU is an expensive solution, not affordable to many MMS applications. The input sensors are the most critical elements of the localization functionality.

2.8 Localization sensors and their limitations

This section briefly describes the three main localization sensors of an MMS: a GPS receiver (a type of GNSS receiver), an Inertial Measurement Unit (IMU) and an odometer.

2.8.1 Global Navigation Satellite System (GNSS) receivers

- **Fundamental working principle**

  This sensor family computes the 3D position information (specifically, phase center of the antenna) on the basis of the received satellite signals. In most of literature, it is mentioned as *Global Positioning System* (GPS) receiver, since the receipted signal is only from the GPS satellite constellation governed by United States of America. The position is computed with respect to Earth, and thus serves as a global reference (like WGS84) for all terrestrial applications. Apart from position and a globally synchronized precise clock measurements, the velocity and the yaw can be deduced (other angles are not very useful due to the vertical position is often subjected to large errors). The term GNSS fix (in case of GPS only, called as GPS fix) is used to indicate the output position and velocity signals.

  Apart from GPS, there are a few other GNSS present around the world: *GLObalńaya NAvigatsionnaya Sputnikovaya Sistema* (GLONASS) from Russia, *Galileo* from Europe, and *Compass* from China, apart from a few other regional satellite systems. In the recent developments receiver manufacturers are using all the available signals from different satellite constellations, in order to increase the number of visible satellites.

  A receiver computes its position by knowing the positions of the satellites whose signals are being received, and deducing its pseudorange (not a fixed range, since the satellites are continuously orbiting) to these satellites. At least four satellites are needed to resolve the position in 3D, with four unknowns, three pose and the time. There are plenty of literature available describing the functionality of GNSS or GPS receivers [Hofmann-Wellenhof 08], [Kaplan 06].

  Figure 2.7 sums up the overall GNSS functionality, where a hand held GNSS receiver is shown, held by a man in the middle of the scene. The ground segment

transmits signals to the GPS satellites as well as monitors their health as they pass over its location (shown in orange colored arrow). The user segment receives signals from the space segment (GNSS satellites), shown by red arrows. The signals from the satellites need to pass through the Earth's atmosphere prior being received by the user. The two layers of Earth's atmosphere that introduce significant delays for the electromagnetic signals are the *ionosphere* and the *troposphere*.

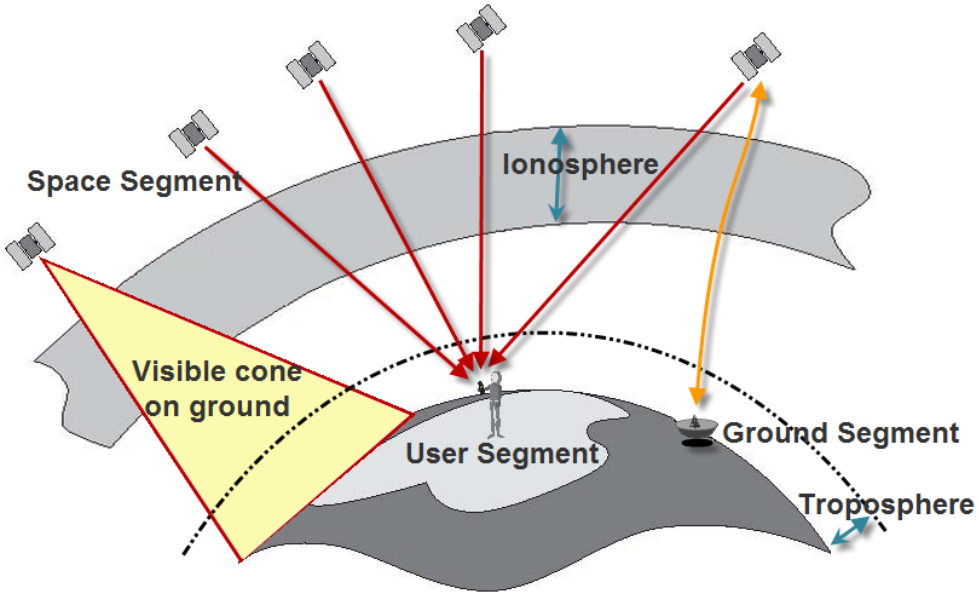

Figure 2.7: GNSS overall functionality with the three segments. An MMS is part of the user segment with a signal receiver.

In this thesis, the term GPS receiver is used to be coherent with other MMS related literatures. The satellites transmit signals in different frequency bands. Most of the commercial receivers can only process the $L1$ frequency signal, therefore, termed as single frequency receivers.

- **GPS error sources**

GPS errors are expressed in the form of *GPS Error Budget*. In table 2.2 a typical example is taken by referring to [Jekeli 00], [Misra 01] and [Schultz 06].

1. Space segment errors

   This includes the satellite clock and the orbital position perturbation. GPS satellites use atomic clocks and the errors are in the magnitude of $1\mu s$ corresponding to an error of $300m$ and it changes slowly over time. Orbital

Segment	Uncorrected source	Range (in m)
Space segment	Satellite clock error	0-3
	Satellite perturbation	0-1
Control segment	Ephemerides error	0-3
	Selective Availability (induced by USA military but not valid since 2000)	30-100
User Segment	Ionosphere	2-20
	Troposphere	0.5-5
	Multipath	0-5
	Receiver clock error	0-10
	Receiver noises like channel biases	0-0.5

Table 2.2: GPS error budget

position perturbations correspond to the slight variations in the orbital position of the satellites compared to the commanded position by the ground control.

2. Control segment errors

   There are two kinds of errors, Ephemerides or the orbital error and the Selective Availability (SA). The first is the error between the satellite position transmitted by the ephemeris message (sent by the GPS satellites) and the true position. Selective Availability (SA) error is induced by the US military, but it is turned off since May 2000.

3. User segment errors

   These errors are linked to specific receiver hardware, geographic location of the user, and time of the GPS signal reception.

   Ionosphere and Troposphere errors are the significant dynamic delays introduced by the Earth's atmosphere, which change depending upon the elevation angle of the satellite with respect to the receiver location, time of the day, presence of solar flares, weather conditions etc.

   The *Receiver clock error* is the offset between the receiver clock and the universal GPS-time. Receiver noise includes channel biases, computational rounding errors etc.

   Multipath is the phenomenon caused by satellite signals taking an indirect path to the receiver antenna (line of sight). This occurs due to the presence of satellite signal reflectors such as glass, water and metal on the line of sight. The signal path therefore gets longer, and this can result in huge errors that sometimes dominate the entire error budget [Schultz 06]. This is one of the main concern for the MMS in the manmade environments.

Signal obstructions are caused by the presence of obstacles masking the clear view to the sky. The more the number of satellites a GPS receiver can lock with, the better its accuracy. Therefore obstructing environments can degrade the accuracy of the results. The obstructions can induce multipath, or narrow down the visibility to the sky (Dilution of precision or DOP), or mask many otherwise visible satellites. These obstacles can be manmade buildings, rocks and mountains, dense foliage, electronic interference, in short everything that comes in the line of sight. These are the reasons, GPS receivers do not work indoors, underwater and underground. These problems are summarized in figure 2.8.

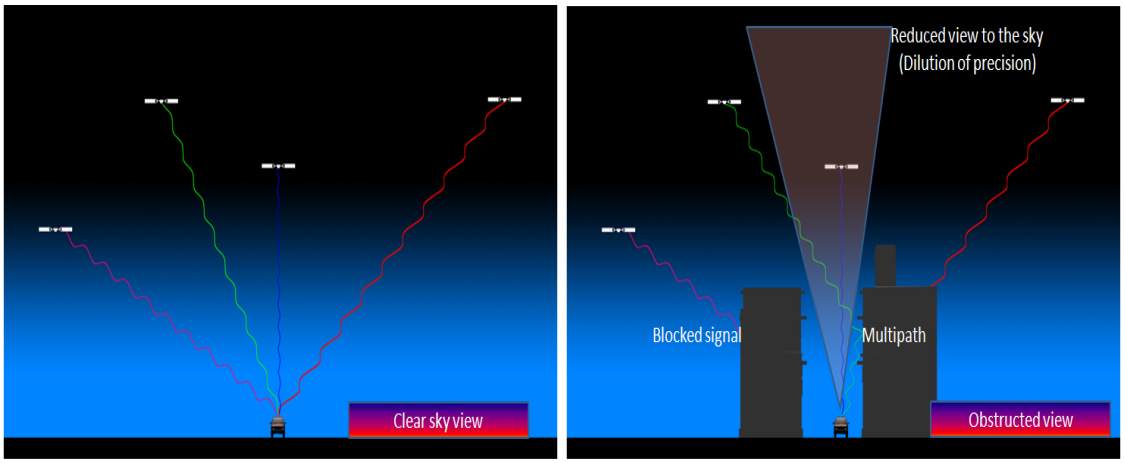

(a) Positioning under clear sky

(b) Positioning in a obstructed environment

Figure 2.8: Computing position using GNSS receivers in open and obstructed environments (objects are not to scale)

In this dissertation, the multipath, high DOP and complete outage of GPS fix errors are termed together as the *User Local Environment Errors (ULEE)*. Even under clear sky, all errors except ULEE do exist. The GNSS technology has evolved over a period of time to address these errors by using augmentation techniques such as Differential GPS (DGPS), Real Time Kinematics (RTK) or offline corrections (refer to Annex B). The principle of these techniques is, to use single or a network of fixed GPS receivers placed in known locations inorder to compute the errors and error budgets. This information is then transmitted to the users in the zone of corrections as shown in figure 2.9. This figure is the same as figure 2.7, but has an additional fixed reference station to provide corrections for the GPS fix. The fixed reference station sends the correction information to the user (shown by dark green arrow).

However, the ULEE's are the errors most difficult to tackle especially for a land-based system like MMS, since, in many occasions the GPS position fix is either

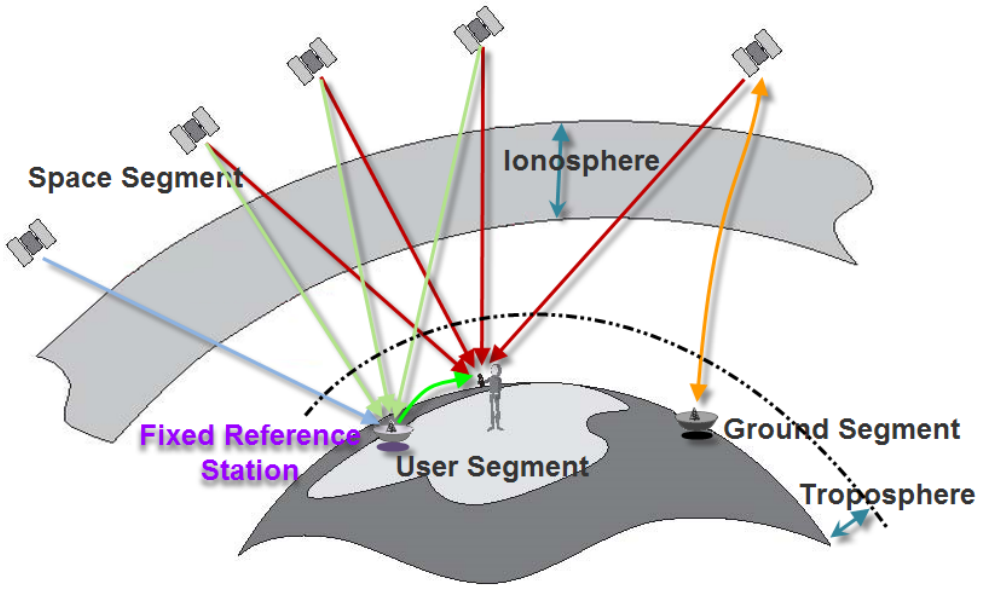

Figure 2.9: GPS error correction using a fixed base station

not available at all, or is discarded due to poor accuracy.

- **Advantages and disadvantages**

  GNSS receivers, principally the GPS receivers, provide 3D positioning around the earth, in a common (Earth fixed) reference frame. They are preferred pose sensors for all outdoor applications including MMS. The errors in the output of these systems do not grow over time (no drift). Most of the systematic errors are mitigated using several correction technologies, and the position accuracy can even reach the precision of decimeter levels.

  However, for the land-based applications, which need precise positioning in the outdoor, indoor or underground environments, GNSS-based positioning cannot work as desired due to the presence of obstacles for the direct view to the sky. These errors are the User Local Environment Errors (ULEE, refer to section 2.8.1), which are nearly impossible to avoid. Additionally, the GNSS receivers provide position fix at a relatively low rate (10Hz to 1Hz), and it is preferred to have higher output rates for several applications including mapping. Finally, there are several external elements involved in the process of computation of the position fix: like the space, control and user atmosphere, user environment, etc. Therefore, the quality and continuity of the obtained position fix depends on all these different elements making it very dynamic for modeling.

2.8.2 Inertial Measurement Unit & Inertial Navigation System

Along with GNSS/ GPS receivers they are the most widely used localization sensors for MMS. Regardless the significant drift errors in the localization, IMU was the principal navigation sensor until GPS became popular, used mainly for military purposes.

- **Fundamental working principle**

  Inertial measurement unit (IMU) is a sensor assembly consisting of a set of gyroscopes and accelerometers, typically 3 of each type. Gyroscopes measure the rotation rate or angular velocity of the assembly, and accelerometers measure the linear acceleration of the unit along with the vertical acceleration, due to gravity. An IMU is analogical to the semicircular canals and vestibule in the human ears, which helps to keep the body in a balanced state by measuring the body rotation and acceleration.

  An Inertial Navigation System (INS) is an IMU signal integrator, which helps compute the *relative localization*, the orientation from angular velocity, and velocity and position from acceleration. It can be noted that if an IMU is moving with a constant velocity in a straight line, then for short periods of time the sensor can mainly measure, only the acceleration due to gravity and not any motion specific parameters. This sensor works based on the principle of inertial frame of reference, and measures anything which tries to change this inertial frame of reference, like the rotation and the acceleration. There are several text books and articles available on the functionalities of the inertial navigation system ([Farrell 99], [Grewal 01], [Schmidt 04], [Schultz 06], [Hou 04] and [Feynman 06]).

  The overall picture of Inertial Measurement Unit (IMU), Inertial Sensor Assembly (ISA) and Inertial Navigation system (INS) is shown in figure 2.10.

  As stated before, IMU consists of an ISA, consisting of accelerometers and gyroscopes. The purpose of gyroscope is to provide the inertial reference frame, while doing so, compute the change in the orientation of the body. IMU makes use of this inertial reference frame information to compute the accelerometer orientations regardless the orientation of the body (e.g. a sensing platform like a vehicle or a robot) which is carrying the IMU. By knowing orientation of the body, vertical direction with respect to Earth can be determined, from which the acceleration due to gravity can be deduced. This is deducted from the measured accelerations to obtain the true acceleration of the body.

  An accelerometer is generally a proof mass that is held in a case by a pair of springs, and it measures the acceleration (proportional to force) along a sensitive axis, by measuring the displacement of the mass corresponding to the applied force. An accelerometer measures all types of accelerations: gravitational, body, and even vibration. Therefore, it is critical to measure the true acceleration of the body by eliminating the acceleration effects from other sources, especially gravity.

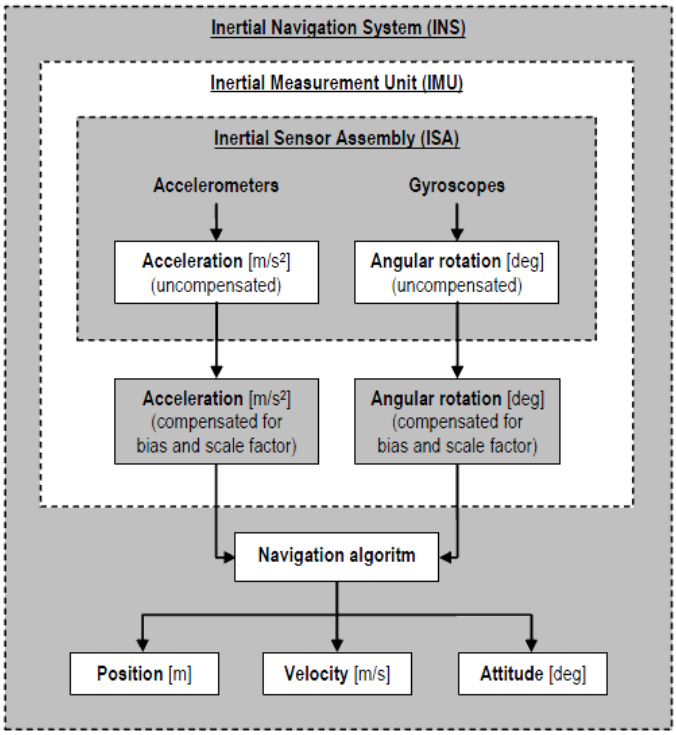

Figure 2.10: Description of Inertial Sensor Assembly (ISA), Inertial Measurement Unit (IMU) and Inertial Navigation system (INS) [Schultz 06]

The initial gyroscopes were purely mechanical and huge in size. However, due to the presence of friction between the spinning parts it was hard to retain the orientation. The optical gyroscopes (ring laser gyroscopes (RLG) and fiber-optic gyroscopes) overcome this, since they measure the rotation rate by observing the change in the phase of the light signal.

From figure 2.10, the INS basically a computer consisting of three integrators; two to compute position from the acceleration and one for the rotation angle from the angular rates. Inertial sensors can be implemented in two different ways to build up an INS: a gimbaled and strap down system (shown in figure 2.11).

A gimbal is a rigid frame with rotation bearings for isolating the inside of the frame from external rotations about the bearing axes. In this arrangement the accelerometers are maintained in a fixed orientation, by retaining the alignment of the stable platform using servo motors controlled by gyro measurements. This kind of systems are more precise, but they are relatively big and heavy due to the mechanical arrangement of gyroscopes.

A strapdown arrangement is where both the accelerometers and gyroscopes are packed in a case and directly mounted on to the sensing platform. In this setup, the

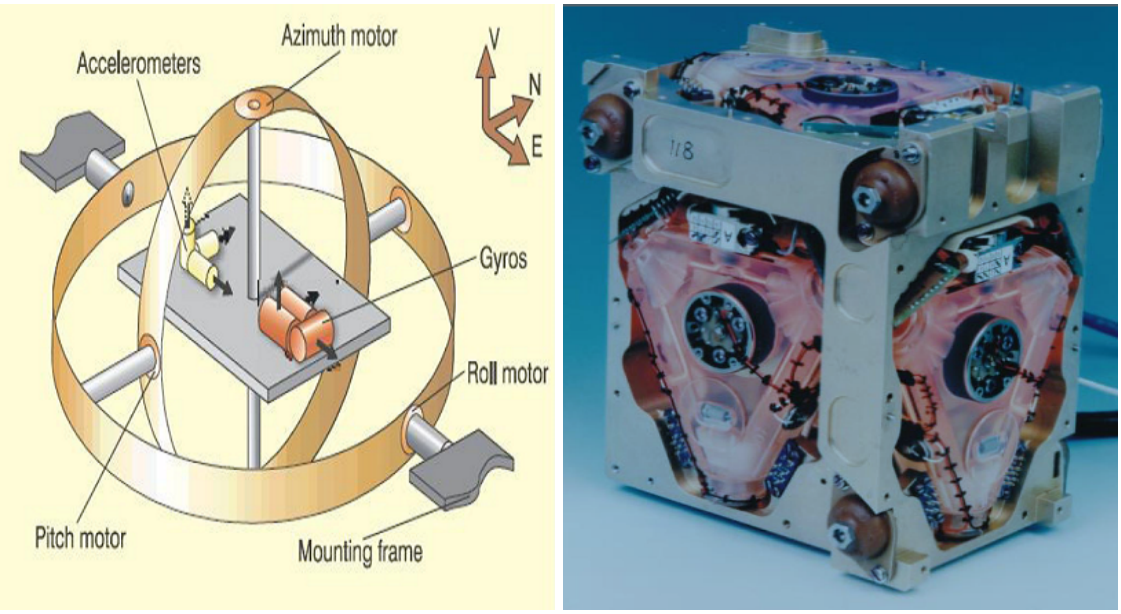

(a) Model of a gimbaled INS (b) A strapdown INS - Marconi FIN3110

Figure 2.11: Gimbaled and strapdown INS

accelerometers do not remain aligned to a specific navigation platform. Therefore, the measured acceleration needs to be transformed to the navigation frame by using the integrated angular rates measured by the gyroscopes. These are the most commonly used IMU arrangement for applications such as MMS, due to the reduced size, weight and cost, compromising slightly accuracy and precision.

- **IMU error sources**

  The main error sources in the INS are due to gyro and accelerometer imperfections, incorrect navigation system initialization, and gravity model errors. However, for most INS, the largest errors are due to the inertial sensors [Schmidt 04].

  The measurement errors can be categorized in bias, bias drift, scale factor and random noises [Flenniken 05]. Apart from these errors, since IMU is an assembly of sensors, it needs to be calibrated for misalignments in the sensor assembly, which can occur over a period time. Even the temperature can cause a drift in the measurements as it increases over a period of usage, and it can disturb the internal mechanical setup.

  As given in [Schwarz 04], IMUs are classified based on the quality of gyros used. Gyros are distinguished according to their drift rates, namely:

  1. strategic gyros (0.0005-0.0010 deg/h or 1 deg/month)

2. navigation-grade gyros (0.002-0.01 deg/h or 1 deg/week)
3. tactical gyros (1-10 deg/h or 1 deg/h)
4. low-accuracy gyros (100-10 000 deg/h or 1 deg/s)

[Cramer 97] compares the quality vs cost of the typical IMUs, given in table 2.3.

Time interval	**High precision (>$750 000)**	**Medium precision (>$100 000)**	**Low precision (>$10 000)**
Position			
1 hour	0.3-0.5 km	1-3 km	200-300 km
1 min	0.3-0.5 m	0.5-3 m	30-50 m
1 sec	0.01-0.02 m	0.03-0.1 m	0.3-0.5 m
Attitude			
1 hour	3-8 mdeg	0.01-0.05 deg	1-3 deg
1 min	0.3-0.5 mdeg	4-5 mdeg	0.2-0.3 deg
1 sec	<0.3 mdeg	0.3-0.5 mdeg	0.01-0.03 deg

Table 2.3: INS quality vs cost classification [Cramer 97]

Most of the mapping applications use tactical grade IMUs. Recent development in the Micro Electro Mechanical Systems (MEMS) IMUs, reduces the size, weight, power consumption and most importantly the cost, thus making it more suitable for the future applications. However, at present, their precision and accuracy are their main limitation.

- **Advantages and disadvantages**

IMU measurements are autonomous (they measure the forces), and do not rely on any external aids or visibility conditions. It can operate in tunnels, underwater or underground. IMU measures the derivatives of position and orientation, therefore, suitable for computing the relative localization. A typical IMU with three accelerometers and three gyros provides a complete 6DOF pose information in the 3D space.

Mapping applications prefer smaller, less heavy and low cost IMU's, making the strapdown IMUs more suitable. Moreover, the output rate of an IMU is in the order of 100 Hz nearly 10 times faster than the typical GNSS receivers.

However, a good quality IMU costs a lot. Lower-end IMUs have huge biases in the linear acceleration and the angular velocity they observe. Due to integration, these biases produce drifts in the computed linear velocity, orientation as well as in the position. Small errors in the measurement of acceleration and angular velocity are integrated progressively into larger errors in velocity and position. In addition to this, an incorrect gravity model, and a sensor assemblies misalignments can

make IMU outputs nearly unusable. The biases are caused by the initial sensor alignment errors, temperature and electromechanical components of the IMUs.

2.8.3 Odometer

In some MMS, odometers are the main additional sensors used to support GPS/INS setup. However, it can provide only a 2D pose information.

- **Fundamental working principle**

  An odometer indicates the distance traveled by a wheeled sensing platform, by measuring the distance as a function of rotation rate of the wheels. The original odometers dates back to more than 2000 years, but today the device can be electronic, mechanical, or a combination of the two. For most of the mobile robot applications odometry is the common relative positioning approach [Borenstein 02], [Povazan 95].

  The principal idea is to measure motion of a wheeled robot or sensing platform using the kinematics information, i.e., mathematical study of the motion without considering the forces that affect the motion. This is achieved by measuring the rotation rate of the wheels of the sensing platform, and then by using the known radius of the wheels to derive the linear velocity.

  A mechanical odometer is nothing more than a gear train with an incredible gear ratio. The electronic odometer, instead of a gear train uses a toothed wheel mounted on the output of the transmission, and a magnetic sensor that counts the pulses as each tooth of the wheel goes by. Some odometers use a slotted wheel and an optical pickup, like a computer mouse does. By using a computer termed as a serializer, the number of generated pulses are counted, and the distance the robot traveled is deduced.

  The principle of computing the linear velocity from the angular rate is shown in figure 2.13. The conversion of angular rate ω, measured by the wheel rotation counters, to linear velocity v, is a function of the radius r and the angle θ.

  Regarding the modeling of the odometer there are two common approaches adopted; differential and synchronous drive. Differential drive is used in a non-holonomous motion contrary to synchronous drive (i.e., each wheel motion can be independently steered and controlled). For a system like MMS using land vehicles a differential drive model is suitable.

  Most of the mapping platforms have four wheels. Therefore, they use a bicycle or tricycle model to determine the motion of the sensing platform. For four wheeled vehicle, the two front steering wheels are replaced by a one in the middle. Tricycle model is the most commonly used model, where the wheel rotation

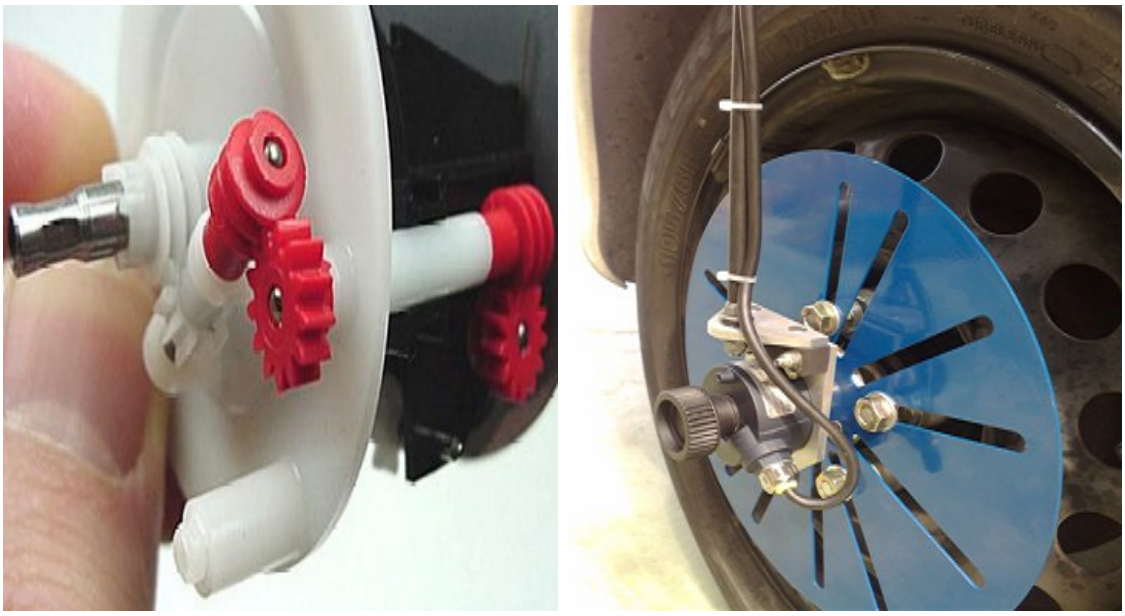

(a) Mechanical odometer - using gear trains ([Works. 10])

(b) Electronic odometer - with a toothed wheel and the wheel counter (from Ecole des Mines)

Figure 2.12: Two types of odometers

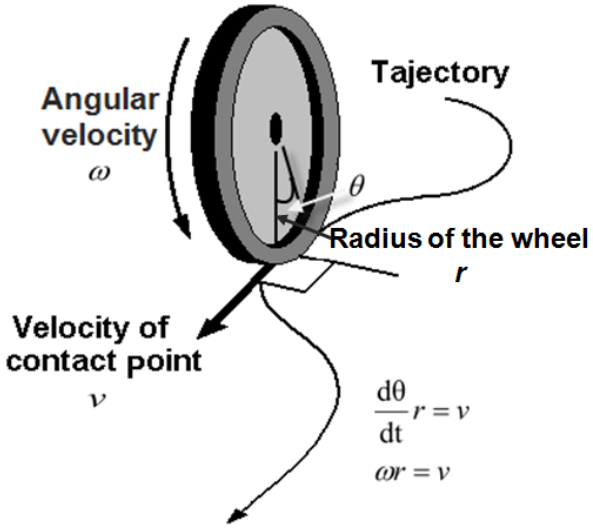

Figure 2.13: Odometer - linear velocity computation

counters are fixed to the rear wheels of the robot as they are not used for steering the vehicle and normally follow a linear motion. These models are described

in [Ribeiro 02], [Povazan 95] and [Abuhadrous 05].

The differential drive expresses the velocity of the vehicle as a function of the velocity of the individual wheels. The odometer is believed to always follow a path with a certain curvature γ, and Instantaneous Center of Curvature (ICC), is the instantaneous center of this hypothetical path. It is obtained by computing the intersection of the rear wheel axis with the line perpendicular to the direction of motion. For a straight path, the radius of curvature is infinity or in other words the velocity of the left and the right wheels are equal. ICC is minimum when heading angle ϕ is maximum (ϕ_{max}). Normally for a robot $|\phi| \leq \phi_{max} < \frac{\pi}{2}$.

- **Odometer error sources**

[Borenstein 02] lists different sources of odometer errors. Apart from the total slippage, the distance estimation inaccuracies are caused by:

1. Systematic errors: They occur due to unequal wheel diameters, misalignment of wheels, uncertainty about the effective wheelbase (due to nonpoint wheel contact with the floor), limited encoder resolution, and limited encoder sampling rate. Considering that these errors lie on the physical structure itself, they accumulate constantly over time.
2. Nonsystematic errors: They mainly occur due to the nature of the surface, including travel over uneven floors or unexpected objects on the floor, wheel-slippage due to slippery floors, over-acceleration, fast turning (skidding), external forces (interaction with external bodies), internal forces (e.g. castor wheels), nonpoint wheel contact with the floor.

On the smooth indoor surfaces systematic error contribution is highest, while on rough surfaces with significant irregularities, nonsystematic errors can be dominant. The precision of the linear approximation of motion depends on the sampling frequency with respect to the speed of the robot. Any orientation errors incurred, grows without bound into lateral position errors.

- **Advantages and disadvantages**

Odometers are the primary localization sensors for the indoor robotic applications, with a price advantage. An electronic odometer is an integral part of the Anti-lock Breaking System (ABS), in most of the automobiles. The equation for the computation of the position involves a single integration,and the formulas are straight forward for implementation. Similar to IMU, odometers are also autonomous, needing no external system to transmit the signals.

However, there are several limitations. The functionality of the odometer is limited by system model, relying on the robot wheels and the surface where the robot is driven. Any irregularities in the robot wheels and planar paths can cause errors

in the computed velocity, resulting in a position drift. If the wheel diameter is different from its specifications due to manufacturing defects or to wear and tear or to the load of the vehicle or to the pressure variations in the tire, the computed velocity gets distorted. Any non-alignment in the wheels also cause an error in the computed models. On the other hand, odometer measures become oblique if the robot is driven on an inclined surface. For an MMS, an odometer is typically modeled for a nonholonomic motion, i.e. with an assumption of no side slippage of the wheels. Many occasions it is not true, especially on rough terrains.

Finally, odometer measures the pose in 2D space with 3DOF. For many 3D applications this cannot be used as a primary pose sensor. Compared to GPS, it can provide only a relative pose (DR type). Thus the integrated position is prone to drift errors due to the accumulation of the errors in the computed velocity.

2.9 Conclusion

This chapter described the functionalities of Mobile Mapping Systems (MMS). MMS evolved because of the two sensor technologies, a GPS receiver and an Inertial Measurement Unit (IMU). Nearly 40 MMS are studied, all have dedicated localization sensors comprising of the GPS receiver and IMU. These sensors together can provide the complete 3D pose for all the 6 degrees of freedom (rotation and translation).

However, the present MMS limitations can raise from the dependency on these sensors, such as, the inability to map the GPS signal degraded environments, e.g. indoor, underground and urban environments.

Chapitre 3

Amélioration de la localisation par lissage des données

Comme décrit au chapitre 2, les limitations des deux principaux capteurs d'un MMS pénalisent la précision des résultats obtenus. Ces difficultés sont mises en évidence sur les cartes numériques générées par le système embarqué sur la plateforme LARA-3D, un véhicule terrestre. LARA-3D est une réalisation du laboratoire de robotique de l'École des Mines de Paris.

Les résultats de deux jeux de données de test montrent les erreurs typiques des capteurs de position. Les erreurs portent principalement sur l'altitude et la direction (erreur de lacet) de la trajectoire estimée. Les récepteurs GPS sont généralement sujets à des erreurs d'altitude plus importantes que les erreurs de position horizontale. Les erreurs les plus pénalisantes affectant les trajectoires calculées par les centrales à inertie sont des dérives de lacet.

Pour corriger de telles erreurs, quand elles sont évidentes, nous avons employé une méthode de post-traitement par lissage des données. Cette approche nous a permis d'améliorer les cartes générées par un MMS. Le post-traitement suppose que la méthode soit appliquée sur une trajectoire complète, de façon à avoir, pour chaque instant, une vision du passé et du futur.

Le lissage est effectué en imposant à la continuité de la trajectoire des contraintes acquises par expérience. Cette méthode permet de corriger tant des erreurs dues aux capteurs que des erreurs générées par le processus de fusion de données, y compris des imprécisions affectant les modèles des capteurs. Le filtre de Kalman étendu, utilisé pour réaliser la fusion des données, diminue également les sauts d'altitude, rendant leur détection et leur correction plus difficiles.

Dans ce chapitre, nous présentons une méthode de détection et de correction automatique des sauts d'altitude. Une approche complémentaire de lissage, fondée sur les splines, nous permet de montrer que les erreurs triviales de trajectoire peuvent être corrigées. Les résultats ont été publiés dans l'article [Narayana 09].

Une telle méthode de lissage, fondée sur des contraintes de continuité, ne permet cependant pas d'atteindre un positionnement précis. Cette approche est, notamment, incapable de compenser les dérives lentes des centrales à inertie. Une autre solution, qui permette de déterminer la position en 3D d'une plateforme MMS, est hautement souhaitable. Une telle solution nouvelle doit idéalement fonctionner dans un environnement où la qualité de réception du signal GPS est dégradée, sans souffrir des mêmes dérives que celles liées aux centrales à inertie. La plateforme LARA-3D utilise des scanners à laser comme capteurs perceptifs de cartographie. Nous explorons, de ce fait, la possibilité d'utiliser ces mêmes capteurs pour estimer la position du véhicule.

Chapter 3

A smoothing approach for localization improvement

Contents

3.1 Introduction

Chapter 2 gave an overall view to the MMS and the localization functionality. This chapter, first, presents the land-based mobile mapping prototype platform *LARA-3D*,

with a couple of generated 3D maps, typical localization limitations are demonstrated. The smoothing solution we propose in this chapter, aims to identify and rectify the effect of these limitations on the 3D maps.

The chapter is organized as follows:

LARA-3D platform is presented in section 3.3, and its localization functionality in section 3.4. Section 3.5 illustrates some of the most recurrent problems of MMS, by using two data sets acquired by *LARA-3D*. We propose to use a post-mission processing technique to correct these errors. Section 3.6 gives a brief introduction to existing techniques, and section 3.7 presents our constraint-based smoothing approach. Obtained results and improvements from our approach is given in section 3.8. A short conclusion in section 3.9 ends the chapter.

3.2 Motivation

As described in chapter 2, most of the existing MMS suffer due to the shortcomings of its input localization sensors, especially GPS receivers. Several solutions has been analyzed in various literatures to address these limitations, such as, improving the sensor qualities (depends on cost), adding several aiding sensors (still limitation in pose space), improving the data fusion techniques etc. A feasible alternative is to rectify the problems in generated trajectories by applying some realistic constraints. This algorithmic approach does not need any additional sensors, and an effective way to improve the 3D maps generated by an MMS.

3.3 Land-based laser mobile mapping platform *LARA-3D*

Prototype vehicle platform *LARA-3D* designed and developed by the Center of Robotics (CAOR) of *Ecole des Mines de Paris (Mines ParisTech)*. It is a land-based MMS, comprising of a four wheel vehicle (Renault Espace) equipped with a set of localization sensors and a laser scanner as perception sensor. The initial system was developed in the PhD thesis [Abuhadrous 05].

LARA-3D platform has evolved over the years. The first configuration of the system had a single frequency differential GPS receiver (Model: Trimble Ag132, [Trimble 99]) with GBAS signals from Omnistar, an IMU (Model: Crossbow VG600, [Crossbow 01]), and a laser range finder (Model: IBEO LD A AF Series, [IBEO 09]). Later, a fisheye camera is added to obtain the texture information of the scene objects. The embedded computer has been upgraded to cope up with the increased data bandwidth during acquisitions. The present system configuration, like many medium cost MMS, uses a

single frequency GPS receiver (not a DGPS or a RTK), and a tactical grade IMU for the localization.

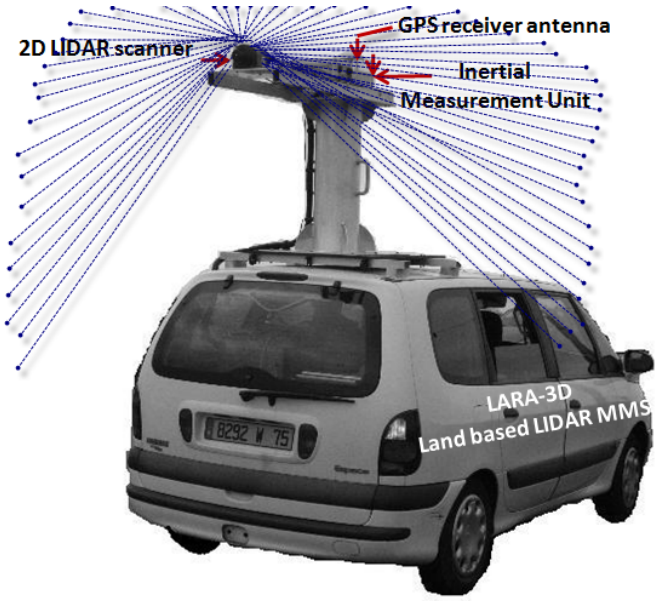

Figure 3.1: *LARA-3D* prototype mobile mapping platform - present configuration

A summary of all the potential sensors which has been used or can be used with the existing system configuration is given in figure 3.2.

These sensors are fitted to the vehicle on a stable platform and remain in a fixed location with respect to the body of the vehicle. The calibrated locations of individual sensors are applied to transform the measurements from sensor coordinate to body coordinates.

The work flow of *LARA-3D* is given in figure 3.3. During data acquisition, measurements of the perception and the localization sensors are captured, and logged with precise timestamps (precision μs). ^{RT}Maps from Intempora S.A. ([Intempora 07]) is used as the logging software. Different sensors can have different output rates, thus the accurate time stamping is critical for later processing.

In the present system configuration, the sensor output frequencies are: 5 Hz for Ag132 GPS receiver, 84 Hz for the IMU Crossbow VG600, and 10 Hz for IBEO laser profiles (i.e., 10 scans per second, with 1440 points per scan). The laser scanner has an angular resolution of 0.25 degrees. The fisheye camera is capable of providing 15 images per second, but used with a lower rate of 2 images per second, to not to overload the data logging. For the data processing, logged data can be replayed at different data rates with ^{RT}Maps components, providing ample time for the processing algorithms in

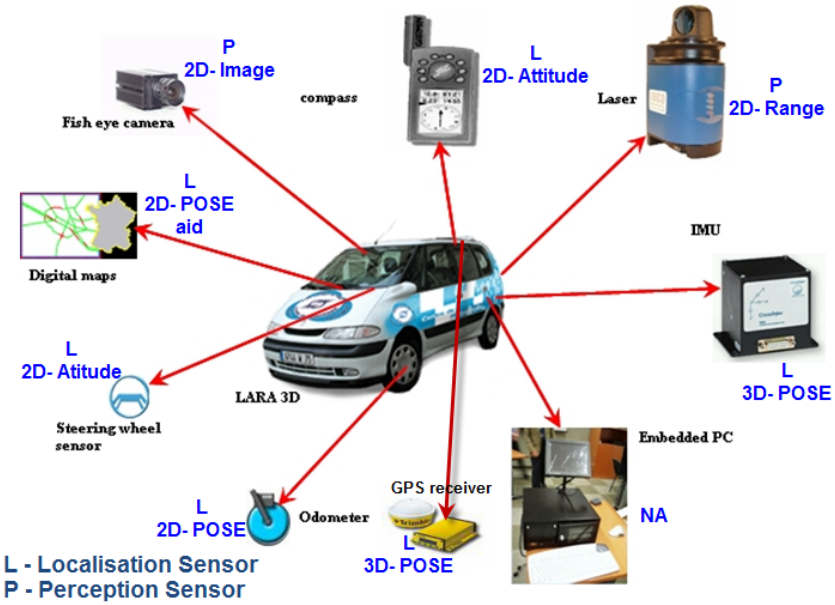

Figure 3.2: Different input sensors that can be used with *LARA-3D*. The localization and perception sensors are indicated by letters 'L' and 'P' respectively.

offline mode.

Figure 3.4 shows a typical 3D map (point clouds) obtained using *LARA-3D* platform.

3.4 *LARA-3D* localization functionality

The framework of laser MMS validation platform *LARA-3D* is given in figure 3.5, which is very similar to most of the MMS. As briefed in section 3.3, *LARA-3D* uses a single frequency GPS receiver and an IMU, as the localization sensors. The perception or mapping sensors comprises of a set of 2D laser scanners.

The localization functionality of *LARA-3D* is shown in figure 3.6.

In figure 3.6, r_{GPS} is the position in WGS84 (latitude, longitude and altitude - LLA) coordinate and v_{GPS} is the velocity determined by GPS receiver in the Local Tangent Plane (LTP) coordinate. Parameters r_{INS}, v_{INS}, and ρ_{INS} corresponds to the integrated position, linear velocity and attitude angles. The IMU measures only linear accelerations and angular rates, therefore, integrating it once, the velocity is computed, and twice, the position. Absolute values for the attitude angles of azimuth (yaw) ψ_{IMU}, roll ϕ_{IMU} and pitch θ_{IMU} are computed by integrating the angular rate measurements.

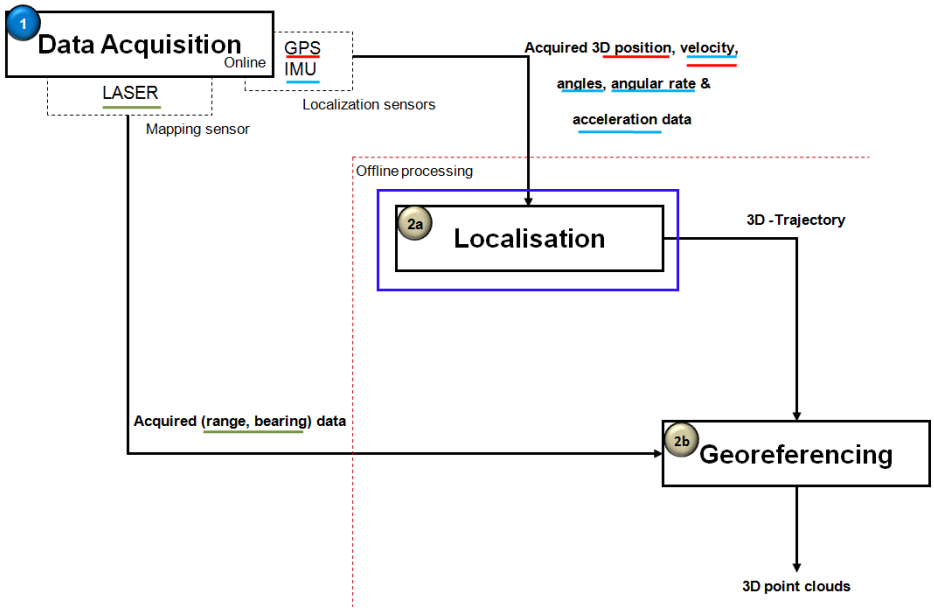

Figure 3.3: *LARA-3D* process of 3D point cloud generation, a real-time sensor data logging is done during data acquisition, and then they are processed. Each observables are underlined by the same color as the measuring sensor. These measurements are processed offline.

First Order Filters(FOF) are introduced to reduce the high frequency noise in the input IMU measures. The integration of the IMU measures to compute the state variables (pose information) is done by the INS mechanization functionality.

3.5 *LARA-3D* experimental results and analysis

The mobile mapping experimental platform *LARA-3D* performs well under normal conditions but like any other MMS, when used in environments with GPS signal disturbances, it demonstrates common localization problems.

- Acquisition framework

  Two separate data acquisitions are conducted in 2008, in France covering both urban and rural environments. The urban acquisitions (*Itinerary 01*) are conducted near the Pantheon in Paris. The rural acquisitions (*Itinerary 02*) are conducted in the region of Côtes d'Armor in Bretagne (France). The itineraries for these acquisitions are shown on the Google map in figure 3.7.

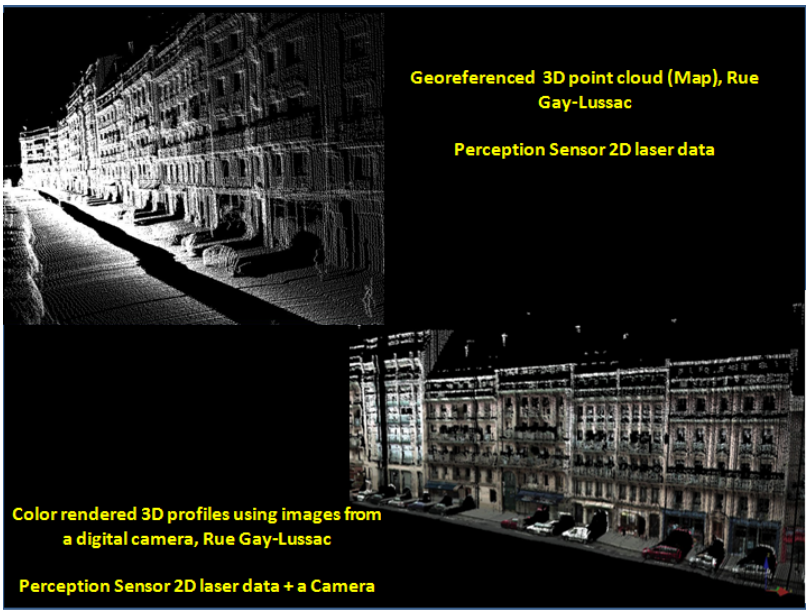

Figure 3.4: *LARA-3D* results - 3D point clouds generated from laser scanner measurements, and textured using the digital image

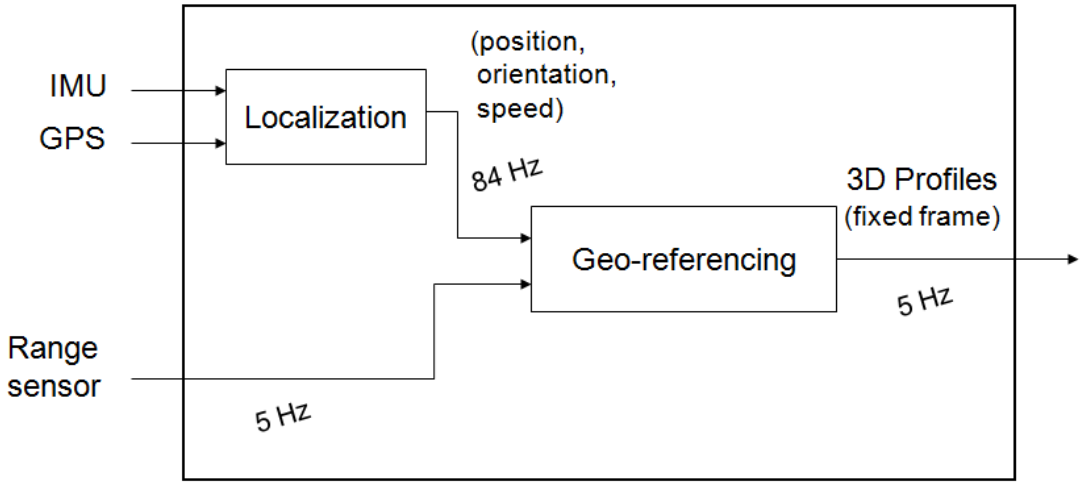

Figure 3.5: *LARA-3D* system architecture [Goulette 06]

Figures 3.8 and 3.9 provides the generated 3D point clouds from the direct georeferencing of *LARA-3D*. The global shape of the point clouds given in figures 3.8

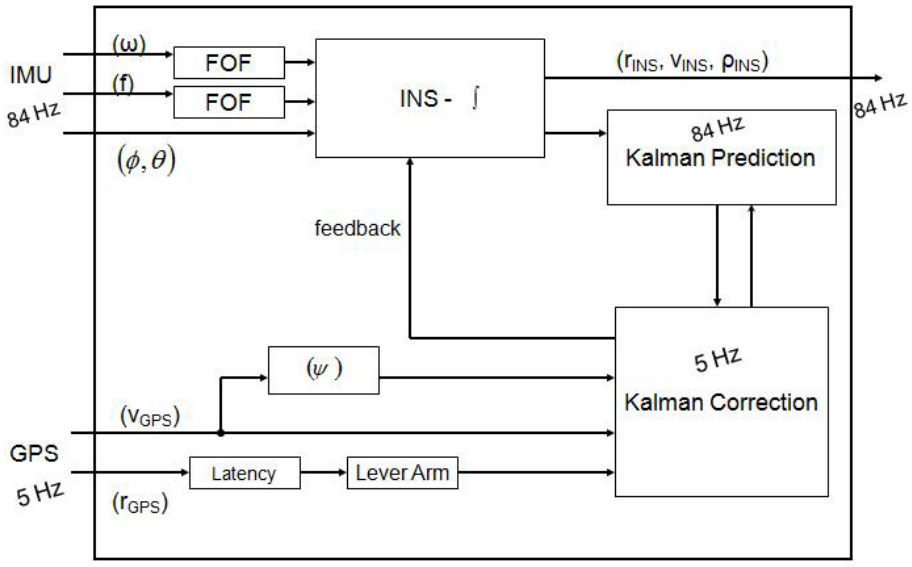

Figure 3.6: *LARA-3D* localization architecture depicting EKF as a data fusion filter with a loosely-coupled integration scheme, and a feedback calibration technique.

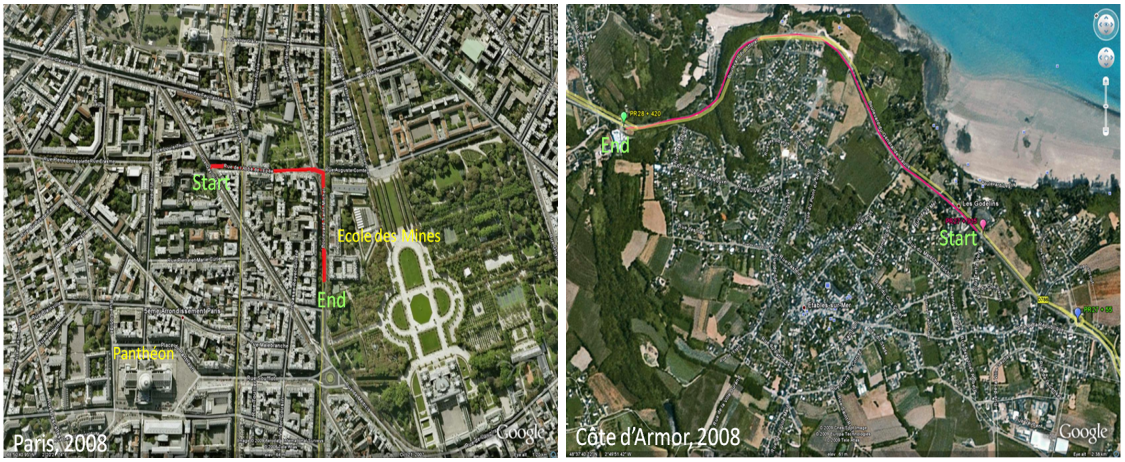

(a) *Itinerary 01*-an urban area (Paris,France) (b) *Itinerary 02*-a rural area (Côte d'Armor, France)

Figure 3.7: Two itineraries used for data acquisition with *LARA-3D*, from rural and urban areas.

and 3.9 match the itineraries shown in figures 3.7a and 3.7b respectively.

- Analysis

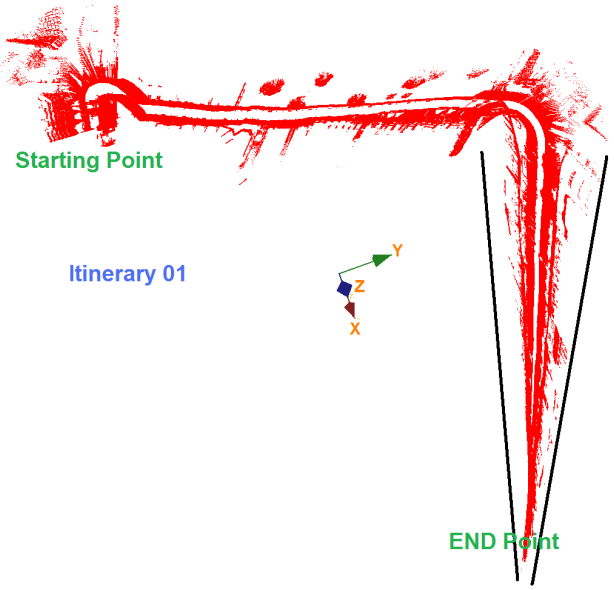

Figure 3.8: Top view of the point cloud for *Itinerary 01*. It shows the heading (yaw or azimuth) drift problem, resulting in the convergence of the point cloud at the end of the trajectory (shown by the converging black lines).

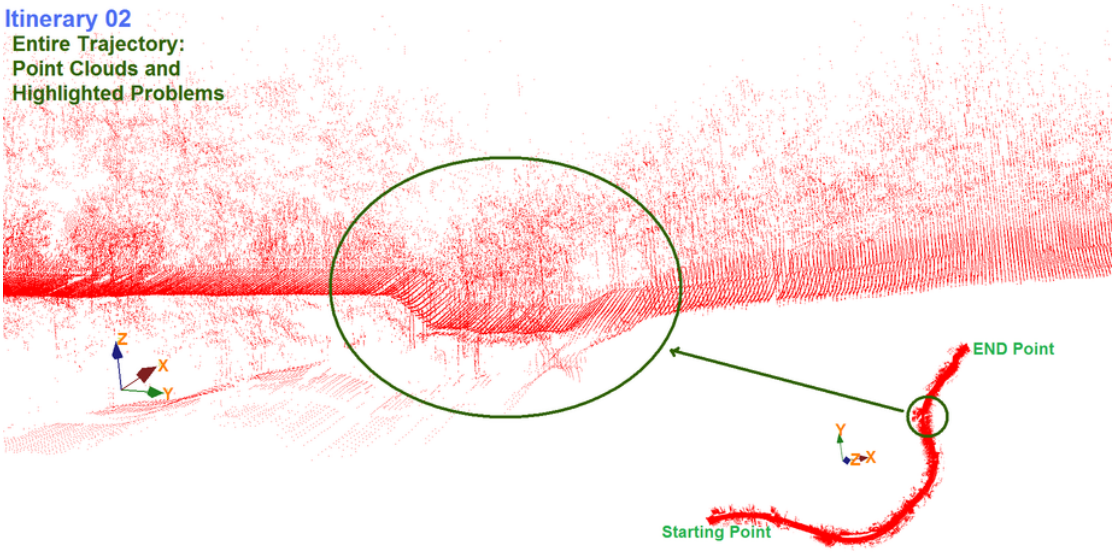

Figure 3.9: The main figure is the side view of the point cloud depicting the observed altitude jump. On the bottom the point cloud for the entire *Itinerary 02* is given.

As explained in figure 3.6, in *LARA-3D*, the correction step of Extended Kalman Filter (EKF) is performed only at 5 Hz, and not at all during the periods with no GPS position fix. This implies that the influence of the IMU bias on the computed trajectories is quite high during the GPS signal degradations.

The problem of the altitude jump is shown again in figure 3.10, by plotting altitude vs. curvilinear abscissa.

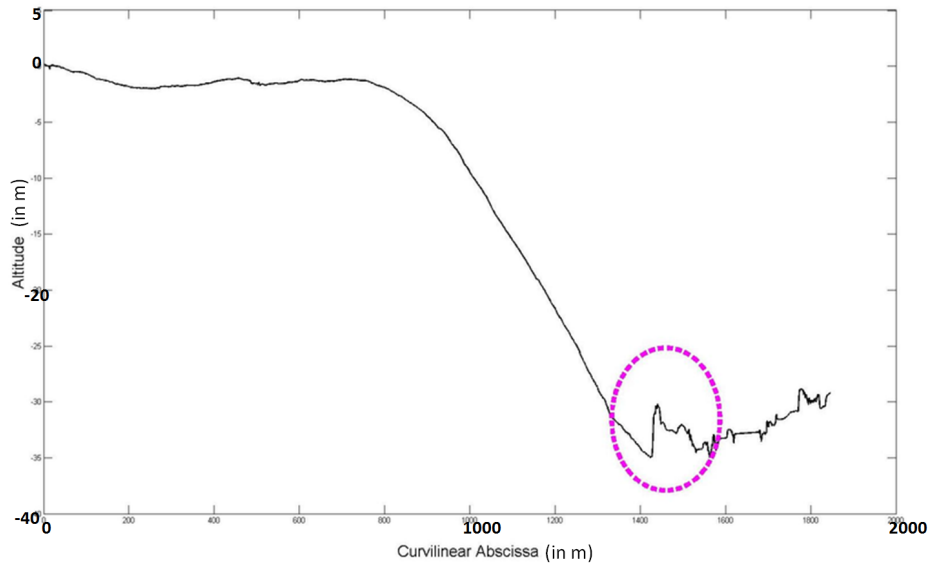

Figure 3.10: *Itinerary 02* - altitude vs. curvilinear abscissa, demonstrating the zone of altitude jump (encircled in magenta)

As shown in figure 3.11, the altitude jump occurs in the zone of GPS fix perturbations.

In addition, during the convergence of the Extended Kalman Filter (EKF), at the initial part of the trajectory, an unstable (discontinuous) yaw rate is observed. During this period, *LARA-3D* mobile platform is maintained stationary (for ~ 10 minutes).

3.6 Post-mission processing techniques

In [Schwarz 04], three branches of the post-mission processing techniques are discussed: Denoising, Auto Regression (AR) modeling and Smoothing. Denoising is a noise reduction applied directly on the sensor measurements (system inputs). For example, in [Skaloud 99], a wavelet filter is applied on the noisy IMU measurements, shows an

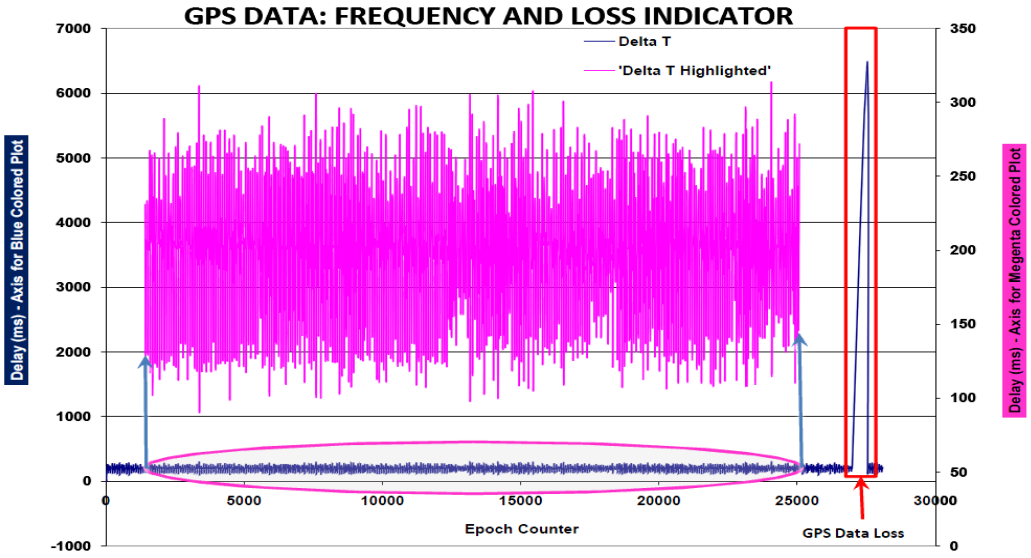

Figure 3.11: Here the acquired GPS data for the *Itinerary 02* is shown. The vertical axis has two scales corresponding to the time in milliseconds, and the horizontal axis corresponds to the epochs (tick counter measuring the output rate, which is at 84 Hz). The plot in magenta is the zoomed portion of the blue one, and shows the mean time for the received GPS measure corresponding to a frequency of 5 Hz (250 ms). The blue plot shows the lack of GPS position fix for a duration of 6.5 seconds around epoch 28000.

improvement in the precision of orientation by an order of 5, and in the precision of acceleration by a factor of 200. Alternatively, AR modeling techniques reduce the noise in the data fusion step. A Kalman smoother using forward and backward Kalman filters is an example of this method [Fraser 02]. They are applied in several systems including the POS/LV from Applanix [Bourke 05], [Graefe 01]. Alternatively, a simple numerical smoothing can be applied on the already generated trajectories.

The observed problems in section 3.5 can be resolved by an offline post-mission processing approach, using constraint-based smoothing techniques. The input for this approach consists of the real time estimation of the trajectory and related statistics.

Prior demonstrating our approach of trajectory smoothing, we present the two common techniques popularly used to improve the localization results. Our smoothing approach is in line with the requirements of minimizing the effects of degraded GPS fix, presented in chapter 1.

3.6.1 Kalman smoother

This is an auto regression method (AR) for smoothing, making use of two Kalman filters, forward and backward.

- **Difference between Kalman filter and smoother**

Both the techniques can be used to estimate the parameters of a time series model. The Kalman filter approximates the maximum likelihood estimates, while the smoother (also termed as Bryson Frazier Smoother [Graefe 01]) make exact estimates. Both are a form of prediction-error decomposition, where the goal is to minimize the residual (i.e. difference between prediction and observation). In the filter, each observation y_k is predicted based on all prior observations Y_{k-1}, that is, $y_1 \dots y_{k-1}$. In the Kalman smoother, the prediction of y_k is not only based on all previous observations Y_{k-1}, but also on all later observations Y_{k+1}, that is $y_{k+1} \dots y_T$, where T is the entire observation period. Hence, the filter is referred to as an *online* estimation procedure, because it requires only the previous observations. In contrast, the Kalman smoother is an *offline* procedure, since it requires both the measurements from the past and the future.

- **Kalman smoother**

This method of trajectory smoothing is applied in [Ohno 04], [Bourke 05] and [Sedlak 94]. In this literature, the smoothed trajectory is obtained by processing the data backward in-time, and then combining it with the estimates from the forward in-time Kalman filter. The smoothing with its error estimates and covariances are obtained by using a variance-weighted combination of the forward and backward estimated errors and their covariance data. The smoothed error estimates are based on all available information from the past and the future. Hence it is more accurate than a forward-only approach.

The functioning of this method is shown using figure 3.12. A smoothing procedure combines optimally both the forward prediction and the backward prediction and gives an improved estimation of the trajectory as given by $E3$.

The smoother combines the state estimations of the forward and backward filters weighed by their corresponding state covariances. The resulting smoothed covariance $\mathbf{P^s_{k|k}}$ at epoch $\mathbf{k}$ can be expressed as:

$$\mathbf{P^s_{k|k}} = ((\mathbf{P^f_{k|k}})^{-1} + (\mathbf{P^b_{k|k}})^{-1})^{-1} \tag{3.1}$$

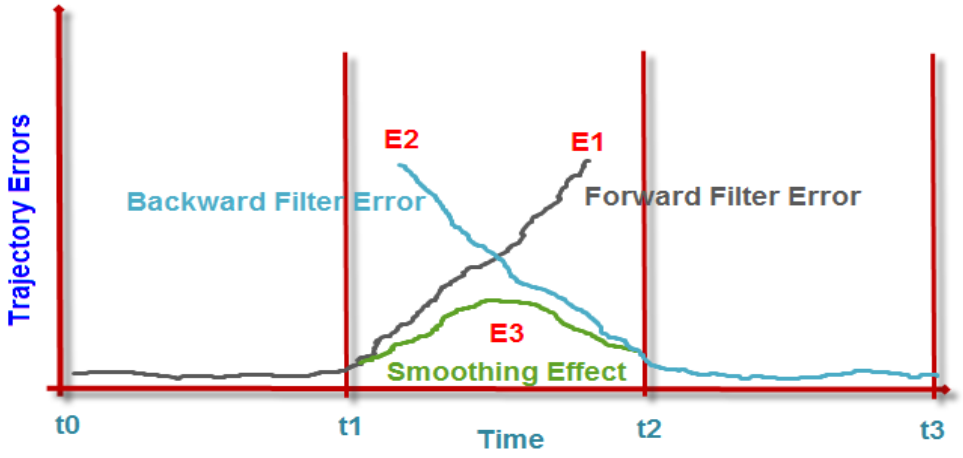

Figure 3.12: Forward and backward prediction and smoothing errors (inspired from [El-Sheimy 96]). Between the time $t1$ and $t2$, the estimation from the forward Kalman filter, backward Kalman filter and the Kalman Smoother are shown with their respective error curves $E1$, $E2$, and $E3$. In a statistical sense, $E2$ is the mirror image of $E1$.

where $\mathbf{P^f_{k|k}}$ is the covariance of the forward Kalman filter, $\mathbf{P^b_{k|k}}$ is the covariance of the backward Kalman filter at epoch k. The notation $k|j$ indicates a quantity estimated using the sensor data through time t_j, and propagated (if $k \neq j$) to time t_k.

Further, $P^f_{k|k-1}$ and $P^b_{k|k+1}$ are computed using the Kalman filter propagation form as given below:

$$\mathbf{P^f_{k|k-1}} = \mathbf{\Phi P^f_{k-1|k-1}\Phi^T} + \mathbf{Q} \quad \mathbf{P^b_{k|k+1}} = \mathbf{\Phi P^b_{k+1|k+1}\Phi^T} - \mathbf{Q} \tag{3.2}$$

where, Φ is the state transition or Jacobian matrix and $\mathbf{Q}$ is the process noise covariance.

From these covariances, the smoothed state X^s_k is computed as:

$$\mathbf{X^s_k} = \mathbf{P^s_k}((\mathbf{P^f_{k|k}})^{-1}\mathbf{X^f_{k|k}} + (\mathbf{P^b_{k|k}})^{-1}\mathbf{X^b_{k|k}}) \tag{3.3}$$

equation 3.4 is obtained by applying equation 3.1 in equation 3.3 as:

$$\mathbf{X_k^s} = \mathbf{X_{k|k}^f} + \mathbf{P_k^s}(\mathbf{P_{k|k}^b})^{-1}(\mathbf{X_{k|k}^b} - \mathbf{X_{k|k}^f}) \tag{3.4}$$

Note how the smoother works by inspecting equations 3.1 and 3.3. When either of the estimator diverges its covariance tends to be very high, and its contribution to smoothing is very less as given in equation 3.1.

The forward filter starts with a relatively large uncertainty, as no data is available. Thus the smoothed state is dominated by the backward estimate until the observation data decreases the forward covariance. Similarly, the forward estimate predominates at the end of the data span.

From equations 3.1 and 3.4, show that the storage requirement of implementing this method is high because, the error covariances and full states need to be saved for the entire trajectory. In general implementations, during the online run of a forward Kalman filter, these values are computed and stored, along with the observation data and the reference vectors. This avoids repetitive computations. In the offline mode, smoother and backward filters are run simultaneously. The backward filter processes the stored values of the forward run but in reverse time order.

- **Advantages and disadvantages**

This method makes use of the auto regression in both forward and backward in time. It makes use of the entire trajectory information, therefore reducing the errors in the final results. This smoothing process takes into account of both the model and measurement uncertainties.

However the main drawback is, it requires substantial storage space in order to run the backward filter. All the states, their covariances, observations and reference vectors need to be stored to perform smoothing.

One improvement is to run the backward filter at a lower frequency, thus reducing the necessity of storing these values at every step of the forward filter. However, this leads to a reduction in the smoothing quality.

3.6.2 A spline-based smoothing approach

- **A brief introduction to spline interpolation**

The spline is a set of piecewise polynomials, which interpolate a given sequence of data points, termed as knots or control points. If the control points are equally spaced

then the spline is termed as uniform. The degree of the polynomials is normally selected to be less than or equal to three in order to avoid oscillations (Runge's phenomenon). If third order polynomials are used, the splines are called cubic splines. They are the most popular interpolants, due to the control they provide for interpolation. If the polynomials are constructed in the form of piecewise Bézier curves by using a set of basis functions, the splines are called B-Splines (Basis Splines). The B-Splines provide better local control for the interpolation compared to Bézier curves, implying changing a single control point does not alter the entire curve. Basis functions provide a computationally efficient method of interpolation. A smoothed interpolation without oscillations, and with local control over the knots is obtained using cubic B-Splines. A B-spline curve of degree m with n control points consist of $(n - m)$ Bézier curve segments. Therefore, a cubic B-Spline is constructed for every set of four control points. These segments all have C^2 continuity (same first and second order derivatives) at the join points [Andersson 03].

Mathematically, cubic B-Splines are expressed using the following simple form:

$$\mathbf{S^m(t)} = \sum_{i=0}^{n} \mathbf{P_i B_{i,m}(t)} \tag{3.5}$$

where P is the control point or knot vector, B the basis function, n the number of control points, m the degree of the curve and $t \in [0, 1]$.

There exists several basis functions to achieve different interpolation objectives. They act as weight functions for each control point in the interval of t. One way to compute the basis functions for a polynomial of m^{th} degree is to use the terms of the expansion of $((1 - t) + t)^m$.

Though this method does not take into consideration the kinematics or dynamics of a system, certain physical motion properties ensure that the trajectory is confined to piecewise smooth curves. For example, the velocity is continuous if the force applied is finite, which is the case in normal motion. This continuity of the velocity ensures that the position is continuous and derivable. Spline interpolation is suitable for a trajectory modeling because it is both continuous and derivable.

- **Spline applied in trajectory smoothing**

The cubic splines are used for smoothing the GPS receiver output data in [McLoughlin 08], with the assumption that the movement of a vehicle on the man-made roads is piecewise continuous. The original work on this smoothing method is given in [Reinsch 67]. It is a regression fitting of a curve to the data points by minimizing two criteria: the first, is that the spline curve is reasonably close to the data points and is dictated by the uncertainties in the coordinate measurements (GPS uncertainty).

The second condition balances the first constraint and prevents a direct interpolation by minimizing the curvature of the spline. A reliable fit is obtained when the two terms are balanced properly using weighting factors.

In [McLoughlin 08], the improvement due to cubic spline smoothing is demonstrated by the mapped road studs in the centerline of the road (figure 3.13).

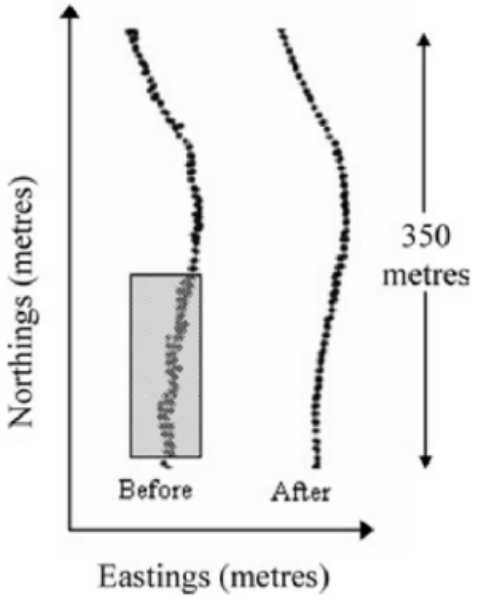

Figure 3.13: Effect of cubic spline smoothing [McLoughlin 08], left: raw GPS pose data, and right: result after smoothing using splines.

- **Advantages and Disadvantages**

Spline is a numerical interpolation method, and it uses the continuity properties of the curve to smooth the data. It does not have the memory requirements of an auto regression methods. Even regression techniques can be applied to obtain C^2 continuity with splines, by not exactly fitting the curve to the control points (knots).

Its main drawback is the influence of the control points on the curve shape. In the absence of a mechanism to choose the appropriate control points, the trajectory can deviate from the true path. Since the smoothing technique does not use the kinematics or dynamics of the system, it may not be a foolproof approach for all the cases.

3.7 A numerical trajectory smoothing approach

We propose to improve the approach given in [Choi 07], by adding some missing functionalities and automatizing the process. We applied our approach on the new experimental data sets. The results of this work is published in the article [Narayana 09].

Our proposed improvements include:

1. A new algorithm to automatically detect and correct altitude jumps.
2. An additional X and Y computation step from the smoothed yaw at the end of the post mission processing chain.

The schema of this process is explained in figure 3.14.

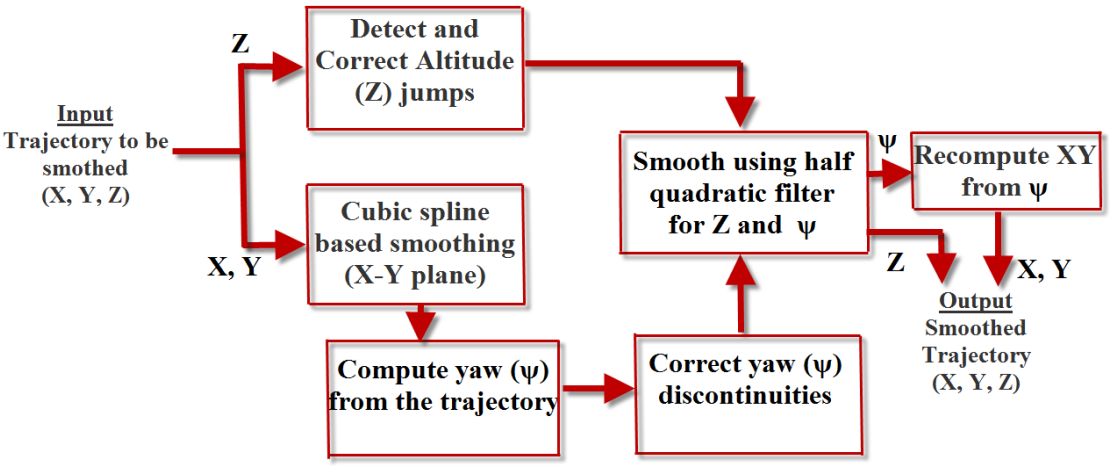

Figure 3.14: Our automated post-mission processing technique - handles common problems of altitude jumps and yaw drifts.

The input of this technique is in the form of trajectories which are already computed, expressed in 3D Cartesian coordinate system, (X, Y, Z). We tested the method using the trajectory generated from the direct georeferencing process of *LARA-3D*.

3.7.1 Altitude jump detection and correction

The goal of this step is to detect the abnormal changes in the altitude or Z values, within a short period of time. In [Choi 07], this step is performed manually. We propose a new set of algorithms to detect and correct these jumps. The detection is non trivial due to the variation of the Z can be under the noise threshold between successive

measurements. Moreover, these jumps evolve slowly due to the smoothing done by the EKF. Therefore, the first order difference cannot be applied for detection. We propose a method to automatically determine the jump detection thresholds. Once detected, jumps are corrected by numerical interpolation, using a novel set of basis functions.

The origin of the altitude jumps are the inaccurate altitude values provided by the GPS receiver. The vertical accuracy of a GPS fix is normally lower than the horizontal accuracies. This is taken care of during the data fusion step, where the vertical component trust is reduced based on the quality indicator, Vertical Dilution of Precision (VDOP).

However, the advantage of the post-mission processing approach is that it uses pose measurements both from the past and the future. Therefore, it can help in obtaining better smoothed trajectories compared to the filtering improvements. Additionally, knowledge-based constraint, such as the feasible gradient of a manmade road if applied, ensures a more realistic smoothing.

- **Altitude jump detection**

The first step in detection is to down sample the trajectory by using a configurable frequency, which helps:

1. To cope with the slow jumps introduced by EKF.
2. To reduce the influence of high frequency noise in the process of detecting the jumps.

The algorithm 3.1 details this detection process.

A jump is detected using a a jump detector threshold given by the first order function $F_{gradthresh}(Velocity_{x,y}, \nabla)$, where $Velocity_{x,y}$ is the longitudinal velocity, and ∇ is a configurable maximum feasible gradient of the road. T_{max} is the total number of epochs in the trajectory. S^f is chosen based on the velocity of the vehicle during the data acquisition process, and the original trajectory sampling frequency (i.e. the trajectory output rate of an MMS).

The result of this step is shown in figure 3.15.

- **Altitude correction**

Once the jumps are detected, the next step is to correct these values. A realistic constraint of a road model is applied, to ensure the slope is piecewise continuous. Meaning the evolution of Z over the shorter sampling periods must be piecewise continuous.

Algorithm 3.1 Altitude jump detection

Require: $Z \neq \{\}$, $S^t \geq 1$ and $JumpList \leftarrow \{\}$
Ensure: $JumpList$ contains all the indices where a discontinuity in the altitude is detected
Sample Z with a periodicity of S^t corresponding to a lower sampling frequency S^f
$t \leftarrow 1$
while $t \leq (T_{max} - S^t)$ **do**
$\Delta Z_t \leftarrow (Z_{t+S^t} - Z_t)/S^t$
$MaxRoadGradient \leftarrow F_{gradthresh}(Velocity_{x,y}, \nabla)$
If the change in the altitude is greater than the maximum feasible gradient, an altitude jump is detected
if $|\Delta Z_t| \geq MaxRoadGradient$ **then**
$JumpList \leftarrow JumpList \cup \{((t-1)/S^t) + 1\}$
end if
$t \leftarrow (t + S^t)$
end while

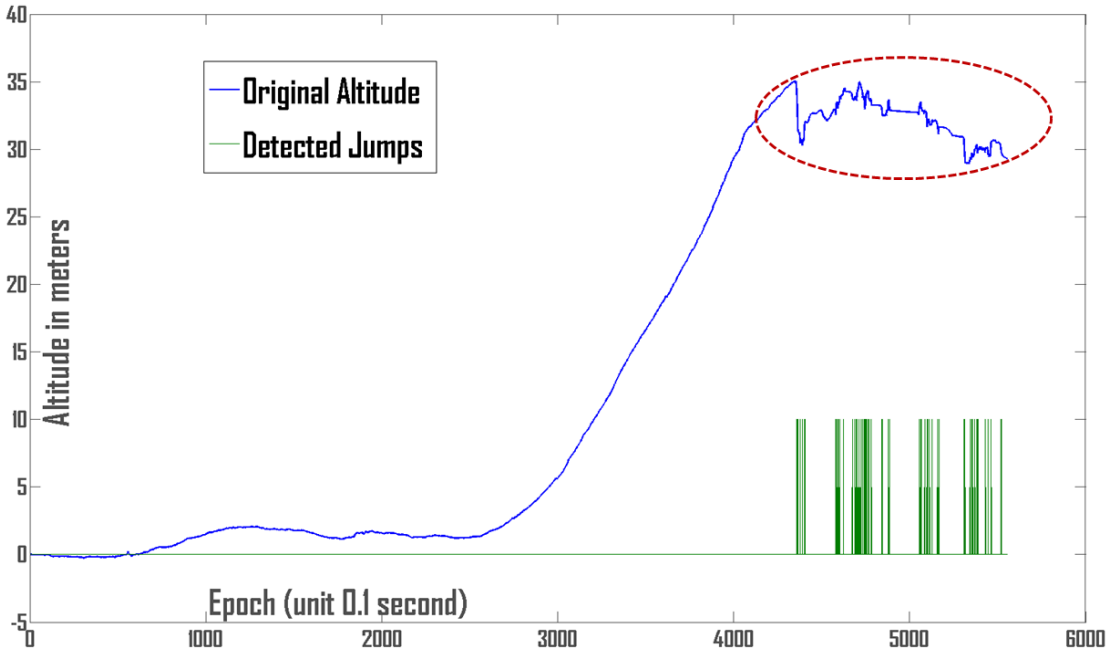

Figure 3.15: Itinerary 02-detected altitude jumps. Zone of jump is encircled in red on the altitude signal, and detection indicators are shown in green on the bottom.

When a jump is detected between two sampling periods, it is corrected by interpolating the slopes of Z, before and after the jump. However, the slopes cannot be computed directly from a noisy signal, since the differentials are even more noisier, the signal Z is

first smoothed Z_{smooth} using a simple moving average filter. The purpose is to compute an average slope just prior ($SlopeS$) and after the jump ($SlopeE$), for interpolation.

A pair of interpolation basis functions (named F_1 and F_2) needs to be defined fulfilling the following:

1. Simple to compute
2. $F_1(k) + F_2(k) = 1$, at any given instant k in the period of interpolation.
3. The interpolated curve has to be equal to $SlopeS$ at the beginning and to $SlopeE$ at the end.
4. The results need to be realistic, showing the properties like inertia for the changes and nonlinearity.

Two suitable functions are defined in equations 3.6 and 3.7

$$\mathbf{F_1}(\theta) = 0.5 + 0.5\sin(\theta) \tag{3.6}$$

$$\mathbf{F_2}(\theta) = 0.5 - 0.5\sin(\theta) \tag{3.7}$$

where $\theta \in [\frac{\pi}{2}, \frac{3\pi}{2}]$.

The function property are shown in figure 3.16.

The interpolation is achieved using the equation 3.8

$$\mathbf{SlopeI} = \mathbf{F_1}(\theta) \times \mathbf{SlopeS} + \mathbf{F_2}(\theta) \times \mathbf{SlopeE} \tag{3.8}$$

The altitude correction process is described in algorithm 3.2.

Function $F_{smooth}(s, ind, w)$ provides an average slope for a configured window period (w) for a signal s starting from the index ind. This function helps minimize the effect of noise in the computed slope.

The result of this step is shown in figures 3.17 and 3.18:

3.7.2 Spline-based trajectory smoothing in 2D

Instead of using the noisier yaw computed by the INS, it is possible to compute the same from a smoothed 2D trajectory, as shown in figure 3.19.

Algorithm 3.2 Altitude jump correction

Require: $Z \neq \{\}$, $S^t \geq 1$, $JumpList \neq \{\}$, and $W \geq 1$
Ensure: For all the indices in $JumpList$, the errors are replaced by interpolated values.

$Ind \leftarrow 1$
$EndInd \leftarrow 1$
Compute the slope of the entire Z, with the assumption that the time period is uniformly sampled
$SlopeZ \leftarrow Z_{i+1} - Z_i, i \in [1, T_{max}]$
Compute Z_{smooth} from Z by using a moving window (w) average filter
$Z_{smooth} \leftarrow AverageFilter(Z, w)$
while $EndInd \leq |JumpList|$ **do**
  while $(EndInd + 1 < |JumpList|)$ and $JumpList(EndInd + 1) = (JumpList(EndInd) + 1)$ **do**
    $EndInd \leftarrow EndInd + 1$
    Any continuity in the elements of $JumpList$ is identified, indicating a long term erroneous altitude between multiple sampling periods
  end while
  Obtain the slopes of Z prior and after the jump computed using Z_{smooth}
  $SInd = ((JumpList(Ind) - 1) * S^t + 1 - w)$
  if $SInd > 1$ **then**
    $StartSlope \leftarrow F_{smooth}(Z_{smooth}, SInd, w)$
  else
    $StartSlope \leftarrow 0$
  end if
  $EInd = (JumpList(EndInd)) * S^t + 1$
  if $EInd < |DeltaZList|$ **then**
    $EndSlope \leftarrow F_{smooth}(Z_{smooth}, EInd, w)$
  else
    $EndSlope \leftarrow 0$
  end if
  CORRECT THE ALTITUDE JUMP USING A NOVEL BASIS FUNCTION
  Sample the interval π between $\frac{\pi}{2}$ to $\frac{3\pi}{2}$ by the number of points in Z, where the slope needs to be interpolated
  $ThetaVect \leftarrow [\frac{\pi}{2}, \frac{3\pi}{2}]$ with sampling period $\frac{S^t \pi}{EndInd - Ind + 1}$
  Compute interpolation coefficients
  $WeightS \leftarrow 0.5 + 0.5 * sin(ThetaVect)$
  $WeightE \leftarrow 0.5 - 0.5 * sin(ThetaVect)$
  For all the points in Z $iPt \in [(((JumpList(Ind) - 1)S^t) + 1), ((JumpList(EndInd)S^t) + 1)]$ recompute the $SlopeZ$
  Check for boundary conditions of $JumpList$ prior performing this operation
  $SlopeZ(iPt) \leftarrow (WeightS \times StartSlope) + (WeightE \times EndSlope)$
end while
Recompute the Z using the Slope $SlopeZ$ and the initial Z value Z_{t0}

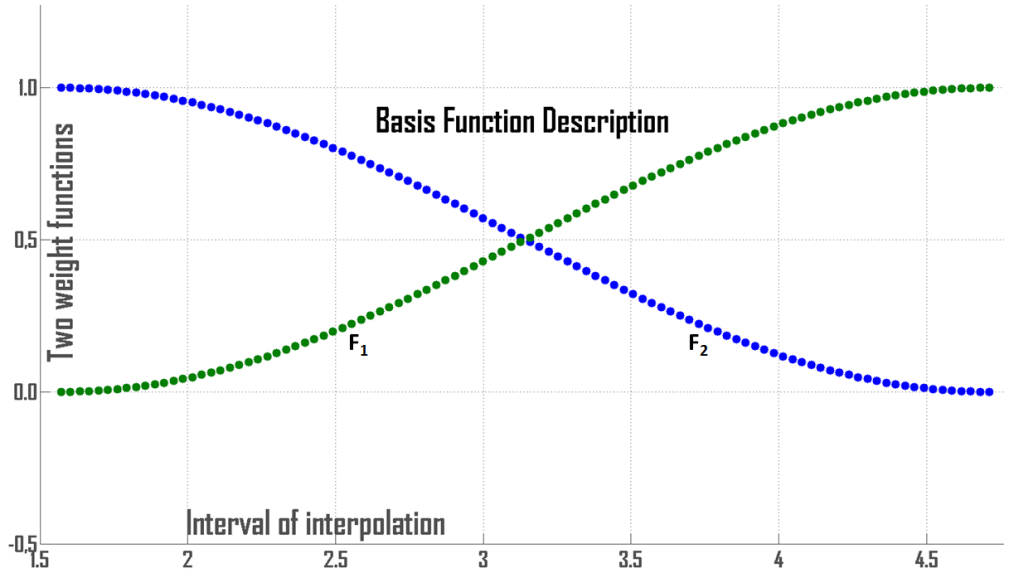

Figure 3.16: Two basis functions for altitude jump correction, F_1 and F_2. These functions form the weights for the slopes of signal Z during the interpolation.

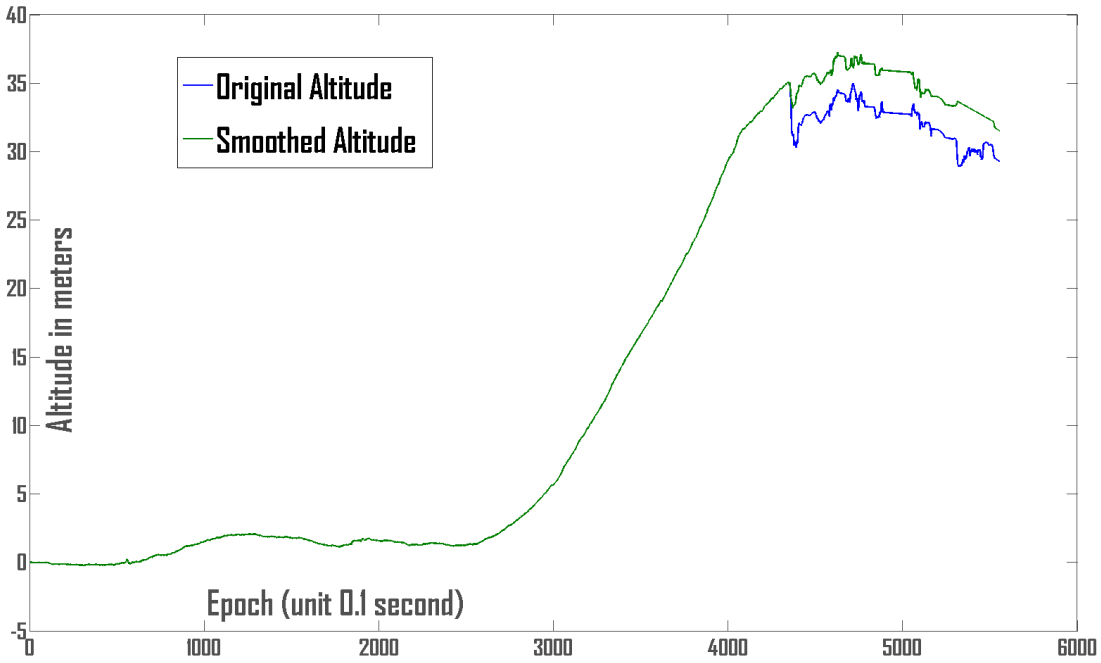

Figure 3.17: Corrected altitude jumps for itinerary 02.

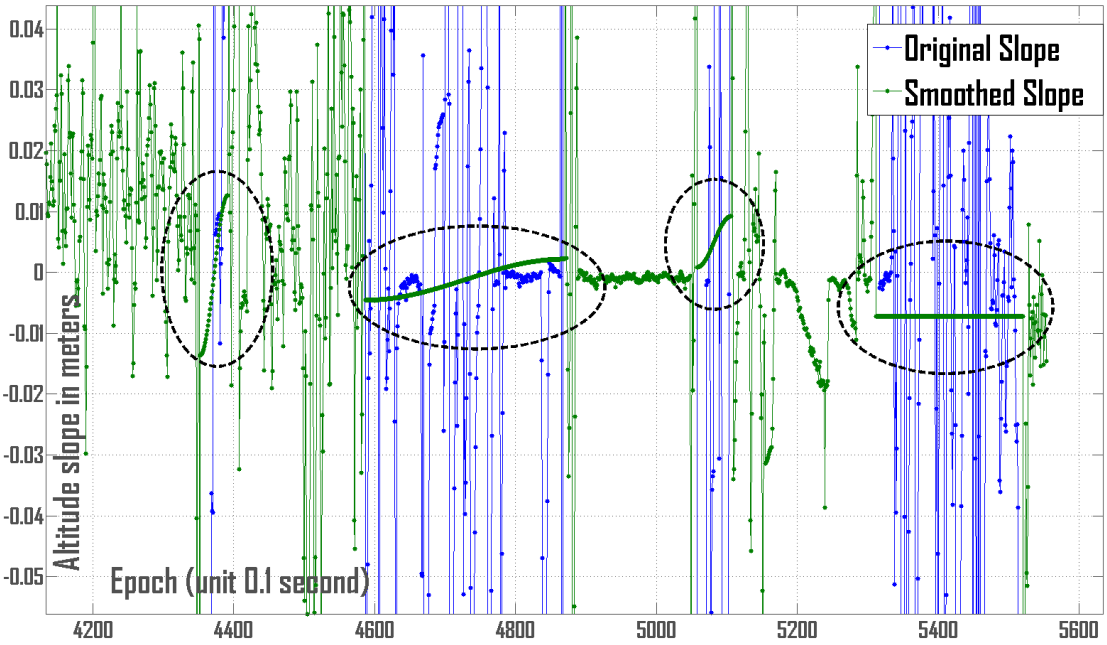

Figure 3.18: Close view of the altitude interpolation (encircled regions) for itinerary 02. Interpolation is done only for the span of the signal where a jump is detected.

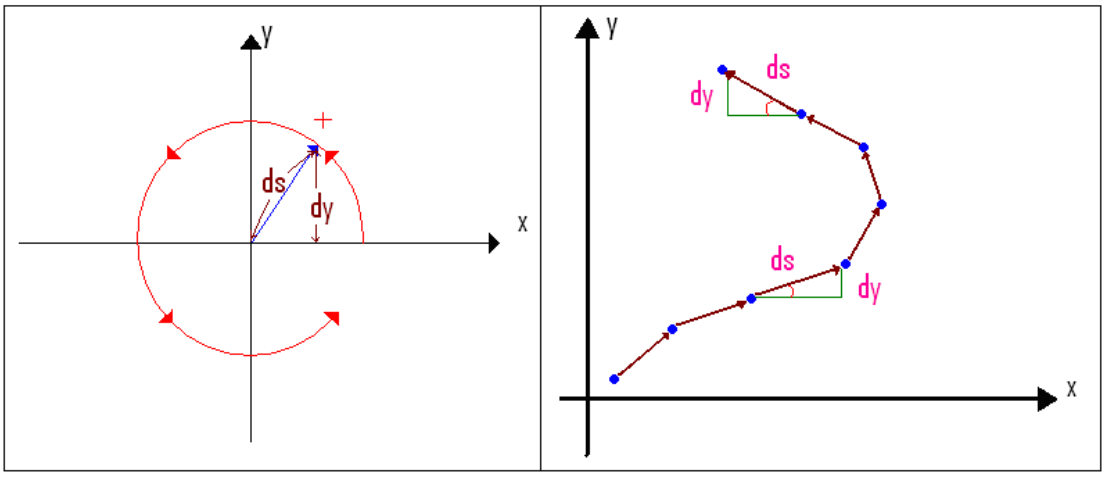

Figure 3.19: Yaw computation from the trajectory: $\psi = \arcsin(\frac{dy}{ds})$.

X, Y coordinate values of the trajectory are applied to compute the yaw information. However, since the X, Y (in other words the position in 2D) values are noisier, it is required to model the X and Y profile using a smoothing function. The trajectory is a spatial distribution of the position with respect to time. This implies, multiple points

of Y are obtained for the same values of X at different times. A function of the type $(X, g(X))$ is not applicable, since it provides a one to one mapping. The best suitable model is a spline-based model for the XY axis, which uses the data in a sequential order of time. The control points or knots for the spline-based model are selected by uniformly re-sampling the trajectory with a lower frequency, but sufficiently high so that the number of control points still retains the shape of the trajectory.

As discussed in section 3.6.2, a cubic B-Spline is used for the interpolation. This provides the local control on the knots without introducing any oscillations.

3.7.3 Address yaw problems

Once the planimetric trajectory is smoothed by splines, a smoother yaw signal is computed from it (as shown in figure 3.19.

However, even the smoothed trajectory has some discontinuities in the yaw, especially during the EKF convergence during the initialization, as shown in figure 3.20. During this initial acquisition period, the *LARA-3D* platform (i.e. the vehicle) is maintained stationary to allow the algorithms to converge. Therefore, a new constraint of a static yaw value for a stationary vehicle can be applied. This is obtained from the sequence of yaw values computed immediately after the convergence of algorithms. Once the vehicle starts to move, yaw is a continuous function.

3.7.4 Smoothing using half quadratic filtering

Further, a half quadratic filtering method developed by LRPC Strasbourg [Charbonnier 97] and [Charbonnier 09] is used to smooth, already processed altitude and yaw. This filtering technique is mainly used in the digital image processing for edge preserving regularization. In our work, it serves as an outlier detector (edge detections) as well a smoothing filter (quadratic or regularization property).

Half quadratic filtering method is a technique, similar to the least square estimate with an additional regularization term. The problem of smoothing is expressed as minimizing the function $\mathbf{J}(\mathbf{f})$.

$$\mathbf{J}(\mathbf{f}) = \int_{\Omega} (\mathbf{f} - \mathbf{p})^{\mathbf{2}} + \lambda \int_{\Omega} \phi(|\Delta \mathbf{f}|) \tag{3.9}$$

where $\mathbf{f}$ is the model, $\mathbf{p}$ is the observation or data, and λ is a configurable parameter. Thus the term $\int_{\Omega} (\mathbf{f} - \mathbf{p})^{\mathbf{2}}$ is treated as a least square problem. The half quadratic

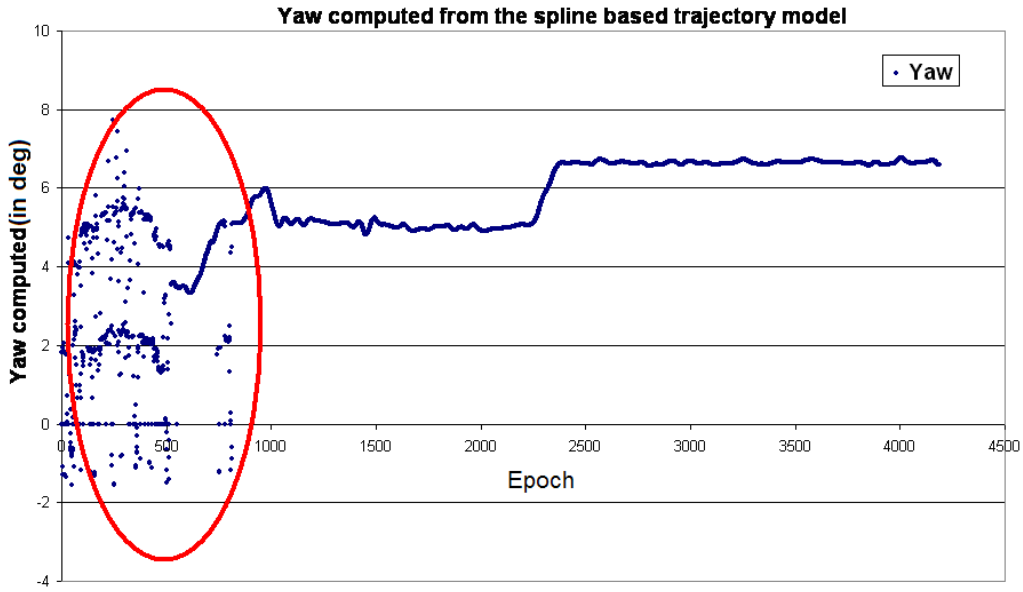

Figure 3.20: Deduced yaw from the smoothed planimetric trajectory for itinerary 01. The yaw shows discontinuities in the beginning, during the EKF convergence.

regularization term $\lambda \int_{\Omega} \phi(|\Delta \mathbf{f}|)$ is a function of the second derivative of $\mathbf{f}$ and aids in selecting $\mathbf{f}$ by favoring a solution with a constant piecewise slope of $\mathbf{f}$ (piecewise C^1), which represents the nature of manmade roads. In order to achieve this, the desired properties of the function $\phi(|\Delta \mathbf{f}|)$ are:

$$\lim_{|\Delta \mathbf{f}| \to 0} \frac{\phi'(|\Delta \mathbf{f}|)}{2|\Delta \mathbf{f}|} = 1 \tag{3.10}$$

$$\lim_{|\Delta \mathbf{f}| \to \infty} \frac{\phi'(|\Delta \mathbf{f}|)}{2|\Delta \mathbf{f}|} = 0 \tag{3.11}$$

$$\phi'(|\Delta \mathbf{f}|) \text{ is a strictly decreasing function} \tag{3.12}$$

These properties allow us to exclude the outlier data $\mathbf{p}$ which has a larger magnitude of the second derivative (i.e. noisy).

We use one of the functions satisfying these properties from [Charbonnier 97].

$\phi(|\Delta\mathbf{f}|) = 2\sqrt{\epsilon + |\Delta\mathbf{f}|^2} - 2$ for our application,

where ϵ is the rounding error. In practice, we use a multiplicative extension of the criteria from equation 3.9, which is easier to solve by introducing an auxiliary variable $\mathbf{b}$.

The mathematical form of this extension can be given as:

$$\mathbf{J}(\mathbf{f}) = \int_{\Omega} (\mathbf{f} - \mathbf{p})^{\mathbf{2}} + \lambda \int_{\Omega} (|\Delta\mathbf{f}|^2\mathbf{b} + \psi(\mathbf{b})) \tag{3.13}$$

where $\mathbf{b} = \frac{\phi'(|\Delta\mathbf{f}|)}{2|\Delta\mathbf{f}|}$ which is further deduced as:

$$\mathbf{b} = \frac{1}{\sqrt{\epsilon + |\Delta\mathbf{f}|^2}} \tag{3.14}$$

In this general form, the function $\psi(\mathbf{b})$ is strictly convex and neglected in our minimization.

To find $\mathbf{f}$, which minimizes the criteria of the equation 3.13, we fix $\mathbf{b}$ and equate the derivative of equation 3.13 to zero. The value of $\mathbf{f}$ is given as:

$$\mathbf{f} = (\mathbf{I} + \lambda\Delta^T\mathbf{B}\Delta)^{-1} \times \mathbf{p} \tag{3.15}$$

where $\mathbf{B} = diag(\mathbf{b_i})$

For the details of the half quadratic theory refer to [Charbonnier 97] and [Charbonnier 09].

The results of the half quadratic filtering is shown in figure 3.21, after applying the algorithm on the signal corrected for altitude jumps, given in figure 3.17.

3.7.5 Re-computation of X, Y from the smoothed yaw

This is the final step introduced to the algorithm, without it, smoothing yaw has no sense. We recompute the X and Y from the smoothed yaw value. It is a reverse operation compared to the yaw computation explained in section 3.7.3

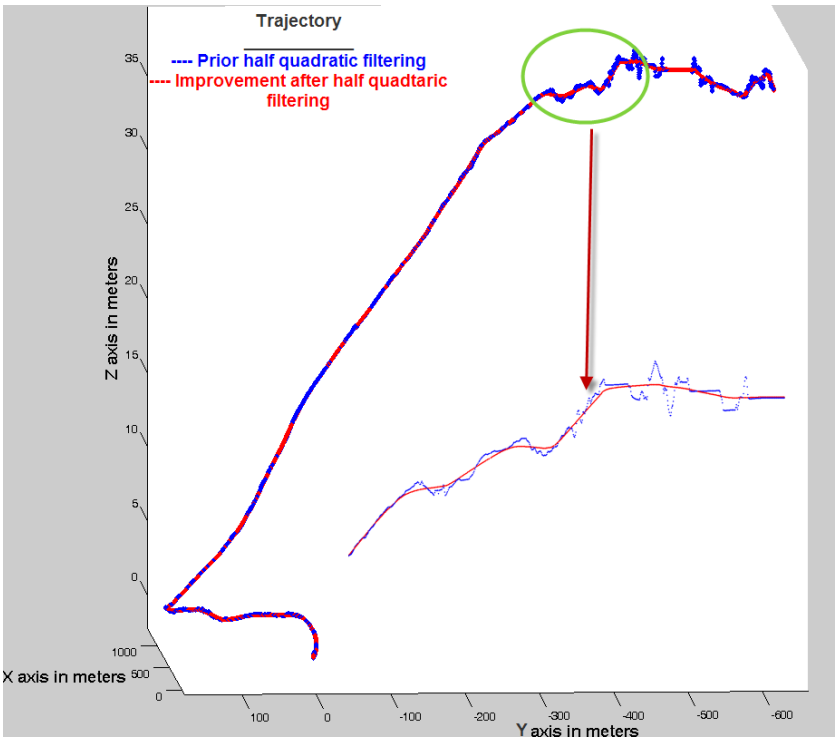

Figure 3.21: Altitude signal improvement by using half quadratic filtering. The highlight of the signal indicates a reduction in the high frequency noise.

As a final step, the smoothed trajectory is used as an input to the direct georeferencing, to regenerate the new 3D point clouds. The final results are shown in figures 3.22 and 3.25.

3.8 *LARA-3D* post-mission processing improvements

This section presents the 3D point clouds generated after applying the post-mission processing approach given in section 3.7. The results are more realistic and depicts significant improvements.

Figure 3.22, corresponds to the *Itinerary 01*, before (red point cloud) and after (violet point cloud) the post-mission processing.

Applying, a further validation of the violet point cloud is done by verifying the area circled in green in figure 3.22, against the Google street viewer generated image in figure 3.23.

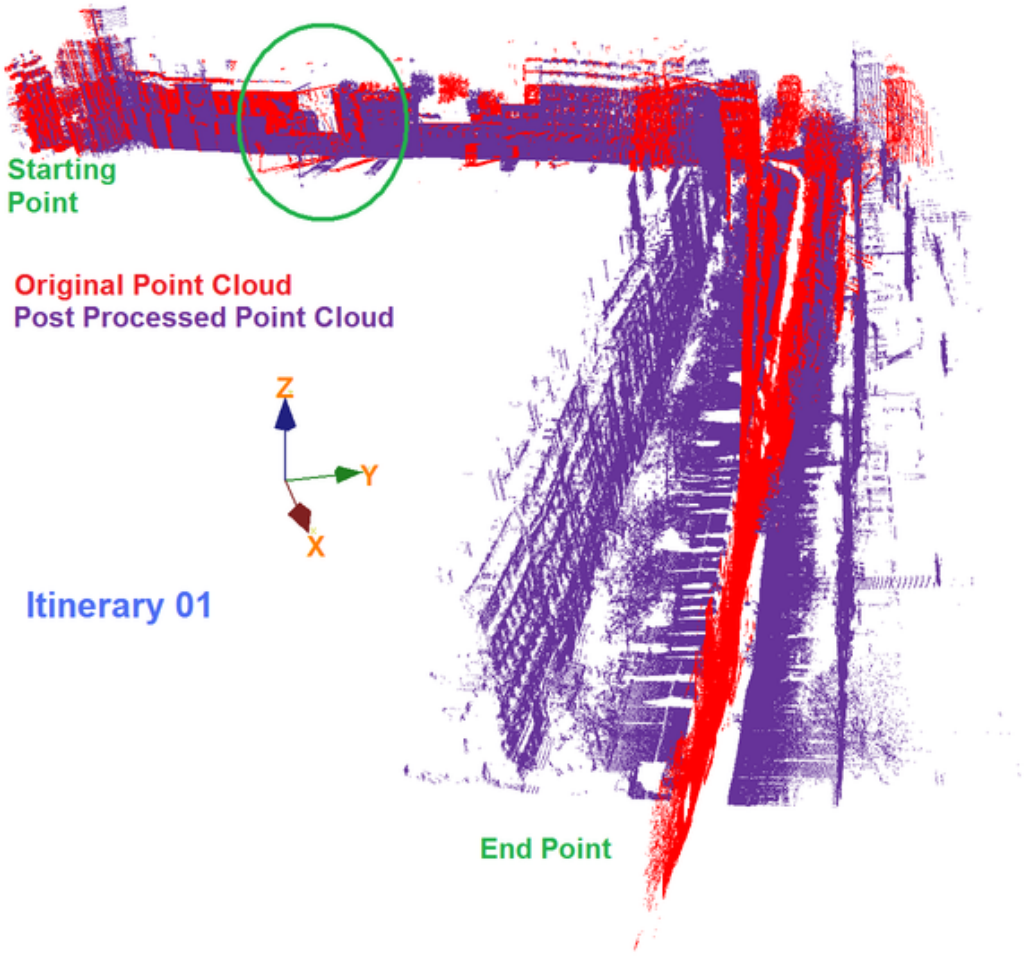

Figure 3.22: Heading drift and discontinuities corrected 3D point cloud after applying post-mission processing for Itinerary 01.

In figure 3.24, the same geographical area is highlighted by the two point clouds, generated before and after post-mission processing. The figure confirms the realistic nature of the post processed trajectory.

The point clouds for the *Itinerary 02*, obtained before and after post-mission processing are shown in figure 3.25. The circled area highlights the point where the altitude jump, shown in figure 3.9 occurs. The red point cloud generated by direct georeferencing, without post-mission processing shows this jump, where as the post processed point cloud in violet depicts the corrected jump.

Improved 3D maps permits the point clouds to be used for applications such as colorization and texture rendering of the objects, etc. The improved results can be used

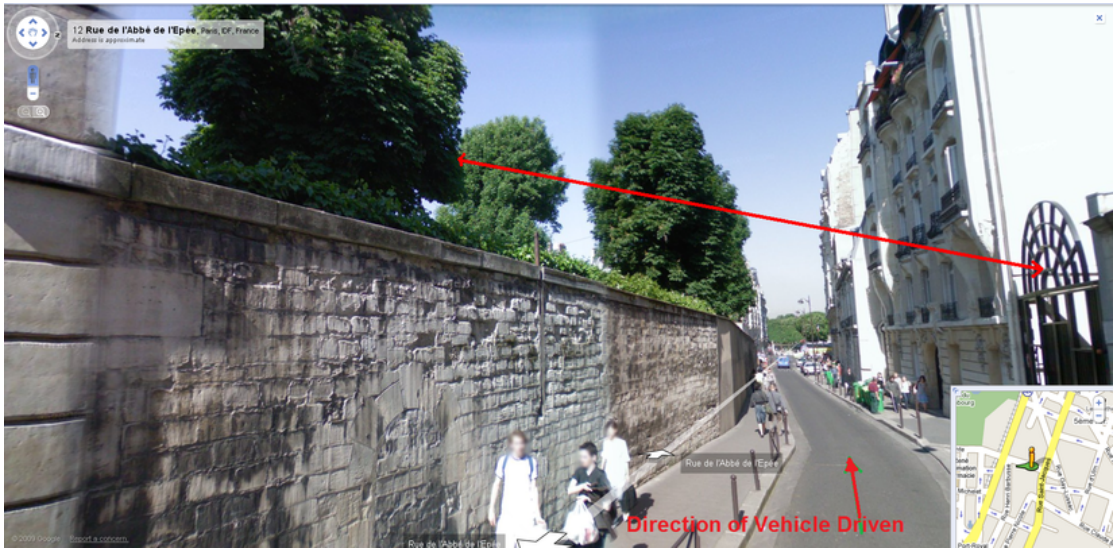

Figure 3.23: Google street viewer image of the scene with yaw problems (Itinerary 01). In the figure, the red line points to two objects in space: a metallic arch and a tree. The direction of the *LARA-3D* data acquisition is shown by the red arrow, in the bottom of the image. During the acquisition, the information of the tree is encountered first, and then the arch. Geographically, the tree is almost in front of the arch.

as benchmarks for further amelioration of localization.

3.9 Conclusion

This chapter briefed on the mobile mapping platform *LARA-3D* and its functionalities. The obtained results suggest the typical scenarios and problems encounterd by most MMS.

We proposed an automated smoothing approach to correct the obvious but important localization errors, such as altitude jumps, discontinuities and drifts in the heading. This method is suitable for offline processing, but sufficient for most of the applications of Mobile Mapping Systems, as the system is not limited by real-time localization constraints.

This method is applied on the two data sets acquired by the MMS platform *LARA-3D*, characterizing the typical problems of GPS fix outages and sensor quality limitations. The results of this approach show significant improvements in the 3D maps, meeting both the objectives of this thesis.

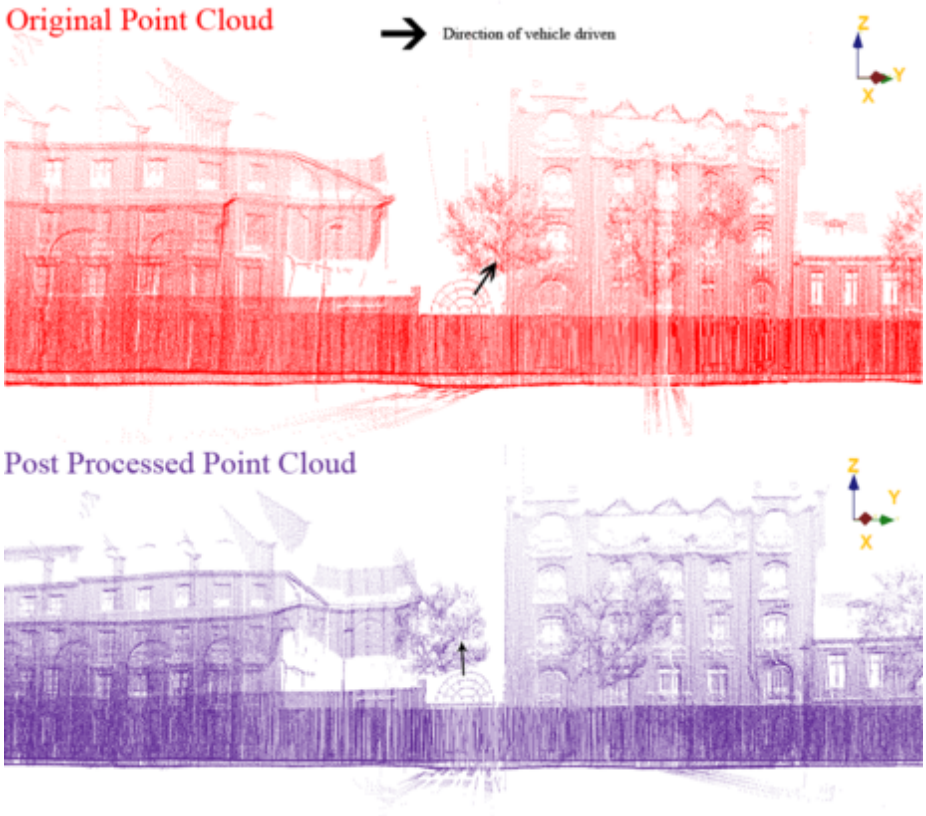

Figure 3.24: Ground check on the point clouds, obtained prior and after post processing for itinerary 01.

However, this post-mission approach needs to be further enhanced to make it more reliable. It serves the goal of improving the visual appearance of 3D maps. It is inadequate to correct the slowly varying error components such as IMU biases, and slow GPS fix degradations. It does not depend on any measurements or the dynamic nature of the moving mapping platform. Therefore, for precise positioning applications alternative solutions of localization are desired.

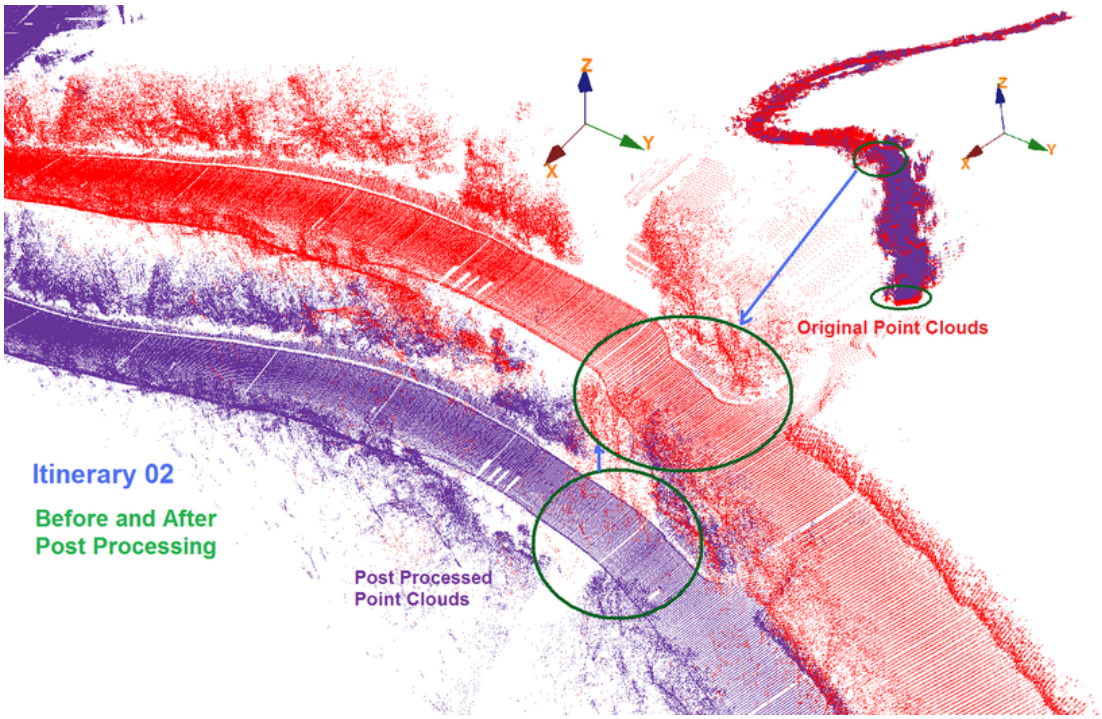

Figure 3.25: Correction of altitude jumps observed in the middle of the road, after applying post-mission processing, for Itinerary 02.

Chapitre 4

Introduction à la localisation par capteurs perceptifs

Comme annoncé au chapitre précédent, notre recherche se concentre maintenant sur l'utilisation des mesures effectuées par les scanners à laser pour calculer le mouvement d'une plateforme de cartographie.

De tels capteurs perceptifs, scanners à laser et caméras numériques, sont employés en robotique pour localiser un mobile, notamment en environnement intérieur. Cette technique est connue sous le nom de localisation et cartographie simultanées (Simultaneous Localization and Mapping - SLAM).

Deux approches sont utilisées dans le cadre des techniques de SLAM : l'approche probabiliste et l'approche optimisation. L'approche probabiliste emploie des filtres Bayésiens, tels que les filtres de Kalman étendus. Elle combine les informations issues de capteurs de localisation (typiquement des odomètres) et de perception de l'environnement (lasers, sonars) pour estimer, à chaque instant, la position la plus probable d'un robot. Les capteurs perceptifs sont utilisés pour identifier des éléments caractéristiques de l'environnement (land-marks). La position du robot, estimée par les capteurs dédiés, est corrigée par l'observation de ces éléments caractéristiques.

L'approche optimisation repose principalement sur les données des capteurs perceptifs. La position du robot est estimée en corrélant deux séries de mesures (typiquement des distances) sur l'environnement statique, mesures prises à partir de positions différentes. Le déplacement apparent, observé par les mesures, correspond à la réciproque du mouvement du robot. Dans cette approche, les éléments caractéristiques de l'environnement ne sont généralement pas utilisés, l'ensemble des informations de distance sont corrélées.

Ces deux approches ne peuvent aboutir que si la correspondance entre deux ensembles de données peut être établie ; que cette correspondance porte sur des éléments caractéristiques de l'environnement, ou sur les données brutes issues des mesures de distances. Cette question de l'identification de correspondance est connue sous le nom problème d'association de données (Data Association - DA).

La difficulté principale rencontrée dans l'approche probabiliste provient de ce que l'association est faite à partir d'une carte globale d'éléments caractéristiques, les incertitudes de positions de ces éléments et de celle du robot se cumulent au cours du temps. D'un autre côté, l'approche par optimisation, qui associe les données brutes, mobilise d'importantes ressources de calcul, donc de temps et de volume mémoire.

Nous proposons une approche odométrique, qui utilise des formes planes ; l'association est réalisée à partir de deux ensembles de mesures par laser, effectuées à deux instants proches. Comme dans l'approche par optimisation, le mouvement relatif est calculé à partir de l'association d'éléments caractéristiques. Les structures planes sont fréquentes dans les environnements créés par l'homme, notamment dans les situations où les signaux GPS sont dégradés (canyons urbains). La simplicité géométrique des repères plans permet une économie notable des ressources nécessaires au processus d'association et au calcul de la transformation subie par le véhicule entre deux séries de mesures.

Dans cette perspective, il est essentiel d'extraire rapidement un ensemble de repères, sans que le mouvement du véhicule n'introduise de déformations apparentes de ces repères. Dans un premier temps, au chapitre 5, nous proposons une méthode pour extraire ces repères plans au moyen de deux lasers 2D. Dans le chapitre 6 nous proposons des méthodes d'estimation de la position 3D du mobile, à partir des propriétés géométriques de ces repères plans. Le chapitre 7 présente les résultats expérimentaux obtenus par cette méthode et leur interprétation.

Chapter 4

Preface to perception-based localization

Contents

4.1 Introduction

From the analysis given in chapter 3, it is inferred that the accuracy of the output maps of a mapping application is often limited by the localization functionality, whose accuracy relies on that of the input sensor measurements. The smoothing technique, like the one presented in chapter 3 can improve the visualization of the 3D maps by applying continuity constraints on the trajectory. However the applied constraints often fall short to correct the slowly varying drift errors, and adapt to the dynamic behavior of a moving mapping platform.

Perception sensors like laser scanners and camera, are integral part of Mobile Mapping Systems(MMS), which are normally used for the dedicated *mapping functionality*. However, the perception information, if used for localization, becomes a fitting solution for many terrestrial mapping applications operating in environments rich in features and objects. Therefore, these solutions can work complementary to a GPS (GNSS)

receiver and an IMU. A GPS (GNSS) receiver needs less obstacles and clear view to the sky. Localization from perception also provides a mean to estimate the bias in IMU measurements, therefore, aiding in correcting the drift errors in the computed pose.

This chapter is the preface to the rest of the work done in this thesis (i.e. chapters 5 to 7).

The content flow of this chapter is organized as follows:

At first, in section 4.2, we briefly look at the functioning of the laser scanners, the most commonly used perception sensors. To remind, mobile mapping platform *LARA-3D* also uses laser scanners as perception sensors. In section 4.3, we briefly look to the origin of *Simultaneous Localization and Mapping (SLAM)* technology, which applies perception sensor measurements for pose estimation or correction. This technique is adopted by the robotics domain to aid in the autonomous indoor navigation. In section 4.4, the state of the art of perception-based localization problem solving is detailed along with the shortcomings of these approaches. Following, we propose our approach in section 4.5, with a plan for the rest of the work done in this thesis. A short conclusion is given at the end, in section 4.6.

4.2 Laser scanners

Laser scanners emerged as a novel technology in the last decade, which consists of a distance measuring system (range finders) that uses a laser. A scanning method, implies the ranges are measured and provided as digital values, for a measuring zone of the environment without physically displacing the laser scanners. This is done moving or rotating either the laser emitter or a laser deflecting mirrors, to direct the laser beam to the measuring zone. The actual distance determination is done by a time-of-flight (time it takes for the emitted laser beam to be received after reflecting from the object), phase shift (the phase difference between the emitted beam and the received one, reflecting from the object) or triangulation measurement (a pinhole camera as a receiver, located at a certain distance from the emitter) [Nüchter 09], [Reshetyuk 09]. In the domain of Geodesy these are also called as LiDAR (Light Detection and Ranging) scanners, and a new domain for scanners called Terrestrial Laser Scanners (TLS) often mentioned in many literatures.

A laser scanner, can be a 1D system, measuring a single range per scan, 2D one, scanning in a single plane, ideal for line extraction, or a 3D one, scanning an entire volume. 3D scanners are often obtained from 2D scanners, by adding an additional rotating mirror or rotating the 2D scanner itself. This is an alternative for an assembly with several lasers, scanning a volume simultaneously. In most robotics research, 3D scanners are constructed by rotating 2D scanners in the direction perpendicular to their

scanning plane. This is mainly because the scanners need to be fit to a light weight moving robot, 2D scanners are relatively cheaper, and can be constructed in the lab by using an external servo([Surmann 04]) or stepper([Weingarten 05]) motors. However, due to the limitations of the motor and the optics, these 3D sensors are very slow to complete a single 3D scan (i.e. scan of the entire volume).

An example for a 2D and a 3D laser scanners is shown in figure 4.1. The results of their single scan appears similar to figures 4.4a and 4.6, respectively.

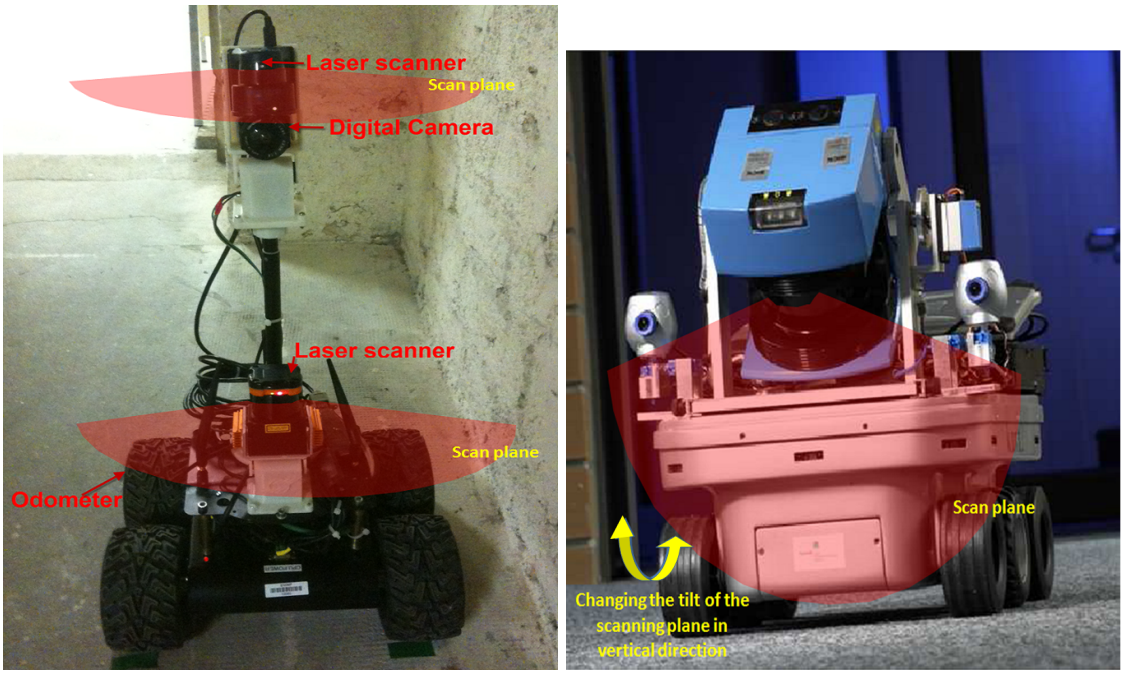

(a) 2D laser scanning (image of corebots, Ecole des Mines de Paris)

(b) 3D laser scanning (original image source: [Surmann 04])

Figure 4.1: 2D and 3D laser scanners in robotics. A 3D scanner is constructed from a 2D scanner fitted with a motor to rotate the scanner itself.

There are several laser scanners available, for varying range of applications. The most commonly used in the robotics navigation are the SICK LMS 2D laser scanners [SICK 06]. These scanners are available in a medium cost ($\sim 10K$ Euros) range, can scan at rate of 75 Hz ($\sim$ 13 ms per scan). In a scan plane, each measurement is taken for an angular step of 1° (angle resolution), and has a 10 mm precision ($\pm$35 mm accuracy) for their measurements with a maximum range of 80 meters. A high-end laser scanner like Optech, used in the Lynx mobile mapping systems [Optech. 10], has a precision of 8 mm with a maximum range of 200 meters with a capacity to scan at a rate of 80 Hz to 200 Hz. The stationary 3D scanners like Trimble GS Series [Trimble. 10], has a precision of less than 3 mm for a range of 100 m. However, due to their size and cost, they are not the first choice for the mobile robot applications.

Laser scanners are the most widely used perception sensors, compared to digital cameras, sonar range scanners etc., because they provide dense and accurate range measurements, high sampling rate, high angular resolution, good range resolution and distance [Nguyen 07]. In other words, their measurements are precise, they work in most environments with under varying light conditions, and the 3D position of the measured point can be easily derived.

4.3 Simultaneous Localization and Mapping (SLAM)

For the robotic navigation in indoor applications, GPS signal is normally not available, and they rely on a technique called *Simultaneous Localization and Mapping* (SLAM), for guiding robots in the unknown environments. *SLAM* uses perception sensor observations from a moving robot to create the map of the environment, and also identifies the pose of the robot (referenced with respect to this map), from where the map has been created. In SLAM, this *chicken or egg* problem of mapping and localization, is solved simultaneously. (references about SLAM: [Smith 86], [Smith 90], [Durrant-Whyte 06], [Bailey 06]). The name SLAM, was coined in [Leonard 91], and at instances it is also termed as concurrent mapping [Thrun 98].

The common applications of SLAM is for autonomous robot navigation in the GPS denied environments like indoor, undersea, underground and other planets (refer to figure 4.2).

4.4 Solutions to SLAM problem and their limitations

In MMS, which is used extensively in outdoors, the *chicken or egg* problem is broken into a localization problem first, and then the mapping. Localization is often resolved only by the dedicated sensors (GPS, IMU/INS, Odometer). The technique of SLAM can be applied by using the mapping sensors (or perception sensors) for localization.

There are two main branches for resolving the SLAM problem, one that models it in a random process, and the other, applies optimization techniques.

In random process formulation([Smith 90]), the problem is addressed in a probabilistic framework [Thrun 00a]. The approach assumes that the transformation information of the robot is given by the control inputs, and used for predicting the next pose of the robot. Then, this prediction is corrected using the new observations (perception) of the environment. In the system model, both the initial estimate as well as the perception measurements are considered to be noisy. This problem definition, fits perfectly to a Bayesian filter formulation, and typically solved using an Extended Kalman Filter

(a) Indoor

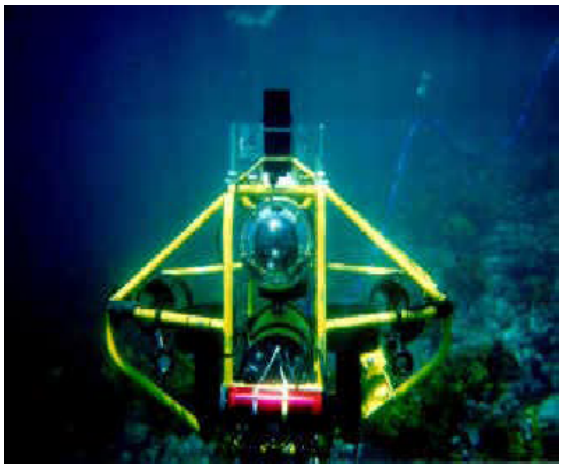

(b) Undersea

(c) Underground

(d) Other Planets

Figure 4.2: Applications of GPS less navigation ([Montemerlo 03a])

(EKF) [Dissanayake 01], [Kiriy 02]. In this approach, localization sensors provide the control inputs, and the perception sensors provide observations of the scene, for correcting predicted pose. The problem is simplified limiting the map to certain identifiable features or landmarks (figure 4.3). Pose of both the vehicle and the landmarks are referred in a global map (fixed reference frame, FRF). The robot pose is corrected using already mapped landmarks, and the map is updated for the newly observed ones. The key to the correction step is the accurate determination of the correspondence between the landmarks observed in the past (represented in a map) with the current measurements. The process determining this, is called the Data Association (DA) [Montemerlo 03b].

The other approach is termed as scan correlation or scan matching

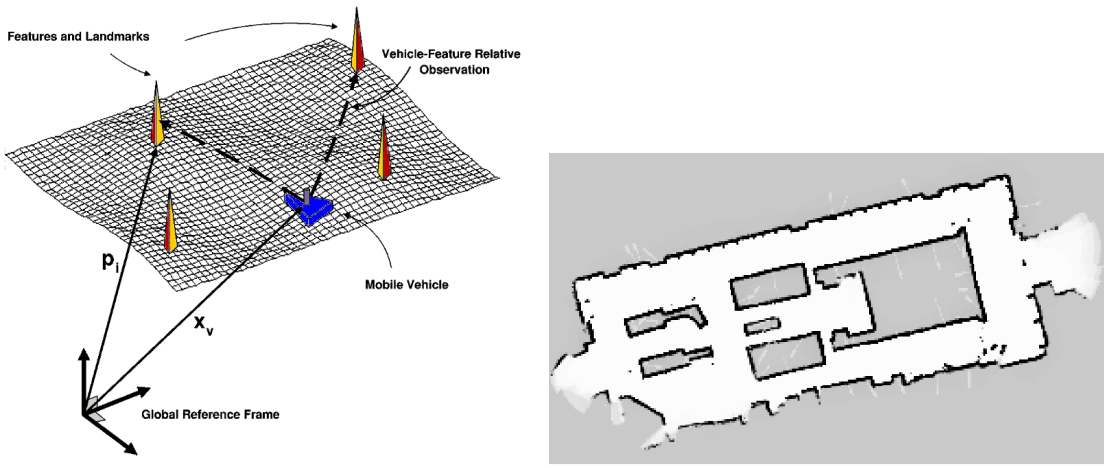

(a) A vehicle taking relative measurements to environmental landmarks (source: [Dissanayake 01])

(b) Common map representation in SLAM - occupancy grids([Thrun 00a])

Figure 4.3: Feature based approach for SLAM problem. Maps contain identifiable landmarks, and represented by space occupied by them.

([Lu 97], [Bengtsson 03], [Martínez 06a], [Martínez 06b]). It estimates the pose of the measuring platform (vehicle) using optimization techniques to match the successive set of observations (scans). Therefore, in this approach the perception observations are trusted to compute the pose. Transformation of the robot between two scans, or between a scan and a map of scans [Hellström 06], is identified by matching the raw scan measurements (figure 4.4). The *optimal* transformation applied to one of the scan, to find the best fit with the other, solves the robot pose. This optimal transformation is selected by sampling several transformation possibilities, and then choosing the one, that fits the best. Both measurement and vehicle motion noises are assumed to be same for short interval of time, therefore gets canceled in a differential process. The principle advantage of this approach is, it does not require any modeling of the landmarks, therefore, works in environments without confining to specific features. However, it requires overlapping (or redundant) information between the scans. The iterative optimization algorithms require substantial time and space complexities for solving the transformation, because the Data Association is unknown, and resolved implicitly. These iterative algorithms have different forms, but they are based on the principle of maximum likelihood. They are, Iterative Dual Correspondence (IDC) [Lu 97], Iterative Closest Point (ICP) [Besl 92], [Chen 02] and approaches like Gaussian sum [Nieto 06], [Steux 10].

Both SLAM approaches often use range scanners like 2D laser scanners [en Gutmann 97], [Thrun 00a], [Nieto 06] or sonars [Leonard 92], [Mallios 09] for mapping. Alternatively, in some cases the mapping is done by one [Davison 07] or more [Sola 07], [Sola 08]) digital cameras. As already mentioned laser scanners are the vastly used perception sensors.

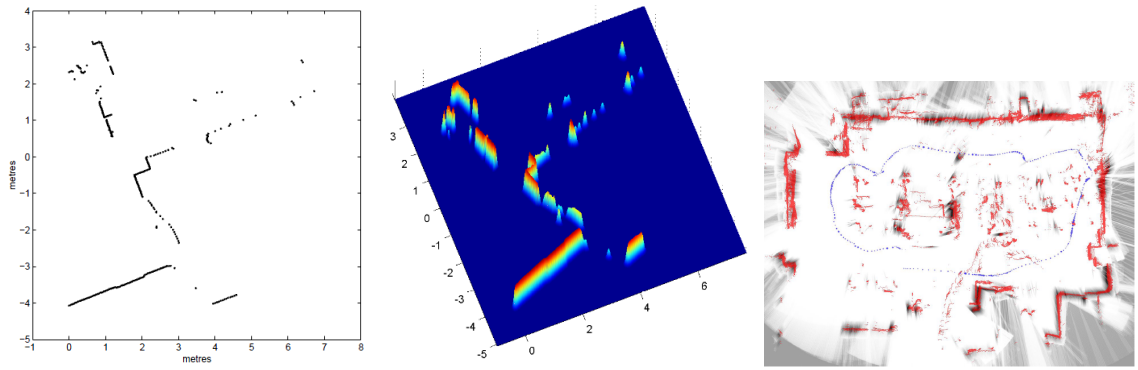

(a) A 2D laser range scan (source: [Nieto 06])

(b) Adding uncertainties to the laser scanners (source: [Nieto 06])

(c) Scan Matching results (source [Steux 10])

Figure 4.4: Scan correlation an optimization approach to SLAM problem. Here a range scan is correlated with a range map (or a previous scan) to compute the relative transformation of the scanning robot.

In land-based applications, both these approaches limit both *localization* and *mapping* problems to 2D space([Martínez 06b], [Nieto 06], [Steux 10]), with 3 Degrees of Freedom (3DOF, with 1DOF rotation and 2DOF translation). This is mainly due to the complexity of the SLAM problem with unknown DA. In most SLAM approaches odometers [Thrun 00a] are the most recurrently used external pose sensors. This is contrary to MMS, which opts IMU to support its 3D outdoor localization with 6DOF (3DOF rotation and 3DOF translation).

These rate sensors provide the control inputs for the EKF prediction of the robot and landmark poses. In the optimization algorithms, these sensors are utilized to provide an initial robot pose estimate, in order to speedup the transformation estimation. Some literatures discuss about 3D maps, yet rely on a 2D space for localization [Thrun 00b]. In [Früh 04] a two step process is used: first, the pose is computed with a flat world assumption (2D space) by applying scan matching technique, and then corrected for the 3D pose using already generated aerial maps or using *Digital Surface Models (DSM)*.

Among the few SLAM approaches which address the 3D localization, [Weingarten 04] and [Weingarten 05] utilize the planar landmarks to solve the SLAM problem in EKF framework. This is an improvement to the commonly chosen 2D landmarks, such as lines and circles [Nieto 06]. In this work, they use odometer measurements to estimate the motion of the robot, and a 3D laser scanner for the perception. They extract the planar landmarks (figure 4.5) from the georeferenced data (i.e., the information already mapped to an FRF), to correct their pose estimates. This implies, their features incorporate errors from both localization and mapping processes.

In scan matching, iterative optimization algorithm, called ICP, is employed to find

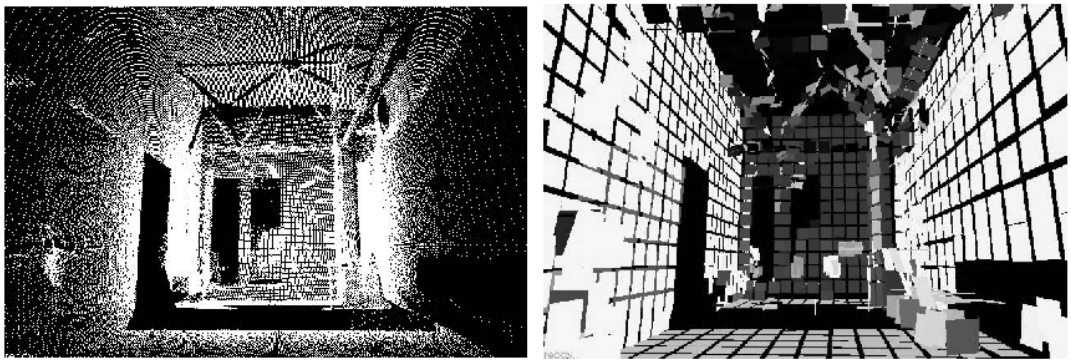

Figure 4.5: 3D scans and the extracted planar features - in an EKF framework [Weingarten 05]

the optimal transformation in 3D space ([Nüchter 05b], [Nüchter 07], [Nüchter 09]). In order to estimate a 3D pose with 6DOF, 2D range scans are not sufficient. Therefore, they acquire the volumetric information of the scene by using 3D laser scanners. However, the data acquisition takes substantial time (nearly **9000** milliseconds per 3D scan), obliging the robot to follow a "stop and go" motion, for avoiding deformation of the volumetric point cloud (figure 4.6).

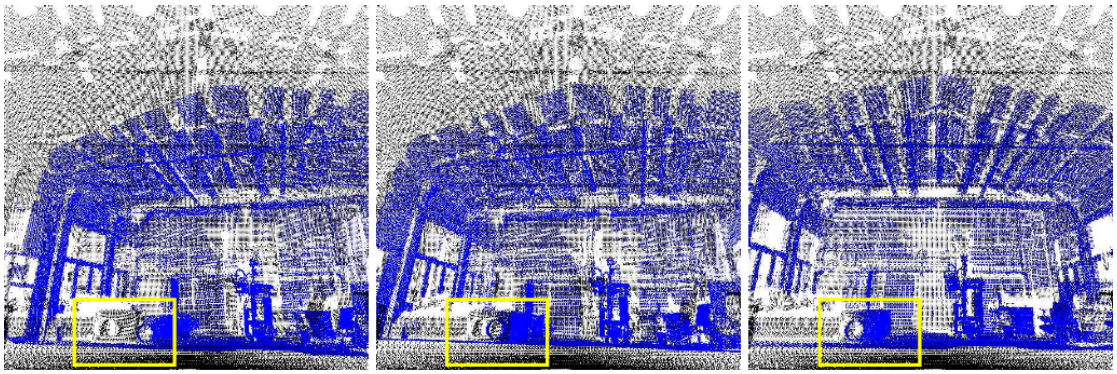

Figure 4.6: Correlating two 3D point clouds [Nuchter 05a], blue and gray colored points are the two 3D scans and the yellow square shows a mug which is matched by applying ICP algorithm, giving the notion of the robot motion.

For both of these approaches, the main limitation comes from the Data Association (DA) problem, i.e., to identify a landmark or part of a scan, on the other map or scan, respectively. In [Weingarten 05], the motion in 3D is predicted from a 2D odometer pose, by introducing a larger uncertainty for the unobservable vertical motion. Once the robot starts to move these uncertainties grow for both robot and landmark poses.

As stated by [Montemerlo 03b], EKF framework based solutions often fail, due to the erroneous data associations resulting from the accumulated errors in the robot pose estimations.

The FastSLAM [Montemerlo 03a], is a combined method of EKF and particle filter (together termed as Rao-Blackwellised filter). The goal is to tackle the nonlinear association and motion estimation. In this solution, all the uncertainties are tracked by separate particles (consisting of the hypothesis for both the pose and the maps) until there are means to resolve it. This approach can address the nonlinearity quite effectively but requires huge resource power to track all the different particles.

On the contrary, since most scan correlation techniques compare two successive scans the problem of growing uncertainties is not a limitation for this approach. However, the iterative optimization algorithms require substantial time and space complexities to converge to an optimal transformation, due to the additional burden of implicit DA. Time complexities are in the order of $O(n^2)$, where n is the number of scanned points, i.e. typically $\sim 100K$ points per a volumetric scan.

4.5 Prelude to our laser odometry approach

We opted to use an approach, which takes advantage of both feature-based (like EKF) and the scan correlation SLAM techniques. First, we decided to use 2D laser scanners because they provide reliable and precise range points of the scene. In contrary to 3D laser scanners, their data acquisition time can be **30** ms (for a low scanning rate of **38** Hz, e.g. SICK LMS scanners). We selected the planar landmarks, the most recurring feature in manmade environments, to reduce both the measurement noise and the solution search space, by representing several raw measurements in a single feature (similar to the work done in [Gee 07]). This intern scales down the complex optimization problem to a simple geometric one. The pose is computed similar to the scan matching, where two closely related observation sets of the landmarks are used for DA, to avoid growing uncertainties. This implies, the trust is more on the observations compared to any control inputs, as done in scan matching. This is because the laser scanner measurements have higher precision compared to localization sensors. Additionally, the noise in the measurements are reduced while extracting the landmarks, by applying smoothing techniques. However, the common approach of nearest neighbor (distance based constraint) relationship cannot be applied to resolve DA, due to the associations are performed in robot's reference frame (moving reference frame, MRF). Therefore, we rely on the properties of the planar landmarks and their intra set relationships to resolve the DA. Once associated, we compute the relative transformation using the geometrical properties of the landmarks. In ideal environments, properties of planar landmarks permits to resolve the 3D pose for at least 5DOF (3DOF Rotation and 2DOF Translation).

The approach computes the relative transformation between two sets of observations, similar to the dead reckoning principle applied in odometry. Therefore, in comparison to camera baseed visual odometry [Nistér 06] (image-based dead reckoning) approaches, this technology can be grouped under the laser odometry ([Bailey 01], [Selkainaho 02]). [Bailey 01] states that, *tracking the relative pose of sequential batch observations (observations taken from a single scan) provides an alternative dead reckoning source that, while perhaps more noisy than odometry, is largely free of systematic errors. Sequential tracking does not require a vehicle model, and operates successfully while ever there are observable features in the sensors field-of-view.* In addition, by using the properties of the selected features pose for more than 3DOF can be resolved, which is never the case with the traditional odometry alone.

The following chapters highlights, the work of 3D laser odometry using planar landmarks. To attain these functionalities there are two important stages to achieve: one, the extraction of the planar landmarks from an environment mostly planar, and the second is to use the extracted landmarks to compute the 3D pose. The first is addressed in chapter 5, and the second stage is detailed in chapter 6. Chapter 7 provides the results of the trajectory computation.

4.6 Conclusion

This chapter prefaces the remaining work done in this thesis, from chapter 5 to 7, which focuses on computing the 3D pose using the planar features extracted from 2D laser scanners. These features are abundant in manmade environments, therefore, the ability to compute an independent pose solution from the perception sensors, can help several applications including Mobile Mapping Systems.

Chapitre 5

Une nouvelle approche pour l'extraction de repères plans

Comme annoncé dans le précédent chapitre, la première étape dans la réalisation d'une odométrie par laser consiste à identifier rapidement des repères caractéristiques. Pour retrouver des repères plans, les méthodes disponibles actuellement utilisent des nuages de points déjà géoréférencés. Comme nous nous proposons d'estimer la position en 3D indépendamment des autres capteurs, ces techniques ne conviennent pas.

Nous proposons un agencement spécifique de scanners laser 2D pour identifier les repères plans. Ces formes géométriques peuvent être caractérisées par trois points non alignés, ou par deux segments de droite. Chacun des scanners 2D peut extraire un segment de droite à partir d'une surface plane. Nous proposons donc d'utiliser deux scanners à faisceaux parallèles et synchrones. Le synchronisme facilite le repérage de segments issus d'une même forme plane. Les faisceaux des lasers sont inclinés de façon à éviter, autant que possible, les obstacles mobiles.

De façon à élargir le champ d'observation, deux paires de scanners à laser sont utilisés : l'une des paires pointe vers l'avant du véhicule, l'autre vers l'arrière. Grâce à cette organisation, un repère plan identifié par les lasers pointant vers l'avant reste visible plus longtemps : quand le véhicule avance, ce même repère est identifié ensuite par la paire de scanners qui pointent vers l'arrière. Cette allongement de la période de visibilité des repères facilite la correction des dérives dans l'estimation de la trajectoire. Un indicateur de confiance, fondé sur la bonne planéité du repère et sur le nombre de points de mesure associés, est attaché à chacun des plans identifiés.

Les algorithmes d'extraction des repères plans sont validés par des tests en simulation et des mesures prises dans un environnement réel. La chaine des algorithmes proposés est compatible avec un traitement concurrent. À l'heure actuelle, ces algorithmes sont

implémentés et testés avec MATLAB. Les algorithmes d'extraction de motifs plans sont transposables, directement, ou avec de légères modifications, aux données issues des scanners à laser 3D. Les travaux de ce chapitre ont été publiés dans l'article [Narayana 10].

Chapter 5

A new approach to planar landmark extraction

Contents

5.1 Introduction

As introduced in chapter 4, the extraction of the planar landmarks is the first step in realizing the 3D laser odometry using planar features. The planar features are arguably most recurrent in the manmade environment (e.g. building facades), especially like

urban canyons, indoor and industrial environments, etc. It is also where the localization functionality of the mobile mapping applications suffers the most due to the degradation of the GPS signal.

The chapter describes our approach to extract the planar landmarks from the 2D laser scanner measurements. The related work is published in [Narayana 10].

The organization of this chapter is as follows:

The first section 5.2, describes our motivation to this work. Section 5.3 presents our novel design to acquire planar landmarks from the raw range scans without georeferencing the measured points. Further, the chain of algorithms for extracting the planar patches is elaborated in section 5.4. The results and analysis obtained using the planar landmark extraction process are presented in section 5.5. Finally, section 5.6 concludes this chapter.

5.2 Motivation

In the works of [Weingarten 04] and [Weingarten 05] planar landmarks are extracted from already georeferenced laser points, incorporating both localization and laser measurement errors. Their goal was to correct the localization errors by applying constraints of planar observations, rather than estimating the pose using them. As mentioned in chapter 4, they use 3D laser scanners for perception. A similar work is also done in [Thrun 00b] where camera and a set of 2D scanners are used for the extraction and creation of maps with planar features. They still apply a 2D localization techniques and the landmarks are extracted after georeferencing.

For an approach of laser odometer, the ability to extract the landmarks without georeferencing is critical. Moreover, it is not just a single landmark to be observed but a set of landmarks, that too in a short span of time, such that these observations do not deform the properties of the landmarks. In [Bailey 01], this observation process is termed as *batch observations*, to indicate a set of landmarks are observed in each observation epoch. The aim is to estimate of the vehicle (or measuring sensor platform/robot) transformation using the intrinsic properties of the landmarks. That is, similar to the principle of odometry and scan matching, it is assumed that no other pose information is available.

Due to these constraints, a 2D laser scanner is preferred over a 3D laser scanners, to reduce the time required for data acquisitions. In the 3D scan matching approaches [Nüchter 07], [Nüchter 09], typically the robot remains stationary till a single scan is finished. The choice is to avoid 'stop and go' motion, therefore an alternative method is chosen with the assumption that the scene is rich with the chosen landmark

features, i.e., planes. However, a single 2D scanner is only suitable for extracting geometrical primitives such as lines or curves. Unless several synchronized 2D scanners are used, obtaining a 3D volumetric scan in quick time (in a rough order of less than 30 ms) is still a challenge. Therefore, the extraction of the planar landmarks needs to be acquired without scanning the entire scene or even the planar surface itself.

For the extraction of a planar landmark, a minimum of *three* non collinear 3D points are required. These points help determine the orientation of the planar landmark in a scene, from the point of measure. Moreover, they can be extracted using *two* 2D laser scanners, as part of the two coplanar lines. However, these lines are formed at the intersection of the laser scan plane and the planar features present in the scene. Therefore, it not sufficient to identify the boundaries of the landmark itself. That is the reason this planar extraction process is termed as **extraction from partial landmark information**. The extraction aims at deducing the basic properties of the landmarks sufficient for helping its identification in space, and also it leads to a simpler landmark extraction process.

An isoclinal pair of synchronized 2D laser scanners are used for extracting the 2 coplanar lines, from which the *three* 3D points belonging to the planar patches are obtained. This implies the process of line extraction is the same for each laser pair, therefore, it can be parallelized. As mentioned in chapter 4, a noise reduction step is a must, since in the odometry approach the measurements are trusted but affected by both motion and measurement process noises. The line extraction process from each 2D laser scanner has an inherent smoothing process, due to line modeling. A confidence factor for each plane, indicating its quality and trust is a must, since it provides an indicator for the future use of the obtained results.

All these processes and related algorithms are detailed in this chapter.

5.3 2D laser scanner-based plane extraction system

Section 5.2 described that an isoclinal pair of 2D synchronized laser scanners are sufficient to extract the planar landmarks. The reliance on the extracted landmarks implies, the system can perform better with more of such features in the scene and the ability to observe them. Therefore, a second pair of laser scanner is introduced to increase the visibility of the mapping environment. The second pair is oriented to the direction unobserved by the first. One way to achieve this, is to point the first pair to the forward, and the second to the backward direction with respect to the direction of motion of the vehicle. Laser scanners with the capability to observe a large zone in the scanning plane (high field of view) are preferred. The scanning planes of an isoclinal pair of laser scanners are parallel.

In figure 5.1, the system configuration is shown from three different poses of the vehicle, illustrating the laser scanner arrangements and their scan planes.

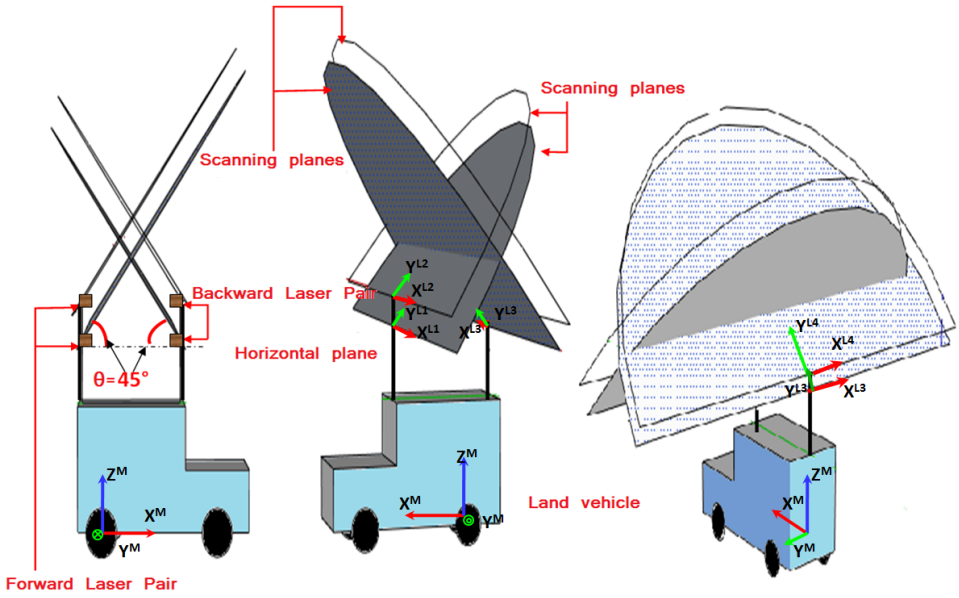

Figure 5.1: The laser scanner configuration used in our approach. Two isoclinal pairs of laser scanners are mounted on a vehicle with an angle θ, with respect to the horizontal plane.

5.3.1 Justification: usage of a pair of parallel scanners

The parallel laser scanners allows to spot the planar patches independent of the distance to the facades from the measuring location.

This is depicted in figure 5.2 with two possible configurations. It contains two poses for the laser pairs with a wall located at distances $d1$ and $d2$.

As shown in *configuration 1*, when the distance to the wall increases ($d2 > d1$), the laser beam diverges and hits different planes of the facade. Such problems are less frequent in *configuration 2*. This is clarified by observing the laser impact points on the wall at distance $d2$.

To simplify the computation, the two lasers are positioned so that the origins of their beams or the optical centers (laser reference frames, LRF) are aligned horizontally, yet vertically shifted.

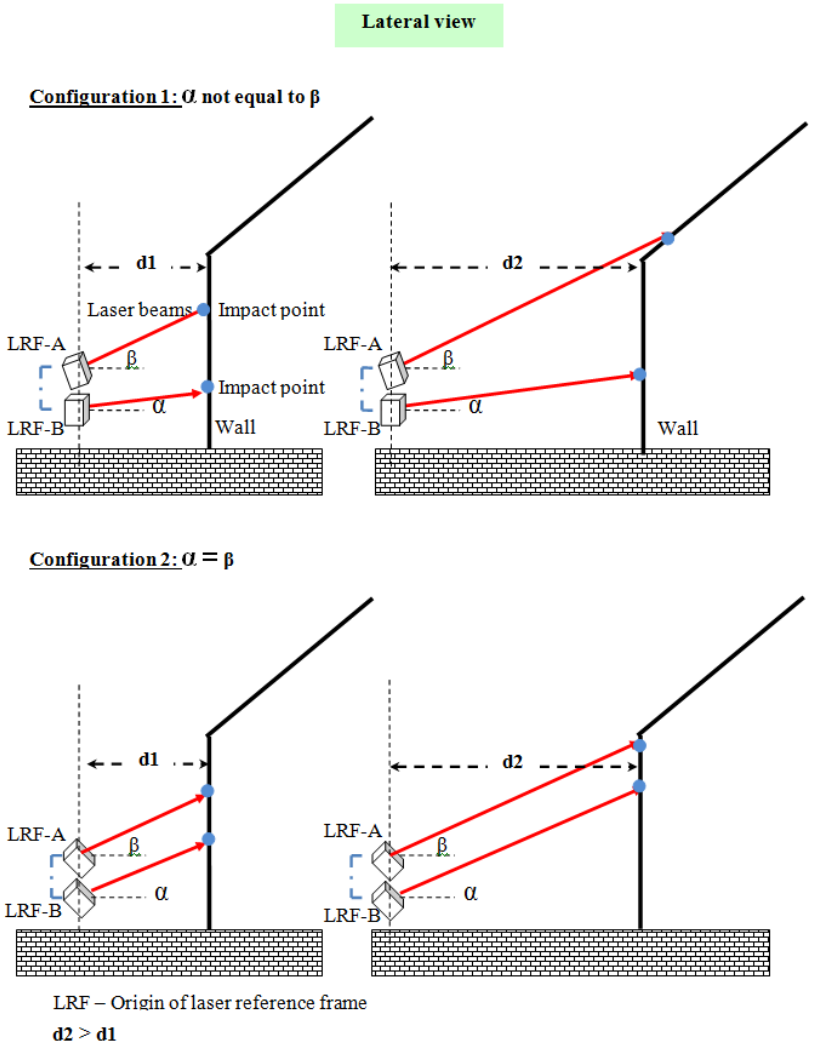

Figure 5.2: Two configurations of a laser scanner pair used to extract planar features. (Top) Non isoclinal beams result in a divergence effect and a dependence of the distance to the analyzed object. (Bottom) Isoclinal lasers lead to a higher probability of detecting the planar features independent of the distance. The impact locations of the laser scans on the wall are represented by blue points.

5.3.2 Justification: inclination of the scanning planes

Occlusions is one of the major bottleneck for the perception based approaches, which mask the desired landmarks or disturb their clear view. They originate from two sources; the first category results from the geometry of the object itself and the angle of observation. The second category is due to the occlusion by other objects (shadow) [Yoo 09]. It

is difficult to tackle the first category of occlusions, but the second category can be diminished by avoiding the zone frequented by the shadowing objects, especially the moving objects. There is a dedicated branch of study to tackle the moving object problem, called *Simultaneous Localization, Mapping and Moving Object Tracking (SLAMMOT)* or *Detection and Tracking of Moving Objects (DTMO)* [Wang 04], which is typically related to autonomous navigation. The issue of moving objects are not addressed in this thesis.

In our design, the inclination θ, of the laser scanners of an isoclinal pair with respect to horizontal plane is a configurable parameter, and is altered depending on the properties of the scene being scanned. For example, in an urban canyon with tall buildings, the inclination can be set to $\pm\mathbf{45}^\circ$, to avoid moving obstacles and to point to the building facades at higher elevation. In an indoor or underground environments, with only a few moving objects, the inclination can be set to $\mathbf{0}^\circ$ or more.

5.3.3 Justification: two isoclinal laser pairs

As mentioned earlier, the first benefit of using two isoclinal pairs of laser scanners is that, it increases the *visibility of the mapping environment* (i.e., spatial visibility).

The second, as the vehicle/robot moves, the backward pair of lasers is able to observe the landmarks already observed by the forward laser. This means, it improves the *visibility period* for a given landmark (i.e., temporal visibility).

This reinforces the observation of the same landmarks over a period of time, and this property can be exploited to correct the drift errors, one of the most common problem of SLAM as well as odometry approaches. One way to correct the drift errors, is to assume the first observations are accurate and therefore, trusted. This assumption is true, because normally the initial observations are done from the vehicle at rest, so there is less noise. Once the vehicle starts to move, if the landmarks observed in the past remain observable, then any drift in the pose can be corrected by correcting the errors in the new observations of the trusted landmark positions.

This concept is explained using an example, given in figure 5.3, where two sets of landmark observations are shown. Any properties which remain time invariant, can be corrected comparing the changes in the two set of associated landmarks. Normally drift errors effect the pose of the landmarks in a fixed reference frame (FRF), like map reference frame. Even these errors can be corrected once the association is done, which are directly related to the pose drift of the vehicle.

A large delay of Δt facilitates longterm drift corrections. Forward and backward isoclinal laser pairs help increase Δt.

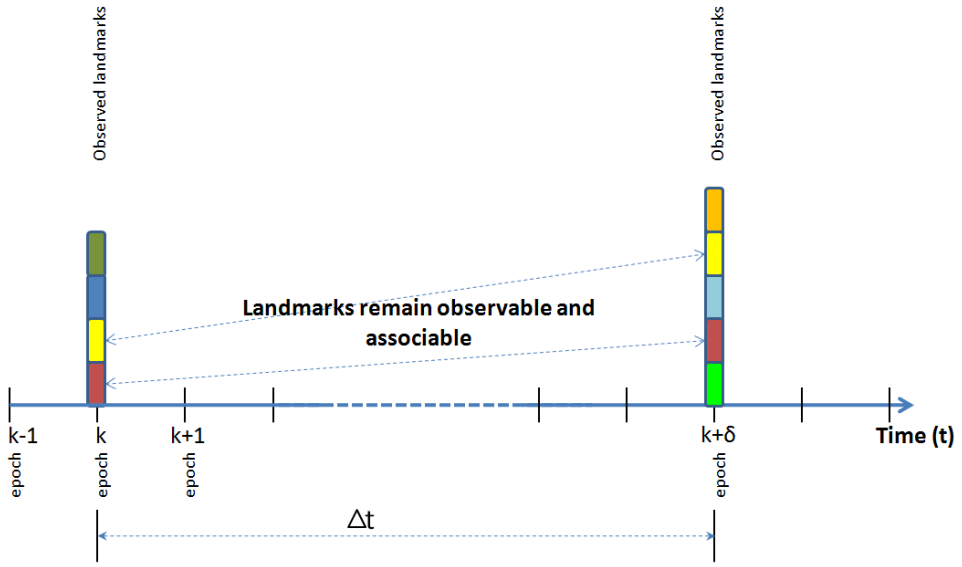

Figure 5.3: Benefit of increased temporal observability of landmarks. Each landmark is depicted by a rectangle of the unique color, and the color represents the time invariant unique property of the landmark, which can be exploited to identify it across two epochs. Therefore, the identified identical landmarks at k and $k + \delta = k + \Delta t$ are denoted by the same color.

5.4 Algorithms for the extraction of planar patches

This section describes the algorithms used for extracting the planar patches from the measurements of an isoclinal pair of laser scanners. The planar patch extraction process is summed up in figure 5.4 and algorithm 5.1.

The algorithms are implemented in MATLAB and executed sequentially. The line extraction step is identical for two lasers of the same isoclinal pair, inducing the possibility of parallel processing. Thus the plane extraction process can be adapted for real time applications if implemented in C/C++. The algorithm is detailed below.

5.4.1 Input - 2D laser scanner profiles

A range scan at a discrete time k is considered as a set of points, as expressed using equation 5.1.

$$\mathbf{P_k} = \{\mathbf{q_{kj}} = (\mathbf{r_{kj}}, \alpha_{\mathbf{kj}}) | j = 1 \dots N\} \tag{5.1}$$

Algorithm 5.1 Extraction of planar patches at time k for an isoclinal pair of lasers

Require: P_{kl}, is profile of laser scanner l and $l \in \{1, 2\}$.

1. **Line Extraction:** for each l

   (a) **Preprocessing -** Select the corresponding valid ranges $\mathbf{V_{kl}}$ from $\mathbf{P_{kl}}$. Convert $\mathbf{V_{kl}}$ given in polar coordinates $\mathbf{V_{kl}^{L,p}}$ to Cartesian coordinates, in both the laser $\mathbf{V_{kl}^{L,c}}$ and vehicle/mapping reference frames $\mathbf{V_{kl}^{M,c}}$.

   (b) **Data Discontinuity Detection**

   - Clustering - Identify the discontinuity in valid ranges $\mathbf{V_{kl}^{L,p}}$ and form a set of data clusters $\mathbf{C_{kl}^{L,c}}$
   - Segmentation - Detect the candidate line segments (to separate corners, overlapping regions etc) within the clusters. Repeat for all the clusters in a profile and store the results in $\mathbf{S_{kl}^{L,c}}$.

   (c) **Line Estimation**

   - Parameter Computation - Apply the RANSAC algorithm to determine the line parameters by removing the outliers. This step also helps remove nonlinear segments.
   - Confidence Indicator Determination - Define a quality parameter to indicate the bounded confidence ($\mathbf{Confidence_s}$ denoted as **CLEF**) of each retained line segment. Store these values along with the line parameters in the set $\mathbf{L_{kl}^{M,c}}$ for further processing.

2. **Line Correlation:** From the sets of line segments $\mathbf{L_{kl}^{M,c}}$ for the two laser scanners of an isoclinal pair, determine the matching pairs of lines. Once matched, compute a combined confidence factor (indicated as **CPEF**). Store the results in the set $\mathbf{Match_{k12}^{M,c}}$

3. **Plane Fitting:**

   - For each member of $\mathbf{Match_{k12}^{M,c}}$, select three points ($\mathbf{Pt1}, \mathbf{Pt2}$ and $\mathbf{Pt3}$) - Two points from the pair of line segments with the highest $\mathbf{Confidence_s}$ value and one from another line segment
   - Estimate plane parameters (Normal vector and offset from the origin) using these three selected points ($\mathbf{Pt1}, \mathbf{Pt2}$ and $\mathbf{Pt3}$). Store it for further processing in the set $\mathbf{Plane_{k12}^{M,c}}$

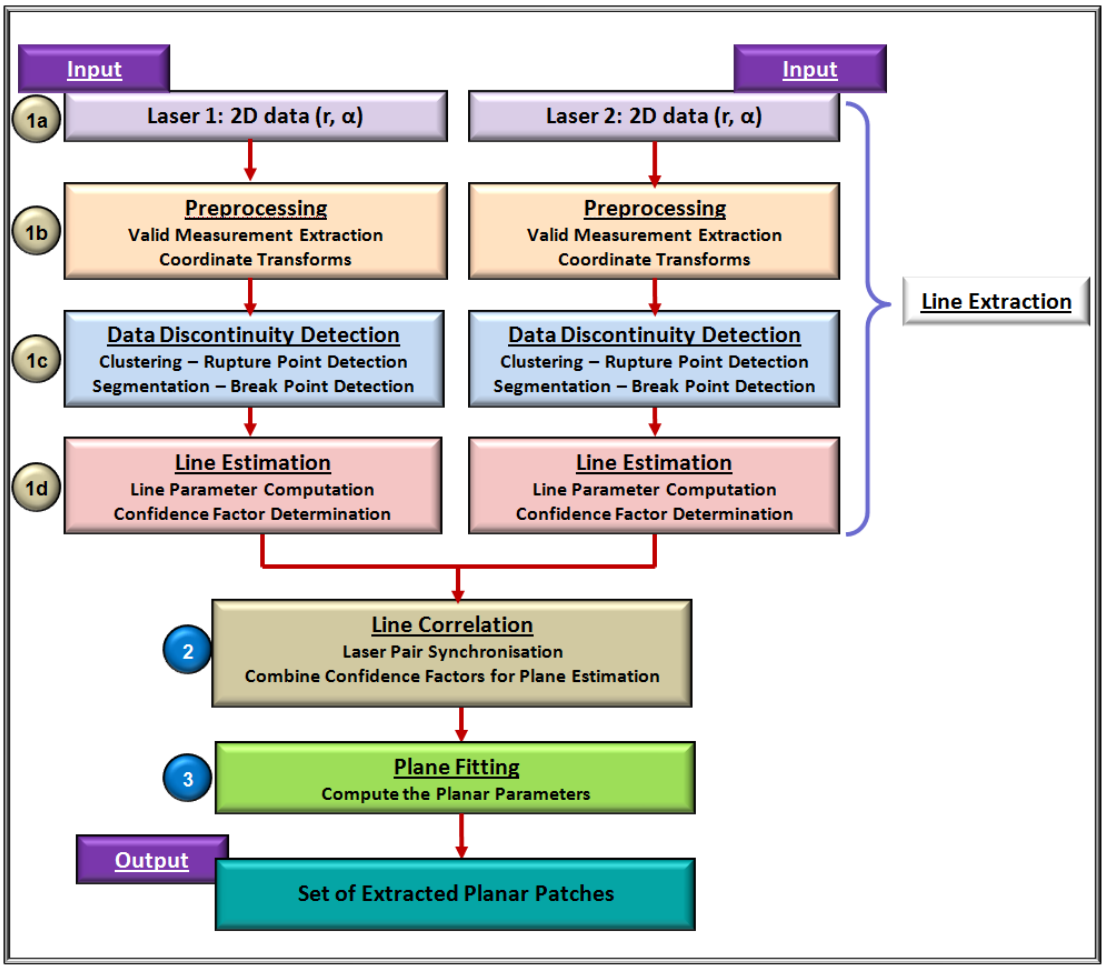

Figure 5.4: Planar landmark extraction process using the measurements of an isoclinal pair of 2D laser scanners.

$\mathbf{P_k}$ is the profile with points $\mathbf{q_{kj}}$ represented in polar coordinates as a range $\mathbf{r_{kj}}$ and the laser bearing angle $\alpha_{\mathbf{kj}}$. The starting angle for the scan is given as $\alpha_{\mathbf{min}}$. The ranges correspond to the successive intersections of the laser ray with the closest objects in the vicinity. The scan angles are assumed to be uniformly spaced, with a fixed resolution $\mathbf{\Gamma}$. $\mathbf{N}$ is the number of points per profile, which is a constant value. It is determined as a function of the field of view $\mathbf{\Upsilon}$ and $\mathbf{\Gamma}$.

The 2D laser scanner measurements and the related concepts are well explained in [Borges 04]. The feasible maximum values for $\mathbf{\Upsilon}$ and $\mathbf{\Gamma}$ are normally given in the laser scanner specifications. For some scanners, however, these values are configured within their maximum limits. In figure 5.1, $\mathbf{\Upsilon} = \mathbf{180}^\circ$ is the expected field of view for the

studied system design. The frequency of the laser scanner $\mathbf{F_{laser}}$, is the number of profiles $\mathbf{P_k}$ provided in one second. When the scanning frequency is high enough, a better frozen view of the environment can be obtained in spite of the vehicle motion. The output of commercially available 2D laser scanners (e.g. SICK LMS laser scanner [SICK 06]) is usually a fixed size stream of points (a fixed size profile) at each discrete time $\mathbf{k}$.

In figure 5.5, a laser scan plane is shown, with an inclination of 45°, $\mathbf{\Upsilon = 180°}$ and $\alpha_{\mathbf{min}} = \mathbf{0°}$. The maximum measured range $\mathbf{r_{kj}} = \mathbf{R_{max}}$ is fixed, depending on the application. The 'valid ranges' (set $\mathbf{V_k}$) corresponding to the detected objects at a distance $\mathbf{r_{kj}} \in [\mathbf{R_{min}}, \mathbf{R_{max}}]$. If $\mathbf{r_{kj}} \geq \mathbf{R_{max}}$ then $\mathbf{r_{kj}} = \mathbf{R_{max}}$, is called the 'infinity measure' (set $\mathbf{I_k}$). If $\mathbf{r_{kj}} \leq \mathbf{R_{min}}$, the measurements is discarded. For simplicity, we can consider it as part of the set $\mathbf{I_k}$. Therefore, the set of valid measures $\mathbf{V_k}$ is a subset of a laser profile at time k. That is, $\mathbf{V_k} \subseteq \mathbf{P_k}$ and $\mathbf{V_k} \cup \mathbf{I_k} = \mathbf{P_k}$.

Though currently $\mathbf{I_k}$ is neglected, they provide the valuable information of the empty spaces. In future, this information can be utilized to improve the algorithms.

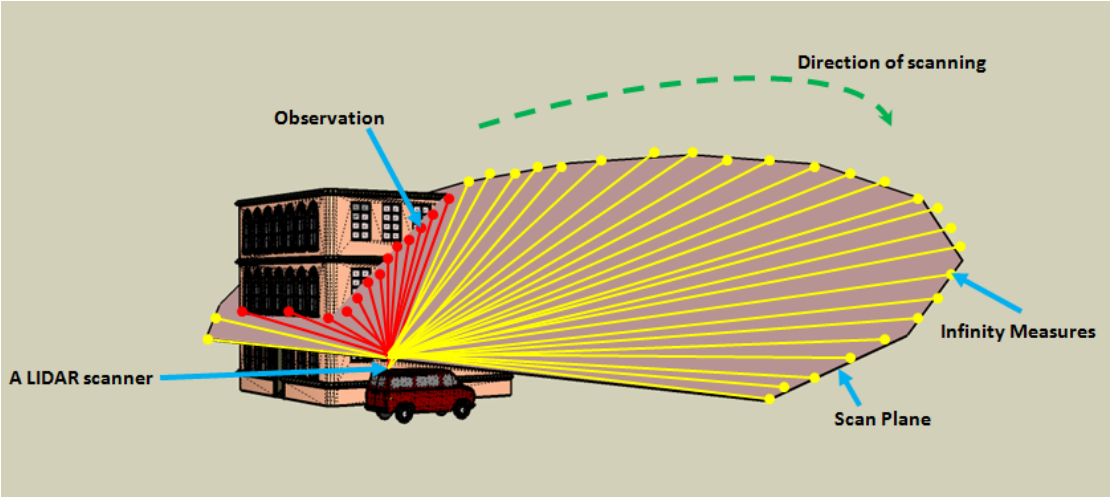

Figure 5.5: A 2D laser scanner profile is shown here, has an inclination of 45° and field of view**180°**. The lines in red and yellow correspond to the range measurements. Valid ranges are shown in red, and the infinity measures are in yellow.

In this study, a simpler noise model for the laser measurement is used. The deviations in the step $\mathbf{j}$ of the scanning angle $\alpha_{\mathbf{kj}}$ are neglected, as done in several other works [Kapp 06], [Borges 04]. The precision of the laser range is determined empirically by computing the standard deviation of the range measures $\sigma_{\mathbf{laser}}$. A more sophisticated noise model for the laser measures can be introduced later.

5.4.2 Line extraction

1. **Preprocessing**
   There are two preprocessing steps: first, the selection of valid measurements, and second, coordinate conversions and transforms. The coordinate conversion step computes the equivalent Cartesian coordinate values for the laser measurements expressed in polar coordinates. The coordinate transform changes the reference frame of the measurements by applying the appropriate rotations and translations.

   - Valid measurements selection

     At first, the input data given in equation 5.1 is converted to the form of equation 5.2.

     $$\mathbf{V_{kl}} = \{\mathbf{q_{kv}} = (\mathbf{r_{kv}}, \alpha_{\mathbf{kv}}) | (\mathbf{R_{min}} < \mathbf{r_{kv}} < \mathbf{R_{max}})\}_l \tag{5.2}$$

     where, index $\mathbf{v} \in \{\mathbf{1} \ldots \mathbf{N_V}\}$ with $\mathbf{N_V}$ represents the number of valid points. An additional index l is used to identify the lasers within a pair.

   - Coordinate conversion and transforms

     Within the scope of this chapter, two reference coordinate systems are used: a sensor (laser) reference frame **LRF** (superscript notation **L**), and a moving (vehicle/robot) reference frame **MRF** (superscript notation **M**). In addition to this, there is also another frame, which is a fixed mapping frame denoted by **FRF**, but it is not applicable in the scope of landmark extraction.
     LRF is a 2D frame covering the laser scanning plane, whereas **MRF** refers to a 3D space with an origin at the center of the rear wheel axis of the vehicle/robot. Figure 5.6 gives a brief description of these reference frames.
     Polar to Cartesian coordinate system

     Data in $\mathbf{V_{kl}}$ is expressed in the polar coordinate form. Subfigure 2 of figure 5.6 illustrates the conversion of this data to the corresponding Cartesian coordinate form. To distinguish the coordinate system, two superscripts are added: polar ($\mathbf{p}$) and Cartesian ($\mathbf{c}$). The converted valid ranges $\mathbf{V_{kl}^{L,c}}$ expressed in the Cartesian coordinate as given in equation 5.3.

     $$\mathbf{V_{kl}^{L,c}} = \{\mathbf{p_{kv}} = (\mathbf{x_{kv}^L}, \mathbf{y_{kv}^L}, \mathbf{z_{kv}^L}) | \mathbf{v} \in \{\mathbf{1} \ldots \mathbf{N_V}\}\} \tag{5.3}$$

     From LRF to MRF

     This corresponds to the subfigures 3 and 4 of figure 5.6. The coordinate transform function is given as:

     $$\left.\begin{aligned} &\mathbf{V_{kl}^{L,c}} \rightarrow \mathbf{V_{kl}^{M,c}} \\ &\mathbf{V_{kl}^{M,c}} = \mathbf{Rot}(\mathbf{Y^M}, \theta)(\mathbf{V_{kl}^{L,c}})^{\mathbf{T}} + \mathbf{Trans}(\mathbf{X^M}, \mathbf{Y^M}, \mathbf{Z^M})^{\mathbf{T}} \end{aligned}\right\} \tag{5.4}$$

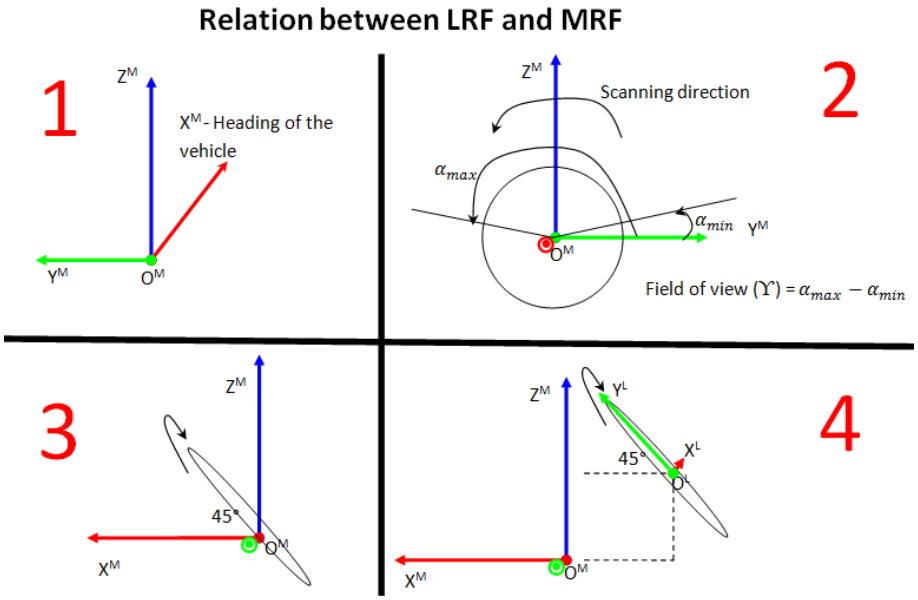

1. Moving (mapping) reference frame MRF, located on the center of rear wheel axis with origin O^M
2. Laser scanning plane seen from the front of the vehicle. The LRF is translated to the origin of the MRF
3. Lateral view of the laser scanning plane
4. LRF with origin O^L translated to its origin with respect to MRF

Figure 5.6: Measurements expressed in the laser reference frame (LRF) is transformed to vehicle reference frame (MRF).

$\mathbf{Rot}(\mathbf{Y^M}, \theta)$, stands for the rotation matrix around the $\mathbf{Y^M}$ axis of an angle θ. For the presented design in section 5.3, we assume the scenario of an urban canyon, indicating an inclination of $\theta = \mathbf{45}^\circ$ and $\theta = -\mathbf{45}^\circ$ for the forward and backward isoclinal pairs respectively. $(\mathbf{V^{L,c}_{kl}})^\mathbf{T}$ is the transpose of $\mathbf{V^{L,c}_{kl}}$. $\mathbf{Trans}(\mathbf{X^M}, \mathbf{Y^M}, \mathbf{Z^M})$ is the translation vector from **LRF** to **MRF**, different for each laser even within an isoclinal pair. The translation is only applied in $\mathbf{Z^M}$ axis for a parallel laser pair setup.

2. **Data discontinuity detection**

The first two kinds of discontinuities described in table 5.1, is taken from [Borges 04]. The system presented in this thesis, aims at minimizing the effect of occlusions by avoiding, measuring the likely zones of their occurrence.

The percentage of data corresponding to 'missing objects' in urban canyons or indoor scenes is small. *Although the absence of detectable objects in the scan region is a drawback for the SLAM approach, it indicates an open space where the GPS receiver provides better positioning solution.* This indicator can be derived

Type	Cause	Name	Handling Methods
Missing objects	Absence of obstacles in the scanning direction	Rupture points	Clustering
Object discontinuity	Change in the surface of the object	Break points	Segmentation
Occlusions	Masking obstacles	Break points	Segmentation and Segment merging

Table 5.1: Different forms of data discontinuities in the range measurements.

from the cardinality of the set of infinity measures $\mathbf{I_k}$.

- **Clustering**

  All the continuous valid measures between two rupture points are considered as a cluster. The set of these clusters is denoted as $\mathbf{C_{kl}^{L,c}}$.

  $$\mathbf{C_{kl}^{L,c}} = \{\mathbf{C_{klj}^{L,c}} | \mathbf{j} = \{\mathbf{1} \ldots \mathbf{N_{Ckl}}\}\} \tag{5.5}$$

  $\mathbf{N_{Ckl}}$ is the number of identified clusters.
  Clustering plays an important role to ensure that the line extraction does not merge two parallel coplanar lines from two sections of data. It also reduces the space for the segment merging algorithms. As mentioned in [Nguyen 07], the lines are normally split into several segments due to the presence of obstacles. If clustering is done, the merging operation is only necessary within a cluster. A detected cluster can contain zero or more line segments, required for the detection the planar patches.

- **Segmentation**

  Segmentation is carried out within each identified clusters in the set $\mathbf{C_{kl}^{L,c}}$. The goal is to detect the discontinuities in the data, due to change in the surface of the object itself, or occlusions. This step does not extract lines but determines the possible line segments. This simplifies the line extraction process, and makes the plane fitting step robust to outliers.
  This segmentation method works similar to the line extraction, therefore, algorithm such as **Iterative End Point Fit (IEPF)** given in [Borges 04] can be applied. This algorithm is very similar to the Split and Merge Algorithm in [Nguyen 07]. Its advantages are: simplicity to implement, required execution time, and conserving the input data point order required for later processing. Methods like *RANdom SAmple Consensus (RANSAC)* algorithm [Fischler 81] and *Hough transforms* omit the data order, making them more suitable for image processing than laser scanner measurements. We

noted that the IEPF, functions exactly same as the Ramer-Douglas-Peucker (or chord) algorithm [Douglas 73].

The IEPF is a recursive algorithm, in which we included the **Adaptive Breakpoint Algorithm (ABA)** [Borges 04]. The ABA algorithm separates any collinear points from two buildings located at a far distance. The breakpoint detector $\mathbf{D_{max}}$, indicating the maximum allowed distance between two successive collinear points, is adapted according to the range of these two points. $\mathbf{D_{max}}$ depends on a predefined angle of incidence $\phi = (\pi/\mathbf{2}) - \lambda$, where λ is defined in [Borges 04], as the angle between the planar surface and the direction of the laser range measurement.

$$\mathbf{D_{max}} = \mathbf{r_{k(j-1)}} \times \frac{\sin \mathbf{\Gamma}}{\sin(\pi/\mathbf{2}) - (\phi + \mathbf{\Gamma})} + \mathbf{3.29} \times \sigma_{\mathbf{laser}} \tag{5.6}$$

where $\mathbf{\Gamma}$ as defined before, is the angular resolution, $\mathbf{r_{k(j-1)}}$ is the immediately previous range measurement. The constant **3.29** corresponds to **99**% of the values in a normal distribution.

In the present implementation, ϕ is set to **79**°. As a limitation, two successive measured points of a building with an angle of incidence close to **90**°, located at a far distance, are considered break points. However, this situation cannot occur often in manmade environments.

The IEPF algorithm connects the first (**SI**) and the last point (**EI**) of an input set of points by a **Line**(**SI**, **EI**). It then detects the furthest point **FI** to this line in the input set. If the distance **d** to this point is less than the threshold $\mathbf{D_{far}}$, the segmentation step is finished. All the points between the first and the last points are considered to be part of the segment. However, if $\mathbf{d} \geq \mathbf{D_{far}}$, the set of points is divided in two. The first set is from the first point **SI** to the furthest point **FI**, and the second is from **FI** to the last point **EI**. Then IEPF is executed recursively for these two new sets until no more division occurs. The feasible segments in the set of input points are output. These steps are demonstrated using a self explanatory example in figure 5.7.

In the present implementation, $\mathbf{D_{far}} = \mathbf{3.29} \times \sigma_{\mathbf{laser}} \times \mathbf{K_1}$. As already given, the constant **3.29** corresponds to **99**% of the values in a normal distribution. $\mathbf{K_1} = \mathbf{2}$ is a configuration parameter taking into account the errors due to the numerical conversion and infinitesimal motion.

The final segment $\mathbf{S_{kl}^{L,c}}$ in a profile is the union of all the sets $\mathbf{S_{klj}^{L,c}}$ of identified segments of the $\mathbf{j^{th}}$ cluster $\mathbf{C_{klj}^{L,c}}$, at a given time **k**.

$$\mathbf{S_{kl}^{L,c}} = \{\mathbf{S_{klj}^{L,c}} | \mathbf{j} = \{\mathbf{1} \ldots \mathbf{N_{Ckl}}\}\} \tag{5.7}$$

$|\mathbf{S_{kl}^{L,c}}| = \mathbf{N_{Skl}}$ where $\mathbf{N_{Skl}}$ is the total number of segments detected for a given laser.

The result of the segmentation process are shown in figure 5.8.

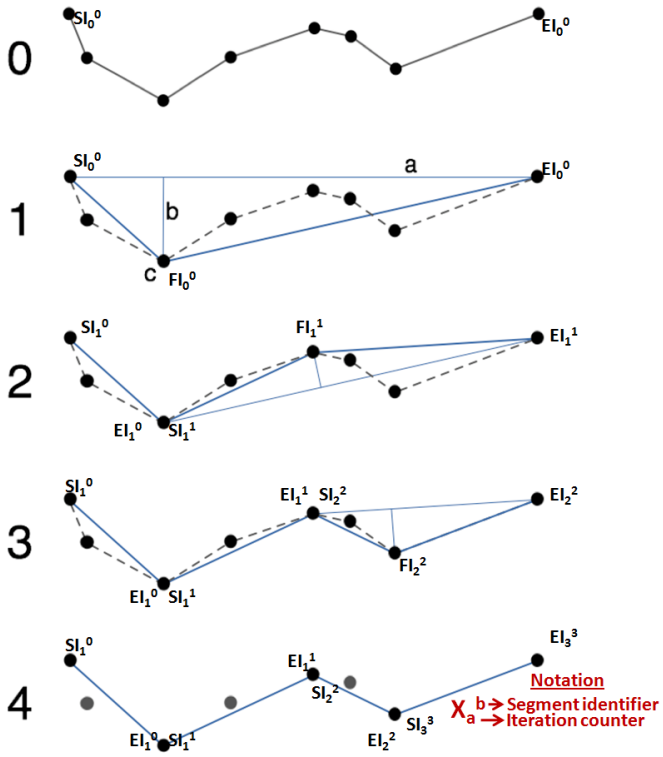

Figure 5.7: Demonstration of the working of recursive segmentation algorithm (chord or IEPF).

3. Line estimation

- Line parameter computation
  In [Borges 04] and [Nguyen 07], the IEPF algorithm is used for the line extraction. As described before, IEPF fits line between the first and the last points of the segment. Therefore, the direct application of the algorithm results in a non-optimal solution, since the first and the last points of the estimated segment are also prone to noise.

  Therefore, the line estimation is performed using the **RANdom SAmple Consensus (RANSAC)** algorithm [Fischler 81] for each segment $\mathbf{S_{kl}^{L,c}}$. RANSAC is an iterative algorithm for estimating parameters of a mathematical model from an observed dataset with outliers. Before calling RANSAC, each segment with less than $\mathbf{P_{min}}$ points is discarded to avoid spurious landmark detections. In the current implementation $\mathbf{P_{min}} = \mathbf{5}$.

  The RANSAC algorithm first selects a random set of points from the given segment called a sample set. These points are assumed to belong to a straight line, $\mathbf{ax + by + c = 0}$ whose parameters a, b and c are estimated. The algorithm then checks for the points of the segment fitting the estimated

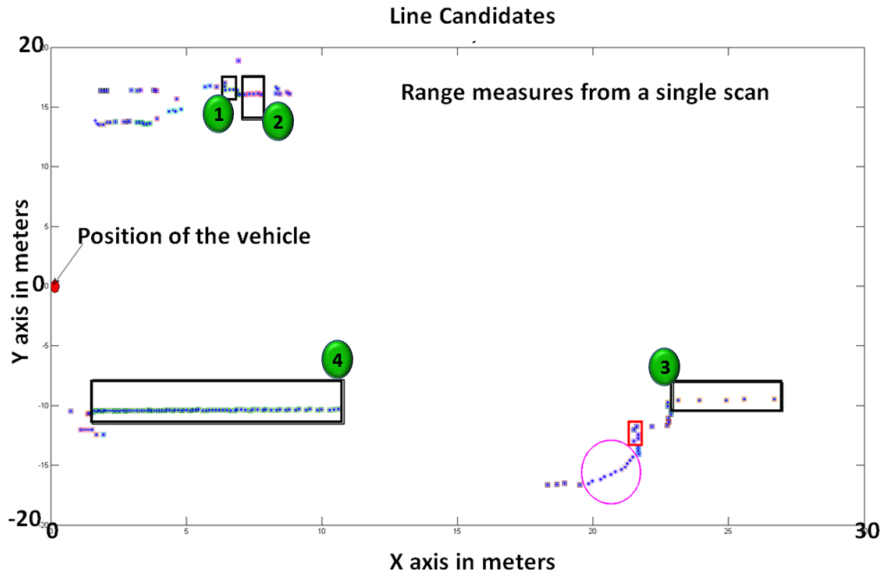

Figure 5.8: Figure shows the result of a segmentation. The measurements of a single laser at a given instant **k** correspond to the displayed points. The displayed data is from a laser of the forward isoclinal pair. Each segment is shown in unique colored points. The black rectangles (with tagged identifiers) show the feasible line segments, the red rectangle, shows a feasible segment but omitted due to significant noise, and the ellipse in magenta shows a curved segment.

line. The conformed points and the sample set form the consensuses set. To include a point in the consensus set, the distance between the point and the constructed line has to be less than the threshold of $\sigma_{\mathbf{RANSAC}}$. $\sigma_{\mathbf{RANSAC}}$ is presently set to $\mathbf{D_{far}}$, to ensure the accepted level of noise remains the same for both, extraction of lines and the segmentation (this avoids splitting of line segments).

By combining the IEPF with the robust RANSAC algorithm, the line extraction time is reduced, and the process remains robust to the outliers. It also minimizes the uniformly distributed noise from the laser measurements. The data within a segment remains ordered, and have the same level of noise.

Since RANSAC fits the line in the least squares sense, the boundaries of the line need to be defined using the measured points. This is achieved by projecting the start and end points of the segment onto the extracted line. These points are then transformed to the **MRF**, since the plane fitting is performed in the **3D** space. The line start and end points are denoted as $(\mathbf{LS^{M,c}}, \mathbf{LE^{M,c}})$ respectively.

- Confidence indicator determination

Each extracted line is evaluated using the confidence measure. First, the ratio of the number of points in the consensus set $\mathbf{N_{consensus}}$ to the number of points in the segment $\mathbf{N_{segment}}$, given as $\frac{\mathbf{N_{consensus}}}{\mathbf{N_{segment}}} > \mathbf{K_2}$ is checked. The configuration parameter $\mathbf{K_2}$ is set to $\mathbf{0.8}$ to ensure that at least 80% of the points in the segment adhers to the estimated line. Then the average squared error **SqErr** between the points $(\mathbf{y_p}, \mathbf{z_p})$ in the consensus set $\mathbf{N_{consensus}}$ to the estimated line is checked. The error $\mathbf{E_p}$ in fitting each point $(\mathbf{y_p}, \mathbf{z_p})$ to the line is given by equation 5.8.

$$\mathbf{E_p} = \mathbf{a}(\mathbf{y_p}) + \mathbf{b}(\mathbf{z_p}) + \mathbf{c} \tag{5.8}$$

The normalized squared error **SqErr** for the point $\mathbf{p}$ is computed as

$$\mathbf{SqErr_p} = \frac{\mathbf{E_p^2}}{\mathbf{a^2 + b^2}} \tag{5.9}$$

This error is summed up for all the points in the consensus set and normalized by the number of points $(\mathbf{N_{consensus}})_\mathbf{s}$ in the line segment $\mathbf{s}$.

$$\mathbf{ErrUse_s} = \sqrt{\frac{\sum_p \mathbf{SqErr_p}}{(\mathbf{N_{consensus}})_\mathbf{s}}} \tag{5.10}$$

The confidence (Confidence on Line Estimation Factor, **CLEF**) is then given as:

$$\mathbf{Confidence_s} = \frac{(\mathbf{N_{consensus}})_\mathbf{s}}{\mathbf{ErrUse_s}} \tag{5.11}$$

Practically, $\mathbf{0} < \mathbf{ErrUse_s} < \sigma_\mathbf{RANSAC}$, i.e., $\mathbf{ErrUse_s} = 0$, meaning all the points have a perfect fit to the line, which is never the case in reality, and the maximum bound of σ_{RANSAC} is the cutoff noise threshold for a point to be considered as part of the line segment. Therefore, the average noise cannot be greater than this threshold. This also implies, $\frac{\mathbf{N_{consensuss}}}{\sigma_\mathbf{RANSAC}} < \mathbf{Confidence_s} < \infty$. Again if $\mathbf{ErrUse_s} = 0$, then the $\mathbf{Confidence_s}$ tends to ∞, indicating a very high confidence.

The relationship between the distance to the plane, the precision of the laser range measurements (as per [Skolnik 80]), and the number of points on a line segment are shown in figure 5.9. Farther the plane from the laser scanner, lower the precision of the measurement, but the distance also reduces the number of points measured for the plane. Therefore, the number of points measured on a plane is a good indicator for the confidence on the plane.

We choose to define a bounded confidence to simplify computations, and to provide a standard interface to the output of the chain of algorithms. Therefore, **MaxConf**, a maximum value for the $\mathbf{Confidence_s}$ is defined,

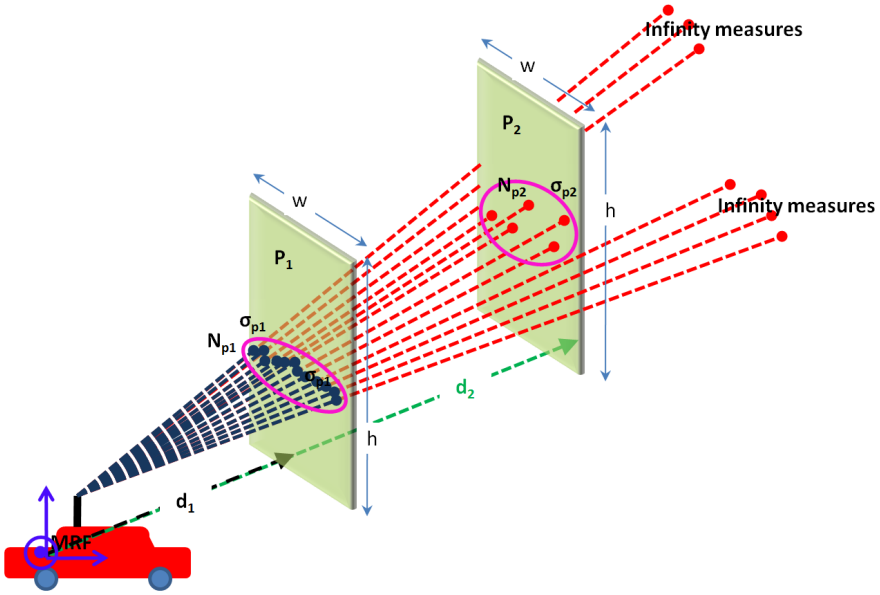

Figure 5.9: From Skolnick's formula, distance $\mathbf{d} \propto \sigma$ (standard deviation of the measurements). Similarly, the number of points, $\mathbf{N} \propto \frac{\mathbf{1}}{\mathbf{d}}$. Therefore, larger $\mathbf{N}$ corresponds to higher quality measurements. In this example: Given that area of planes $\mathbf{P_1}$ and $\mathbf{P_2}$ are same, and they are parallelly located at a distance of $\mathbf{d_1}$ and $\mathbf{d_2}$ from MRF. Since $\mathbf{d_1} < \mathbf{d_2}$, it implies, $\sigma_{\mathbf{P_1}} \leq \sigma_{\mathbf{P_2}}$ and $\mathbf{N}_{\mathbf{P_1}} \geq \mathbf{N}_{\mathbf{P_2}}$. This indicates that plane $\mathbf{P_1}$ has higher or equal confidence as $\mathbf{P_2}$.

and presently set to **1000**. Any $\mathbf{Confidence_s} > \mathbf{MaxConf}$ is cutoff to **MaxConf**. The normalization is performed by dividing the resulting confidence by **MaxConf** value, thus bounding the confidence to $[\mathbf{0}, \mathbf{1}]$. This implies, if the ratio of number of points to the average error is greater than **MaxConf**, the confidence on the line segment is **1**, indicating a highest confidence. This bounded confidence is termed as **CLEF**, and defined for each feasible line segment.

For the line candidates from figure 5.8, the estimated confidence is summed up in table 5.2.

Segment id	$(\mathbf{N_{consensus}})_\mathbf{s}$	$\mathbf{ErrUse_s}$	**CLEF**
1	6	0.02980	0.20127
2	5	0.03073	0.16270
3	5	0.01933	0.25861
4	76	0.02353	1.0

Table 5.2: Confidence indicator (CLEF) for the line segments.

There are three important points to to note: The segments *id 2* and *id 3*, despite having the same number of points **5**, do not have the same **CLEF**. This is due to the variation in the average noise of the measured points with respect to the corresponding estimations of the lines. Despite having more number of points (**6** in comparison to **5**), the segment *id 1* has less confidence (**CLEF**), than the segment *id 3*. Segment *id 4* has considerably high noise than segment *id 3*, yet has the full confidence $\mathbf{CLEF} = \mathbf{1}$. This is because, there is sufficiently large number of points (**76**) to estimate the planes. Higher the number of points, higher the ability to filter out the noise for estimation of a better line segment, therefore, higher the confidence.
All the confidence indicators in this thesis are derived from the confidence indicator **CLEF**.

Finally, the constructed line record $\mathbf{L_R}$ is stored for further use.

$$\mathbf{L_R} = \{\mathbf{CLEF_s}, \mathbf{LS^{M,c}}, \mathbf{LE^{M,c}}\} \tag{5.12}$$

The output of this algorithm is a set of all the line segments for a given laser $\mathbf{l}$ at time $\mathbf{k}$ indicated as $\mathbf{L_{kl}^{M,c}}$.

5.4.3 Line correlation

After processing the individual laser scanner measurements, the line segments $\mathbf{L_{kl}^{M,c}}$ between the two laser scanners, $\mathbf{l} = \mathbf{1}$ and **2** of an isoclinal pair, need to be matched for obtaining the required three non collinear points on the plane. Any error in this correlation process of the two line pairs leads to incorrect plane fittings.

As this is the critical step, a possible synchronization of multiple laser scanners at the hardware level is verified with the SICK laser manufacturers. The synchronization is achieved using an external square signal generator with a specific signal frequency (for SICK LMS scanners it is at **75Hz**). This method can reduce the sync delay to a very short insignificant time span. From the experiments conducted in the laboratory, the SICK LMS laser scanners of an isoclinal pairs are synced with a time delay of less than $\mathbf{10}\mu s$. Therefore, synchronizing each profile $\mathbf{P_k}$, measured at epoch $\mathbf{k}$, for the two lasers of an isoclinal pair, is considered feasible.

The two lasers of an isoclinal pair, scan in the same direction, and their scan origins (LRF) are aligned with only a vertical shift. Therefore, the two lines measured in the same angular ranges ($\mathbf{j}$ for the scanning angle $\alpha_{\mathbf{kj}}$ (equation 5.1), correspond to the same planar surface.

Once a match is identified, an additional test is performed to verify whether the matched lines are parallel. This test ignores any pair of line segments which does not

belong to a planar feature. The information about the order of the line segments is very useful in this stage. This is the reason for not directly applying RANSAC or Hough transform to estimate the line segments is important, as they do not retain the order of the input data.

The lines are correlated when fulfilling the following conditions: equality, containment, and overlapping. However, mutual exclusivity and non-parallelism results in non-correlated lines. In figure 5.10, these five conditions are illustrated by two sets of line segments, estimated by the laser scanners of an isoclinal pair. Since the scanning angles (equation 5.1) are incremented by a constant value, it is sufficient to compare the indices **i** and **j** of the two scanners instead of the measuring angles. For each line segment, the starting and ending scanning angles are shown with the subscripts *start* and *end*. As explained earlier, the scanning angles of the two synchronized lasers have a fixed angular difference, which is predetermined using calibration. Once this angular difference is compensated, the two indices can be compared directly.

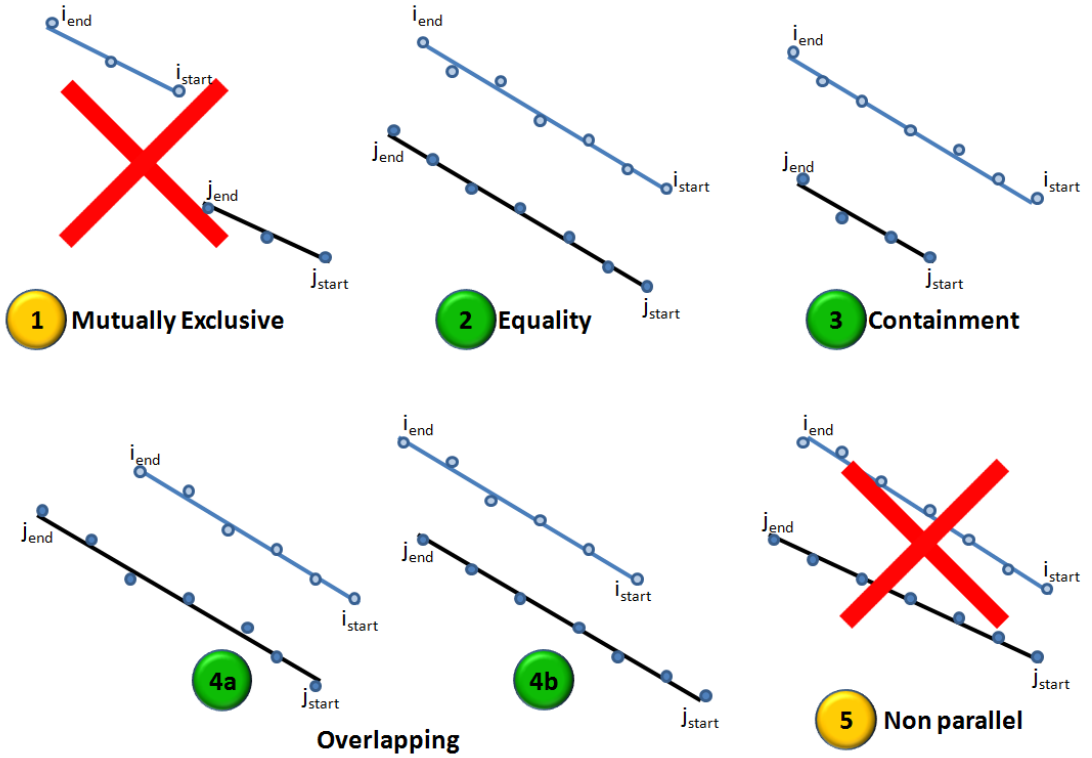

Figure 5.10: Five conditions applied in line correlation, to identify the line segments belonging to the same planar landmark, but observed by the two lasers of an isoclinal pair.

The tests of the indices $(\mathbf{i_{start}}, \mathbf{i_{end}})$ and $(\mathbf{j_{start}}, \mathbf{j_{end}})$ used for determining these

conditions are given below.

1. **Mutually exclusivity**: $(\mathbf{i_{start}} > \mathbf{j_{end}}) \vee (\mathbf{j_{start}} > \mathbf{i_{end}})$
2. **Equality**: $(\mathbf{i_{start}} = \mathbf{j_{start}}) \wedge (\mathbf{i_{end}} = \mathbf{j_{end}})$
3. **Containment**: if $S = \mathbf{j_{start}} - \mathbf{i_{start}}$ and $E = \mathbf{j_{end}} - \mathbf{i_{end}}$ then the condition is $((S \geq 0) \wedge (E \leq 0)) \vee ((S \leq 0) \wedge (E \geq 0))$.
4. **Overlapping**: This is the remaining condition for the index comparison of the segments, provided it does not satisfy any of the above three criteria.
5. **Non parallelism**: If the matching process yields an equality, a containment or an overlapping condition, the angle L_{ij} between the two line vectors is computed as

$$\mathbf{L_{ij}} = \arccos\left(\frac{(\mathbf{LE_j^{M,c}} - \mathbf{LS_j^{M,c}}) \odot (\mathbf{LE_i^{M,c}} - \mathbf{LS_i^{M,c}})}{||(\mathbf{LE_j^{M,c}} - \mathbf{LS_j^{M,c}})||\ ||(\mathbf{LE_i^{M,c}} - \mathbf{LS_i^{M,c}})||}\right) \tag{5.13}$$

   where $\odot$ is the vector dot product, and the line boundaries in MRF $(\mathbf{LS^{M,c}}, \mathbf{LE^{M,c}})$ (defined in section 3), for segments **i** and **j**.

   If $L_{ij} \simeq 0°$, the two lines are considered parallel and stored for further processing to extract the planar landmarks. The similarly equal symbol $\simeq$ is used, to take the angular noise into consideration. We have experimentally set this angle to $\mathbf{3}°$.

The concept of the confidence indicator on the line estimation **CLEF**, described in section 3, is extended to the matched pair of lines. It is defined as the *Confidence on the Plane Estimation Factor* **CPEF**, given in equation 5.14.

$$\left.\begin{aligned} \mathbf{Confidence_{high}} &= max(\mathbf{Confidence_{si}}, \mathbf{Confidence_{sj}}) \\ \mathbf{Confidence_{low}} &= min(\mathbf{Confidence_{si}}, \mathbf{Confidence_{sj}}) \\ \mathbf{Confidence_{ij}} &= \frac{(\mathbf{2} \times \mathbf{Confidence_{high}}) + (\mathbf{1} \times \mathbf{Confidence_{low}})}{\mathbf{3}} \end{aligned}\right\} \tag{5.14}$$

The scaling factors (two and one) used in the computation of **CPEF** in equation 5.14, indicate the number of points each line contributes to the plane estimation. The line with highest confidence contributes twice as much as the other. $\mathbf{Confidence_{si}}$ is the computed **CLEF** for the line segment **i** of the first laser, and $\mathbf{Confidence_{sj}}$ for the second.

The output of this algorithm is the set of pairs of matched line records $(\mathbf{L_{k1i}^{M,c}}, \mathbf{L_{k2j}^{M,c}})$, and their corresponding confidence value **CPEF** indicated by $\mathbf{Confidence_{ij}}$. $\mathbf{L_{k1i}^{M,c}}$ and

$\mathbf{L^{M,c}_{k2j}}$ represent the $\mathbf{i^{th}}$ line of the set $\mathbf{L^{M,c}_{k1}}$ and $\mathbf{j^{th}}$ line of the set $\mathbf{L^{M,c}_{k2}}$ respectively. In equation 5.15 the cardinality of the set $\mathbf{S}$ is denoted by $|\mathbf{S}|$.

$$\mathbf{Match^{M,c}_{k12}} = \{(\mathbf{L^{M,c}_{k1i}}, \mathbf{L^{M,c}_{k2j}}, \mathbf{Confidence_{ij}})|\mathbf{i} \in \{1 \ldots |\mathbf{L^{M,c}_{k1}}|\} \text{and} \mathbf{j} \in \{1 \ldots |\mathbf{L^{M,c}_{k2}}|\}\} \tag{5.15}$$

In [Weingarten 04], two consecutive georeferenced scans from the same laser are used to extract the planes. In our method, the planar features are extracted by using synced pairs of lasers, from a given vehicle position, neither moving the vehicle nor georeferencing the data.

5.4.4 Plane fitting

To fit planes three non-colinear points **Pt1**, **Pt2** and **Pt3** are needed. They are chosen from the matched pairs of lines from the set $\mathbf{Match^{M,c}_{k12}}$, based on their confidence indicator **CLEF**.

As explained in equation 5.14, among the two lines selected for estimating a plane, the one with the higher **CLEF** contributes two points $(\mathbf{Pt1}, \mathbf{Pt2})$, while the other contributes a single point $(\mathbf{Pt3})$. $(\mathbf{Pt1}, \mathbf{Pt2})$ constitute the boundaries of the line with the highest **CLEF** value. $(\mathbf{Pt3})$ is computed as the midpoint of the line segment with the lowest **CLEF**. This point selection minimizes the errors in the segment estimation algorithm, which has difficulties in resolving the corner points between two walls. Note that the points **Pt1**, **Pt2** and **Pt3** are expressed in **MRF** thus in **3D** space.

However, the dynamic choice of these points can cause problems when the surface normal needs to be determined. The direction of the normal vector changes based on the order of the three selected points. In order to maintain the direction of the normal vector of the plane between epochs, a direction indicator **D** is used. For estimating the plane, if the first laser provides the line with highest CLEF, then **D** is set to $\mathbf{1}$ otherwise **D** is set to $-\mathbf{1}$, to ensure the consistent orientation of the normal vectors. This also ensures that between two epochs, where a plane is observed, its normal is pointed in the same direction, regardless the laser scans contributing the points gets interchanged.

A plane in **3D** can be represented in several ways as given in [Weingarten 04]. In this thesis, the Hessian normal form is chosen, with the normalized surface normal vector $(\mathbf{N}_\rho)$ with parameters $(\mathbf{n_x}, \mathbf{n_y}, \mathbf{n_z})$ and a **3D** point to represent a plane. The parameters of the normal vector $\mathbf{N}_\rho$ are computed for the plane ρ from the cross product of $(\overrightarrow{\mathbf{Pt1\ Pt2}})$ and $(\overrightarrow{\mathbf{Pt1\ Pt3}})$.

$$\mathbf{N}_\rho = (\mathbf{n_x}, \mathbf{n_y}, \mathbf{n_z}) = \frac{(\mathbf{Pt2} - \mathbf{Pt1}) \otimes (\mathbf{Pt3} - \mathbf{Pt1})}{||(\mathbf{Pt2} - \mathbf{Pt1}) \otimes (\mathbf{Pt3} - \mathbf{Pt1})||} \tag{5.16}$$

where $\otimes$ indicates the vector cross product. The equation of the plane is given as:

$$\mathbf{n_x x} + \mathbf{n_y y} + \mathbf{n_z z} + \mathbf{d} = \mathbf{0} \tag{5.17}$$

The offset from the origin **d** can be found by substituting any of the three points **Pt1**, **Pt2** and **Pt3** in the above plane equation. The set of planes is finally estimated for an epoch **k** for an isoclinal pair of laser scans.

The extracted planes from the matched line segments of the isoclinal pairs is shown in figure 5.12a.

The noise in the extracted planar landmarks are filtered in two levels: first, while fitting the lines in least square sense with the removal of outliers by RANSAC, and the second, while choosing the three points, where the two points are taken from the most trusted line, and the remaining third point from the middle of the corresponding parallel line.

5.5 Experimentations and results

5.5.1 Test performed using simulated data

- Test data generation - using simulation platform SIVIC

  The simulation platform SIVIC [Gruyer 06] is capable of generating the measurement data from different sensors mounted onto a mobile vehicle. We used it for creating the test data for the validation of the devised algorithms. SIVIC simulates an urban environment, and a vehicle fitted with different sensors, including the **2D** laser scanners. It generates sensor measurements as the vehicle moves in the designed urban scene.

  A typical scene of SIVIC is shown in figure 5.11.

  In the data acquisition process, the SIVIC car navigates along the specified trajectory, and creates laser profiles corresponding to the scene. *SIVIC is interfaced with the ^{RT}Maps [Intempora 07] software to record these laser profiles as they are generated in near real time.* As a prototype, the planar extraction algorithms are coded in MATLAB, and tested offline using the acquired data.

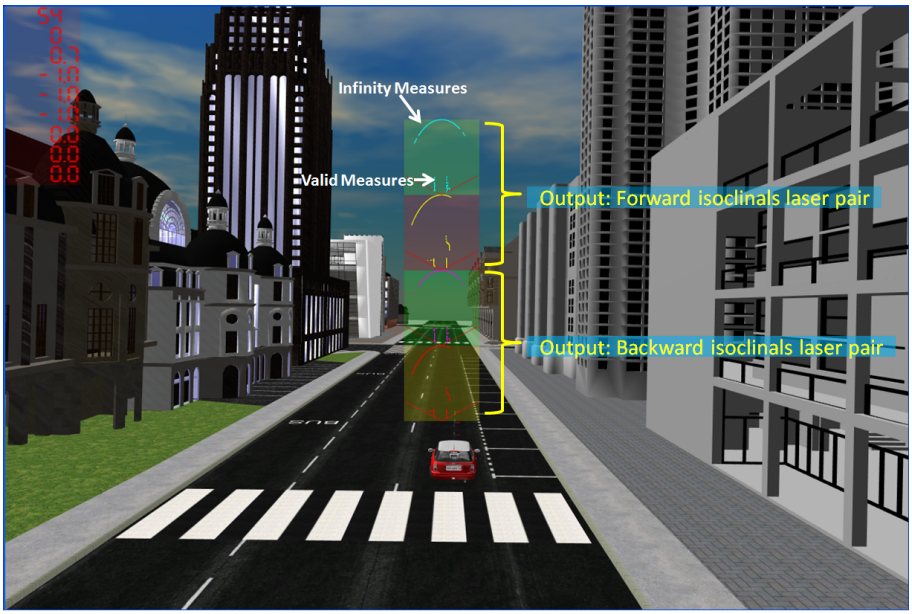

Figure 5.11: An urban test scene - generated using SIVIC. The four rectangular windows above the car depict the output of the four lasers corresponding to the design in figure 5.1. These windows show the laser range measurements at the corresponding scanning angle, observed in the current epoch. The infinity measures are shown when there are no objects present within the maximum allowed range. The valid measurements are shown within this range, corresponding to the measured points to the scan intersecting objects. In the figure, both the valid and the infinity measures are highlighted for a single laser.

- Selected test configurations

  The configurations of the parameters defined in section 5.4.1 and the vehicle speed are given in table 5.3.

  The standard deviation of the SIVIC laser measurements $\sigma_{\mathbf{laser}}$ is computed by maintaining the SIVIC vehicle stationary, and acquiring data for the same environment several times. In these tests the computed $\sigma_{\mathbf{laser}}$ value is **2**cm. This value is worse than the standard deviation of some commercially available 2D laser scanners including a SICK LMS laser scanner [SICK 06]. With the set configuration, the number of points per profile **N** is **301**. A laser scanner in SIVIC has a maximum field of view of **150**°. This field of view is smaller compared to most commercially available 2D laser scanners. As mentioned in section 5.3, higher the field of view more the observation ability of the laser scanners, therefore, a higher probability to observe landmarks.

  The origins of the two laser scanners in an isoclinal pair have a vertical shift of **0.5**meters. As for the orientation, the lasers in an isoclinal pair have the same

Parameter	Configured Value
Field of view ($\boldsymbol{\Upsilon}$)	**150**°
Resolution ($\boldsymbol{\Gamma}$)	**0.5**°
Starting Angle ($\alpha_{\mathbf{min}}$)	**15**°
Minimum Range ($\mathbf{R_{min}}$)	**0.5**meters
Maximum Range ($\mathbf{R_{max}}$)	**80**meters
Frequency of the laser scanner ($\mathbf{F_{laser}}$)	**25**Hz
Laser measurement noise ($\mathbf{1}\sigma_{\mathbf{laser}}$)	**2**cm
Velocity of the vehicle ($\mathbf{v}$)	**5**kmph

Table 5.3: Plane extraction: configuration parameters, used in the SIVIC environment

bearing and elevation with respect to the origin of the moving platform. SIVIC and ^{RT}Maps ensure that the scanning profiles are synchronized for the lasers in an isoclinal pair, and that the profiles are correctly timestamped during the data acquisition.

- Test results

The results obtained from the plane extraction algorithms for the scene shown in figure 5.11 are given in figure 5.12. To facilitate viewing, these results are mapped back to the SIVIC coordinate system using the SIVIC's own localization data (position and orientation).

The small number of the planar landmarks extracted can be explained by the fact that the scene in figure 5.11 does not correspond to an urban canyon. Urban canyons have taller buildings and narrower streets compared to the experimental test data used here.

In the present configuration, a line segment is extracted if a minimum of 5 points (i.e.$\mathbf{P_{min}} = \mathbf{5}$) are measured from it. To estimate a plane, two such corresponding line segments are identified from an isoclinal pair of laser scanners. Therefore, some planes are not detected, where the data is noisier due to the geometry of the buildings.

In this two isoclinal scan profiles, by ignoring the infinity measures from the 4 laser scans, there are **677** valid points measured. In a 3D space this corresponds to **2031** scalar values. From this data, **13** planar patches have been extracted, each represented by a 3D normal vector and a point thus corresponding to **78** scalar values. It is a clear indicator for the advantage in terms of storage when representing the data using the primitive landmarks, thus allowing scalability of the final maps.

5.5.2 Test performed using real data

- Test data generation - real data

  The real test data is generated in the mechatronics laboratory in the Ecole des Mines de Paris, using a test platform equipped with two pairs of SICK LMS 221 laser scanners. This platform is mounted on wheels and can navigated manually inside the laboratory. An urban-like scene is constructed by installing cardboard boxes. The scene consists of both planar and non-planar objects with various degrees of light (laser) reflectivity. In these tests, only a pair of laser data (single isoclinal pair) is used, since the goal is to test the ability of the planar landmark extraction algorithms in a real environment.

  Figure 5.13 shows the used test platform and the test environments.

- Selected test configurations

  Table 5.4 elaborates the configuration used in the tests with the SICK LMS laser scanner pair. These real scanners have better noise characteristics compared to the SIVIC lasers. A maximum measurable range of **32** meters is chosen for an indoor environment resulting in a precision in millimeters. The $\sigma_{\mathbf{laser}}$ is measured empirically, by taking the observations of a static environment from a fixed position of the measuring platform.

Parameter	**Configured Value**
Field of view ($\boldsymbol{\Upsilon}$)	$\mathbf{180}^\circ$
Resolution ($\boldsymbol{\Gamma}$)	$\mathbf{0.5}^\circ$
Starting Angle ($\alpha_{\mathbf{min}}$)	$\mathbf{0}^\circ$
Minimum Range ($\mathbf{R_{min}}$)	**0.5**meters
Maximum Range ($\mathbf{R_{max}}$)	**32**meters
Frequency of the laser scanner ($\mathbf{F_{laser}}$)	**38.47**Hz
Laser measurement noise ($\mathbf{1}\sigma_{\mathbf{laser}}$)	**6**mm
Velocity of the vehicle ($\mathbf{v}$)	static

Table 5.4: Plane extraction: configuration parameters for real data

The SICK LMS scanners, the scanning rate ($\mathbf{F_{laser}}$) is set, depending upon the configurable resolution ($\boldsymbol{\Gamma}$).

The calibration is performed to obtain the spatial alignment of the lasers in an isoclinal pair. For the used laser setup of a forward isoclinal pair, a vertical shift of **0.6** meters is measured between their scan origins. This is achieved by measuring the ranges to a fixed planar region located parallely to the direction of motion of the platform. For the orientation, the shifts in the azimuth and

elevation between the two lasers is measured as well. The azimuth difference is measured by fixing a static object to the platform and measuring it from both the lasers. The calibrated delta azimuth value is determined as three angular indices (i.e. $\mathbf{1.5}^\circ$, since the resolution is $\mathbf{0.5}^\circ$) between the bottom and the top laser pair. The elevation is measured manually and is the difference of $\mathbf{1}^\circ$ between the two lasers, which corresponds to the error in the inclination of the mounting platform. Since the test data is scanned from a fixed position, the profile time stamps are used for synchronizing the two laser scanner measures. In the final system, an external pulse generator we already tested, can be used as recommended by the SICK laser scanner manufacturers, for synchronizing the scanning profiles of the lasers. Otherwise, the scanning can start at different times, and the temporal offset between the two lasers is measured at the initialization phase.

- Test results

  Figure 5.14 shows the extracted planar patches.

  In the scene, a special wooden board with two protruded small planar surfaces is placed on the right. The protrusions are located so that the two lasers hit these objects from a given static position in their corresponding profiles. The goal is to induce some false detections. The aim of planar patch extraction is to obtain the characteristic geometric planes rather than the real physical ones. For localization algorithms, it is considered sufficient if the characteristic planes are consistently detected between successive epochs.

  The obtained results show that the planar patches visible in the scanning planes of the two lasers are successfully identified. The protruded planar patches proved to be too small to raise a false detection. The false detection is avoided due to the constraint on the minimum of number of points ($\mathbf{P_{min} = 5}$) required to detect a line segment.

  The protruded planar surfaces represent typical manmade structures. Thus an improvement for this set of algorithms is to introduce a merging strategy to detect and merge line segments which are split into several smaller segments.

  From the analysis of this test, there are **646** valid range measurements from the two laser profiles, for the epoch at which the planar patches are extracted. The infinity measures are ignored. In a 3D space, this corresponds to **1938** scalar values. From this data, **5** planar patches are extracted, and each represented by a 3D normal vector and a point thus corresponding to **30** scalar values.

5.6 Conclusion

This chapter presented a specific 2D laser scanner based system configuration designed for extracting the planar landmarks. The feasibility of this system design is validated

with both simulated data from a moving vehicle, and real data acquired in a static environment with planar and non planar landmarks.

The available planar landmark extraction methods uses georeferenced data acquired from either 2D or 3D laser scanners. In the case of 2D laser scanners, so far single scanner is used, meaning the planar patches are extracted after the entire laser scans have been georeferenced. Unlike these approaches, in our method, the planar features are extracted from a synced pairs of 2D laser scanners, from a given vehicle position, neither moving the vehicle nor georeferencing the data. Our approach ensures that the extraction of planar landmarks is independent of other sensor errors, which is not the case if georeferenced data is used. By using 2D laser scanners, the profile scan time is reduced, therefore, landmarks can be even extracted from a platform under motion. This is an important step for localization improvement by perception, which will be elaborated in chapter 6.

The analysis in the chapter shows that mapping applications can use specific arrangements of low cost perception sensors to extract the characteristic landmarks from the mapping environment. These extracted landmarks can be used as inputs for different localization approaches. They also reduce the storage space needed thus increasing the scalability of the maps.

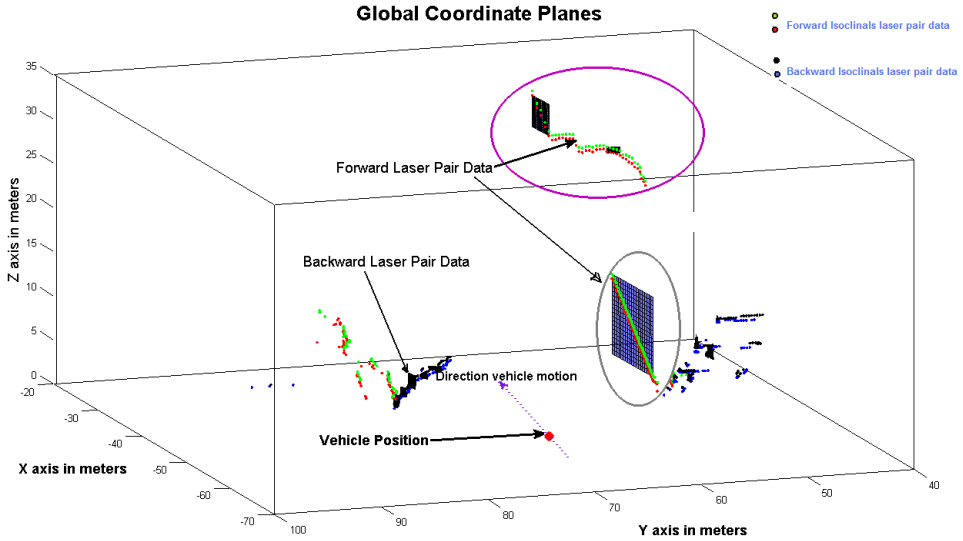

(a) Extracted planar patches - simulated data from SIVIC

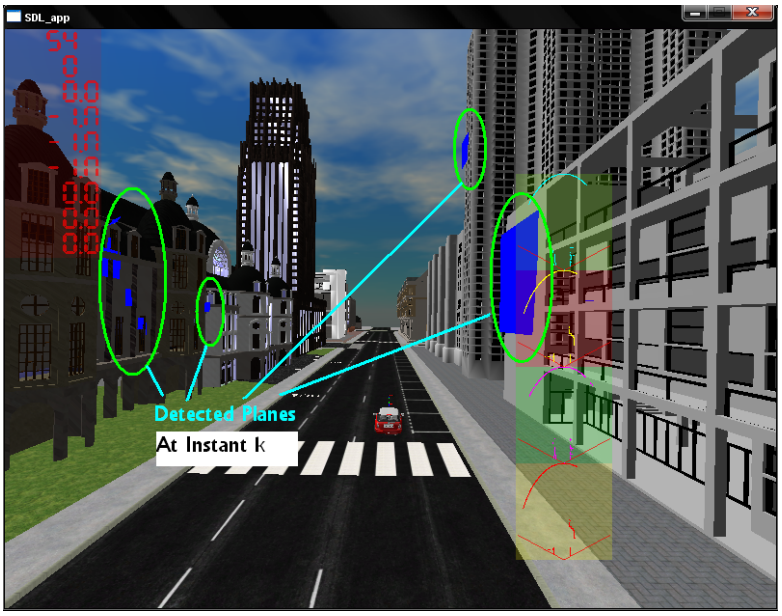

(b) Planar patches mapped back on to the SIVIC scene

Figure 5.12: Validation of planar patch extraction with simulated data using SIVIC. In figure 5.12a, the red and green points correspond to the valid measurements of the forward isoclinal laser pair. Similarly, the blue and black dots correspond to the backward isoclinal laser pair. The violet arrow on the vehicle position (red dot in the middle) shows the motion direction of the vehicle. The magenta circle corresponds to the planar patches of the tall building on the right side of the image. The large planar patch highlighted by a gray circle on the right corresponds to the building with a larger planar section. Several smaller planar patches were identified on the left side of the street. These extracted planes are mapped in blue on the SIVIC scene in figure 5.12b, showing the identified planar patches of the buildings.

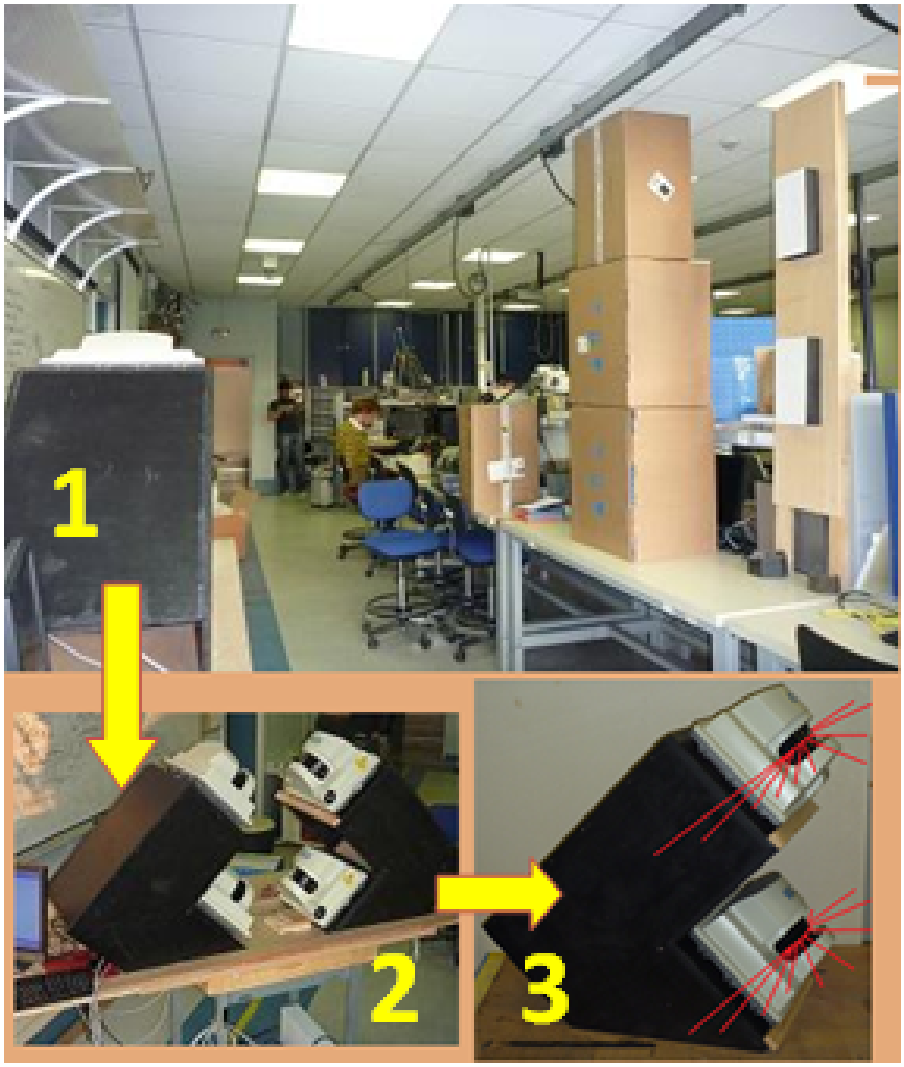

Figure 5.13: The figure shows the test platform used for indoor planar patch extraction. This image consists of three parts. Part 1 shows the environment where the test data is acquired with the camera pointing to the direction of data acquisition (forward isoclinal pair). Part 2 and 3 highlight the setup of the laser scanners used for acquiring the data sets. In part 2, both isoclinal pairs of lasers are shown, though only the forward pair is operational. In part 3, the direction of the laser beams in a profile is shown by using hand drawn lines, for an isoclinal pair of laser scanners.

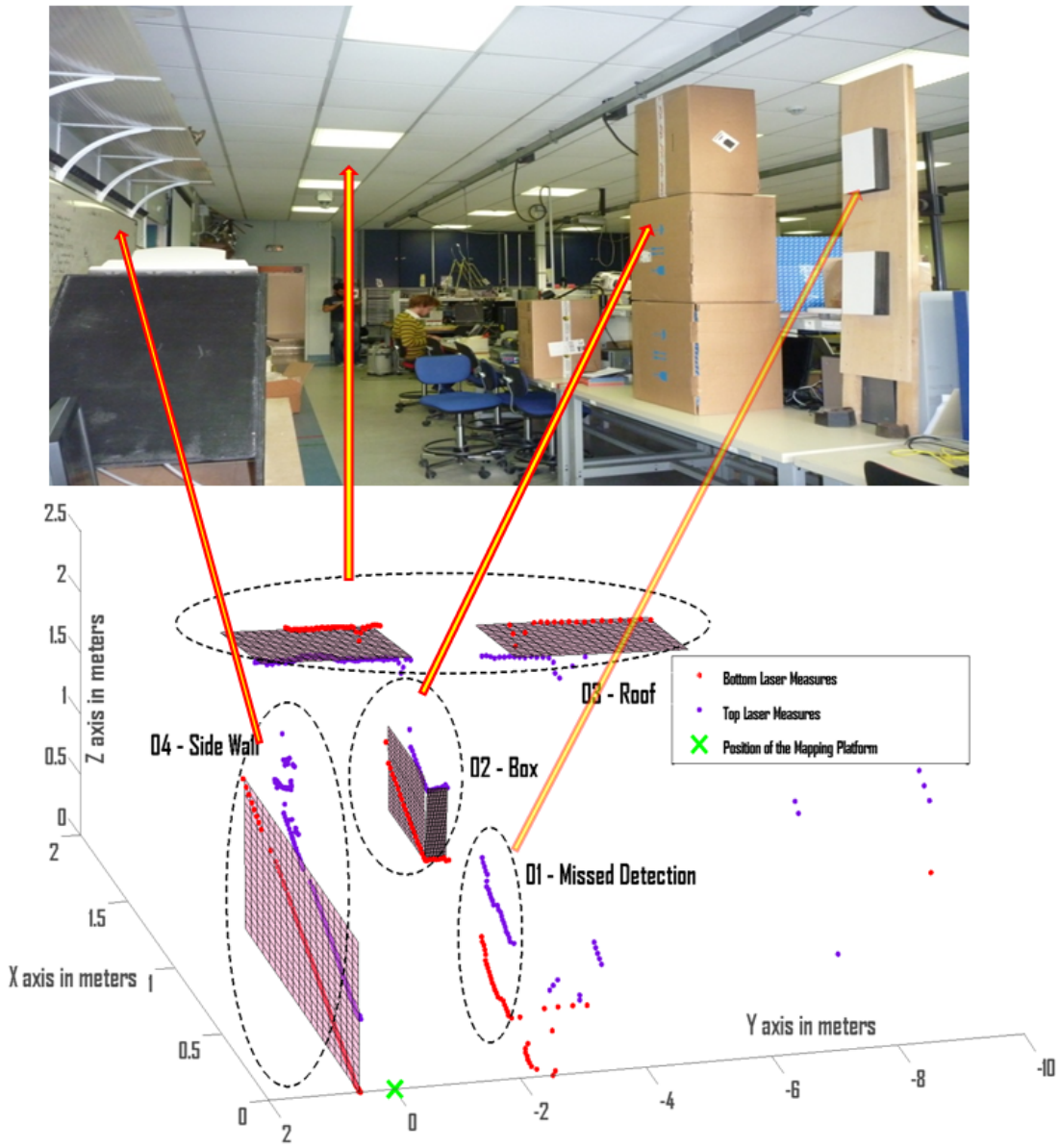

Figure 5.14: Results of the planar patch extraction using real data. The top part of the figure corresponds to the scene shown in figure 5.13, whereas the bottom part shows the extracted planar patches and the measured data points. The red points are, the measures of the bottom laser and the violet points are the measures of the top laser. The correspondence between the extracted planar patches and the regions in the scene to which they belong are drawn using four arrows.

Chapitre 6

Odométrie laser au moyen de motifs plans

Les caractéristiques des motifs plans étant identifiées, l'étape suivante, dans l'élaboration d'un odomètre à laser, consiste à estimer le mouvement du véhicule à partir des seules propriétés géométriques de ces repères. Le chapitre 5 a présenté une méthode d'identification de ces motifs.

Des structures planes facilitent le calcul du déplacement en 3D : ils permettent de séparer rotation et translation. Le calcul de la rotation nécessite la construction d'un repère de référence. Un tel système d'axes, en 3D, peut être généré à partir des vecteurs normaux de deux plans non parallèles. Le calcul de la translation nécessite l'identification d'un point de référence dans l'espace. Un tel point de référence, à partir de motifs plans, suppose qu'il existe un point d'intersection entre trois plans. Une telle configuration est cependant rarement observée dans les environnements artificiels. Nous proposons donc de restreindre le calcul de la translation à sa projection sur le plan horizontal, qui n'exige que la présence de deux plans non parallèles. Le mouvement est donc résolu pour 5 degrés de liberté.

Il est donc nécessaire de reconnaitre le même jeu de plans dans deux séries de mesures, il s'agit d'un problème d'association de données (Data Association - DA). Comme nous avons besoin de deux plans non parallèles pour calculer la transformation à 5 degrés de liberté, l'association concerne une paire de tels plans. L'angle entre les deux plans est utilisé comme premier critère de sélection. La continuité du mouvement d'un véhicule routier permet de rejeter d'éventuelles associations aberrantes. Cela implique que les motifs plans en correspondance, repérés à deux époques proches, soient suffisamment voisins dans le repère du véhicule. Comme les plans correspondants apparaissent comme alignés, il doit y avoir un recouvrement minimum quand on projette l'un des motifs sur l'autre.

La séparation entre rotation et translation, dans l'estimation du mouvement, nous permet d'effectuer la recherche de l'association entre motifs avec deux niveaux de contraintes : une association stricte (Strict Data Association - SDA), ou, si trop de possibilités apparaissent, une association tolérante (Lenient Data Association - LDA). La seconde, appliquée avant toute connaissance du mouvement, permet de connaitre la rotation ; l'association stricte est alors applicable pour estimer la translation. Cette séparation en étapes successives de la localisation en 3D est une approche originale.

La méthode d'association tolérante peut conduire à des associations incorrectes, ou à des ambiguïtés. Pour traiter de telles situations, et choisir l'association qui estime le mieux le mouvement, nous avons développé un nouvel algorithme appelé sélection optimale du candidat par consensus (Optimal Candidate Selection by Consensus - OCSC) et sa variante pondérée (WOCSC). Cet algorithme peut être utilisé pour résoudre n'importe quel système surdéterminé. Il élimine également les échecs rencontrés dans les approches par calcul de valeurs moyennes en présence de valeurs aberrantes.

Ces concepts sont implémentés dans deux chaines de traitement :

1 - LDA, rotation estimée par WOCSC, SDA puis translation estimée par un calcul de moyenne (centre de gravité de toutes les translations). L'association stricte est appliquée avant le calcul de la translation pour éliminer les cas aberrants de façon à assurer que la relation entre les deux ensembles de données est injective.

2 - LDA, rotation estimée par WOCSC, translation estimée par WOCSC. Dans ce cas, l'association stricte est complètement optionnelle.

Les résultats de ces implémentations sont présentés au chapitre 7.

Chapter 6

Laser odometry using planar landmarks

Contents

6.1 Introduction

This chapter focuses on the two functionalities of the trajectory estimation:

Transformation computation of the mapping platform using only the time-invariant geometrical properties of the landmarks, independent of any other pose sensors. In 3D space this problem alone has 6DOF, 3DOF rotation and 3DOF translation.

Data association (DA) matches the landmarks across two data sets (observations to observations or observations to map) from two time steps. This problem is nontrivial, because landmarks can newly appear or disappear as the senor platform displaces. Moreover, the lack of identifiable features of individual landmarks increase the difficulties in association, and often lead to ambiguities. If not resolved, these ambiguities can induce incorrect transformation estimations.

Apart from these two main functions, an important task is to chose the best minimal set of associated landmarks to estimate the transformation in the presence of multiple candidate associations. The presence of multiple candidates also means possible outliers and possibility to choose an optimal transformation solution from the subset of associations. This problem we term as **Optimal Candidate Selection** overcomes the typical failures of the mean-based or least squares error-based methods when subjected to outliers. In this case, the outliers are in the form of ambiguous or incorrect associations typically occurring in the cluttered environments.

This chapter addresses these three problems in the context of trajectory estimation using planar landmarks. The approach presented can work with the planar landmarks extracted at discrete time steps, from any sensor or method including the one presented in chapter 5.

This chapter is organized as follows:

Motivation to our work is presented in section 6.2, followed by a short description of the state of the art of laser odometry in section 6.3. Then we introduce, our approach of laser odometry in section 6.4. This is followed by the description of each of the functionalities applied in our approach: Data Association section 6.5) with lenient (section 6.5.1) and strict association (section 6.5.2) methods, transformation computation using geometrical properties of the associated planar landmarks(section 6.6), and finally the new approach to overcome ambiguities in case of multiple associations(section 6.7.1), and its application to compute optimal transformation (sections 6.7.2and 6.7.3). We also demonstrate a mean-based method (section 6.7.4) to compute translation, prior concluding the chapter in section 6.9.

6.2 Motivation

As mentioned in chapter 4, most SLAM approaches are implemented in 2D space, mainly due to the complexity of the 3D pose problem with 6DOF and unknown DA. Therefore, our main motivation in this work is to simplify the 3D transformation estimation problem.

In our approach, the transformation is estimated from the time-invariant geometrical properties of the observed planar landmarks. This estimate is independent of other pose sensors and vehicle motion model (see chapter 4 for comparison). We compensate the lack of pose sensors with a minimal set of motion constraints on the angular and linear velocities. Similar work is proposed in [Bailey 01], where a 3DOF pose in 2D space is resolved by using the geometrical properties of the observed lines and point features. Our approach resolves Data Association (DA) and transformation estimation in 3D space.

This approach can be categorized as laser odometery, because it computes the relative transformation between two sets of observations, extracted from 2D laser scanners. We apply this approach on the planar landmarks extracted using the methods and algorithms given in chapter 5. However, it can also be applied to all 3D planar landmarks extracted from any perception sensor, such as 3D laser scanners, multi-layered laser scanners, sonars or digital cameras.

This work, focuses on simplifying the 6DOF pose estimation problem by using Divide and Conquer (D&C) approach. Like EKF SLAM, we apply explicit DA and transformation computation as two distinct operations, rather than treating it as a single problem, as done in scan matching technique. Moreover, we split these two operations in two, and perform them sequentially as: **Lenient Data Association (LDA), Rotation resolution, Strict Data Association (SDA) and Translation resolution**. The separation of the rotation from translation simplifies drastically the complex 6DOF pose estimation problem. Given the transformation is unknown, LDA applies relaxed constraints to associate the landmarks. Using a minimal subset of associated landmarks, rotation can be estimated. Once the rotation is compensated, there is only the translation to resolve. This implies that more stringent conditions can be applied to reduce the number of erroneous but retained associations. Therefore, the SDA is performed prior translation estimation.

The relaxed constraints applied in LDA, can result in retaining the outliers or wrong associations as feasible candidate solution. However, only a subset of the retained associations is necessary to compute the transformation. Therefore, an algorithm which even in the presence of outliers, choses the optimal minimal set of associations to compute the transformation is needed. A novel algorithm, we term as **Optimal Candidate Selection by Consensus (OCSC)**, is designed for this purpose. The inspirations for its design are drawn from the Expectation Maximization (EM) ([Dempster 77] and [Moon 96]) and the RANSAC algorithms [Fischler 81]. We further improve OCSC by adding weight

to the optimization condition, and this variant is called as **Weighted Optimal Candidate Selection by Consensus (WOCSC)**. These algorithms can be applied to any overdetermined system to chose the optimal solution from a set of feasible candidates including some outliers. Moreover, it resolves ambiguity in DA as well as chooses the optimal transformation solution. By applying WOCSC to compute translation, it can be demonstrated that even the SDA becomes redundant.

As already mentioned, the search space for the transformation estimation is reduced by using extracted features rather than observed scans or points. Moreover, the explicit DA step reduces the iterative optimization problem of transformation computation in scan matching, to a simple geometrical one.

6.3 Laser odometry from time invariant properties of the landmarks

Laser odometry, or laser-based dead reckoning, is presented in [Bailey 01] and [Selkainaho 02]. In [Bailey 01], line and point features extracted from two successive laser scans are used, whereas [Selkainaho 02] uses the raw point images, applying scan matching algorithm presented in [Selkainaho 01]. [Hellström 06] improves the scan matching by performing matches between a data base of georeferenced scans and the new scan.

The fundamental assumption behind this approach is that the time interval, and hence the displacement of the robot, between successive scan lines is small [Selkainaho 01]. All these approaches resolve pose for 3DOF in 2D space.

As introduced before, in this thesis, we use feature based approach similar to [Bailey 01] and [Bailey 02]. This approach can work only if the sensor in use supports batch observations, similar to a laser scanner or a camera. *Batch observations* are a set of observations (i.e., viewed features) sensed simultaneously, or within such a short timespan that motion compensation can offset any geometric distortion [Bailey 01]. The approach of planar landmark extraction using synchronized parallel laser scans, given in chapter 5, is a batch observation process. The *batch data association* [Bailey 02] uses the relative geometry between the features in the same scan to correlate them with the features of the other scan. This approach can be summed up in figure 6.1.

Traditional data association methods, using statistical distances (applied in the EKF SLAM framework), suffer from their reliance on knowledge of the vehicle pose estimate. As the time progresses, the uncertainty in the pose often grows, making these methods quite brittle, particularly in the cluttered environments. The *batch data association* helps to overcome the increasing uncertainty in association.

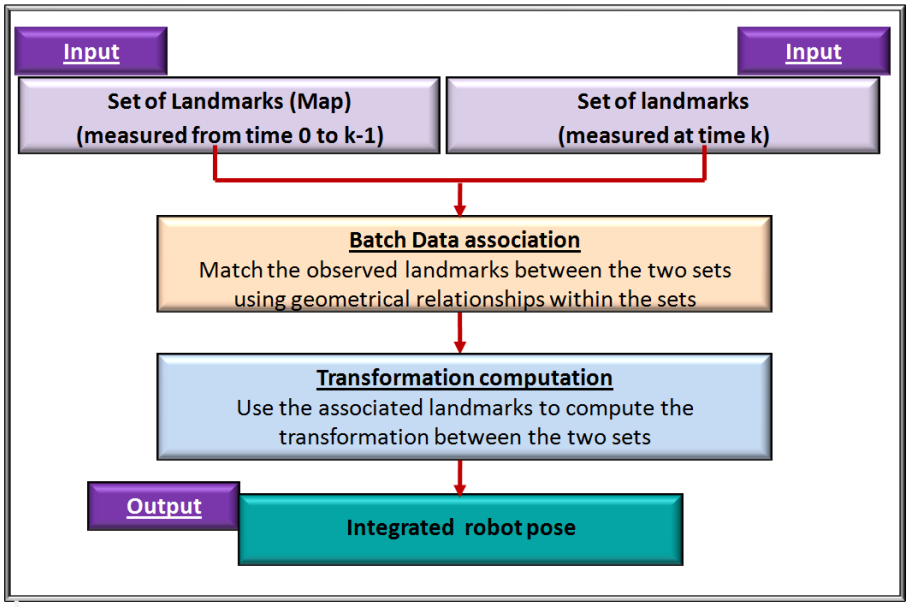

Figure 6.1: Pose determination using geometrical properties of landmarks

6.4 Improved laser odometery - Divide & Conquer approach

This is our approach to solve the complex 6DOF problem of the 3D space, shown in figure 6.2. We apply the *batch data association* on the time-invariant geometrical properties of the static planar landmarks. The significant difference with the earlier approaches is that we split the two step process further into two, for simplifying the computation. From our knowledge, no one has solved the 3D pose problem in this way.

Normal vectors of the planar landmarks are effected only by rotation and remain independent of the translation. Therefore, the 3DOF rotation can be separated from translation. This property is also exploited in the works of [Dold 04] and [Dold 06], performed independently to this thesis. In order to compute the rotation, planar landmarks from the two data sets need to be associated. This is done by performing DA, with relative constraints (Batch DA) and relaxed absolute constraints. As explained in [Bailey 02], the constraints, based on the relations across the two sets are absolute constraints, and those within each set are relative constraints. Absolute constraints are relationships tested in most of the SLAM approaches. In our approach, these constraints are relaxed (or tolerant) to compensate associations with unknown transformations. This DA, we term as Lenient Data Association (LDA).

However, these non rigid constraints cannot resolve all the ambiguities in association,

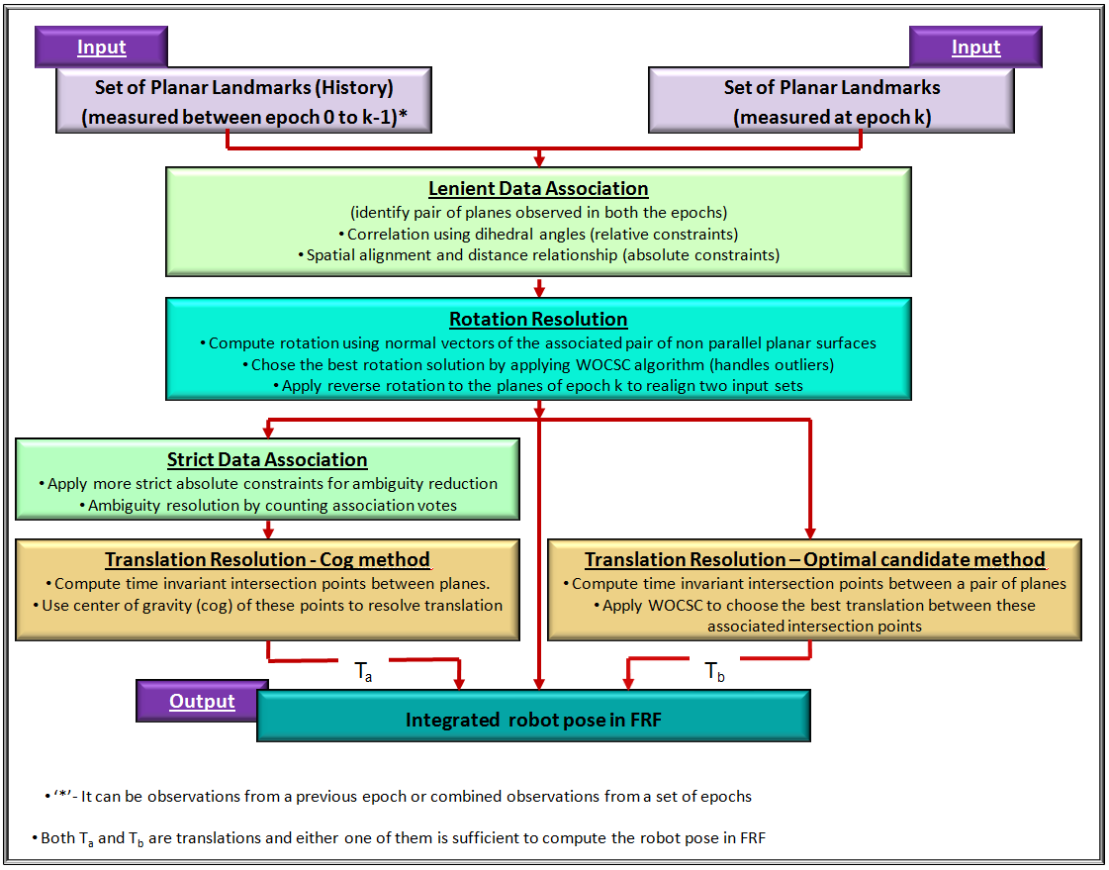

Figure 6.2: Divide & Conquer approach for pose computation using planar landmarks.

leading to some erroneous associations to be retained. Therefore, the WOCSC algorithm is applied to chose the set of associated planes for the computation optimal rotation.

Once the rotation is compensated for one of the data set, it gets aligned with the other. Then more stringent constraints can be applied to remove any remaining ambiguous associations. This step is called as Strict Data Association (SDA). If no rotation effect is present, the intersection points of the planar landmarks within the two sets denote the translation. This geometrical property is used for computing the translation between the two data sets.

However, there can be several associated intersection points available for estimating the undergone translation. This offers choice of using all the available intersection points or the one which best describes the translation. We present these two approaches: first, by estimating the translation of the center of gravity (cog) of the associated intersection points across two datasets, and second by applying again the WOCSC algorithm to find the optimal translation between the associated best candidate intersection points. Since

the WOCSC approach handles outliers, we show that even the SDA becomes optional.

6.5 Data Association (DA)

The problem of determining the correct mapping of observations to landmarks is commonly referred to as **Data Association**, or **correspondence problem** [Montemerlo 03b]. To simplify, we can also call it as landmark matching between two epochs. This is arguably the most critical aspect of the SLAM algorithm and has always been a critical issue for practical SLAM implementations [Bailey 06]. The reliability of the pose depends on the association accuracy of the new observations with the 'reference observations'. The latter can be expressed in several forms: as an input map, an incrementally built map consisting of all the 'observations of interest' from the past, only the 'observations of interest' from the previous epochs (DR type localization) or new estimated locations of the previous 'observations of interest'.

The data association can be generalized as a problem of identifying common elements between two sets. For a continuous observation process, two sets of observations can be used as the association sets. Typically, the sets are observed at epoch $\mathbf{k} - \delta$ and $\mathbf{k}$. We term δ, as the *associable period*, where, there are still some associable common elements between the two association sets. For a continuous association process, δ, can be either of equal lengths or unequal lengths (or varying periods). In our approach, at present we use discrete, fixed times steps of δ.

- **Association process**

  Generally a DA problem can be divided in two steps.

  1. A **correlation** - identifies the corresponding feasible matches between the two sets.
  2. An **ambiguity resolution** - a relationship between two entities is identified based on their characteristics. Often, there are ambiguities to identify the entities based on a chosen criteria. For a successful DA, these ambiguities must be resolved.

  These two steps are explained in figure 6.3.

- **Handling ambiguities**

  In [Bailey 06], the ambiguity resolution is subdivided into ambiguity reduction and ambiguity management. Ambiguity reduction implies reducing the number of wrong association possibilities. Ambiguity management implies determining how to resolve ambiguous associations if such a situation arises.

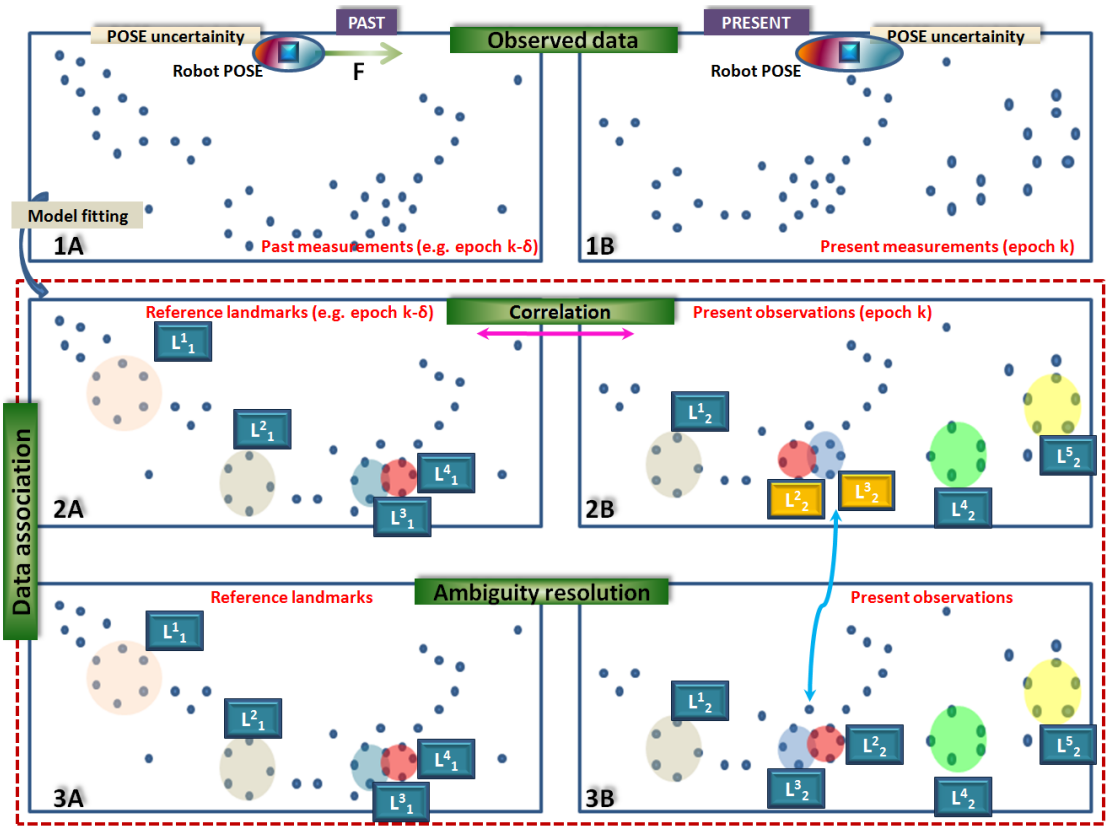

Figure 6.3: An example to describe the Data Association. The two columns of this image is identified as A and B, corresponding to the measured data from the past and the present. Data indicated as $\mathbf{k}-\delta$ can be either the observation from the previous epoch, or all the landmarks observed so far (from $\mathbf{0}$ to $\mathbf{k}-\delta$). Row 1 shows the raw 2D laser measurements for the two data sets. It also shows the vehicle pose and the pose uncertainties (surrounding ellipse). In this example, the landmarks are circular objects, which are extracted using model fitting algorithms. The landmarks across the two data sets (or epochs) need to be correlated in order to compute the transformation. Since the robot moves between $\mathbf{k}-\delta$ and $\mathbf{k}$, the same set of landmarks may not be observed between the two data sets. For example, at $\mathbf{k}$, landmark $\mathbf{L_1^1}$ has disappeared and $\mathbf{L_2^4}$ and $\mathbf{L_2^5}$ have appeared. There is moreover an ambiguity in identifying the two landmarks $\mathbf{L_2^2}$ and $\mathbf{L_2^3}$ with $\mathbf{L_1^3}$ and $\mathbf{L_1^4}$. The reason for this can be the accumulated uncertainties in the robot pose, noises in the measurement process affecting the landmarks, or the extraction process of the selected characteristics.

Many DA approaches do not distinguish **correlation** and **ambiguity resolution**. Earlier SLAM approaches assumed to have performed a perfect correlation, so there was hardly any check for ambiguities. This resulted in total system failures.

The **ambiguity resolution** can be performed instantly when the conflicts occur or tracked until there is a mean to resolve it. Algorithms tracking multiple hypothesis generated by the conflicts are termed as Multiple Hypothesis Tracking(MHT) [Reid 02]. They require substantial computational resources compared to the Single Hypothesis Tracking(SHT).

In this thesis, the ambiguity reduction is considered as a part of the correlation process, and then ambiguity management is ambiguity resolution. The LDA utilizes correlation and ambiguity reduction, whereas the SDA applies ambiguity reduction and ambiguity resolution to the correlated associations retained after LDA. In addition, we present a new approach for resolving ambiguities to choose an optimal association using **Optimal Candidate Selection by Consensus (OCSC)** and its weighted variant **Weighted Optimal Candidate Selection Consensus (WOCSC)** algorithms.

- **Applicable constraint types**

DA can be considered as the process of matching objects in two sets of data by applying some constraints. As mentioned before, the constraints based on the relations across the two sets are **absolute constraints**, and those within each set are **relative constraints** [Bailey 02]. These are explained using the observation and landmark (based on the knowledge, gained by previous observation or provided as input) sets.

Most of the SLAM DA algorithms use only absolute constraints. Such relationships between two different sets need all objects to be uniformly referenced for the chosen property. The absolute pose is the preferred choice, because, in most cases, robot pose estimation is assumed to be known along with the observations and the landmarks. This is employed by the EKF and the Particle Filter SLAM [Montemerlo 02] approaches.

In this thesis, only the landmarks and the observations are assumed to be known with their uncertainty indicators, but without prior pose information. Therefore the relative relationships are the appropriate correlation constraints.

- **Associable relationships**

The key to the correlation process is matching observations sharing the same characteristic relationships. In the laser odometer, these relationships are used to associate two sets of observations from two different epochs.

  - **Distance relationship**

A distance relationship is the obvious choice for two objects in space, provided they are referred in a FRF. A distance can be used as an absolute or relative constraints [Bailey 02].

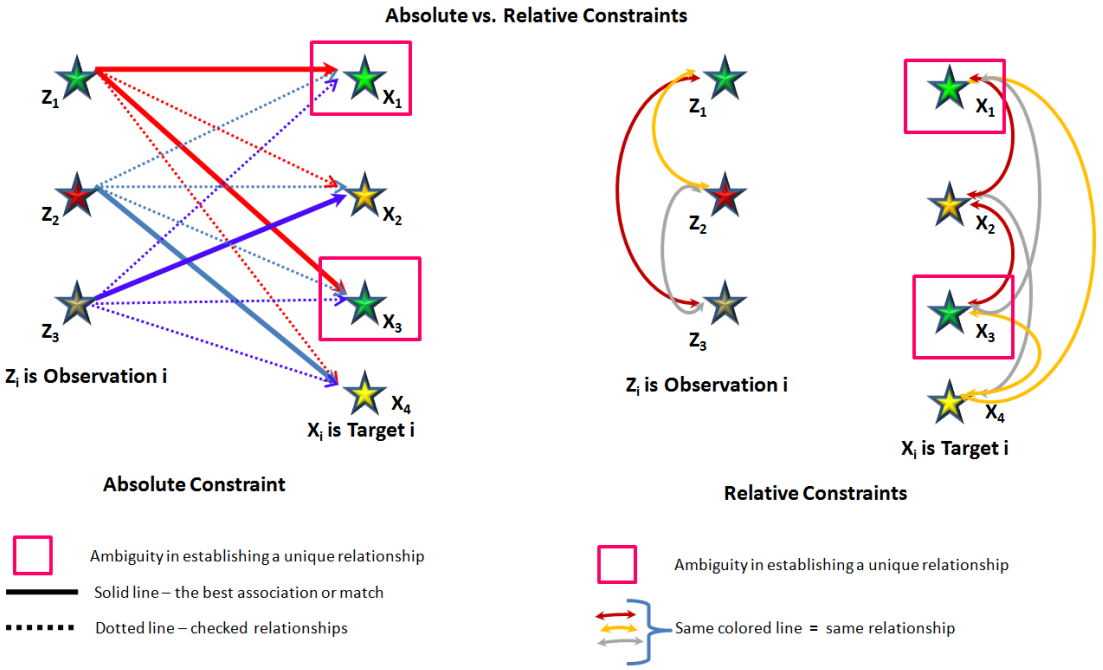

Figure 6.4: Data Association - absolute vs. relative constraints

In a flat space, distance is resolved using Euclidean geometry. However, the observations are not single point entities, as they are often noisier. Most of the algorithms opt for the **Mahalanobis distance** (or Normalized Innovation Squared (NIS)), where the uncertainties in the observations are taken into account. Mahalanobis distance $\mathbf{D_{ij}}$ is expressed as the statistical distance between the observations, z_i and z_j, considering their covariance $\mathbf{Cov_{ij}}$, as given in equation 6.1.

$$\mathbf{D_{ij}} = \sqrt{(\mathbf{z_i} - \mathbf{z_j})^{\mathbf{T}} \mathbf{Cov_{ij}} (\mathbf{z_i} - \mathbf{z_j})} \tag{6.1}$$

A comparison between the Euclidean and the Mahalanobis distance is shown in figure 6.5.

[Weingarten 05], which uses planar landmarks, resolves DA by applying Mahalanobis distance, similar to any typical EKF SLAM approaches. In our laser odometry implementation, the covariance for DA does not grow over a period of time as opposed to the classical SLAM. Therefore, for simplification, we use fixed noise thresholds as a function of landmark confidence to compare the distances.

- **Individual object characteristics**

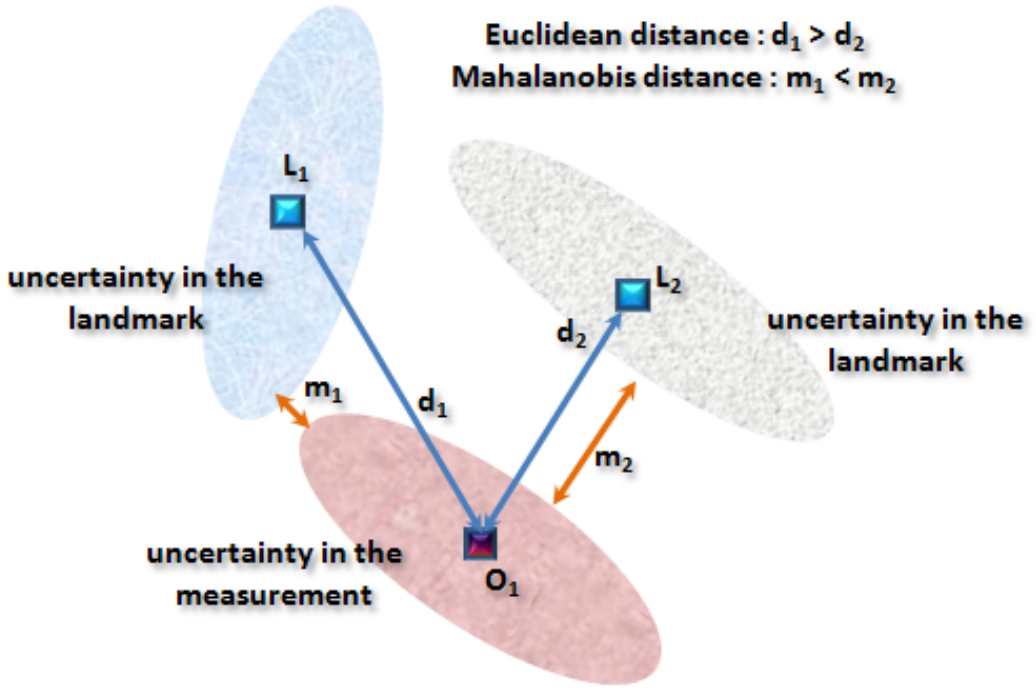

Figure 6.5: Euclidean vs. Mahalanobis distance. If the uncertainty information is not taken into account, the nearest object for the observation O_1 is L_2, whereas L_1 is close to O_1 than L_2.

In the works of [Dold 04] and [Dold 06], properties of the individual landmarks such as planar surface area, boundary length, bounding box and the mean intensity value of the laser observation per plane are used for associations. These can be applied as absolute constraints for DA.

From the perspective of future development, we can use the intensity of the laser measurements to distinguish different materials. Our present implementation do not use any other individual landmark properties, since the planar landmarks extracted in chapter 5 are taken from non overlapping scans(explained in section 7.2.1). This implies that the observed planar patches of a landmark can vary in size from one epoch to the other.

- **Geometrical relationships**

Geometrical relationships like corner points, subtending angles etc. can be exploited in addition to the widely used distance relationships, while using the high-level features (like lines, planes, circles etc.). However, most SLAM algorithms use point landmarks and only some of the line approaches use relative constraints, such as physical corners between the landmarks as rela-

tionships.

Angular relationships are often retained between objects of the same set because the measurement noises remain in the same order. In our approach, we implement correlation by using relative constraints on the dihedral angles (angles between planes) between the landmarks.

- **Order of observation**

  The order of observation is one of the most important relationships, but it has not yet been exploited. This can be applied in the SLAM approaches which extract landmarks in a particular order from the given *batch observations*. However, random object detection algorithms like RANSAC, Hough Transform etc. cannot take advantage of this information.

  The measurements of a range scanner are an ordered information, where the order of observations are retained within a short span of time, since the motion of the terrestrial mobile mapping system does not permit abrupt angular inversions. To give an example, if the objects (a1, b1, c1) are observed in one epoch, then it is guaranteed that they will be observed in no other but the same or partial order. This property is applied for the ambiguity reduction step.

6.5.1 Lenient Data Association (LDA)

Data Association (DA) in this thesis, associates two sets of planar landmarks observed at two epochs, without any knowledge about the motion of the mapping platform. This limits the direct application of absolute constraints, since the motion of the mapping platform is complex (involving both rotation and translation) and the planar landmarks are extracted from non overlapping scans (partial vision, explained in section 7.2.1). Therefore, the common SLAM approach to use the nearest neighbor method for associating the landmarks on a map, is not applicable. However, the use of *batch data association* is more reliable since the relationship constraints rely on the relative characteristics within each set of landmarks and observations.

To remind, the assumption behind this laser odometry approach is that the time interval, and hence the displacement of the robot, between successive scan lines is small. Moreover, from the definition of the batch observation, all the landmarks within a scan is assumed to have observed simultaneously. Therefore, the association of the observation sets is feasible in the Moving Reference Frame (MRF). This is explained in figure 6.6.

Correlation between planar landmarks is performed using the relative relationship of dihedral angles. This property remains time invariant, keeping intact the association between the planes. In order to compensate for the unknown transformation of the vehicle and also to eliminate the ambiguities in some obvious erroneous associations,

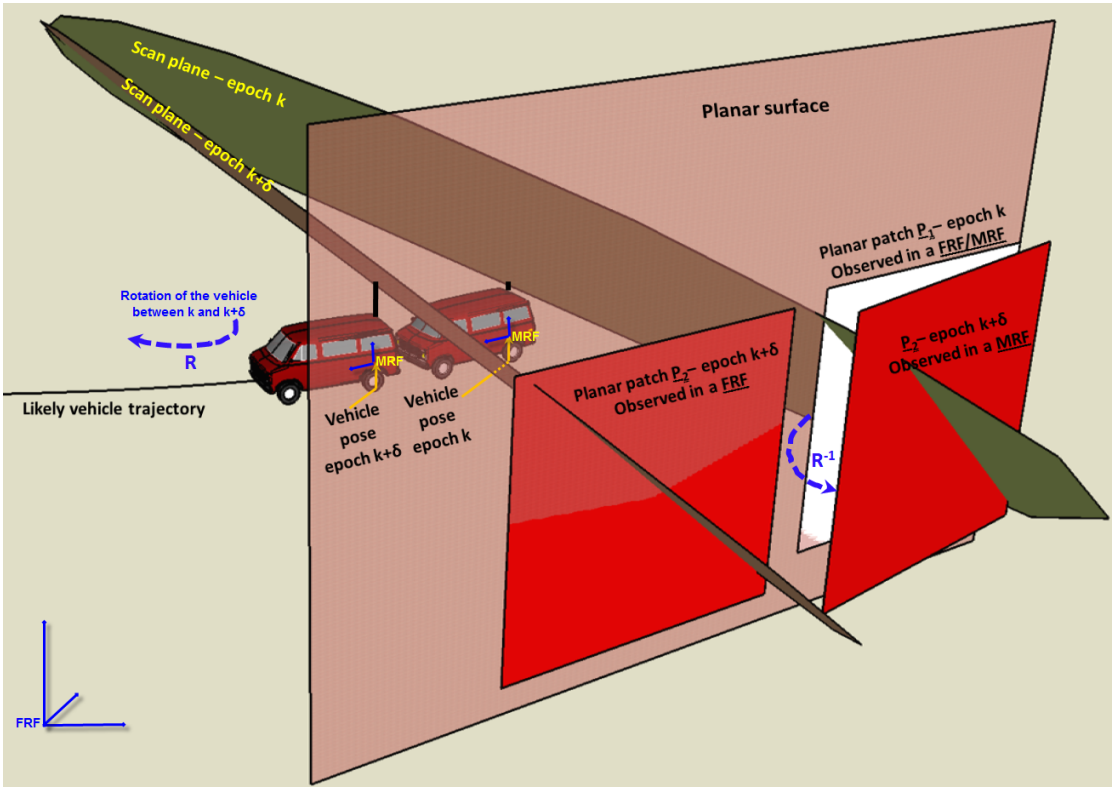

Figure 6.6: Corresponding planar patches in a MRF is described using two planar patches P_1 and P_2 of the same planar surface, with considerably larger time δ between the two epochs (in order to have a clear picture of the planar patches in FRF and MRF). However, DA is feasible if δ is sufficiently small so that P_1 and P_2 (in FRF) have some overlapping region between them (as in figure 7.1). In MRF, the planes P_1 and P_2, extracted from the same physical static planar surface, characterize the vehicle transformation. DA between P_1 and P_2 is performed in the MRF.

a set of lenient (non rigid) absolute constraints are applied. These are, a distance relationship and a mutual containment between the correlated landmarks in the two sets of observations.

Correlation

Dihedral angles are computed for each pair of planes in an observation set. This relationship is shown in figure 6.7.

If $\mathbf{n_k}$ is the number of planes extracted at epoch k, then $\binom{\mathbf{n_k}}{\mathbf{2}}$ number of angles must

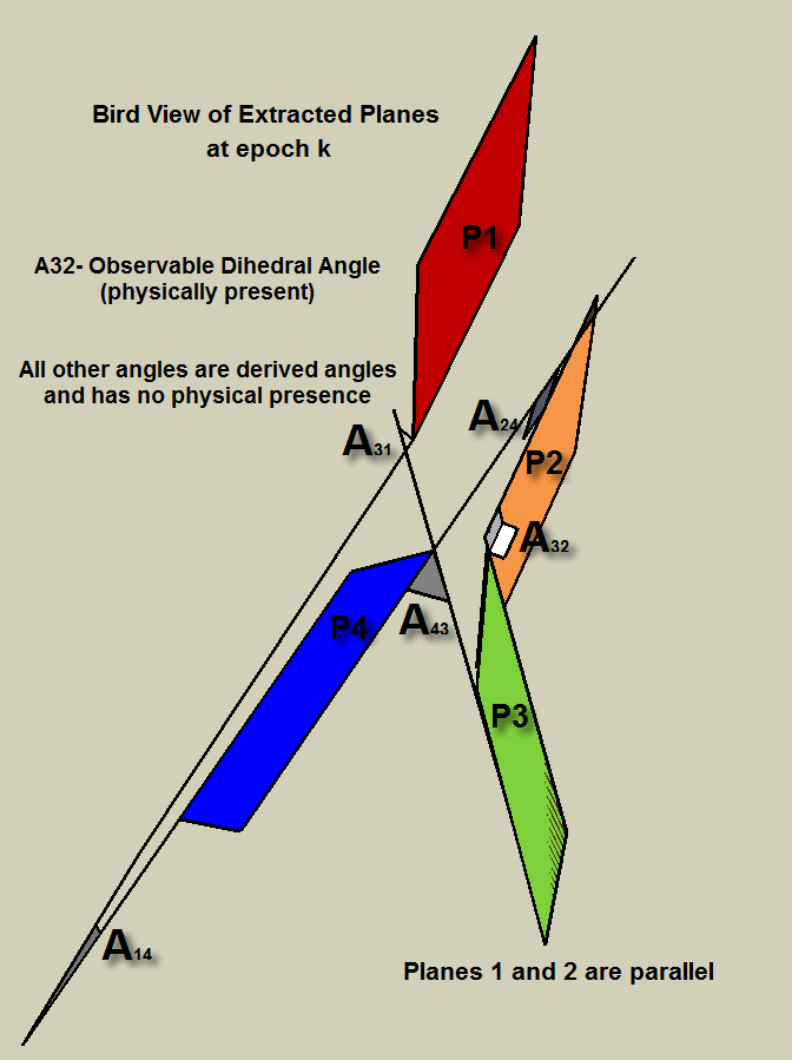

Figure 6.7: Relative constraint - dihedral angle

be computed. The dihedral angle $\varphi^{\mathbf{i,j}}$ between the planes **i** and **j** at epoch **k** is computed using their normals $\overrightarrow{N^i}$ and $\overrightarrow{N^j}$, as given in equation 6.2. The set of all dihedral angles constitutes a skew symmetric matrix (SSM) $\mathbf{D_k}$. The symmetry is due to the fact that the angle between a given pair of planes (P_1, P_2) is same as (P_2, P_1). Similarly the set of $\varphi^{\mathbf{i,j}}$ for planes of epoch $k + \delta$ constitutes the SSM $\mathbf{D_{k+\delta}}$.

$$\mathbf{D_k} = \{\varphi^{\mathbf{i,j}} = \arccos\left(\frac{\overrightarrow{N^i} \odot \overrightarrow{N^j}}{||\overrightarrow{N^i}||\ ||\overrightarrow{N^j}||}\right) \forall(\mathbf{j} > \mathbf{i})\}_k \tag{6.2}$$

where, $\odot$ is the vector dot product, and the vectors are normalized (symbol $||.||$) to compensate for any numerical noises.

The set $\mathbf{D_k}$ at epoch k is stored for further processing. The relative constraints between epochs k and $k+\delta$ is illustrated by the correlation quadruple $\hat{\mathbf{C}}^{\mathbf{1}}_{\mathbf{k},\mathbf{k}+\delta}$.

$$\begin{aligned}\hat{\mathbf{C}}^{\mathbf{1}}_{\mathbf{k},\mathbf{k}+\delta} = \{\mathbf{c}_{\mathbf{k},\mathbf{k}+\delta} = (\rho^{\mathbf{i}}_{\mathbf{k}}, \rho^{\mathbf{j}}_{\mathbf{k}}, \rho^{\mathbf{p}}_{\mathbf{k}+\delta}, \rho^{\mathbf{q}}_{\mathbf{k}+\delta}) | (i \neq j) \wedge (p \neq q) \wedge (i,j \in \{1 \dots n_k\}) \\ \wedge ((p,q) \in \{1 \dots n_{k+\delta}\}) \wedge (\varphi^{\rho^{\mathbf{i}}_{\mathbf{k}}, \rho^{\mathbf{j}}_{\mathbf{k}}} \simeq \varphi^{\rho^{\mathbf{p}}_{\mathbf{k}+\delta}, \rho^{\mathbf{q}}_{\mathbf{k}+\delta}})\}\end{aligned} \tag{6.3}$$

The superscript 1 in the notation of set $\hat{\mathbf{C}}^{\mathbf{1}}_{\mathbf{k},\mathbf{k}+\delta}$ indicates that it is the first step of LDA. The angle comparison uses $\simeq$ to indicate the margin ($\mathbf{K}_\varphi$) for the noises. $\mathbf{n_k}$ and $\mathbf{n_{k+\delta}}$ are the number of extracted planes in epochs $\mathbf{k}$ and $\mathbf{k}+\delta$. As explained earlier, since the order of observation is retained, in a record $\mathbf{c}_{\mathbf{k},\mathbf{k}+\delta}$, plane $\rho^{\mathbf{i}}_{\mathbf{k}}$ cannot be plane $\rho^{\mathbf{q}}_{\mathbf{k}+\delta}$ and plane $\rho^{\mathbf{j}}_{\mathbf{k}}$ cannot be plane $\rho^{\mathbf{p}}_{\mathbf{k}+\delta}$.

In order to compute transformation (see section 6.6) from planar landmarks, we need associated non parallel planes. However, due to this constraint, all the parallel planes in the observation sets are removed from the set $\hat{\mathbf{C}}^{\mathbf{1}}_{\mathbf{k},\mathbf{k}+\delta}$. The reduced correlation set is termed as $\hat{\mathbf{C}}^{\mathbf{2}}_{\mathbf{k},\mathbf{k}+\delta}$.

Ambiguity reduction

In this ambiguity reduction phase, a set of absolute constraints is used. An absolute constraint tests a relationship between the correlated planes $\rho_{\mathbf{k}}, \rho_{\mathbf{k}+\delta}$ of the two observation sets. That is for each record $\mathbf{c}_{\mathbf{k},\mathbf{k}+\delta}$ of the set $\hat{\mathbf{C}}^{\mathbf{2}}_{\mathbf{k},\mathbf{k}+\delta}$, plane $\rho^{\mathbf{i}}_{\mathbf{k}}$ is tested with $\rho^{\mathbf{p}}_{\mathbf{k}+\delta}$ and $\rho^{\mathbf{j}}_{\mathbf{k}}$ with $\rho^{\mathbf{q}}_{\mathbf{k}+\delta}$. The goal of this reduction step is not to ensure a one to one match, but to remove any spatially impossible associations.

Unlike conventional methods where the distance threshold test (also known as *validation gate*) are applied in a FRF, in our case, without any external pose information, the new planar features can be mapped only to the MRF. Therefore, the absolute constraints are resolved in the MRF itself. Additional pose information can be integrated later, as an improvement.

Two absolute relationships can be tested: a distance relationship defining the spatial neighborhood constraint and a boundary-based containment relationship for spatial alignment. These absolute constraints are applicable because the scope of this thesis is limited to a terrestrial mapping platform with a restricted motion capability. As mentioned earlier, the displacement of the vehicle is assumed to be very small between two scans performed within a short period of δ. Linear displacements are limited but the

rotational effect can induce a marginally higher displacement for the planes when observed in the MRF, especially if the planes are located far from its origin. Therefore, the *validation gate* is designed to ensure that even those planes are considered as neighbors.

The mid points of the planar patches are chosen to compute the distance and to test the containment relation, because they remain in the most probable zone of common observations between two successive epochs.

The distance is computed between the mid point of a plane and its corresponding projection on the other plane. Then the containment relationship verify if this point belongs to the planar patch of the other data set.

These two relationships are explained using figure 6.8.

Using the notations used in figure 6.8, the absolute constraints are thresholded by a distance $\mathbf{D_{LDA}}$ for $\mathbf{d_i}$ and $\mathbf{d_j}$, and the boundary containment for the projected points $\mathbf{m_j^i}$ and $\mathbf{m_i^j}$ within the planes on which they are projected. If at least one of the two distance tests and at least one of the two containments tests are passed, the correlation association is considered valid.

The criteria to consider the correlation association as valid are given in equation 6.4.

$$\begin{aligned} \mathbf{d_i} < \mathbf{D_{LDA}} \text{ or } \mathbf{d_j} < \mathbf{D_{LDA}} \\ \mathbf{m_j^i} \in \mathbf{P1_{k+\delta}^{MRF}} \text{ or } \mathbf{m_i^j} \in \mathbf{P1_k^{MRF}} \end{aligned} \tag{6.4}$$

A correlation record contains two planar relations: a mapping of two interrelated planes across two observation sets. For retaining a correlation quadruple, the absolute constraints need to be matched for both absolute planar relations, i.e. absolute constraints between $\mathbf{P1_k^{MRF}}$ and $\mathbf{P1_{k+\delta}^{MRF}}$ and $\mathbf{P2_k^{MRF}}$ and $\mathbf{P2_{k+\delta}^{MRF}}$. The reduced correlated quadruple set is denoted as $\hat{\mathbf{C}}_{\mathbf{k,k+\delta}}^{\mathbf{3}}$.

Preferably, $\mathbf{D_{LDA}} = \mathbf{F}(\omega_{\mathbf{k-\delta}}, \sigma_{\mathbf{laser}}, \mathbf{K_{D_{LDA}}})$, where $\omega_{\mathbf{k-\delta}}$ is proportional to the angular and linear velocities of the vehicle from the previous instant $\mathbf{k-\delta}$, σ_{laser} laser scanner precision and $K_{\mathbf{D_{LDA}}}$ is a tuning parameter. In the current implementation, a naive constant threshold of $\omega_{\mathbf{k-\delta}} = \mathbf{8}$ meters is used and $\mathbf{K_{D_{LDA}}} = 1.5$, where $\mathbf{F}(\cdot)$ adds the noise factor to the $\omega_{\mathbf{k-\delta}}$. $\omega_{\mathbf{k-\delta}} = \mathbf{8}$ meters per epoch, is equivalent to observe a plane at a distance of **80** meters (the maximum observation range selected for many MMS applications) or the time during which the mapping platform undergoes a rotation of more than $\mathbf{5}^\circ$. 8 meters correspond to an orthogonal linear velocity of $\mathbf{720}kmph$ (for a $\mathbf{25}Hz$ observation frequency), and a rotation of $\mathbf{5}^\circ$ per observation means a vehicle can turn $\mathbf{125}^\circ$ per second.

The purpose of such a lenient association step is to remove any spatially impossible

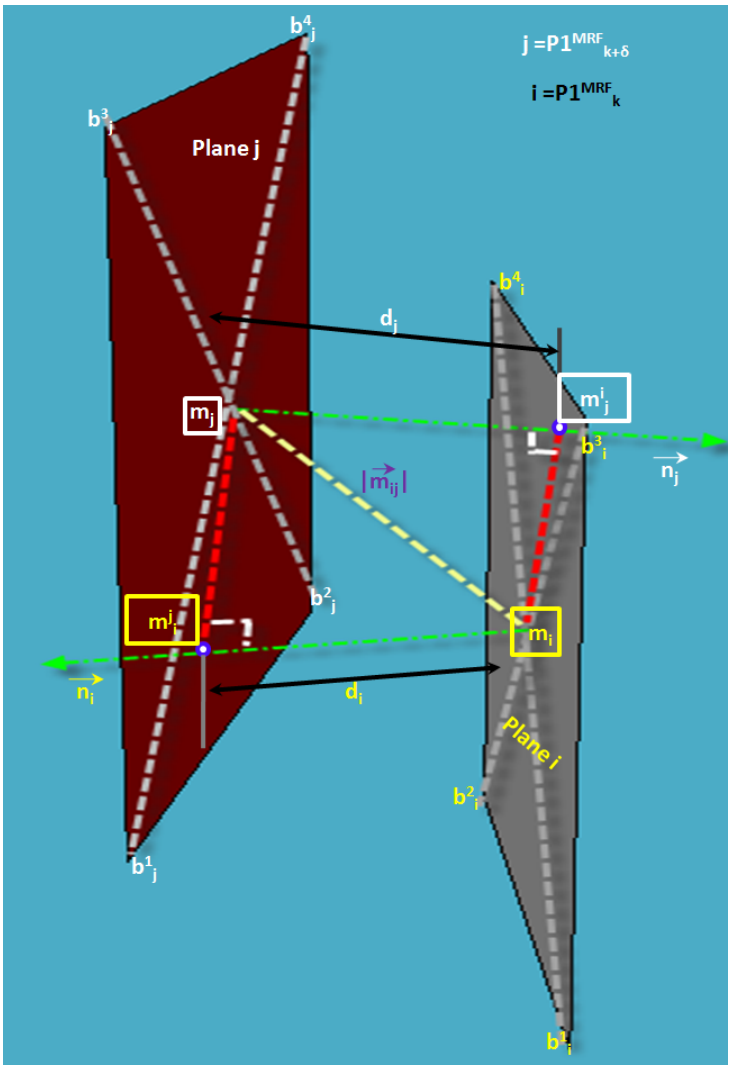

Figure 6.8: Applying absolute constraints to reduce ambiguities. Two planes $\mathbf{P1}_{\mathbf{k}}^{\mathbf{MRF}}$ and $\mathbf{P1}_{\mathbf{k+\delta}}^{\mathbf{MRF}}$ represent the same planar landmark $\mathbf{P1}$, observed at epochs $\mathbf{k}$ and $\mathbf{k}+\delta$. The shift in them occurs due to the motion of the vehicle (MRF). For simplicity of notation, plane parameters are noted with notations of $\mathbf{i}$ and $\mathbf{j}$ for the planes $\mathbf{P1}_{\mathbf{k}}^{\mathbf{MRF}}$ and $\mathbf{P1}_{\mathbf{k+\delta}}^{\mathbf{MRF}}$ respectively. The planes have the boundary points $[\mathbf{b_i^1}, \mathbf{b_i^2}, \mathbf{b_i^3}, \mathbf{b_i^4}]$ and $[\mathbf{b_j^1}, \mathbf{b_j^2}, \mathbf{b_j^3}, \mathbf{b_j^4}]$. The mid points of the planar patches $\mathbf{i}$ and $\mathbf{j}$ are noted $\mathbf{m_i}$ and $\mathbf{m_j}$. The length of the distance vector $\mathbf{m_{ij}}$, between $\mathbf{m_i}$ and $\mathbf{m_j}$ in the direction of the normals $\mathbf{n_i}$ and $\mathbf{n_j}$ is given as $\mathbf{d_i}$ and $\mathbf{d_j}$ respectively. The projection of the vector $\mathbf{m_{ij}}$ is shown using the red lines. The projection points $\mathbf{m_j^i}$ and $\mathbf{m_i^j}$ are the projection of $\mathbf{m_i}$ on the plane $\mathbf{j}$ and $\mathbf{m_j}$ on plane $\mathbf{i}$.

associations to reduce the cardinality of the correlated quadruple set.

6.5.2 Strict Data Association (SDA)

This step is performed after computing the rotation estimation. However, it is explained here in order to have a continuity on the DA concept. We will also demonstrate that this step becomes optional if we choose to compute the best translation estimate using a single quadruple record of associated pair of planes. The best estimate is obtained by applying the OCSC algorithm (section 6.7.1), which is explained in section 6.7.3.

Prior applying SDA, computed rotation estimation is applied to the data set from epoch $\mathbf{k}$, to align it with the data set from the epoch $\mathbf{k}+\delta$. A more stringent relationship is then tested on the retained association set $\hat{\mathbf{C}}^{\mathbf{3}}_{\mathbf{k},\mathbf{k}+\delta}$ to eliminate the remaining ambiguities. This can be treated as an ambiguity reduction by narrowing down the *validation gate*.

Further, an additional ambiguity resolution (also known as ambiguity management) algorithm, based on voting, is demonstrated to ensure injective associations.

Stringent ambiguity reduction

The set of absolute constraints given in section 6.5.1 are reapplied to the set of associations $\hat{\mathbf{C}}^{\mathbf{3}}_{\mathbf{k},\mathbf{k}+\delta}$, yet narrowing the threshold for the distance relationship.

As mentioned before, the stringent condition is applied after the two observation sets are realigned, by applying the computed rotation on one of the data sets. Applying $\mathbf{R}'_{\mathbf{k}}$ (computed in the equation 6.28) to the observation set of epoch $\mathbf{k}$, transforms it into a set of planes almost parallel to the observation set of epoch $\mathbf{k}+\delta$. The same result can be obtained by applying $\mathbf{R}'^{\,-\mathbf{1}}_{\mathbf{k}}$ to the set of epoch $\mathbf{k}+\delta$. The distance between the corresponding planes in the two data sets is then minimized, according to the rotated translation vector.

Like LDA in section 6.5.1, $\mathbf{D_{SDA}} = \mathbf{F}(\omega_{\mathbf{k}-\delta}, \sigma_{\mathbf{laser}}, \mathbf{K_{D_{SDA}}})$. However, in the current implementation, a naive constant threshold of $\omega_{\mathbf{k}-\delta} = \mathbf{3}$ meters is used and $K_{\mathbf{D_{SDA}}} = 1.5$, where $\mathbf{F}(\cdot)$ adds the noise factor to the $\omega_{\mathbf{k}-\delta}$. $\omega_{\mathbf{k}-\delta} = \mathbf{3}$ meters per epoch, is equivalent to an orthogonal linear velocity of $\mathbf{270}kmph$ (for a $\mathbf{25}Hz$ observation frequency). This is still high but it is assigned to ensure that there is enough margin for various uncertainties.

At the end, the remaining associated matches are termed as the quadruple set $\hat{\mathbf{C}}^{\mathbf{4}}_{\mathbf{k},\mathbf{k}+\delta}$.

Ambiguity resolution

An additional but optional algorithm is designed to tackle the ambiguities, remaining after applying all the previously mentioned ambiguity reduction processes. These remaining conflicts are resolved using a voting scheme to ensure a one to one pairing between the observations across the two data sets. The individual pairings are mapped to a frequency matrix which is derived from the correlation set. This is similar to the multiple target tracking algorithm applied to ensure an injective optimal association set (explained in [Bailey 02]). These algorithms work based on the principle of maximum likelihood.

As most of the conflicts have already been resolved, the use of a mean-based method for computing the translation is sufficient. However, in the presence of any ambiguities, the computed translation gets biased. The algorithm steps are illustrated using an example shown in figure 6.9.

At first, the algorithm generates a voting matrix $\mathbf{V^{ij}_{k,k+\delta}}$. Each row of the matrix represents a distinct plane observed in epoch $\mathbf{k}$. Each column is a plane from epoch $\mathbf{k}+\delta$. This matrix contains the votes of the matched planes pairs retained in the quadruple set $\hat{\mathbf{C}}^{\mathbf{4}}_{\mathbf{k},\mathbf{k}+\delta}$.

The first step is to ensure that there is no more than one association per plane. A conflict in association is illustrated by an equal number of maximum votes for different associations per plane. If this is not the case, the algorithm provides inconsistent results.

In the given example, plane $\mathbf{P5_k}$ has a maximum vote of 2 for $\mathbf{P5_{k+\delta}}$ and $\mathbf{P6_{k+\delta}}$, indicating an ambiguity to associate $\mathbf{P5_k}$ in the data set of epoch $\mathbf{k}+\delta$. This conflict is resolved using the **'appearance test'**, by applying the computed rotation matrix to align the two sets of planes. The closest aligned planes in the sense of smallest dihedral angle are selected and the first level of ambiguity is resolved.

In the example, the plane $\mathbf{P6_{k+\delta}}$, is considered a more suitable match for $\mathbf{P5_k}$. In the case of a column conflict, the rotation $(\mathbf{R^{'}_k})^{\mathbf{-1}}$ is applied to the column plane of epoch $\mathbf{k}+\delta$ and is compared with its row matches of epoch $\mathbf{k}$.

In the second step, a row voting is done, and the entry with the best row vote is retained, resetting the other entries to $\mathbf{0}$. Although, the row voting resolves some column conflicts, such as columns $\mathbf{P1_{k+\delta}}$, $\mathbf{P4_{k+\delta}}$ and $\mathbf{P5_{k+\delta}}$, it does not eliminate all the ambiguities ($\mathbf{P2_{k+\delta}}$).

The third step is to perform a column scan to retain the rows with the maximum vote resulting in a one to one matches.

For notational purposes, the algorithm generates a conflict-less quadruple set $\hat{\mathbf{C}}^{\mathbf{5}}_{\mathbf{k},\mathbf{k}+\delta}$.

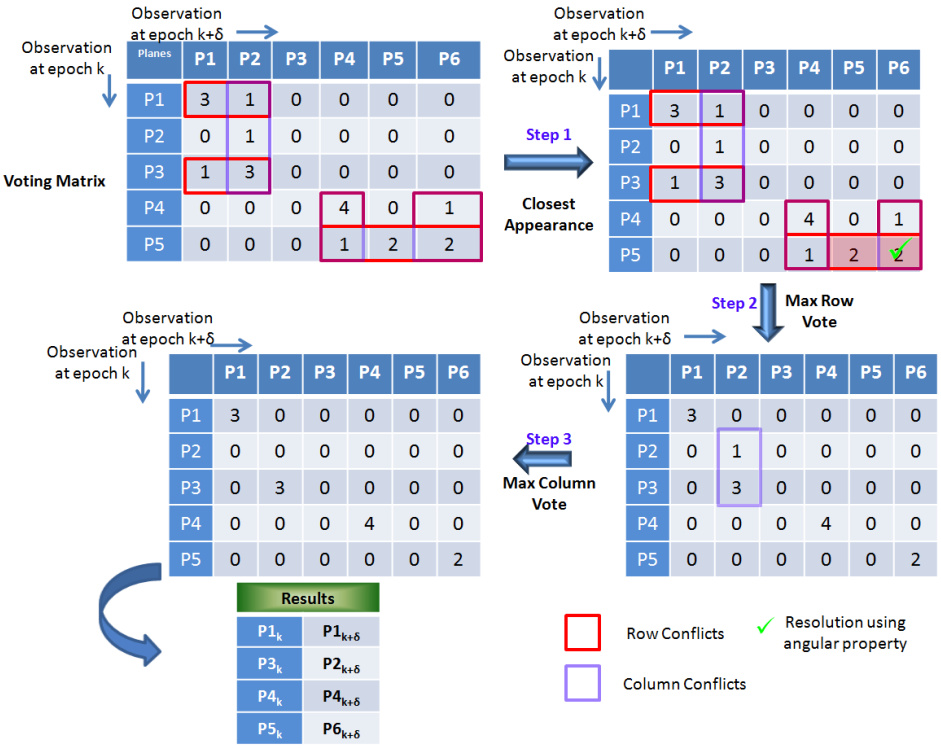

Figure 6.9: Ambiguity resolution - voting steps

This algorithm is a simple way to resolve ambiguities. It provides a minimal set of matches without any conflicts. In most observed cases only one or two row or column conflicts remain prior ambiguity resolution. From the observations made in the test experiments, the matrix shown in figure 6.9 is a worst case. However, the ambiguities can increase as the environments gets cluttered. In such scenarios, either the appearance test can be used to resolve all conflicts or a more sophisticated ambiguity resolution algorithm needs to be implemented. It is to be noted that in some cases, interchanging **step2** and **step3** of the voting method leads to different results.

In any case, the matching is done based on several relationship parameters and the best suitable match is retained without any conflict. No ambiguity resolution algorithm can guarantee a perfect solution, as all the constraints cannot be applied simultaneously. This simple ambiguity resolution algorithm is proved good enough in practice for testing the pose computation problem using planar landmarks.

Alternatively, the **Optimal Candidate Selection by Consensus** algorithm can be applied to choose the required minimal set (in this case a single quadruple set record) of associations to compute the transformations. Since these algorithms not only provide the minimal set but also compute the optimal transformation, we first present our approach

to compute the transformation using associated planar landmarks.

6.6 Transformation resolution from associated landmarks

This thesis shows that the transformation problem can also be resolved analytically by using the time invariant geometrical properties of the selected landmarks.

The common EKF and Particle filter approaches rely on an observation model, to which the measurements are incrementally fitted. This step is no more necessary in our approach. The problem is resolved by direct computation of the transformation from the associated data. This inversion of the mapping problem helps to localize the mobile mapping systems.

As mentioned in section 6.2 and shown in figure 6.10, the 3D transformation problem is split in two: first a 3D rotation resolution and then a separate translation resolution.

Like the DA, transformation estimation is also resolved in the moving reference frame (MRF) (refer to chapter 5 for definition). The only knowledge of the mobile platform about its environment is the position of landmarks in its own reference frame (MRF). It is however possible to estimate the movement of the platform by estimating the fixed transformation between 2 observation epochs k and $k + \delta$, of the same set of static objects in the fixed reference frame (FRF). The only constraint is to associate correctly these 2 set of landmarks, and this done using the DA explained in section 6.5.

6.6.1 Splitting the transformation problem

Most of the approaches address the rotation and translation as a single problem. EKF-based SLAM approaches formulate the position and orientation in the same state vector. The particle filter samples this vector for each component and tracks the multiple hypotheses. Iterative optimization algorithm, like ICP, even combines transformation with DA.

The transformation problem can also be solved at two levels: first a rotation, and then a translation problem. This converts the 3D transformation problem with six degrees of freedom (6DOF) in two 3DOF problems: one for each rotation and translation. Similar splitting of the transformation problem is recently identified in [Dold 04] and [Dold 06] in the domain of laser scan registration, where two point clouds are matched automatically. They apply this method to overcome the limitations of the standard registration algorithm of ICP. This work is not related to the SLAM domain, where a continuous pose (trajectory) estimation needs to be done using the planar patches.

The splitting can be explained using figure 6.10. The critical issue is to identify the geometrical properties which remain unaffected by translations, but affected by only rotations, to resolve the unknown $R_k^{'}$. The translation vector $T_k^{'}$ is deduced after compensating for the computed rotation. However the problem in our case is non trivial, since the uniform planar patches extracted from partial vision (refer figure 7.1) do not provide any distinguishable point features shown in $Frame1$ and $Frame2$.

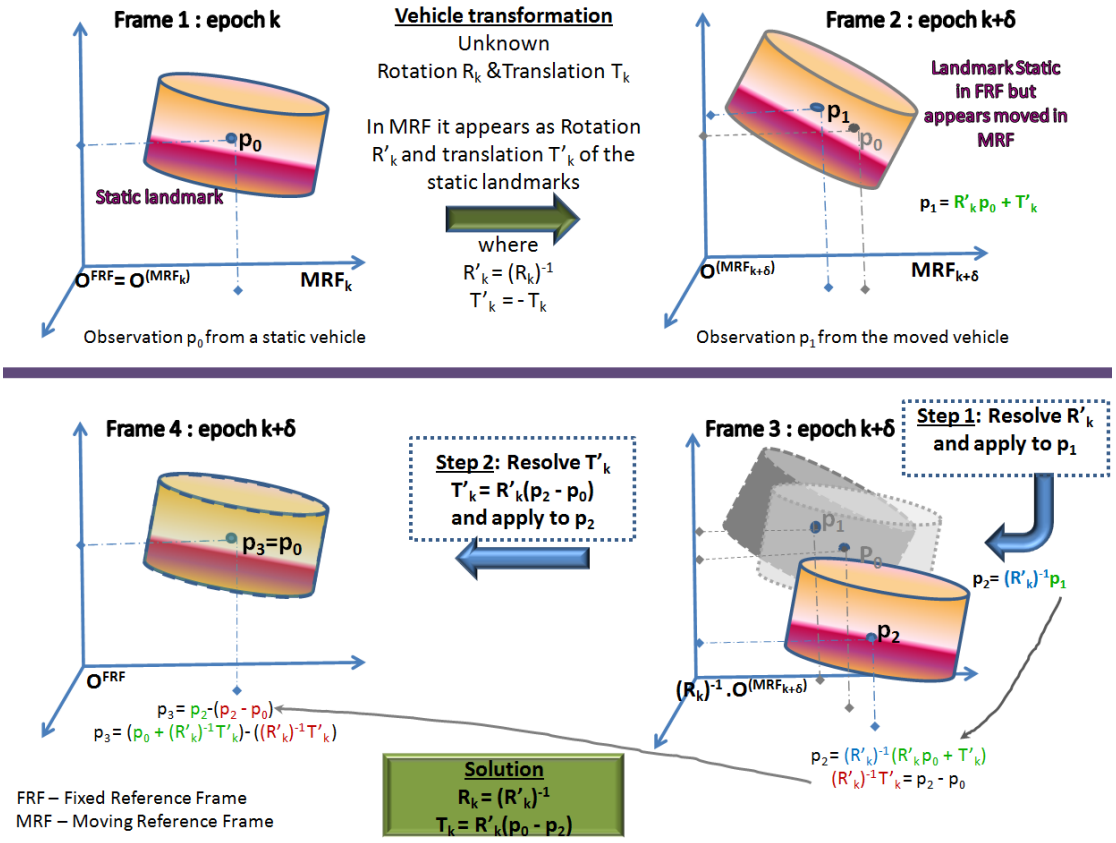

Figure 6.10: Splitting the transformation to a rotation and a translation. Figure has four frames, where $Frame1$ and $Frame2$ correspond to a landmark observation, as seen by the mapping platform (MRF) at two instants $\mathbf{k}$ and $\mathbf{k}+\delta$, whereas $Frame3$ and $Frame4$ show the computation of rotation and translation.

The sections to follow describe the rotation and translation computation using planar landmarks.

6.6.2 3D rotation

As shown in figure 6.10, the first step in determining 3D transformation from the planar landmarks is to resolve the rotation component ($R_k^{'}$).

3D rotation from a non parallel pair of corresponding planar landmarks

To measure the rotation of a vehicle in a 3D space, three independent vectors are needed, observed at both the epochs between which the rotation has taken place. At the first epoch, two independent unit vectors $\mathbf{N^m}$ and $\mathbf{N^n}$ can be identified by the normals of two non parallel planes $\rho^{\mathbf{m}}$ and $\rho^{\mathbf{n}}$. Their outer product (vector cross product) gives the required third vector $\mathbf{N^o}$, as in equation 6.5. These three vectors will form the reference frame for the rotation, termed as the Object Reference Frame (ORF).

$$\overrightarrow{N^o} = \frac{\overrightarrow{N^m} \otimes \overrightarrow{N^n}}{||\overrightarrow{N^m} \otimes \overrightarrow{N^n}||} \tag{6.5}$$

where $\otimes$ indicates the vector cross product. Since $\overrightarrow{N^m}$ and $\overrightarrow{N^n}$ are normalized, even $\overrightarrow{N^o}$ is normalized. However, an explicit normalization is added to avoid numerical noises in calculation.

The methodology for determining the rotation using planar landmarks is shown in figure 6.11. A rotation operation in a Euclidean space is isometric. Thus the rotation $\mathbf{R_k}$ retains the same angular relationships between the vectors $\mathbf{N^m}, \mathbf{N^n}, \mathbf{N^o}$, what ever the rotation of the MRF are. Thus by taking any two non parallel planes in two observation epochs, it is possible to compute the 3D rotation $\mathbf{R_k}$.

The observations at epoch $\mathbf{k}$ are the two normal vectors $\mathbf{N^i}$ and $\mathbf{N^j}$, for two non parallel planes $\rho^{\mathbf{i}}$ and $\rho^{\mathbf{j}}$. The same two planes are observed and identified using DA, in the epoch $\mathbf{k}+\delta$. These two planes are referred to as $\hat{\rho}^{\mathbf{i}}$ and $\hat{\rho}^{\mathbf{j}}$, whose respective normals are $\hat{\mathbf{N}}^{\mathbf{i}}$ and $\hat{\mathbf{N}}^{\mathbf{j}}$. The third perpendicular vector can be computed using the equation 6.5.

Equation 6.6 gives the relation between the 2 reference frames (ORFs) $\mathbf{U_k}$ and $\mathbf{U_{k+\delta}}$ as:

$$\mathbf{U_{k+\delta}} = \mathbf{R_k^{'}} \mathbf{U_k} \tag{6.6}$$

$$\text{where } \mathbf{U_k} = \begin{pmatrix} \mathbf{N^i}_\mathbf{x} & \mathbf{N^j}_\mathbf{x} & \mathbf{N^o}_\mathbf{x} \\ \mathbf{N^i}_\mathbf{y} & \mathbf{N^j}_\mathbf{y} & \mathbf{N^o}_\mathbf{y} \\ \mathbf{N^i}_\mathbf{z} & \mathbf{N^j}_\mathbf{z} & \mathbf{N^o}_\mathbf{z} \end{pmatrix} \text{ and } \mathbf{U_{k+\delta}} = \begin{pmatrix} \hat{\mathbf{N}}^\mathbf{i}_\mathbf{x} & \hat{\mathbf{N}}^\mathbf{j}_\mathbf{x} & \hat{\mathbf{N}}^\mathbf{o}_\mathbf{x} \\ \hat{\mathbf{N}}^\mathbf{i}_\mathbf{y} & \hat{\mathbf{N}}^\mathbf{j}_\mathbf{y} & \hat{\mathbf{N}}^\mathbf{o}_\mathbf{y} \\ \hat{\mathbf{N}}^\mathbf{i}_\mathbf{z} & \hat{\mathbf{N}}^\mathbf{j}_\mathbf{z} & \hat{\mathbf{N}}^\mathbf{o}_\mathbf{z} \end{pmatrix}.$$

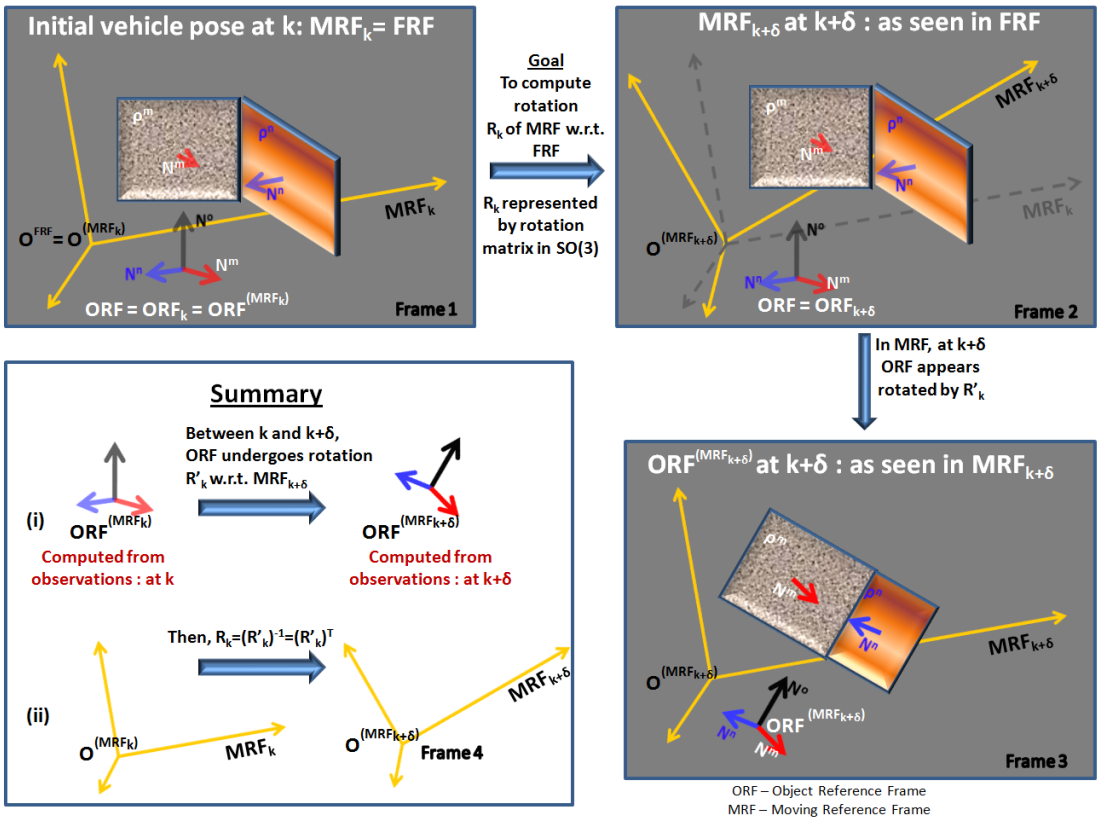

Figure 6.11: Figure describes the rotation resolution using planar features. Following the convention used before, there are four parts in figure 6.11. *Frame*1 and *Frame*2 show the rotation of the MRF between the epochs $\mathbf{k}$ and $\mathbf{k}+\delta$ with respect to the FRF. *Frame*1 is the observation done by the mapping platform at epoch $\mathbf{k}$. *Frame*3 depicts the observation of the mapping platform at $k+\delta$ where its own rotation $\mathbf{R_k}$ appears as the rotation of the ORF expressed as $\mathbf{R_k^{'}}$.

The notations $\mathbf{h_x}, \mathbf{h_y}, \mathbf{h_z}$ refer to the $\mathbf{x}, \mathbf{y}, \mathbf{z}$ components of the normal vector $\mathbf{h}$.

$\mathbf{R_k^{'}}$ is then derived using equation 6.7.

$$\mathbf{R_k^{'}} = \mathbf{U_{k+\delta}} \mathbf{U_k^{-1}} \tag{6.7}$$

Prior constructing $\mathbf{U_k}$, it is ensured that the normal vectors $\mathbf{N^i}$ and $\mathbf{N^j}$ are not parallel (they form the ORF). This condition is been introduced in LDA to remove all non parallel planes as explained in section 6.5.1. Therefore, for the associated pair of planes, the matrix $\mathbf{U_k}$ is invertible. The 3D rotation of the mapping platform $\mathbf{R_k}$ is

computed by the transpose of $\mathbf{R_k^{'}}$.

An example and use cases

- **3D rotation resolution: an example**

  Using this example, we show that the rotation computation is feasible when two normals are almost parallel, which can be the case in some mapping environments. The example is tested in MATLAB.

  Consider two planes $\rho^{\mathbf{i}}$ and $\rho^{\mathbf{j}}$ with normals $\mathbf{N^i} = (\mathbf{1}, \mathbf{0}, \mathbf{0})^{\mathbf{T}}$ and $\mathbf{N^j} = (\mathbf{1.0000}, -\mathbf{0.00017}, \mathbf{0})^{\mathbf{T}}$ subtending an acute angle of $\mathbf{0.01}^\circ$ between them.

  If the robot undergoes a complex clockwise rotation of $\psi = \mathbf{5}^\circ$ around the $\mathbf{Z}$ axis, and $\phi = \mathbf{10}^\circ$ around the $\mathbf{X}$ axis, between the epochs $\mathbf{k}$ and $\mathbf{k} + \delta$, then this will be seen as a counterclockwise rotationof the same magnitude on the planar patches. The composite rotation matrix of the form $\mathbf{R_{zyx}} = \mathbf{R_z}(\psi)\mathbf{R_y}(\theta)\mathbf{R_x}(\phi)$ is shown in equation 6.8.

$$\left.\begin{array}{l} \mathbf{p_1} \leftarrow \mathbf{c}(\psi)\mathbf{s}(\theta) \\ \mathbf{p_2} \leftarrow \mathbf{s}(\psi)\mathbf{s}(\theta) \\ \mathbf{R_{zyx}} = \begin{pmatrix} \mathbf{c}(\theta)\mathbf{c}(\psi) & \mathbf{p_1} * \mathbf{s}(\phi) - \mathbf{c}(\phi) * \mathbf{s}(\psi) & \mathbf{p_1} * \mathbf{c}(\phi)) + (\mathbf{s}(\phi) * \mathbf{s}(\psi)) \\ \mathbf{c}(\theta)\mathbf{s}(\psi) & (\mathbf{p_2} * \mathbf{s}(\phi)) + (\mathbf{c}(\phi) * \mathbf{c}(\psi)) & (\mathbf{p_2} * \mathbf{c}(\phi)) - (\mathbf{s}(\phi) * \mathbf{c}(\psi)) \\ -\mathbf{s}(\theta) & \mathbf{s}(\phi)\mathbf{c}(\theta) & \mathbf{c}(\phi)\mathbf{c}(\theta) \end{pmatrix} \end{array}\right\} \tag{6.8}$$

  where, $\mathbf{s}$ and $\mathbf{c}$ indicate the trigonometric functions sin and cos respectively, and ϕ, θ and ψ are the respective rotation angles around the three reference axes $\mathbf{X}$, $\mathbf{Y}$ and $\mathbf{Z}$.

  Therefore the composite matrix $\mathbf{R_{zyx}}$ for the above example, has a value rounded to (5 significant digits) as:

$$\mathbf{R_{zyx}} = \begin{pmatrix} \mathbf{0.99619} & -\mathbf{0.089583} & \mathbf{0.01513} \\ \mathbf{0.08716} & \mathbf{0.98106} & -\mathbf{0.17299} \\ \mathbf{0} & \mathbf{0.17365} & \mathbf{0.98481} \end{pmatrix} \tag{6.9}$$

  The rotated normal vectors $\hat{\mathbf{N}}^{\mathbf{i}}$ and $\hat{\mathbf{N}}^{\mathbf{j}}$ for the observed planes $\hat{\rho}^{\mathbf{i}}$ and $\hat{\rho}^{\mathbf{j}}$ at epoch $\mathbf{k} + \delta$ is given as: $\hat{\mathbf{N}}^{\mathbf{i}} = \mathbf{R_{zyx}}\mathbf{n^i} = (\mathbf{0.99619}, \mathbf{0.08716}, \mathbf{0.0174})^{\mathbf{T}}$ and $\hat{\mathbf{N}}^{\mathbf{j}} = \mathbf{R_{zyx}}\mathbf{n^j} = (\mathbf{0.99620}, \mathbf{0.08699}, -\mathbf{0.00003})^{\mathbf{T}}$ respectively. Similarly the respective third normal vectors $\mathbf{N^o}$ and $\hat{\mathbf{N}}^{\mathbf{o}}$ are obtained

by the cross product and have the values $\mathbf{N^o} = (\mathbf{0}, \mathbf{0}, -\mathbf{0.17000})^{\mathbf{T}}$ and $\hat{\mathbf{N}}^{\mathbf{o}} = (-\mathbf{0.00257}, \mathbf{0.02941}, -\mathbf{0.16742})^{\mathbf{T}}$.

Using the matrices $\mathbf{U_k}$ and $\mathbf{U_{k+\delta}}$ the unknown rotation matrix can be computed using equation 6.7. One can notice that the computed $\mathbf{R_k^{'}}$ is equal to the matrix $\mathbf{R_{zyx}}$ shown in equation 6.9. Using equation 6.8, the rotation angles can be finally retrieved. In MATLAB the values $\phi = \mathbf{10.0000}^\circ$, $\theta = \mathbf{0}^\circ$ and $\psi = \mathbf{5.0000}^\circ$ are obtained, matching the applied rotation angles.

Therefore, the 3D rotation can be resolved even when the two planes have an acute angle of $\mathbf{0.01}^\circ$ between them. However, in order to avoid any false detection due to noises, we have experimentally chosen an angle of $\mathbf{3}^\circ$ between two planes to consider them as non parallel. In real world scenarios, the planar surfaces which appear parallel can have an angle of up to $\mathbf{10}^\circ$ between them.

- **Case: no associated planes available**

  At a given epoch, if no planes are visible then nothing can be done. The world can be considered as unobservable.

  If there are observable planes, and if they can be associated in two successive epochs, then the orientation problem can be solved at least in 2D.

  A way to resolve the DA problem in this case, is to use the approach similar to EKF SLAM, using an external pose sensor (e.g. bearing only SLAM, based on Particle filter (Fast SLAM) [Tully 10]). From the system design given in chapter 5, the observed planes do not include the ground. Therefore, in the absence of two non parallel planes, the ground can be considered flat, and the orientation can be resolved in 2D, like in most SLAM algorithms. A plane, which has been associated in both the epochs is chosen, and the second one is obtained from the flat ground given by normal $(0, 0, 1)^T$. Equation 6.7 can be solved using these two normals. In the current implementation of laser odometry, where an external pose sensor is opted not to be used, this problem is not further explored.

  Note that the 2D pose problem is addressed in many previous works. In this thesis, the focus is on the 3D rotation and therefore the considered scenarios are ideal 3D environments for obtaining an independent pose solution.

- **Case: one or more associated non parallel planes**

  In the case where only a single non parallel pair of planes is available, the 3D rotation algorithm given in section 6.6.2 is directly applied.

  However, if there is more than one pair, there are several applicable 3D rotation algorithms. An easy alternative is to compute the rotation using all associated pairs (equation 6.7), followed by averaging all the computed solutions. The averaging can be further improved by using weights derived from the trust indicators of each plane. Applying a simple mean is to neglect this valuable information

and consider all the planes equally. In the presence of outliers, this can cause a potential bias in the computed rotation parameters. Therefore, a weighted mean based approach is suitable only when there are no outliers.

In our case, the quality of the planes can be weighted not only by the $\mathbf{CPEF}^{\rho}$ value (computed in equation 5.14), but also by the subtending angle between them. The estimated rotation parameters are optimal if the pair of planes is orthogonal, and their accuracy decreases along with the angle between the planes. This information is totally independent of the $\mathbf{CPEF}^{\rho}$ value and implies that some plane pairs can have a high $\mathbf{CPEF}^{\rho}$ value but a subtending angle close to $\mathbf{0}^{\circ}$. The weighting and selection of the pair of planar landmarks becomes trickier, and can sometimes lead to hazardous solutions.

To remind, the rotation computation is performed with the associated planes using lenient conditions (refer to section 6.5.1). This implies there can be some outlier associations, and the mean based method becomes inappropriate.

In these scenarios, a more sophisticated algorithm is required to choose the best candidate pair of planes for computing the undergone rotation. The presence of several candidates can be seen as an overdetermined system. Additionally, there can be wrong associations or outliers, resulting from ambiguities. This is a typical problem which can be solved using the **Optimal Candidate Selection by Consensus (OCSC)** algorithm (section 6.7.1), as applied in (section 6.7.2).

6.6.3 3D translation from three associated non parallel planar landmarks

Once the 3D rotation estimation is achieved, the next step in the transformation problem is to estimate the translation as depicted in figure 6.10.

Unlike rotation, three and not two non parallel planes are needed for the computation of the translation in 3D. The translation expressed in a MRF corresponds to its velocity vector.

In this thesis, two ways are proposed to resolve the 3D translation problem.

Two methods to compute translation

- **3D translation using planar intersection points**

  According to figure 6.10, translation $\mathbf{T}_{\mathbf{k}}^{'}$ can be computed by finding the vector between the two corresponding 3D points p_0 and p_2 at the epochs k and $k+\delta$

(equation 6.10). p_2 is the rotated observation of p_1 at $k+\delta$, using the reverse rotation indicated by $(\mathbf{R}'_{\mathbf{k}})^{-\mathbf{1}}$.

$$\mathbf{T}'_{\mathbf{k}} = \mathbf{R}'_{\mathbf{k}}(\mathbf{p_2} - \mathbf{p_0}) \tag{6.10}$$

Finding a 3D point and its association in a uniform plane is challenging. Moreover, for the reasons explained using figure 7.1, a 3D point cannot be chosen, neither from the border points, nor from the center of gravity of the extracted planar patches, as these do not correspond to the same physical points in the two observation epochs.

A way to tackle this problem has been identified in this thesis. Three non parallel planes, whose normals are linearly independent, intersect in a point which remains invariant to the motion of the mapping platform. The point of intersection can be computed by taking three plane equations expressed as given below:

$$\left.\begin{aligned} \mathbf{N^1}\rho^{\mathbf{1}} &= \mathbf{d^1} \\ \mathbf{N^2}\rho^{\mathbf{2}} &= \mathbf{d^2} \\ \mathbf{N^3}\rho^{\mathbf{3}} &= \mathbf{d^3} \end{aligned}\right\} \tag{6.11}$$

where $\mathbf{N^i}$, $\rho^{\mathbf{i}}$ and $\mathbf{d^i}$ are respectively the normal vector, a point on the plane and the offset of the plane with respect to the origin, for a plane $\mathbf{i}$. Then the intersection point $\mathbf{Q^{1,2,3}}$ can be given as:

$$\mathbf{Q^{1,2,3}} = \frac{\mathbf{d^1}(\mathbf{N^2} \otimes \mathbf{N^3}) + \mathbf{d^2}(\mathbf{N^3} \otimes \mathbf{N^1}) + \mathbf{d^3}(\mathbf{N^1} \otimes \mathbf{N^2})}{\mathbf{N^1} \odot (\mathbf{N^2} \otimes \mathbf{N^3})} \tag{6.12}$$

$\odot$ indicates the vector dot product and $\otimes$ is the vector cross product. The expression in the denominator is called the triple product of the three normals, and it is equivalent to the determinant of a 3×3 matrix with the vector normals as columns. This triple product is equal to zero when the vectors are not linearly independent, meaning the normals are coplanar. In this case the planes never intersect at a point. Therefore, this condition needs to be tested prior computing the point $\mathbf{Q^{1,2,3}}$.

- **3D translation using three linearly independent normals**

Instead of the intersection point approach, an alternative method is to use the normal vectors of the planes, and their projection on the velocity vector identified as the translation $\mathbf{T}'_{\mathbf{k}} = \mathbf{\Delta x}, \mathbf{\Delta y}$ and $\mathbf{\Delta z}$.

A plane ρ with normals $\mathbf{N} = (\mathbf{N_x}, \mathbf{N_y}, \mathbf{N_z})$, in two successive epochs k and $k+\delta$ can be expressed as:

$$\left.\begin{aligned} \mathbf{N_x}\rho_{\mathbf{xk}} + \mathbf{N_y}\rho_{\mathbf{yk}} + \mathbf{N_z}\rho_{\mathbf{zk}} + \mathbf{d}^{\rho}_{\mathbf{k}} &= \mathbf{0} \\ \mathbf{N_x}(\rho_{\mathbf{xk}} - \mathbf{\Delta x}) + \mathbf{N_y}(\rho_{\mathbf{yk}} - \mathbf{\Delta y}) + \mathbf{N_z}(\rho_{\mathbf{zk}} - \mathbf{\Delta z}) + \mathbf{d}^{\rho}_{\mathbf{k+\delta}} &= \mathbf{0} \end{aligned}\right\} \quad (6.13)$$

where $(\rho_{xk}, \rho_{yk}, \rho_{zk})$ and $((\rho_{xk} - \Delta x), (\rho_{yk} - \Delta y), (\rho_{zk} - \Delta z))$ are the same point on the plane at epochs k and $k + \delta$. $\mathbf{d}^{\rho}_{\mathbf{k}}$ and $\mathbf{d}^{\rho}_{\mathbf{k+\delta}}$ are the nearest distances to the plane ρ^t from the moving reference frame at epochs k and $k + \delta$, measured in the direction of the normal.

This can be solved by equating:

$$\mathbf{n_x}\mathbf{\Delta x} + \mathbf{n_y}\mathbf{\Delta y} + \mathbf{n_z}\mathbf{\Delta z} = (\mathbf{d}^{\rho}_{\mathbf{k+\delta}} - \mathbf{d}^{\rho}_{\mathbf{k}}) \quad (6.14)$$

In equation 6.14 there are three unknowns $(\mathbf{\Delta x}, \mathbf{\Delta y}, \mathbf{\Delta z})$. Therefore, three equations are required, which can be formed by 3 non parallel planes observed and associated between the epochs k and $k + \delta$.

Use case

- **Case: no associated three mutually non parallel planes available**

  This situation is the most likely case in manmade environments, because they have a lot of vertical facades.

  Unlike rotation, the restriction to find three non parallel planes with non coplanar normals, limits the environments where a 3D translation can be computed.

  Due to this restriction, the definition of an ideal environment with at least 3 mutually non parallel planes is no longer sustainable. A way to overcome this problem is to use an additional perception sensor which provides a global image of the scene to locate a fixed 3D point, like cameras and 3D laser scanners. By combining a camera with laser range measurements, the unknown Z translation can be efficiently solved.

  However, in the present implementation, we have just used the planar features extracted from a pair of 2D laser measurements. Therefore, the translation problem is addressed only in the 2D space, thus resolving the 5DOF pose instead of the 6DOF. To resolve the 2D pose, two non parallel planes are sufficient. The computation of 2D intersection points is explained in section 6.6.4.

6.6.4 2D translation from two associated non parallel planar landmarks

Due to the reasoning given in section 6.6.3, the translation is resolved only in 2D space.

2D translation using projected intersection points

The approach is similar to the one introduced in section 6.6.3 and is adapted to address the translation problem in 2D. The 3D planes are projected on the XY plane. Spatially invariant 2D points are computed using the intersection of the projected lines. They can be used in equation 6.10 to compute the 2D translational vector.

These processes are described using figures 6.12 to 6.14.

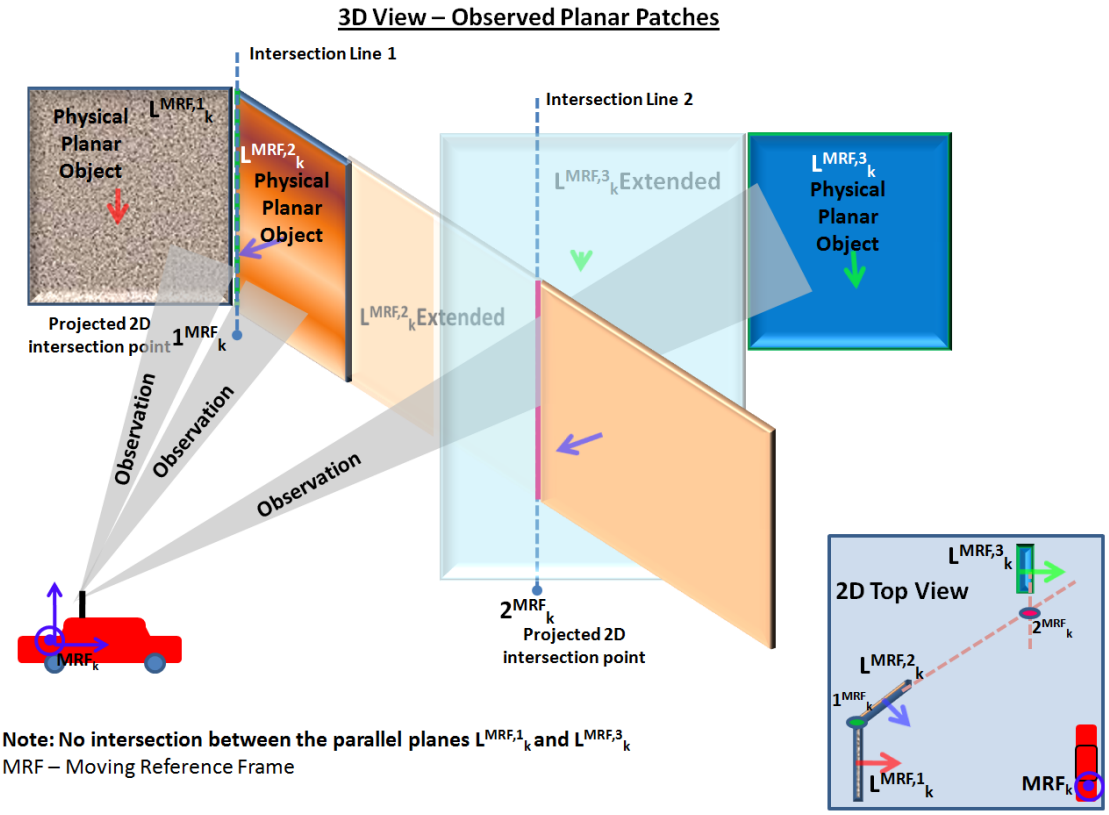

Figure 6.12: 3D and 2D views of the observed planar patches at a given epoch k. The usable 2D intersection points includes not only the physically existing (1_k^{MRF}), but also those analytically determined (2_k^{MRF}).

Consider, two planes ρ_k^i and ρ_k^j, with the normals $\mathbf{N^i} = (\mathbf{N_x^i}, \mathbf{N_y^i}, \mathbf{N_z^i})$ and $\mathbf{N^j} = (\mathbf{N_x^j}, \mathbf{N_y^j}, \mathbf{N_z^j})$, and offset distances to the origin $\mathbf{d^i}$ and $\mathbf{d^j}$. At first, each plane is projected to the XY plane. The equation of the projected two 2D lines are:

$$\left.\begin{aligned} \mathbf{N_x^i x} + \mathbf{N_y^i y} + \mathbf{d^i} = \mathbf{0} \\ \mathbf{N_x^j x} + \mathbf{N_y^j y} + \mathbf{d^j} = \mathbf{0} \end{aligned}\right\} \tag{6.15}$$

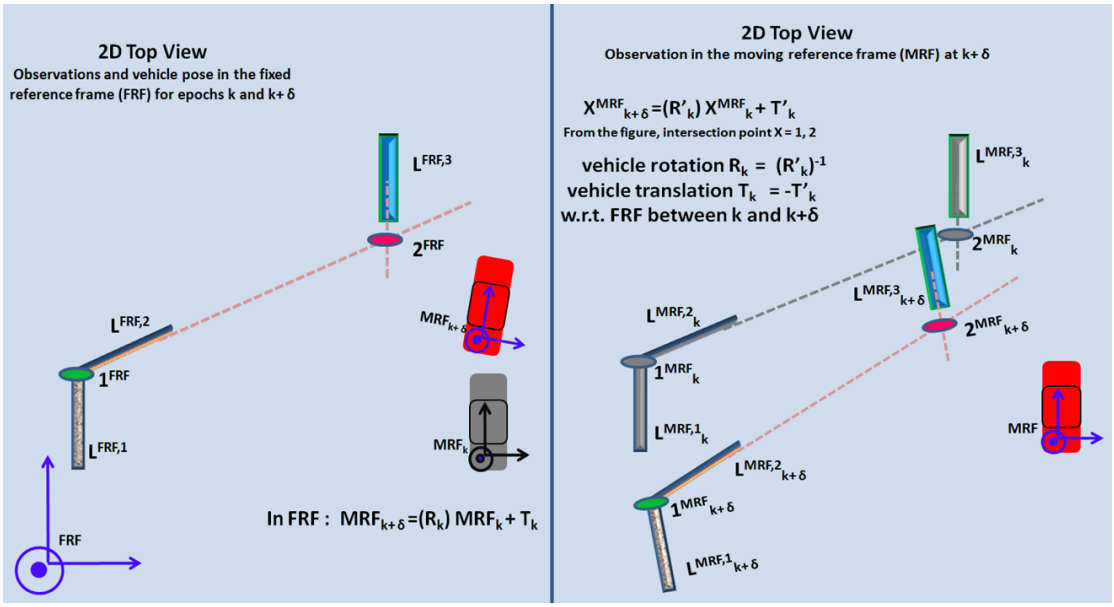

Figure 6.13: Projected planar landmarks and their intersecting points in 2D, in both fixed (FRF) and moving (MRF) reference frames, at a given epoch $k + \delta$.

The 2D intersecting point $\varpi^{\mathbf{i,j}}$ is obtained by solving equation 6.15.

$$\varpi^{\mathbf{i,j}} = \left(\frac{\mathbf{N}^{\mathbf{i}}_{\mathbf{y}}\mathbf{d}^{\mathbf{j}} - \mathbf{N}^{\mathbf{j}}_{\mathbf{y}}\mathbf{d}^{\mathbf{i}}}{\mathbf{N}^{\mathbf{i}}_{\mathbf{x}}\mathbf{N}^{\mathbf{j}}_{\mathbf{y}} - \mathbf{N}^{\mathbf{j}}_{\mathbf{x}}\mathbf{N}^{\mathbf{i}}_{\mathbf{y}}}, \frac{\mathbf{d}^{\mathbf{i}}\mathbf{N}^{\mathbf{j}}_{\mathbf{x}} - \mathbf{d}^{\mathbf{j}}\mathbf{N}^{\mathbf{i}}_{\mathbf{x}}}{\mathbf{N}^{\mathbf{i}}_{\mathbf{x}}\mathbf{N}^{\mathbf{j}}_{\mathbf{y}} - \mathbf{N}^{\mathbf{j}}_{\mathbf{x}}\mathbf{N}^{\mathbf{i}}_{\mathbf{y}}} \right) \tag{6.16}$$

Equation 6.15 is used to compute the intersection points for matching a pair of planes $\rho^{i}_{k+\delta}$ and $\rho^{j}_{k+\delta}$, denoted by $\varpi^{\mathbf{i,j}}_{\mathbf{k}+\delta}$.

$\varpi^{\mathbf{i,j}}_{\mathbf{k}+\delta}$ is compensated for the rotation around the Z axis by applying the deduced yaw (ψ) from the rotation matrix $\mathbf{R}^{'}_{\mathbf{k}}$ as shown in the equation 6.17, denoted by $\mathbf{R}(\psi)^{'}_{\mathbf{k}}$. The new point is termed as $\hat{\varpi}^{\mathbf{i,j}}_{\mathbf{k}+\delta}$.

$$\hat{\varpi}^{\mathbf{i,j}}_{\mathbf{k}+\delta} = (\mathbf{R}(\psi)^{'}_{\mathbf{k}})^{-1}\varpi^{\mathbf{i,j}}_{\mathbf{k}+\delta} \tag{6.17}$$

By using the corresponding intersection points from the two associated epochs, the translation in 2D, $\mathbf{T_k}$ is computed as:

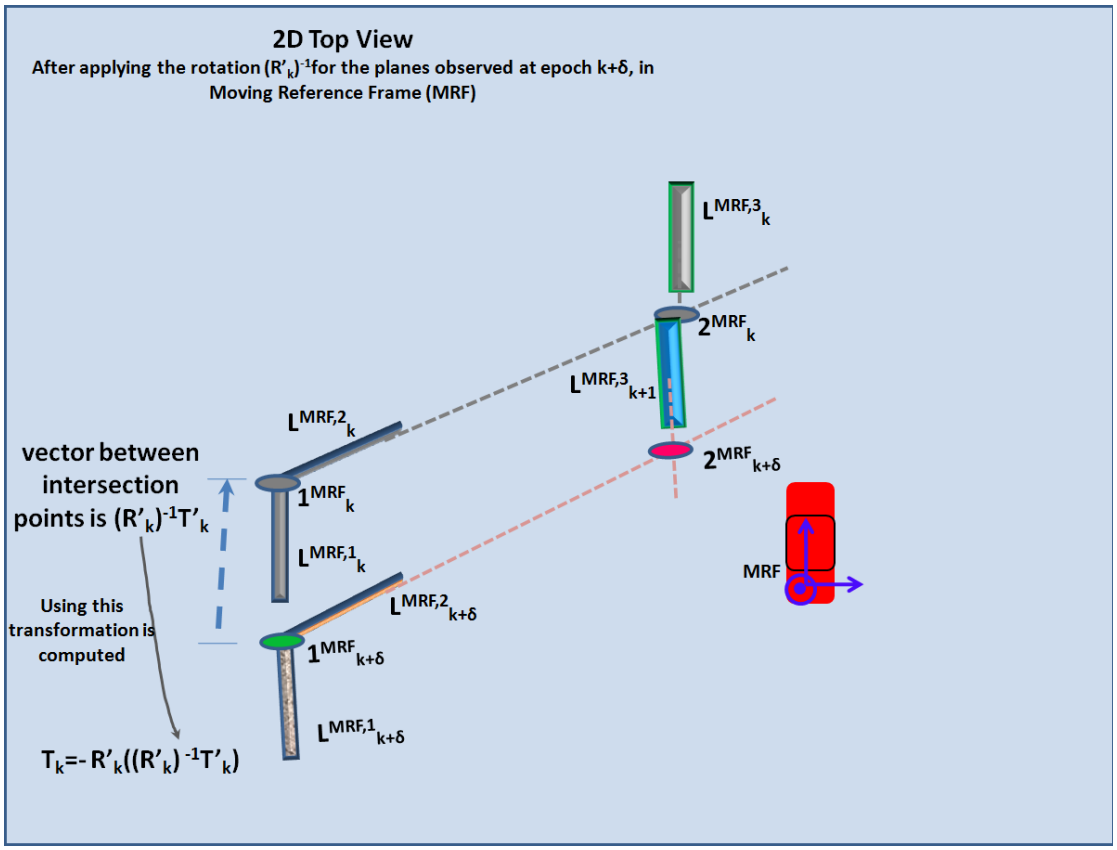

Figure 6.14: Translation computation from rotation compensated intersection points.

$$\mathbf{T_k} = -\mathbf{T'_k} = \mathbf{R}(\psi)'_{\mathbf{k}}(\varpi^{\mathbf{i,j}}_{\mathbf{k}} - \hat{\varpi}^{\mathbf{i,j}}_{\mathbf{k+\delta}}) \tag{6.18}$$

Most 2D SLAM approaches only use physically existing 2D points and corners as landmarks, but not the hypothetical points as done in this thesis. The 2D translation can be computed using any associated pair of intersecting points.

Use cases

- **Case: no associated planes available**

  Like rotation, if no planes are visible in an epoch, translation cannot be estimated, and the world is still unobservable. The long corridors in SLAM is still an open

problem. The focus of the thesis is on transformation computation in ideal environments. However, the long corridor problems may be addressed using both the infinity measures, as well as the landmarks, along with additional pose sensors, like odometer and IMU/INS.

If there are associated planes, the translation vector can be determined either in 1D or 2D, depending upon the number of associated planes and the direction of motion (translation parallel to the plane cannot be detected). The DA can be performed in a map as mentioned in section 6.6.2. The translation computation can be done by the method of normals given in section 6.6.3, which works with even a single associated plane, where as the intersection point approach requires a pair of associated planes.

In this thesis, the 2D translation is addressed using the ideal 3D environments for obtaining an independent pose solution.

- **Case: one or more associated non parallel planes**

If there is only one pair of non parallel planes, the 2D translation algorithm given in section 6.6.4 can be applied directly.

However, if there is more than one pair, then the case is similar to the one explained in section 6.6.2. An approach is to compute the mean translation of the solutions obtained from each associated pair of intersection points. This solution can be preferred for translation computation in comparison to the mean rotation computation, because the outlier associations can be removed by SDA (section 6.5.2) once the rotation is compensated.

However, if there is any false detection of associations, the mean-based method still generates a biased result. In this case too, the **Optimal Candidate Selection by Consensus (OCSC) algorithm** given in section 6.7.1, can be applied for computing the optimal translation (section 6.7.3) to overcome the remaining ambiguous associations (outliers).

6.7 Transformation from multiple associations

From the description of transformation estimation given in section 6.6, only a pair of non parallel associated planes are sufficient to compute transformation of 5DOF (3DOF rotation and 2DOF translation). However, in the cluttered environments there are several landmarks, and therefore several association solutions. As mentioned in sections 6.6.2 and 6.6.4, there are two alternatives to address this issue: one, to compute the mean of the transformation solutions from each associated nonparallel planes, and the second is to chose an association which estimates best the undergone transformation. We term this process as **optimal candidate selection**.

Mean-based methods can reduce noise in the estimation, however it produces biased results in the presence of outliers. As already mentioned, in the D&C approach, rotation is computed from the leniently associated planar landmarks, and therefore subject to some outlier candidate associations. In this case, the **optimal candidate selection** approach becomes a preferred alternative. However, for the translation computation performed after an SDA, a mean-based method can be applied. We present a method to compute the mean translation vector using **center of gravities (cog)** of the associated intersection points.

In this thesis, to choose the *optimal candidate selection*, we designed and implemented a new algorithm called as **Optimal Candidate Selection by Consensus (OCSC)**. We resolve rotation using this algorithm and also apply it as an alternative to compute translation. As we demonstrate with our results, in many cases the SDA is redundant if we apply the OCSC approach, since it handles quite efficiently the outliers. However, the *stringent ambiguity reduction* step and the *appearance test* in the SDA can still be used prior OCSC-based translation to ensure the minimization of outliers.

We present these two alternatives in the order of their application to the transformation computation, that is rotation first, and then the translation. Therefore, we start by providing the theory of OCSC and its weighted variant WOCSC. The algorithm in its general form can be applied to solve any overdetermined system problem. We apply these algorithms to compute the optimal rotation and translation, which is chosen based on a consensus process. Since the true transformation is unknown, and no estimation models are used, we have to rely on the observed measurements. Therefore, the candidate transformation which best suits the ensemble of observations is considered as the optimal one, and it is implemented. Improvements to this solution are to add a transformation candidate based on a model (using external pose sensors), or to generate a sampled set of candidates from the obtained optimal one, as done in particle filters.

After the OCSC, finally, the cog-based translation is explained.

6.7.1 Optimal candidate selection algorithms

The algorithms, OCSC/WOCSC are inspired by the Expectation Maximization (EM) ([Dempster 77] and [Moon 96]) and the RANdom SAmple Consensus (RANSAC) [Fischler 81] algorithms. There are two steps similar to EM: an Expectation step and a Maximization step. However, instead of a simple maximization, a consensus step similar to RANSAC is introduced, to democratically choose a best candidate solution by consulting all other candidate solutions. This step eliminates outliers, deals with noisy candidates and resolves ambiguities. Unlike RANSAC, there is no random sampling of the population nor a predetermined model to which the candidates have to be agreed. The samples are already provided in the form of candidates by an expectation generation step (similar to EM). The Weighted OCSC (WOCSC) algorithm

introduces a weighting for the consensus step, where each candidate casts a weighted normalized vote.

In the scope of this thesis, these algorithms refine the results of the DA. Solving the problem with consensus helps to overcome the typical failures of any least squares error methods when subjected to outliers.

Optimal Candidate Selection by Consensus (OCSC)

To demonstrate the algorithm, let us take an example of a varying population $\mathbf{S_k}$ with respect to a discrete time $\mathbf{k}$, observed by a set of samples $\mathbf{X_k} = \{(\mathbf{x_k^i})|\mathbf{i} = \mathbf{1}\dots\mathbf{p}\}$. The population is considered invariant for the short instant $\mathbf{k}$ where each $\mathbf{x_k^i} \in \mathbf{X_k}$ is observed.

Let us consider an operand $\mathbf{K_k}$ and an operator $\bigtriangledown$, which transforms $\mathbf{S_k}$ to $\mathbf{S_{k+1}}$ (this includes the observations $\mathbf{X_k}$).

$$\mathbf{S_{k+1}} = \mathbf{K_k} \bigtriangledown \mathbf{S_k} \Rightarrow \forall \mathbf{i} \in \{1\dots p\}, \mathbf{x_{k+1}^i} = \mathbf{K_k} \bigtriangledown \mathbf{x_k^i} \tag{6.19}$$

In order to determine the operand $\mathbf{K_k}$ (depending on its degree of freedom), two subsets of the corresponding (or associated) members of $\mathbf{S_k}$ and $\mathbf{S_{k+1}}$ of size ω are needed. However, not all candidates are observed and not all of them are applicable. $\mathbf{C^\star_{k,k+1}}$ is the super candidate list of these combinations from the population with $\binom{\mathbf{p}}{\omega}$ elements.

Therefore, a constrained set of observed candidates $\hat{\mathbf{C}}_{\mathbf{k,k+1}}$ is constructed using the associated subsets $\mathbf{c^j_{k,k+1}}$, with cardinality ω, chosen from the sets $\mathbf{X_k}$ and $\mathbf{X_{k+1}}$, defined in equation 6.20.

$$\hat{\mathbf{C}}_{\mathbf{k,k+1}} = \{\mathbf{c^j_{k,k+1}}|j = 1\dots n\} \subset \mathbf{C^\star_{k,k+1}} \tag{6.20}$$

Each $\mathbf{c^j_{k,k+1}}$ is sufficient to compute the operand $\mathbf{K_k}$, denoted as $\mathbf{K_k^j}$. However, the observations are prone to noise, and associations are prone to ambiguities, requiring an optimization step to choose the optimal estimate of $\mathbf{K_k}$.

The optimization problem at instant $\mathbf{k+1}$ is to identify the optimal estimate of the operand $\mathbf{K_k}$, denoted by $\mathbf{K_k^\star}$, amongst all $\mathbf{K_k^j}$. This also indicates the best candidate $\mathbf{c^j_{k,k+1}}$.

$$\hat{\mathbf{C}}_{\mathbf{k,k+1}} \mapsto \mathbf{K_k} = \{\mathbf{c}^{\mathbf{j}}_{\mathbf{k,k+1}} \mapsto \mathbf{K}^{\mathbf{j}}_{\mathbf{k}} | j = \{1 \dots n\}\} \tag{6.21}$$

$$\mathbf{K}^{\star}_{\mathbf{k}} = \underset{\mathbf{c}^{\mathbf{j}}_{\mathbf{k,k+1}} \mapsto \mathbf{K}^{\mathbf{j}}_{\mathbf{k}}}{\arg\min} \sum_{i} ||(\mathbf{K}^{\mathbf{j}}_{\mathbf{k}} \bigtriangledown \mathbf{x}^{\mathbf{i}}_{\mathbf{k}}) - \mathbf{x}^{\mathbf{i}}_{\mathbf{k+1}}|| \tag{6.22}$$

This optimization problem has two steps, an **Expectation step** and a **Consensus step**, repeated for each candidate.

- **Expectation step**
  In the expectation step, the corresponding operators $\mathbf{K}^{\mathbf{j}}_{\mathbf{k}}$ are mapped by generating an expected solution for the transfer operand $\mathbf{K_k}$, using each candidate $\mathbf{c}^{\mathbf{j}}_{\mathbf{k,k+1}}$, as given in equation 6.21.

- **Consensus step**
  The maximization (or minimization) step is done based on consensus. Each associated sample from the population $\mathbf{x}^{\mathbf{i}}_{\mathbf{k}}$, present in the set $\hat{\mathbf{C}}_{\mathbf{k,k+1}}$, is mapped to its corresponding $\mathbf{x}^{\mathbf{i}}_{\mathbf{k+1}}$ using the selected operand in the expectation step $\mathbf{K}^{\mathbf{j}}_{\mathbf{k}}$. The operand that best fits the relation between the observed samples at the instants $\mathbf{k}$ and $\mathbf{k+1}$, as per the equation 6.22, is considered to be the optimal solution for the problem.

Weighted Optimal Candidate Selection by Consensus (WOCSC)

WOCSC improves the OCSC algorithm by applying a normalized weight to the consensus. A robust weighting helps to overcome scenarios with 50% or more outliers.

- **Generating a normalized weight**

  The observations $\mathbf{x^i}$ normally come with a confidence $\lambda^{\mathbf{i}}$ in the process, used as a weight in the consensus step.

  However, $\lambda^{\mathbf{i}}$ needs to be normalized and consistently chosen from a distribution of all the observations from $\mathbf{k}$ and $\mathbf{k+1}$. Therefore, a combined set of ranked confidences $\mathbf{\Lambda_{k,k+1}}$ is required (equation 6.23).

$$\left.\begin{aligned} \mathbf{X_k} \mapsto \lambda_{\mathbf{k}} &= \{(\mathbf{x}^{\mathbf{i}}_{\mathbf{k}} \mapsto \lambda^{\mathbf{i}}_{\mathbf{k}}) | \mathbf{i} = \{\mathbf{1} \dots \mathbf{p}\} \\ \mathbf{X_{k+1}} \mapsto \lambda_{\mathbf{k+1}} &= \{(\mathbf{x}^{\mathbf{i}}_{\mathbf{k+1}} \mapsto \lambda^{\mathbf{i}}_{\mathbf{k+1}}) | \mathbf{i} = \{\mathbf{1} \dots \mathbf{p}\} \\ \mathbf{\Lambda_{k,k+1}} &= \lambda_{\mathbf{k}} \cup \lambda_{\mathbf{k+1}} \end{aligned}\right\} \tag{6.23}$$

This union operation is a concatenation rather than a set union, indicating that the order within the sets is preserved after the union. This is achieved by using a unique index for each record.

$$\left.\begin{aligned} \mathbf{\Lambda_k} &= \{(\mathbf{\Lambda_k^{\iota}} = \{(\lambda_{\mathbf{k}}^{\mathbf{i}}, \iota))|\mathbf{i} = \iota = \{\mathbf{1} \dots \mathbf{p}\}\} \\ \mathbf{\Lambda_{k+1}} = \{(\mathbf{\Lambda_{k+1}^{\vartheta}} &= \{(\lambda_{\mathbf{k+1}}^{\mathbf{i}}, \vartheta))|\mathbf{i} = \{\mathbf{1} \dots \mathbf{p}\} \wedge \vartheta = \{\mathbf{p+1} \dots \mathbf{2p}\}\} \\ \mathbf{\Lambda_{k,k+1}} &= \mathbf{\Lambda_k} \cup \mathbf{\Lambda_{k+1}} \end{aligned}\right\} \quad (6.24)$$

In order to produce a weight from the combined normalized distribution, the first step is to sort the records of $\mathbf{\Lambda_{k,k+1}}$ based on their λ values.

Based on the ranking, the normalized weights $\mathbf{W} = \{(w_\kappa)|\kappa \leq 2p\}$ are produced. κ can be smaller than cardinality of the set $\mathbf{\Lambda_{k,k+1}}$ because the elements with the same λ values have the same weight w_κ. The weights are normalized so that $\sum_\kappa \mathbf{w}_\kappa = \mathbf{1}$.

The ranking is inversely proportional to the confidence, meaning the sample with the highest confidence has smallest weight and vice versa, because the weights are used in a *minimization optimization function* given in equation 6.22. An operator $\bowtie$ is defined to facilitate the consensus process where a maximization step is used instead of minimization. If applied, the weights are directly proportional to their confidence, yet retaining the normalization.

The rankings are mapped back to the corresponding sample observations from the epochs $\mathbf{k}$ and $\mathbf{k+1}$ using the indices ι and ϑ given in equation 6.24.

- **Modified consensus process**

The consensus step takes into account the computed weights as given in the equation 6.25.

$$\mathbf{K_k^{\star}} = \underset{\mathbf{c_{k,k+1}^j} \mapsto \mathbf{K_k^j}}{\arg\min} \sum_i ||((\mathbf{K_k^j} \bigtriangledown \mathbf{x_k^i}) - \mathbf{x_{k+1}^i})||(\mathbf{w_k^i} \cdot \mathbf{w_{k+1}^i}) \quad (6.25)$$

where $\mathbf{w_k^i}$ and $\mathbf{w_{k+1}^i}$ are the weights of the samples $\mathbf{x_k^i}$ and $\mathbf{x_{k+1}^i}$ respectively. The expectation step remains the same as in the OCSC algorithm.

6.7.2 Rotation resolution using WOCSC algorithm

As already mentioned, rotation is computed from the correlated quadruple set $\hat{\mathbf{C}}_{\mathbf{k,k+\delta}}^{\mathbf{3}}$, generated using the LDA in section 6.5.1. If the cardinality of the set $|\hat{\mathbf{C}}_{\mathbf{k,k+\delta}}^{\mathbf{3}}| > \mathbf{1}$, the system is overdetermined and there are several candidates to compute the transformation. However, these associations can have ambiguities, as the associations are

performed using lenient relationship constraints. Therefore, the WOCSC algorithm (given in section 6.7.1) is applied to compute the rotation. WOCSC is preferred over simple OCSC, since there is a confidence indicator **CPEF** (computed in section 5.4.3) for each measured planes, giving an edge to remove outlier associations.

In the expectation step, rotation candidate is generated using the algorithms given in section 6.6.2. The computed rotation candidate is applied to align all associated pair of planes. The candidate rotation, which optimally aligns all of them is considered as the optimal rotation. The associated pair of planes generating this rotation is the optimal candidate association.

In order to resolve the rotation problem using the WOCSC algorithm, the following analogies are drawn with the algorithm explained in section 6.7.1. The input is the candidate set $\hat{\mathbf{C}}_{\mathbf{k},\mathbf{k}+\delta} = \hat{\mathbf{C}}^{\mathbf{3}}_{\mathbf{k},\mathbf{k}+\delta}$ (with $\mathbf{k}+\mathbf{1}$ replaced by $\mathbf{k}+\delta$, providing option for shift between epochs) composed of records $\mathbf{c}^{\mathbf{j}}_{\mathbf{k},\mathbf{k}+\delta}$, containing 2 pairs of planes from epochs $\mathbf{k}$ and $\mathbf{k}+\delta$, correlated through the LDA process (equation 6.26).

$$\begin{aligned}\hat{\mathbf{C}}_{\mathbf{k},\mathbf{k}+\delta} = \{\mathbf{c}^{\mathbf{j}}_{\mathbf{k},\mathbf{k}+\delta} = ((\rho^{\mathbf{i1}}_{\mathbf{k}}, \rho^{\mathbf{i2}}_{\mathbf{k}}, \rho^{\mathbf{i1}}_{\mathbf{k}+\delta}, \rho^{\mathbf{i2}}_{\mathbf{k}+\delta}))|(i1 \neq i2) \wedge (i1 \in \{1 \dots n\}) \\ \wedge (i2 \in \{1 \dots n\}) \wedge (\rho^{i1}_{k} \nparallel \rho^{i2}_{k}) \wedge (\rho^{i1}_{k+\delta} \nparallel \rho^{i2}_{k+\delta}))\}\end{aligned} \tag{6.26}$$

The transfer operand $\mathbf{K_k}$ is equivalent to the rotation matrix $\mathbf{R}^{'}_{\mathbf{k}}$ of equation 6.7. Operator $\bigtriangledown$ is a matrix and vector multiplication.

Since the true $\mathbf{K_k}$ is never observed, the goal of the algorithm is to obtain an optimal estimate. Thus $\mathbf{K}^{\star}_{\mathbf{k}}$ (in equation 6.22) is treated as the $\mathbf{R}^{'}_{\mathbf{k}}$. The WOCSC algorithm steps are given below.

- **Weight normalization step** According to equation 6.19, the planes used in the consensus step are observed at 2 epochs. Only the plane population which has been data associated is used for generating the weights. Thus all the individual planes for the epoch $\mathbf{k}$ and $\mathbf{k}+\delta$ are selected from the candidate set $\hat{\mathbf{C}}_{\mathbf{k},\mathbf{k}+\delta}$. A plane $\rho^{\mathbf{t}}$ can be present in more than one record $\mathbf{c}^{\mathbf{j}}_{\mathbf{k},\mathbf{k+1}}$ of the candidate set as a part of different nonparallel plane combinations, but it is used only once in the ranking process.

  The confidence indicator λ is taken from the **CPEF** value of each individual plane and normalized.

- **Expectation step**
  The rotation matrix estimate is computed by using each record $\mathbf{c}^{\mathbf{j}}_{\mathbf{k},\mathbf{k}+\delta}$. Each plane's normal vector is used in equation 6.6, for computing the matrices $\mathbf{U_k}$ and $\mathbf{U}_{\mathbf{k}+\delta}$, and the candidate $\mathbf{R}^{\mathbf{j}}_{\mathbf{k}}$ using equation 6.7.

- **Consensus step**
  All the member planes of the candidate set $\hat{\mathbf{C}}_{\mathbf{k},\mathbf{k}+\delta}$ vote to find the optimal rotation solution $\mathbf{R}_{\mathbf{k}}^{'}$.

  In order to simplify the arithmetics, a maximization step is used instead of the minimization equation 6.22. The weights for the maximization process are obtained through the $\bowtie$ operator (defined in section 6.7.1), which provides the normalized weights in reverse order, i.e. the higher the weight, the higher the confidence.

  The maximization condition is based on the scalar product between the normal vectors of the planes. The normal $\mathbf{N}_{\mathbf{k}+\delta}^{\mathbf{t}}$ of the plane $\rho_{\mathbf{k}+\delta}^{\mathbf{t}}$ is estimated by applying the candidate rotation matrix $\mathbf{R}_{\mathbf{k}}^{\mathbf{j}}$ to the normal $\mathbf{N}_{\mathbf{k}}^{\mathbf{t}}$ of the plane $\rho_{\mathbf{k}}^{\mathbf{t}}$. The quality of the computed $\mathbf{R}_{\mathbf{k}}^{\mathbf{j}}$ and the consent of the plane $\rho_{\mathbf{k}}^{\mathbf{t}}$ to the rotation parameters can be estimated by $\mathbf{\Delta}_{\mathbf{k},\mathbf{k}+\delta}^{\mathbf{t}}$, an indicator for the closeness to parallelism between $\rho_{\mathbf{k}+\delta}^{\mathbf{t}}$ and the rotated $\rho_{\mathbf{k}}^{\mathbf{t}}$.

$$\left.\begin{aligned} \hat{\mathbf{N}}_{\mathbf{k}}^{\mathbf{t}} &= \mathbf{R}_{\mathbf{k}}^{\mathbf{j}} \mathbf{N}_{\mathbf{k}}^{\mathbf{t}} \\ \mathbf{\Delta}_{\mathbf{k},\mathbf{k}+\delta}^{\mathbf{t}} &= \frac{\hat{\mathbf{N}}_{\mathbf{k}}^{\mathbf{t}} \odot \mathbf{N}_{\mathbf{k}+\delta}^{\mathbf{t}}}{||\hat{\mathbf{N}}_{\mathbf{k}}^{\mathbf{t}}||\ ||\mathbf{N}_{\mathbf{k}+\delta}^{\mathbf{t}}||} \end{aligned}\right\} \tag{6.27}$$

  As the absolute of the vector dot product $\odot$ for the normalized vectors yields a value in $[0, 1]$, if a plane $\rho^{\mathbf{t}}$ agrees with the rotation matrix $\mathbf{R}_{\mathbf{k}}^{\mathbf{j}}$, then $\mathbf{\Delta}_{\mathbf{k},\mathbf{k}+\delta}^{\mathbf{t}} = 1$, indicating a full vote.

  Therefore, the final optimization based consensus equation can be written as in equation 6.28.

$$\mathbf{R}_{\mathbf{k}}^{'} = \underset{\mathbf{c}_{\mathbf{k},\mathbf{k}+\delta}^{\mathbf{j}} \mapsto \mathbf{R}_{\mathbf{k}}^{\mathbf{j}}}{\arg\max} \sum_{t} |\mathbf{\Delta}_{\mathbf{k},\mathbf{k}+\delta}^{\mathbf{t}}| (\bowtie \mathbf{w}_{\mathbf{k}}^{\mathbf{t}})(\bowtie \mathbf{w}_{\mathbf{k}+\delta}^{\mathbf{t}}) \tag{6.28}$$

  where $\mathbf{w}_{\mathbf{k}}^{\mathbf{t}}$ and $\mathbf{w}_{\mathbf{k}+\delta}^{\mathbf{t}}$ are the weights for the plane $\rho^{\mathbf{t}}$.

- **Rotation confidence estimation**

  If a rotation parameter is computed between two planes **i1** and **i2** from two epochs $\mathbf{k}$ and $\mathbf{k}+\delta$, the trust indicator for the rotation operation is computed by multiplying the normalized **CPEF** values of the pairs of planes at each epoch, i.e. $\mathbf{CPEF}_{\mathbf{k}}^{\mathbf{i1}}$, $\mathbf{CPEF}_{\mathbf{k}}^{\mathbf{i2}}$, $\mathbf{CPEF}_{\mathbf{k}+\delta}^{\mathbf{i1}}$ and $\mathbf{CPEF}_{\mathbf{k}+\delta}^{\mathbf{i2}}$.

  Before doing so, an additional independent confidence indicator is generated, based on the angles between the planes. A linear weight function $\mathbf{w}^{\mathbf{a(i1,i2)}}$ is used, which varies from 0 to 1 for the angles $[0°, 90°]$ correspondingly. This indicator is used because the rotation estimate computed between two planes close to orthogonal is less effected by noise, compared to two planes which are almost parallel.

The final confidence is given in equation 6.29.

$$\mathbf{CPEF}^{\mathbf{i1,i2}}_{\mathbf{k,k+\delta}} = \mathbf{CPEF}^{\mathbf{i1}}_{\mathbf{k}} \cdot \mathbf{CPEF}^{\mathbf{i2}}_{\mathbf{k}} \cdot \mathbf{CPEF}^{\mathbf{i1}}_{\mathbf{k+\delta}} \cdot \mathbf{CPEF}^{\mathbf{i2}}_{\mathbf{k+\delta}} \cdot \mathbf{w}^{\mathbf{a(i1,i2)}} \tag{6.29}$$

6.7.3 Translation resolution using WOCSC algorithm

Similar to rotation, even translation can be resolved by applying the WOCSC algorithm. The input $\hat{\mathbf{C}}_{\mathbf{k,k+\delta}}$ can be the quadruple set $\hat{\mathbf{C}}^{\mathbf{3}}_{\mathbf{k,k+\delta}}$ generated using the LDA (section 6.5.1), or the sets $\hat{\mathbf{C}}^{\mathbf{4}}_{\mathbf{k,k+\delta}}$ or $\hat{\mathbf{C}}^{\mathbf{5}}_{\mathbf{k,k+\delta}}$ generated from SDA (section 6.5.2). In our experimentations all of them produced similar results. However, using the set $\hat{\mathbf{C}}^{\mathbf{4}}_{\mathbf{k,k+\delta}}$ along with the *appearance test* (refer to section 6.5.2) is recommended, since they eliminate remaining ambiguities using ambiguity reduction process.

In the expectation step, translation candidate is generated using the algorithms given in section 6.6.4. The computed translation candidate, once applied, overlays the intersection points, computed from the associated pair of planes between the associated epochs. The candidate, which optimally overlays all the associated intersection points is considered as the optimal translation; and the associated pair, that generated the candidate, is the optimal association.

The correlated set $\hat{\mathbf{C}}_{\mathbf{k,k+\delta}}$ is given as an input for the algorithm given in section 6.6.4, to compute the intersection points $\varpi^{\mathbf{i,j}}_{\mathbf{k}}$ and $\hat{\varpi}^{\mathbf{i,j}}_{\mathbf{k+\delta}}$ (equations 6.15 and 6.17 respectively), for each pair of nonparallel planes at epochs $\mathbf{k}$ and $\mathbf{k}+\delta$. The set $\varpi_{\mathbf{k,k+\delta}}$ contains all the sets of intersection points for each quadruple $\mathbf{c}^{\mathbf{j}}_{\mathbf{k,k+\delta}}$ of the set $\hat{\mathbf{C}}_{\mathbf{k,k+\delta}}$. For notational purposes, $\varpi^{\mathbf{t}}_{\mathbf{k,k+\delta}}$ corresponds to the intersection points $(\varpi^{\mathbf{i,j}}_{\mathbf{k}}, \hat{\varpi}^{\mathbf{i,j}}_{\mathbf{k+\delta}})$ of the matched plane pairs, for the record $\mathbf{c}^{\mathbf{t}}_{\mathbf{k,k+\delta}}$ with index t of the set $\hat{\mathbf{C}}_{\mathbf{k,k+\delta}}$. Each $\varpi^{\mathbf{t}}_{\mathbf{k,k+\delta}} \in \varpi_{\mathbf{k,k+\delta}}$ can compute a translational vector.

Like in rotation, even for this algorithm $\omega = 2$; this indicates that a pair of planes is selected from the observation samples. The transfer operand $\mathbf{K_k}$ is treated equivalently to the rotated translation vector $\hat{\mathbf{T}}'_{\mathbf{k}} = (\mathbf{R}'_{\mathbf{k}})^{-\mathbf{1}}\mathbf{T}'_{\mathbf{k}}$ from equation 6.18. The operator $\bigtriangledown$ is the vector addition of the two intersection point vectors in MRF.

Since the true $\mathbf{K_k} = \mathbf{T_k}$ is never observed, the goal of the algorithm is to obtain an optimal estimate. Therefore, the optimal $\mathbf{K}^{\star}_{\mathbf{k}}$ estimate (in equation 6.22), is treated as $\hat{\mathbf{T}}'_{\mathbf{k}}$. The WOCSC algorithm steps are given below.

- **Weight normalization step**
  This is performed identically to the process applied for the rotation, explained in section 6.7.2.

- **Expectation step**
  The translation vector is computed using each $\varpi^{\mathbf{j}}_{\mathbf{k},\mathbf{k}+\delta}$ of the set $\varpi_{\mathbf{k},\mathbf{k}+\delta}$. The candidate translation vector $\mathbf{T}^{\mathbf{j}}_{\mathbf{k}}$ is computed, for the record $\mathbf{j}$ as shown in equation 6.30.

$$\mathbf{T}^{\mathbf{j}}_{\mathbf{k}} = \hat{\varpi}^{\mathbf{j}}_{\mathbf{k}+\delta} - \varpi^{\mathbf{j}}_{\mathbf{k}} \tag{6.30}$$

  The rotated intersection point $\hat{\varpi}^{\mathbf{j}}_{\mathbf{k}+\delta}$ is computed as per equation 6.17.

- **Consensus step**
  Each candidate intersection point casts a vote based on its consensus to the computed candidate translation $\mathbf{T}^{\mathbf{j}}_{\mathbf{k}}$, to find the optimal translation solution $\mathbf{T}^{'}_{\mathbf{k}}$.

  The minimization condition is constructed based on a summation relation as given in equation 6.31.

$$\hat{\mathbf{T}}^{'}_{\mathbf{k}} = \underset{\mathbf{c}^{\mathbf{j}}_{\mathbf{k},\mathbf{k}+\delta} \mapsto \mathbf{T}^{\mathbf{j}}_{\mathbf{k}}}{\arg\min} \sum_{t=1}^{n} ||(\hat{\varpi}^{t}_{k+\delta} - (\varpi^{t}_{k} + \mathbf{T}^{\mathbf{j}}_{\mathbf{k}}))||(\mathbf{w}^{\mathbf{t}}_{\mathbf{k}})(\mathbf{w}^{\mathbf{t}}_{\mathbf{k}+\delta}) \tag{6.31}$$

  where $\mathbf{w}^{\mathbf{t}}_{\mathbf{k}}$ and $\mathbf{w}^{\mathbf{t}}_{\mathbf{k}+\delta}$ are the weights of the planes $\rho^{\mathbf{i}}$ and $\rho^{\mathbf{j}}$ for which the intersection point in the record $\mathbf{t}$ is computed. Finally translation vector in MRF, $\mathbf{T}_{\mathbf{k}} = -\mathbf{T}^{'}_{\mathbf{k}} = -\mathbf{R}^{'}_{\mathbf{k}}\hat{\mathbf{T}}^{'}_{\mathbf{k}}$ is deduced.

- **Translation confidence estimation**

  If the translation parameter is computed using the WOCSC algorithm between two planes **i1** and **i2** at two successive epochs $\mathbf{k}$ and $\mathbf{k}+\delta$, its trust indicator is computed by multiplying the normalized **CPEF** values as:

$$\mathbf{CPEF}^{\mathbf{i1},\mathbf{i2}}_{\mathbf{k},\mathbf{k}+\delta} = \mathbf{CPEF}^{\mathbf{i1}}_{\mathbf{k}} \cdot \mathbf{CPEF}^{\mathbf{i2}}_{\mathbf{k}} \cdot \mathbf{CPEF}^{\mathbf{i1}}_{\mathbf{k}+\delta} \cdot \mathbf{CPEF}^{\mathbf{i2}}_{\mathbf{k}+\delta} \tag{6.32}$$

6.7.4 Translation resolution using center of gravity

This approach, computes the mean translation of the translation solutions computed from all the pairs of associated intersection points. Therefore, it minimizes the noise by averaging it out. However, the method is sensitive to ambiguous correlations which can result in a biased translation. Therefore, it is essential to resolve all association conflicts, using methods similar to the one given in section 6.5.2, prior to applying this method. The sensitivity to outliers is the shortcoming of all the mean or least square

based algorithms. The input to the algorithm is the correlated quadruple set $\hat{\mathbf{C}}^{\mathbf{5}}_{\mathbf{k},\mathbf{k}+\delta}$ generated from SDA (section 6.5.2).

The center of gravity ($\mathbf{cog_t}$) of all the intersection points $\varpi^{\mathbf{i,j}}_{\mathbf{t}}$ (where $\mathbf{i} \neq \mathbf{j}$, $\mathbf{t} = \mathbf{k}$ and $\mathbf{k}+\delta$, $\mathbf{i} \in \{\mathbf{1} \dots \mathbf{n}\}$ and $\mathbf{j} \in \{\mathbf{1} \dots \mathbf{n}\}$) are the plane identifiers for the plane pairs $(\rho^{\mathbf{i}}, \rho^{\mathbf{j}})$, is computed as:

$$\mathbf{cog_t} = \frac{\sum_{N_\varpi} \mathbf{CPEF}^{\mathbf{i,j}}_{\mathbf{t}} \varpi^{\mathbf{i,j}}_{\mathbf{t}}}{\sum_{N_\varpi} \mathbf{CPEF}^{\mathbf{i,j}}_{\mathbf{t}}} \tag{6.33}$$

where N_ϖ is the number of intersection points, $\mathbf{CPEF}^{\mathbf{i,j}}_{\mathbf{k}} \in [0,1] = \mathbf{CPEF}^{\mathbf{i}}_{\mathbf{k}} \cdot \mathbf{CPEF}^{\mathbf{j}}_{\mathbf{k}}$. The planes from epoch $\mathbf{k}+\delta$ are compensated for the rotation, resulting in rotated intersection point $\hat{\varpi}^{\mathbf{j}}_{\mathbf{k}+\delta}$, computed as per equation 6.17.

This approach is demonstrated using figure 6.15.

The rotated translation vector $\hat{\mathbf{T}}'_{\mathbf{k}}$ between $\mathbf{cog}_{\mathbf{k}+\delta}$ and $\mathbf{cog_k}$ is computed by equation 6.34, with its relation to the translation of the vehicle $\mathbf{T_k}$ in MRF.

$$\hat{\mathbf{T}}'_{\mathbf{k}} = \mathbf{cog}_{\mathbf{k}+\delta} - \mathbf{cog_k} \tag{6.34}$$

$$\mathbf{T_k} = -\mathbf{T}'_{\mathbf{k}} = -\mathbf{R}'_{\mathbf{k}} \hat{\mathbf{T}}'_{\mathbf{k}} \tag{6.35}$$

- **Translation confidence estimation**

  Using the CG method with a constant weight, each pair of corresponding intersecting points $(\varpi^{\mathbf{i,j}}_{\mathbf{k}}, \hat{\varpi}^{\mathbf{i,j}}_{\mathbf{k}+\delta})$ contributes equally to the translation parameters. The trust in the translation parameters depends on the trust indicators given at each epoch, for each plane pair that computed the intersecting points. The trust indicator of a pair of intersecting points is obtained by multiplying, the **CPEF** values of the planes **i1** and **i2** at two associated epochs $\mathbf{k}$ and $\mathbf{k}+\delta$.

$$\mathbf{CPEF}^{\mathbf{i1,i2}}_{\mathbf{k},\mathbf{k}+\delta} = \mathbf{CPEF}^{\mathbf{i1}}_{\mathbf{k}} \cdot \mathbf{CPEF}^{\mathbf{i2}}_{\mathbf{k}} \cdot \mathbf{CPEF}^{\mathbf{i1}}_{\mathbf{k}+\delta} \cdot \mathbf{CPEF}^{\mathbf{i2}}_{\mathbf{k}+\delta} \tag{6.36}$$

  The final trust indicator **CPEF** is computed by taking the average of the $\mathbf{CPEF}^{\mathbf{i1,i2}}_{\mathbf{k},\mathbf{k}+\delta}$ of all the corresponding $\mathbf{N}_\varpi$ interesting points $(\varpi^{\mathbf{i,j}}_{\mathbf{k}}, \hat{\varpi}^{\mathbf{i,j}}_{\mathbf{k}+\delta})$ as:

$$\mathbf{CPEF}^{\mathbf{Trans}}_{\mathbf{k},\mathbf{k}+\delta} = \frac{\sum_{i=1}^{i=\mathbf{N}^\varpi} \mathbf{CPEF}^{\mathbf{i1,i2}}_{(\mathbf{k},\mathbf{k}+\delta)_i}}{\mathbf{N}^\varpi} \tag{6.37}$$

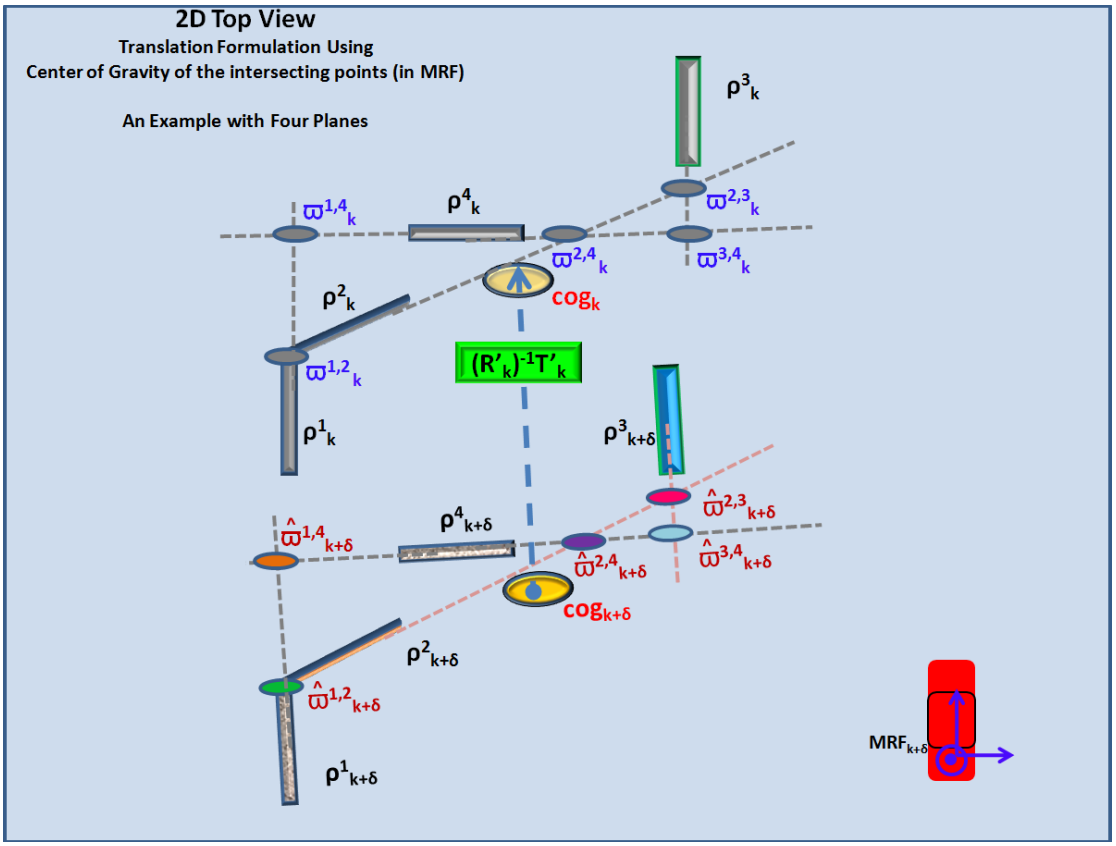

Figure 6.15: Translation computation by center of gravity method. Four planes are shown, which yield five intersection points used for computing *cog*. The vector between the *cog* from the two epochs corresponds to the rotated translation.

6.8 Trajectory estimation

The relative pose estimated using the methods detailed in sections 6.6 and 6.7 needs to be integrated to obtain the trajectory. In ideal environments the trajectory can be continuous and obtained by referring the pose $(\mathbf{p_k}, \mathbf{o_k})^{\mathbf{FRF}}$ (position and orientation respectively) at instant $\mathbf{k}$ in FRF.

The orientation $\mathbf{o}_{\mathbf{k}-\delta}^{\mathbf{FRF}}$, is integrated with the negative of (since the rotation of the vehicle is in opposite direction to the computed rotation rate of planes (ORF)) computed angle rates $[\dot{\phi}, \dot{\theta}, \dot{\psi}]$, around respective $\mathbf{XYZ}$ axes, for the interval $[\mathbf{k}, \mathbf{k}+\delta]$. These integrated angles $\mathbf{o}_{\mathbf{k}}^{\mathbf{FRF}}$ constitutes the rotation matrix $\mathfrak{R}_{\mathbf{k}\mathbf{MRF}}^{\mathbf{FRF}}$, used in the computation of the position $\mathbf{p}_{\mathbf{k}}^{\mathbf{FRF}}$ in FRF using equation 6.38.

$$\mathbf{p_k^{FRF}} = \mathbf{p_{k-\delta}^{FRF}} - \mathfrak{R}_{\mathbf{k}}\mathbf{^{FRF}_{MRF}}\mathbf{T_k'} \tag{6.38}$$

6.9 Conclusion

This chapter presented a new 3D laser odometer approach using planar landmarks. *The transformation is computed solely using the geometrical properties of the observed landmarks.* Therefore, the solution remains independent of other pose sensors. Here, 3D transformation with 6 Degrees of Freedom (DOF), and resolved for 5DOF (3DOF rotation and 2DOF translation), by considering the realistic limitation of most manmade structures being vertical. The missing 6^{th} DOF (vertical translation) can be computed by using a synchronized camera with the 2D laser scanners. This work presents a novel **Divide & Conquer approach** in order to reduce the complexity of the 3D pose problem. It separately performs the explicit Data Association (DA) and transformation computation steps. Moreover, these two operations are split in two, and they are performed sequentially as: **Lenient Data Association (LDA), Rotation resolution, Strict Data Association (SDA) and Translation resolution**. The splitting of these processes drastically simplifies the complex 3D pose estimation problem.

To cope with the unknown transformation, the LDA applies lenient conditions to identify the corresponding landmarks between two observation sets. This implies, the result can retain some outliers or wrong associations as feasible candidate solution. A new algorithm, we term as **Optimal Candidate Selection by Consensus (OCSC)** chooses the candidate that estimates the optimal transformation, even in the presence of outlier candidates. We improve OCSC by adding weight to the consensus process (we call it **WOCSC**), to overcome scenarios with 50% or more outliers. These algorithms can be applied to any overdetermined system to chose the optimal solution from a set of feasible candidates, including some outliers. Moreoever, it eliminates outliers, deals with noisy candidates and resolves ambiguities, along with choosing the optimal transformation (both rotation and translation) solution.

Since rotation is estimated from the associations provided by LDA, it is resolved by WOCSC. However translation can be computed by a mean based method, since SDA has eliminated the remaining outliers, after compensating for the known rotation. Therefore, a center of gravity (weighted mean) based approach is proposed to compute translation. However, the WOCSC can be applied again to estimate the optimal translation, overcoming the need to have an SDA.

These algorithms are validated using two simulated datasets in an ideal environment (with continuous nonparallel planar landmarks). The results and the analysis is presented in chapter 7.

Chapitre 7

Expérimentations, analyse et améliorations

Au chapitre 6 nous avons présenté l'ensemble des algorithmes permettant d'implémenter la méthode d'odométrie par laser.

Le présent chapitre résume les détails d'implémentation des hypothèses et des paramètres de configuration.

Les algorithmes sont validés au moyen de deux jeux de données simulées. Ces données fournissent l'information réelle et permettent de rajouter différents niveaux de bruit aux valeurs mesurées. Le premier scénario est un ensemble de données construit pour l'occasion, le second est créé au moyen de la plateforme de simulation SIVIC.

Pour les tests, quatre niveaux de bruit sont évalués. Les trajectoires estimées sont proches de la réalité. Comme il est prévisible, l'estimation diverge d'autant plus que le niveau de bruit augmente. L'algorithme WOCSC fournit de meilleurs résultats qu'une approche fondée sur la valeur moyenne, surtout quand le niveau de bruit est important ; montrant par là sa capacité à éliminer les cas aberrants.

Les données issues de SIVIC ont été générées en supposant que le véhicule se déplace à une vitesse de 10 km/h, vitesse typique de celle de LARA-3D en phase d'acquisition. Même à cette vitesse, la trajectoire est estimée correctement.

Toutes les trajectoires présentent une dérive liée à l'accumulation des erreurs. Nous proposons une nouvelle technique, l'association retardée des données, pour laquelle l'association n'est pas faite entre deux jeux successifs, mais entre des jeux de données prises à des intervalles temporels plus importants. Cette méthode réduit significativement le bruit dans les trajectoires estimées. Cette approche peut être élargie en effectuant l'as-

sociation dans une carte comportant des ensembles de repères fiables, construite de manière incrémentale. Cette approche de carte à posteriori peut permettre de répondre au problème typique du SLAM, les dérives liées à l'accumulation des erreurs.

Chapter 7

Experiments, analysis and improvements

Contents

7.1 Introduction

This chapter presents the implementation summary of the methods elaborated in chapter 6, with the obtained results, their analysis and a possible improvement.

The input datasets are generated using two simulation platforms, one a self designed model, and the other, generated using the simulation platform SIVIC.

The content flow of this chapter is organized as follows:

First, the implementation details, with the assumptions, process chain of algorithms and a summary of the used configuration parameters are presented (section 7.2). Then, the experimentations are detailed in section 7.3, with the test data generation scenarios, validation tests and their results, along with the analysis. Motivated from our results, we present a *new delayed map update* approach to correct the drift errors encountered by all SLAM approaches (section 7.4). The conclusion of the chapter is given in section 7.5.

7.2 Implementation

The algorithm is implemented in MATLAB, and the naive implementation has a complexity of $\mathbf{O}(\mathbf{p^2})$, where $\mathbf{p}$ is the number of extracted planar landmarks. As already mentioned in chapter 6, this is much better in comparison to the naive implementation of ICP, where the quadratic complexity is dependent on the number of measured range points.

In section 7.2.1, a summary of the applied assumptions is given. Section 7.2.2 presents the algorithms, as defined in figure 6.2. These algorithms consist of Lenient Data Association, rotation resolution, Strict Data Association and translation computation. The chain of algorithms also presents the application of the WOCSC method to estimate the best transformation operand.

7.2.1 Assumptions

The designed data association methods of a laser odometry given in chapter 6, takes all these implementation assumptions into account.

- **Perception characteristics**

  As stated in [Selkainaho 01], the main assumption behind this approach is that the time interval, and hence the displacement of the robot, between successive scan lines, is small. This constraint can be controlled by two parameters: the data acquisition rate (scanning rate of laser scanners), and the velocity of the mapping platform.

  The ICP-based approach in [Nüchter 05b], [Nüchter 07], [Nüchter 09], uses a "stop and go" motion of the robot as the 3D laser scans takes $\sim$ 9000 ms. However, the data acquisition rate of planar landmarks, using a synchronized 2D laser scanners given in chapter 5, requires only the time needed for a single 2D scan ($\sim$ 30 ms), therefore can avoid "stop and go" motion.

The second assumption is about the *batch observations*, where a set of observations (i.e., viewed features) are sensed simultaneously, or within such a short time-span that motion compensation can offset any geometric distortion [Bailey 01]. This again implies that scanning rate of the perception sensor is sufficiently quick so as to compensate for the second order errors like linear and angular accelerations. Even this constraint can be controlled by the same two parameters, the data acquisition rate and the velocity of the mapping platform. In our implementations, we consider normally distributed motion errors for the short time span of single scan.

As mentioned in chapter 4, the SICK LMS laser scanners [SICK 06] are widely used in many robotic SLAM approaches. Therefore, we consider their specification as our benchmark. From our observations with SICK LMS 221 laser scanners, we obtained a precision of 6 mm with a maximum range of 32 meters, scanning at a rate of 26 ms per scan, and an angular resolution of 0.5°. For a localization approach like a laser odometry, it is important to have a good quality input perception sensor. A high-end laser scanner like Optech [Optech. 10] or Velodyne [Velodyne. 10], can perform better for laser scanner based localization applications.

Like earlier works [Kapp 06], [Borges 04], any variation in the angular rate of a laser scanner is assumed to be negligible. Laser scanners scan the field of view in only one direction, clockwise or anticlockwise. This implies, they do not move like a windscreen wiper but in a circular fashion, scanning a limited angle of the circle. This means the order of observing the landmarks (given in associable relationships in section 6.5) is maintained between scans, meeting directly (without any conversion) the specification of the correlation method described in section 6.5.1. However, the landmarks appear and disappear as the mapping platform moves, making the Data Association process nontrivial.

- **Noise distribution**

The noise in a modeled planar surface, extracted using the measurements of a set of 2D laser scanners fixed to a moving mapping platform, can be decomposed as given in equation 7.1.

$$\eta^{\mathbf{2}}_{\mathbf{points}} = \eta^{\mathbf{2}}_{\mathbf{laser}} + \eta^{\mathbf{2}}_{\mathbf{motion}} + \eta^{\mathbf{2}}_{\mathbf{surface}} \tag{7.1}$$

$\eta_{\mathbf{laser}}$ denotes the laser measurement errors, typically in the millimeter range. These errors result from the range to the object, the environmental conditions etc. Since the speed of light is the reference for time, the degradation of the laser measurement is only due to the dispersion and absorption of the laser beam, and not due to its signal travel latency. A laser scanner specifies these errors in a combined form of σ_{laser}, as explained in chapter 5.

For the extraction of the planes and their association, we consider that the precision of the laser scanner is more important than the accuracy itself. Precision gives the measure of closeness in the repeated observations. A planar feature extracted from a high precision laser scanner retains the characteristics such as normals and dihedral angles, needed for the association methods described in chapter 6.

$\eta_{\mathbf{motion}}$ is the error in the laser observations due to the motion of the mapping platform. In contrast to [Gee 07], the velocity is not assumed to be constant. However, it is desired to have a low $\eta_{\mathbf{motion}}$ by minimizing accelerations during data acquisition. For a snapshot (or a single scan), the motion error is treated as a white Gaussian noise. Thus it will have an increasing effect on the value of σ_{laser}. Therefore, as mentioned in chapter 5, the value of σ_{laser} is doubled. The value of σ_{laser} and the factor of 2 (i.e., $\eta_{\mathbf{motion}} = \sigma_{laser}$) were determined empirically for the tested data sets.

The effect of roughness or undetectable unevenness and reflectivity of the planar surfaces is given as $\eta_{\mathbf{surface}}$. This is mostly a systematic error, since these properties of the planar surface remain the same between two associated epochs. In a differential process, a systematic error like this can be neglected. We assume that, since these errors are uniform, it does not perturb the Data Association.

Due to the inherent smoothing done (refer to: chapter 5) while estimating the line segments and choosing the three coplanar points, the effect of the total noise is minimized significantly for each plane. The effect of the noise on the planar surface estimation is given in the form of **CPEF**. This is a function of the confidence in each of the two line segments **CLEF**; weighed by the number of points, each line segment contributes to the estimation of the plane. **CLEF** is a function of the number of points detected in a line segment and the average linear error of its estimation, from the given set of points.

- **Limitations of planar landmarks**

Planar landmarks help in reducing the storage size, each of them represents several measured range points by a single feature property. However, as stated in chapter 6, they also have certain limitations for SLAM like approaches. Planar surfaces are uniform, and do not provide any salient feature points which can be associated directly.

The methodology given in chapter 5 extracts planar landmarks elicited from the partially observed data. Therefore, the boundaries of these observed planar patches do not correspond to the physical boundaries of the planar surfaces in the scene. As stated before, this is true either due to occlusions or to the laser scanner arrangements. Thus the center of gravity of the landmark is not relevant, as illustrated in figure 7.1.

The extraction methodology of the planar landmarks is not limited to the one given in chapter 5. They can also be extracted using a 3D laser scanner, a multilayer

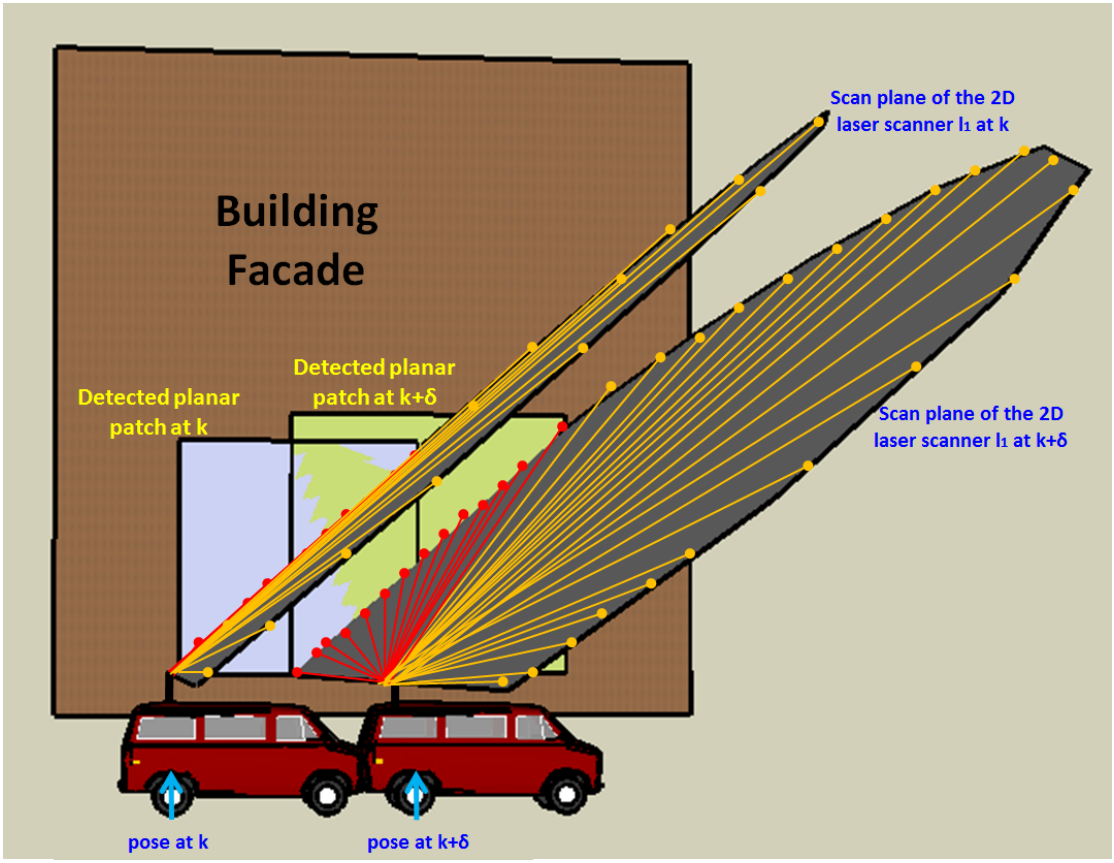

Figure 7.1: Figure shows the effect of partial vision of a planar surface due to the limitation of a 2D laser scanner arrangement. Here two planar patches extracted at epochs $\mathbf{k}$ and $\mathbf{k}+\delta$, using the methodology given in chapter 5, are shown. Only one of the two lasers ($\mathbf{l_1}$) of the synchronized pair is shown to simplify the image. Red points show the *observations*, and the yellow points show the *infinity measures*. Due to the vehicle motion, the observed planar patches correspond to different regions of the same building facade. Therefore, the boundaries of the observations can vary from one epoch to another, and these observation boundaries do not correspond to the real boundaries of the physical facade.

laser scanner, different arrangements of 2D laser scanners, sonars or from an image. The methods of data association and transformation computation given in chapter 6 is still applicable, with some minor tuning. In ideal environments, the method given in chapter 5 is an efficient way to extract planar landmarks using a mobile mapping platform.

7.2.2 Algorithm

The implemented algorithm follows the same steps given in figure 6.2. In the laser odometry implementation, two sets of planes ($\mathbf{P_k}$ and $\mathbf{P_{k+\delta}}$) observed at epochs $\mathbf{k}$ and $\mathbf{k}+\delta$ are compared, to estimate the relative transformation of the mapping platform taken place between this period of time. As already mentioned, the input set of planes are extracted either using the approach given in chapter 5, or any other sensors and their arrangements. The only condition is, the planes must retain their time invariant properties, which are used for their identification and association.

Algorithm 7.2.1 Transformation estimation

Require: $\mathbf{P_k} = \{\rho^{\mathbf{i}} | \mathbf{i} = \{\mathbf{1} \dots \mathbf{N_k}\}$, $\mathbf{P_{k+\delta}} = \{\rho^{\mathbf{j}} | \mathbf{j} = \{\mathbf{1} \dots \mathbf{N_{k+\delta}}\}$ is the two set of planes extracted epochs $\mathbf{k}$ and $\mathbf{k}+\delta$, where $|\mathbf{P_k}| = \mathbf{N_k}$ and $|\mathbf{P_{k+\delta}}| = \mathbf{N_{k+\delta}}$. Both $\mathbf{N_k} > \mathbf{1}$ and $\mathbf{N_{k+\delta}} > \mathbf{1}$.

1. **Lenient Data Association (LDA)**

   (a) **Correlation:** Based on the time invariant properties of the data sets, associate the elements within the sets.

      i. Generate the skew symmetric matrix (SSM) $\mathbf{D_k}$ with dihedral angles, for each plane pairs (indexed by $(\mathbf{i}, \mathbf{j})$, such that $\mathbf{j} > \mathbf{i}$) in the set $\mathbf{P_k}$ (equation 6.2).

      ii. Generate the skew symmetric matrix (SSM) $\mathbf{D_{k+\delta}}$ with dihedral angles, for each plane pairs (indexed by $(\mathbf{p}, \mathbf{q})$, such that $\mathbf{q} > \mathbf{p}$) in the set $\mathbf{P_{k+\delta}}$ (equation 6.2).

      iii. Compare the elements upper triangular matrix of $\mathbf{D_k}$ with each elements of upper triangular matrix of $\mathbf{D_{k+\delta}}$ to check if $\varphi^{\mathbf{i,j}} \simeq \varphi^{\mathbf{p,q}}$. There is a tolerance level $\mathbf{K}_\varphi$ for this equality check to take into account of the noise. If they match the planes, $(\rho_{\mathbf{i}}, \rho_{\mathbf{j}})$ and $(\rho_{\mathbf{p}}, \rho_{\mathbf{q}})$ is added to the set $\hat{\mathbf{C}}^{\mathbf{1}}_{\mathbf{k},\mathbf{k}+\delta}$ (equation 6.3).

      iv. Remove parallel plane records: if $\varphi^{\mathbf{i,j}}$ or $\varphi^{\mathbf{p,q}}$ is equal to either $(0 \pm \mathbf{K}_\varphi)$ or $(\pi \pm \mathbf{K}_\varphi)$, remove the entire record from $\hat{\mathbf{C}}^{\mathbf{1}}_{\mathbf{k},\mathbf{k}+\delta}$ and the reduced set is termed as $\hat{\mathbf{C}}^{\mathbf{2}}_{\mathbf{k},\mathbf{k}+\delta}$.

   (b) **Ambiguity reduction:** The purpose of such a lenient association step is to remove any spatially impossible associations reducing the cardinality of the correlated quadruple set.

      i. For each record in $\hat{\mathbf{C}}^{\mathbf{2}}_{\mathbf{k},\mathbf{k}+\delta}$, check the spatial alignment of the plane pairs $(\rho_{\mathbf{p}}, \rho_{\mathbf{i}})$ $(\rho_{\mathbf{q}}, \rho_{\mathbf{j}})$ and the spatial neighborhood test using the

distance threshold $\mathbf{D_{LDA}}$ (equation 6.4). If the tests are passed for at least one of the two pairs, the quadruple record $(\rho^{\mathbf{i}}_{\mathbf{k}}, \rho^{\mathbf{j}}_{\mathbf{k}}, \rho^{\mathbf{p}}_{\mathbf{k}+\delta}, \rho^{\mathbf{q}}_{\mathbf{k}+\delta})$ is retained. The remaining quadruple set is termed as $\hat{\mathbf{C}}^{\mathbf{3}}_{\mathbf{k},\mathbf{k}+\delta}$.

2. **Rotation estimation:** The set $\hat{\mathbf{C}}^{\mathbf{3}}_{\mathbf{k},\mathbf{k}+\delta}$ contains planes which are leniently associated. This implies there can be some ambiguous and noisy associations. Therefore, the optimal candidate selection algorithm is applied.

   (a) Apply either OCSC or its variant WOCSC algorithm given in section 6.7.1, to identify the optimal rotation solution. *WOCSC* is preferred, since it can handle more outliers, in an appropriately weighted population (refer to section 6.7.2). The obtained 3D rotation rates between epochs $\mathbf{k}$ and $\mathbf{k}+\delta$ are denoted in rotation matrix form $\mathbf{R}^{'}_{\mathbf{k}}$.

   (b) Apply rotation to the set of planes $\mathbf{P}_{\mathbf{k}+\delta}$ call them $\hat{\mathbf{P}}_{\mathbf{k}+\delta}$. The set of planes $\mathbf{P}_{\mathbf{k}}$ and $\hat{\mathbf{P}}_{\mathbf{k}+\delta}$ are now aligned after the rotation compensation.

3. **Strict Data Association (SDA):** A more stringent relationship constraints can be applied between $\mathbf{P}_{\mathbf{k}}$ and $\hat{\mathbf{P}}_{\mathbf{k}+\delta}$. However, all the following steps are optional, if *OCSC/WOCSC algorithms* are applied to compute the translation.

   (a) **Strict ambiguity reduction:** At first the same set of ambiguity reduction conditions are applied as LDA. However, the relationship constraints are much more stringent.

      i. For each record in $\hat{\mathbf{C}}^{\mathbf{3}}_{\mathbf{k},\mathbf{k}+\delta}$, check for the same relationship of ambiguity reduction in LDA, but with a stringent distance threshold $\mathbf{D_{SDA}}$ (equation 6.4 & section 6.5.2).The remaining quadruple set is termed as $\hat{\mathbf{C}}^{\mathbf{4}}_{\mathbf{k},\mathbf{k}+\delta}$.

   (b) **Ambiguity resolution:** This step ensures an injective relationship between the associated individual planes from the sets $\mathbf{P}_{\mathbf{k}}$ and $\mathbf{P}_{\mathbf{k}+\delta}$.

      i. Construct a voting matrix $\mathbf{V}^{\mathbf{ij}}_{\mathbf{k},\mathbf{k}+\delta}$ from the input quadruple set $\hat{\mathbf{C}}^{\mathbf{4}}_{\mathbf{k},\mathbf{k}+\delta}$ as explained in section 6.5.2.

      ii. Check for obtained votes for each association and, in case of a conflict, apply *appearance test* to resolve ambiguity. Otherwise the association with the maximum number of votes is retained. *appearance test* checks the closeness in alignment between the corresponding planes from the set $\mathbf{P}_{\mathbf{k}}$ and the rotated $\hat{\mathbf{P}}_{\mathbf{k}+\delta}$. The resulting quadruple set is labeled as $\hat{\mathbf{C}}^{\mathbf{5}}_{\mathbf{k},\mathbf{k}+\delta}$.

4. **Translation computation:** Translation computation can be done using two methods: *Center of gravity (cog)* a mean-based method, or the *OCSC/WOCSC method*. For the *cog method* to work, all the ambiguities must absolutely be resolved, using the SDA. WOCSC based translation can work without SDA. However, it is preferable to reduce ambiguities if possible.

   (a) **Cog method**

      i. This mean-based method takes injective quadruple set $\hat{\mathbf{C}}^{\mathbf{5}}_{\mathbf{k},\mathbf{k}+\delta}$ and computes the mean translation between the intersection points for the plane pairs $(\rho^i, \rho^j) \in \mathbf{P_k}$ and rotation compensated planes $(\rho^p, \rho^q) \in \hat{\mathbf{P}}_{\mathbf{k}+\delta}$, where these four planes forms an associated tuple of the set $\hat{\mathbf{C}}^{\mathbf{5}}_{\mathbf{k},\mathbf{k}+\delta}$. The algorithm is given in section 6.7.4.

   (b) **WOCSC method**

      i. This gives an optimal translation solution by applying the algorithm given in section 6.7.3. The input can be any of the set $\hat{\mathbf{C}}^{\mathbf{3}}_{\mathbf{k},\mathbf{k}+\delta}$, $\hat{\mathbf{C}}^{\mathbf{4}}_{\mathbf{k},\mathbf{k}+\delta}$ or $\hat{\mathbf{C}}^{\mathbf{5}}_{\mathbf{k},\mathbf{k}+\delta}$. On most occasions all the sets yields identical results.

7.2.3 Configuration parameters

The following tables (table 7.1 and 7.2) summarizes all the configuration parameters, and their tested/preferred values in the implemented algorithms of plane extraction, data association, and transformation estimation.

Table 7.1, provides the list of input laser scanner parameters in the test scenarios.

Parameter	Tested values	Purpose	Defined in section
$\mathbf{\Gamma}$	$\mathbf{0.5}^\circ$	Angular resolution	5.4.1
$\mathbf{F_{laser}}$	**25** Hz	Scanning frequency	5.4.1
$\sigma_{\mathbf{laser}}$	$\in [\mathbf{0}, \mathbf{0.02}]$ meter	Laser range scanner precision	5.4.1
$\mathbf{R_{max}}$	**80** meter	Maximum range	5.4.1
$\mathbf{\Upsilon}$	$\mathbf{150}^\circ$	Field of view	5.4.1

Table 7.1: Input laser scanner configurations

Table 7.2, provides the list of parameters used and tuned empirically for the tests performed.

Parameter	Current value	Purpose	Used in section
ϕ	$\mathbf{79}^\circ$	Maximum incidence angle	5.4.2
$\mathbf{D_{far}}$	$\mathbf{3.29} \times \sigma_{\mathbf{laser}} \times \mathbf{K_1}$ $\mathbf{K_1 = 2}$	Line segmentation threshold	5.4.2
$\mathbf{P_{min}}$	$\mathbf{5}$	Minimum required points to extract a line	5.4.2
$\sigma_{\mathbf{RANSAC}}$	$\mathbf{D_{far}}$	Precision below which a point is considered part of the line	5.4.2
$\mathbf{K_2}$	$\mathbf{80}\%$	% of segment points retained by RANSAC while fitting a line	5.4.2
$\mathbf{K}_\varphi$	$\mathbf{3}^\circ$	Dihedral angle: noise compensation	6.5.1
$\mathbf{D_{LDA}}$	$\mathbf{8.0} + \sigma_{\mathbf{laser}} \times \mathbf{K_{D_{LDA}}}$ $\mathbf{K_{D_{LDA}}} \in [\mathbf{0}, \mathbf{1.5}]$	Distance threshold for lenient condition	6.5.1
$\mathbf{D_{SDA}}$	$\mathbf{3.0} + \sigma_{\mathbf{laser}} \times \mathbf{K_{D_{SDA}}}$ $\mathbf{K_{D_{SDA}}} \in [\mathbf{0}, \mathbf{1.5}]$	Distance threshold for stringent condition	6.5.2

Table 7.2: Algorithmic parameters

The *velocity of vehicle* is another important control factor for a laser odometry, which needs to be determined according to the laser scanning rate. The factors to choose this parameters are: less motion noise, better frozen view of the scene, and associability of the landmarks within a short span of time, measured by δ epochs. The value of δ depends on the scene and the size of the planar landmarks. Higher the δ, lesser the noise (refer sections 5.3.3 and 7.4).

7.3 Experimentations

In the current implementation, we validate our algorithms in offline mode. The term laser odometry is still applicable, since the process and methods remain exactly the same as an online odometry, where the relative pose of the mapping platform is estimated.

To remind, mobile mapping platform *LARA-3D* applies the similar two step process as explained in figure 3.3: data acquisition step which is real time (online), and the offline data processing. The difference is, only the laser data is acquired and processed in planar environments.

7.3.1 Datasets

Two simulated laser scanner datasets are used for validating the algorithms in a planar environments. In one of the dataset, absolute vehicle trajectory is known, as the laser measurements are generated from our own tool, form each known pose of the vehicle. The other dataset is generated using SIVIC, where the true trajectory is extracted from the SIVIC pose sensors. The first dataset is referred as *Scenario-01*, and the SIVIC data set is referred as *Scenario-02*.

The simulated environments facilitates validation of the newly implemented algorithms by providing provisions to add noise to the observations and better scenario control, while knowing the truth.

- **Test *Scenario-01* description**

  In this scenario, the vehicle completes a trajectory loop of **150** m, in a planar environment as shown in figure 7.2.

  There is no measurement noise ($\sigma_{\mathbf{laser}} = \mathbf{0}$) added to the dataset, and the vehicle when displacing in a straight path steps at **0.5** meters and at the three turns with a fixed angular velocity of **5**°. The associability of the planes is ensured between time steps ($\delta = \mathbf{1}$), meaning at least two non parallel planes observed in epoch $\mathbf{k-1}$ is observed in epoch $\mathbf{k}$. In this dataset, only the forward pair of isoclinal laser pair (explained in section 5.3) is used.

  The laser configuration remains same as the one given in table 7.1. However, the parameter $\mathbf{F}_{\mathbf{laser}}$ has no significance, since the laser measurements are generated at each pose of the trajectory.

  The dataset is tuples of **301** range points measured for a pair of laser at each known pose of the vehicle trajectory. For test purposes, same dataset can be modified by adding external noise to corrupt the measurements.

- **Test *Scenario-02* description**

  In this scenario, data is generated using the simulation software SIVIC. A planar environment, shown in figure 7.3, is created, where the vehicle is driven with nearly a constant velocity. In this dataset, both the forward and the backward isoclinal laser pairs (explained in section 5.3) are used.

  We divided this trajectory in two sections, one to ensure a straight path and the other for a curve. SIVIC simulates real world, like scenario with noisy motion and measurement models. We ensured continuity in associability by using larger non parallel planar sections.

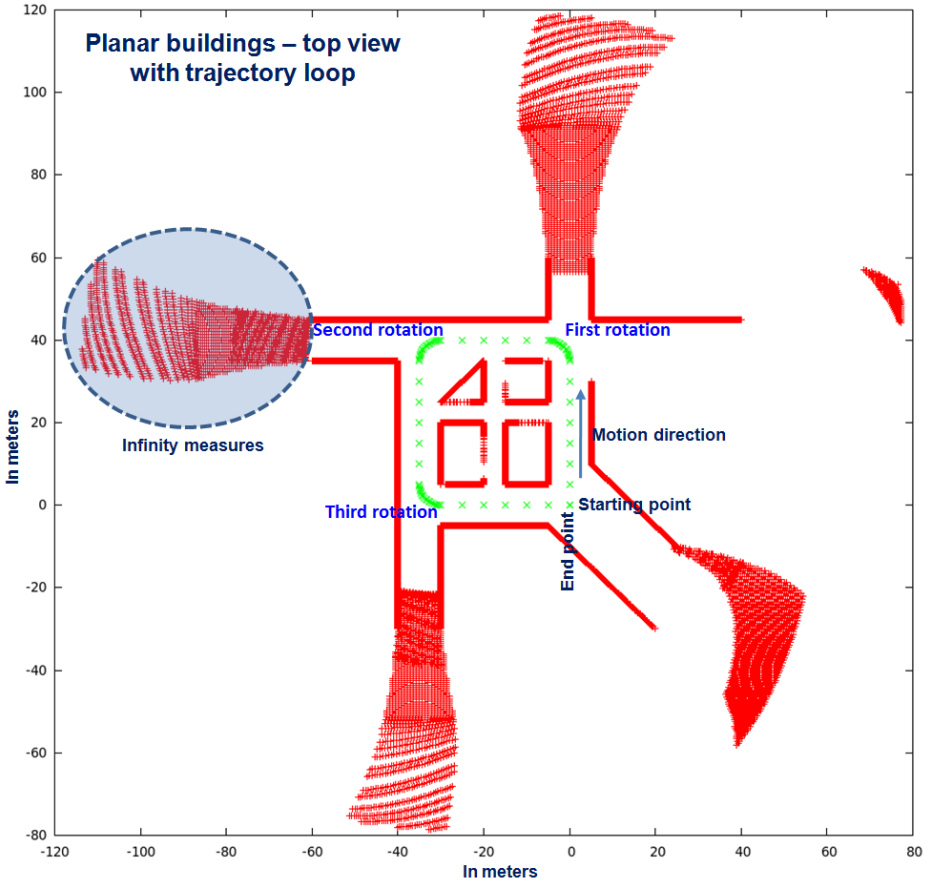

Figure 7.2: Top view of the scenario with a known trajectory. The measurements plotted at the maximum range (the curved section of the points) correspond to the infinity measures (measurements with maximum range $\mathbf{R_{max}}$). Green colored dots indicate the trajectory of the vehicle used for acquisition of the data.

The Gaussian measurement noise has a standard deviation of ($\sigma_{\mathbf{laser}} = \mathbf{2}$ cm), in addition to the vehicle motion noise. Due to the larger planar sections, the associability of the planes is ensured for a larger time steps ($\delta > \mathbf{1}$).

The laser configuration remains the same as the one given in table 7.1.

Similar to *Scenario-01*, dataset is tuples of **301** range points measured for each laser scanner at a rate of **25** Hz. The trajectory is divided into two sections: a straight path (*trajectory section-01*) and a turn (*trajectory section-02*). The dataset resembles the real world for both motion and measurement process.

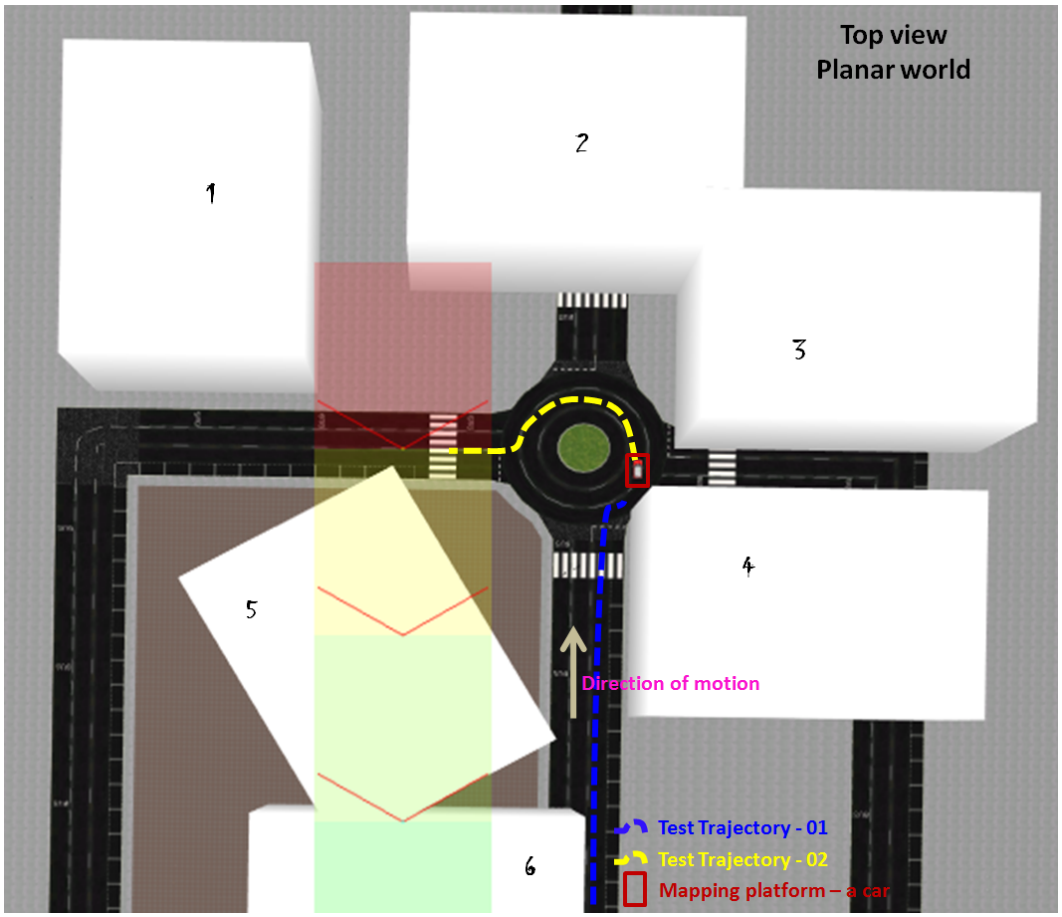

Figure 7.3: A cubic world test data scene generated in SIVIC. Cubic buildings are shown in white, and the car is located at the middle of the trajectory (start of *trajectory section-02*) near the roundabout. The buildings are placed in all directions to ensure that the planes are detected from different angles.

7.3.2 Results and analysis

- ***Scenario-01*: different noise level tests**

  This test scenario is generated using known pose of the vehicle, with relatively high linear velocity (**0.5** meter per epoch, corresponds to **45** kmph with **25** Hz laser scanning frequency). The goal of this scenario, is to validate the algorithms and the concept, exposing it to different levels of noisy inputs.

  The algorithms are first validated by without introducing any noise to the dataset. Then, three new datasets are derived, by adding three different levels of Gaussian

noise to each range measurement: **6** mm ($\sigma_{\mathbf{laser}}$ measured for SICK LMS laser scanner), **2** cm ($\sigma_{\mathbf{laser}}$ of the SIVIC laser scanners in our test scenarios), **10** cm (a maximum error for test purpose). In this section, from here on, these four derived datasets are referred as *the four cases*.

For these *four cases*, the obtained trajectories in a FRF are shown in figure 7.4. First, when there is no noise, the designed algorithms estimates the trajectory very well, therefore validating the concept and the methods. As the measurement noise level increase, expectedly the estimation degrades, but still retains the basic form of the trajectory. These outputs are generated without any signal filters. Any instance of high magnitude error in the MRF can cause a biased result in FRF, due to integration.

The effect of noise is measured for all the 5DOF, i.e., the 3DOF rotation rates $[\dot{\phi}, \dot{\theta}, \dot{\psi}]$, around respective **XYZ** axes (also referred as roll, pitch and yaw rates, respectively) and the 2DOF velocity or translation vector $[\dot{\mathbf{X}}, \dot{\mathbf{Y}}]$. Figure 7.5, depicts the error in the estimation of these three rotation rates, subject to each of *the four cases*.

The pitch rate increases very rapidly with the noise, compared to roll or yaw rate errors. This is due to the specific arrangement of the 2D laser scanners, where the extracted planar patches in the direction perpendicular to the motion (i.e., with incidence angle close to $\mathbf{0}^\circ$) are often small in area (with less range points), and magnitude of the measurement noise acts in the same direction of the pitch. However, the extracted planar patches perpendicular to the direction of motion have a larger surface area (refer to figure 5.5), with more range points, facilitating a better smoothing. This is in addition to the oblique incidence angle resulting in a lesser magnitude of noise on the extracted planes. This is the reason for having lower roll and yaw rates.

Similarly, figure 7.6 shows the effect of noise on the 2DOF translation computed with two alternative methods: optimal candidate solution using WOCSC (refer to section 6.7.3), and the mean-based cog method (refer to section 6.7.4). The WOCSC translation method uses the association results of the LDA (quadruple set $\hat{\mathbf{C}}^{\mathbf{3}}_{\mathbf{k},\mathbf{k}+\delta}$, section 6.5.1) as input, where as the cog uses the results of the SDA (quadruple set $\hat{\mathbf{C}}^{\mathbf{5}}_{\mathbf{k},\mathbf{k}+\delta}$, section 6.5.2). The cog method performs well as long as there is no false associations. However, with the noise $\sigma = \mathbf{10}$ cm, a false association occurs resulting in a jump in the estimated trajectory (figure 7.4), which then gets propagated through the rest of the trajectory. A way to correct this problem is to tune the configuration parameter $\mathbf{D_{SDA}}$, by reducing its magnitude to avoid wrong noisy associations, but keeping it large enough to facilitate the correct association of the remaining noisy data. The WOCSC method struggles to determine the orientation, (cluttering in figure 7.4) when the actual rotation is infinitesimal compared to the effect of the noise (low signal to noise ratio).

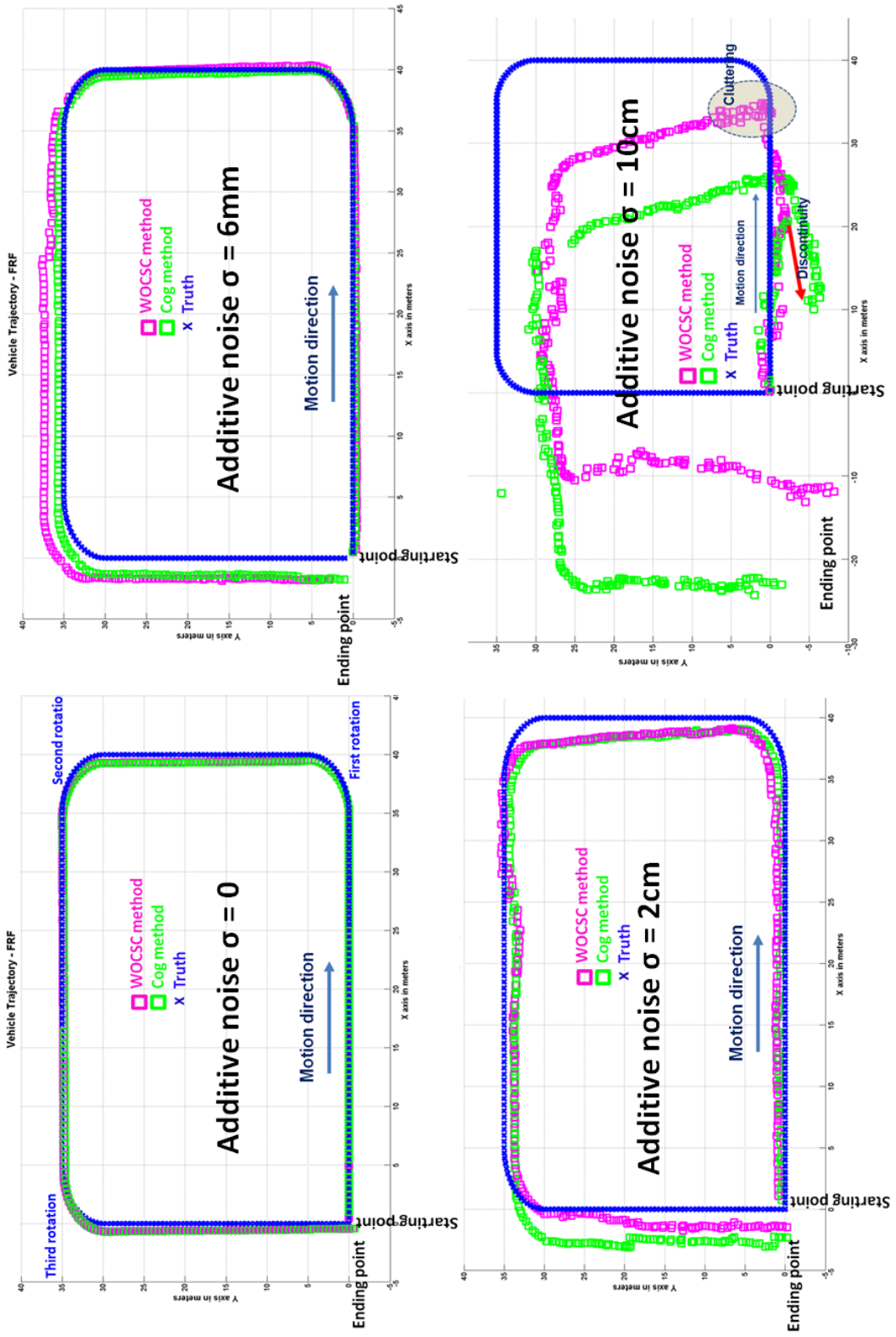

Figure 7.4: Trajectories estimated using two methods with four different noise levels compared against the truth. WOCSC method - both rotation and translation are the optimal estimates. Cog method - rotation estimation by WOCSC method and translation by mean based cog method.

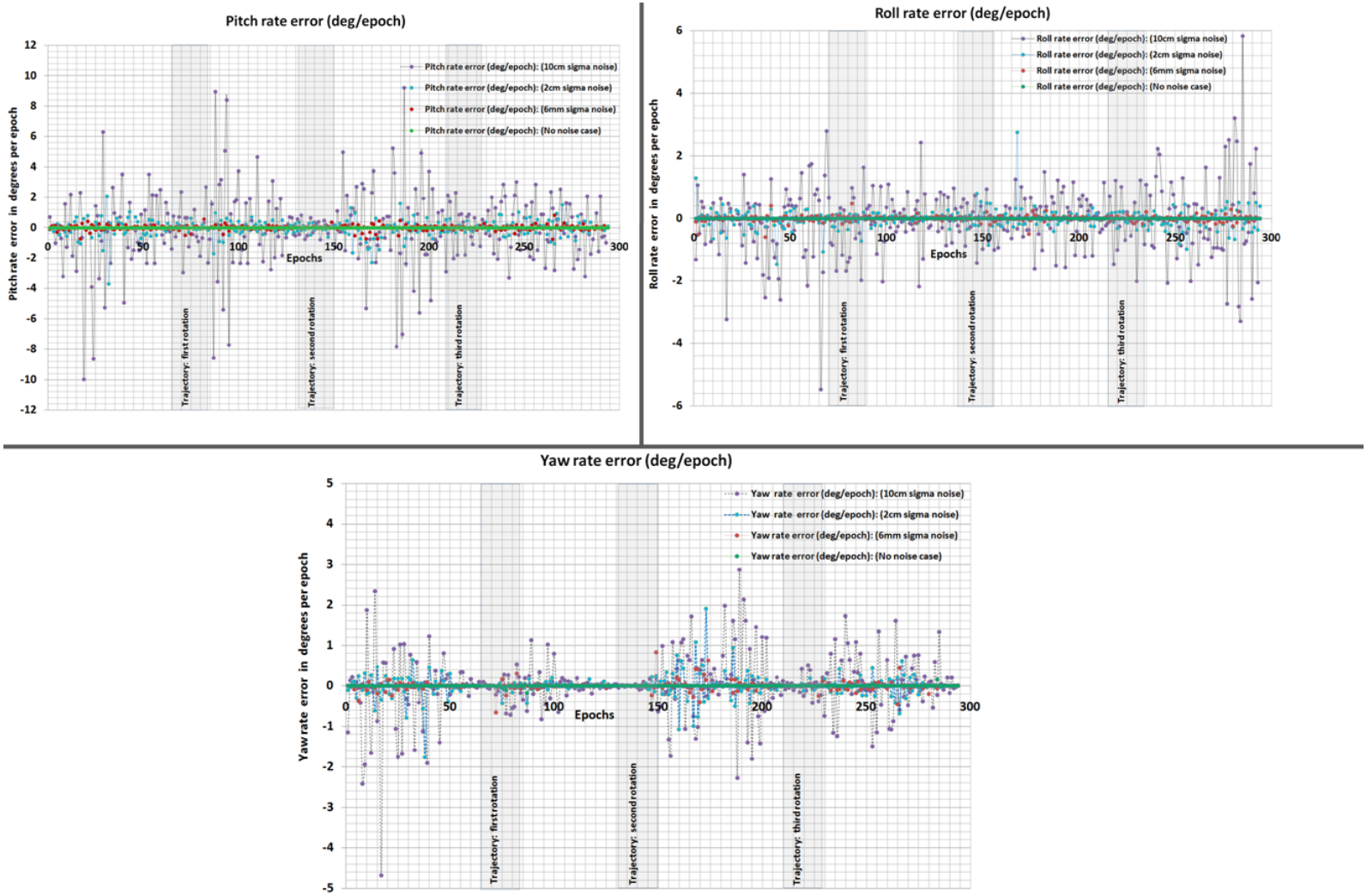

Figure 7.5: Effect of noise on the rotation rate estimation for the trajectory given in figure 7.4. On each plot, the epochs corresponding to the rotations in the trajectory are highlighted, but there is no systematic error identified in this zone.

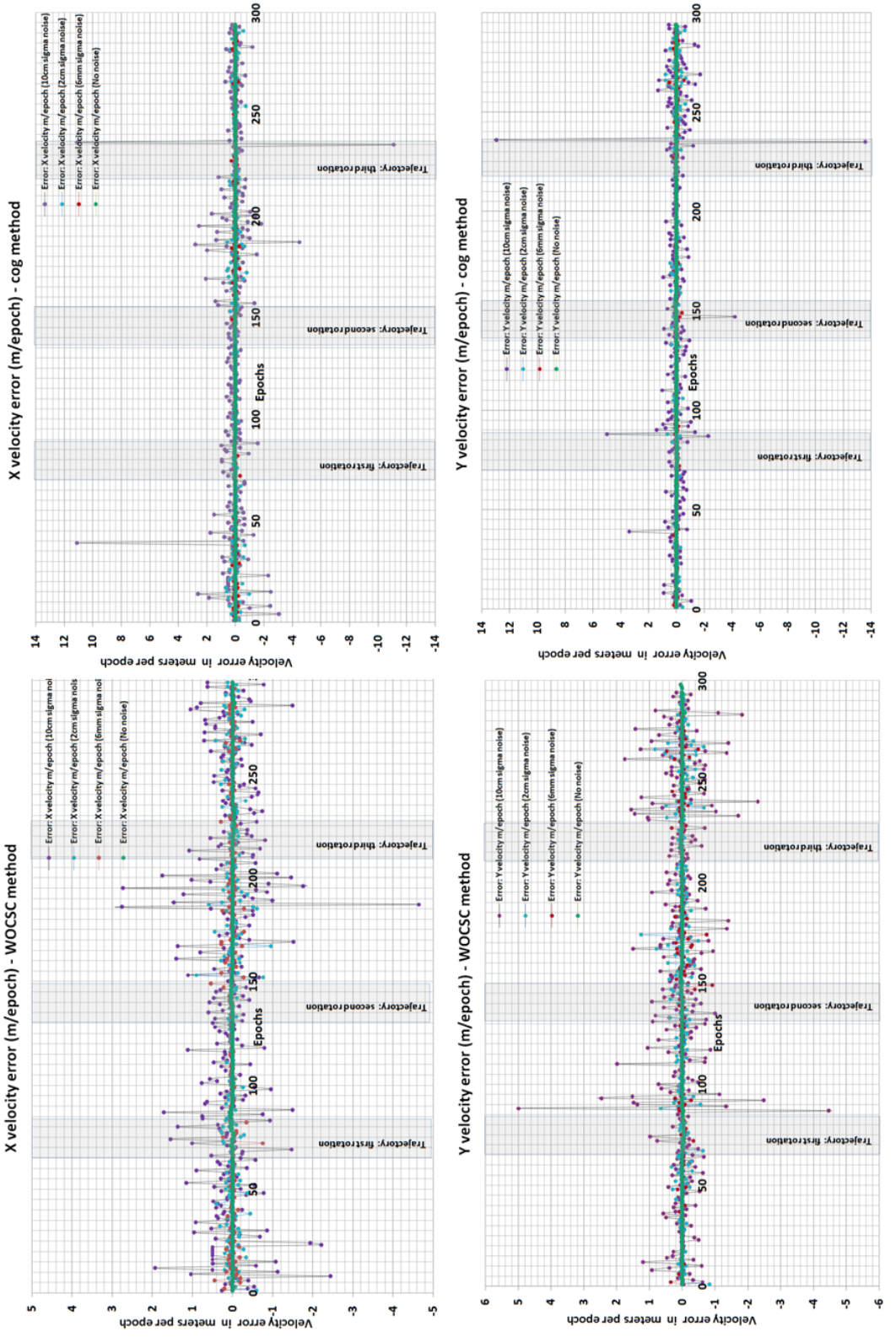

Figure 7.6: Effect of noise on the translation vector estimation for the trajectory given in figure 7.4, for the four noise levels. There are two alternative methods to compute translation: optimal candidate solution using WOCSC (column 1), and the mean-based cog method (column 2). Row 1 of the figure shows X axis error component, and row 2, Y axis error component. On each plot, the epochs corresponding to the rotations in the trajectory are highlighted.

The statistics for the performed tests are given in figure 7.7. The value of mean μ must be close to **0**, and a smaller standard deviation σ indicates a better precision.

	Mean roll rate error (deg/epoch)	Standard deviation (deg/epoch)	Mean pitch rate error (deg/epoch)	Standard deviation (deg/epoch)	Mean yaw rate error (deg/epoch)	Standard deviation (deg/epoch)
No noise	-2.85506E-15	9.51929E-14	1.03948E-14	1.83304E-13	-6.35649E-04	1.62722E-02
Noise σ= 6mm	-5.53156E-03	9.68693E-02	-2.72707E-03	1.75711E-01	-8.34166E-04	1.14980E-01
Noise σ= 2cm	-2.12593E-02	3.18210E-01	-3.00451E-02	5.53417E-01	8.14208E-04	2.72763E-01
Noise σ=10cm	-7.16991E-02	1.12940E+00	-4.70674E-02	2.38289E+00	8.36368E-03	7.65798E-01

	Mean velocity errors (meters/epoch)				Std deviation (meters/epoch)			
	WOCSC		Cog		WOCSC		Cog	
	X	Y	X	Y	X	Y	X	Y
No noise	1.46903E-03	1.75199E-03	1.44865E-03	2.16769E-03	1.48305E-02	1.38290E-02	1.54236E-02	1.52860E-02
Noise σ= 6mm	5.97738E-03	-6.33657E-03	5.94436E-03	-1.41951E-04	9.64136E-02	1.09878E-01	7.19298E-02	7.19869E-02
Noise σ= 2cm	4.98491E-03	7.96491E-04	7.79074E-03	7.90890E-04	1.68949E-01	2.00265E-01	1.98067E-01	1.68686E-01
Noise σ=10cm	4.02695E-02	2.79718E-02	7.82631E-02	5.10067E-03	6.99082E-01	7.16818E-01	1.33231E+00	1.27200E+00

Figure 7.7: Noise statistics for all the 5DOF (3DOF rotation and 2DOF translation) for the trajectory given in figure 7.4. The rows of the table corresponds to four noise levels tested, and columns have mean and standard deviation for each DOF. Translation is computed using two methods: optimal solution using WOCSC and mean based cog.

The precision decreases with the noise for each DOF. The comparison of two translation methods, WOCSC and cog, indicates the advantage of optimal candidate selection algorithm compared to mean-based methods, when the noise level increases (e.g. $\sigma = \mathbf{10}$ cm). The translation computed using WOCSC method (precision **0.7** m) is nearly twice as precise as the cog method (precision **1.3** m).

This confirms our statement that WOCSC eliminates outliers, deals with noisy candidates and resolves ambiguities (in section 6.7.1).

- ***Scenario-01*: OCSC and WOCSC comparison**
  This test is performed to validate our weighting methods using **CPEF** and our statement that WOCSC handles 50% or more of outliers (section 6.7.1), unlike the simple OCSC. The OCSC results can get biased in the presence of 50% or more of outliers. However, if the weighting process is correct, then such situations can be overcome by using WOCSC. The results demonstrate this effect using a particular situation in epoch **83**, as shown in figure 7.8.

  The corresponding trajectories for OCSC and WOCSC are shown in figure 7.9. The results confirms that WOCSC can correctly choose the optimal transformation even with 50% outliers, whereas OCSC fails to do so.

- ***Scenario-01*: WOCSC and cog comparison**
  As already mentioned in chapter 6, *cog method*, like any other mean-based approach, is very sensitive to outliers. An SDA algorithm (section 6.5.2) is indispensable for the *cog method* to function. However, WOCSC algorithm can work

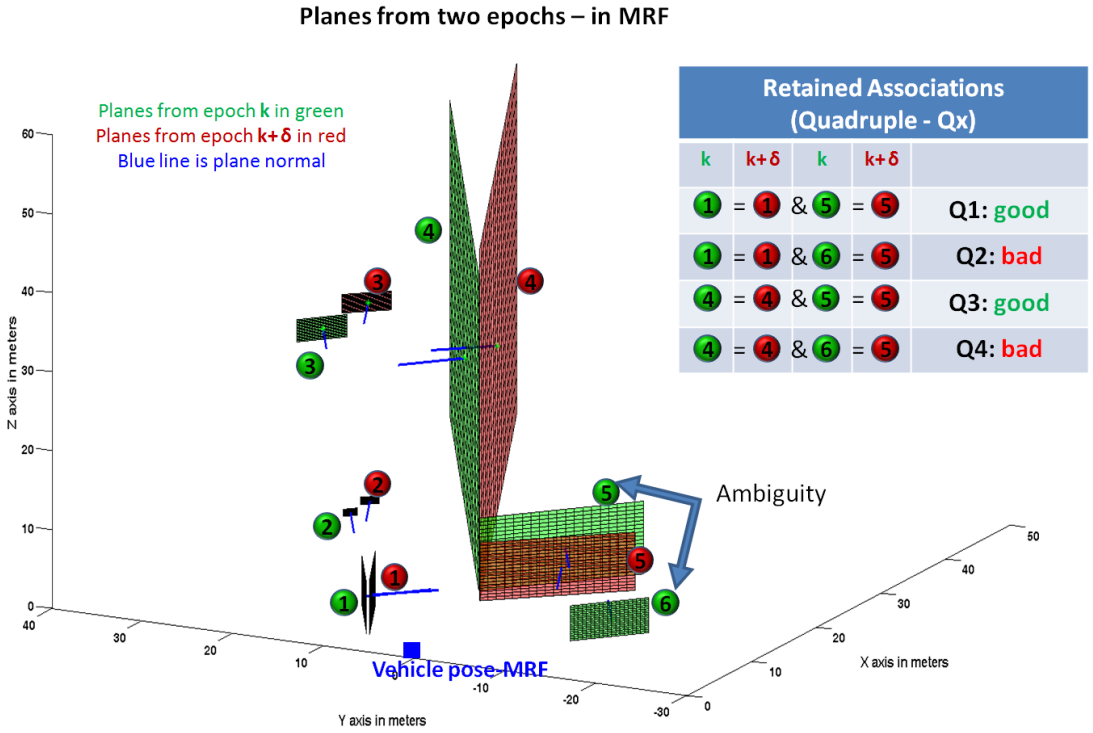

Figure 7.8: Figure shows associated planes from two epochs and the ambiguities in association. Two sets of observed planar patches from the associated epochs $\mathbf{k} = \mathbf{82}$ (green in color) and $\mathbf{k} + \delta = \mathbf{83}$ (red in color). The retained associations (quadruple set $\hat{\mathbf{C}}^{\mathbf{3}}_{\mathbf{k},\mathbf{k}+\delta}$) after LDA (section 6.5.1), has 2 correct associations and 2 incorrect associations. The ambiguity occurs when associating plane **5** (tagged in red), observed at epoch **83**, with the planes tagged (in green) from epoch **82**. Planes **5** and **6** from epoch **82** are parallel and closely located (spatially neighbors). Moreover, the real plane **6** from epoch **82** is not observed in epoch **83**. Therefore, the association relationships applied in LDA are valid for both these combinations (i.e., $\mathbf{5_{82}} = \mathbf{5_{83}}$ and $\mathbf{6_{82}} = \mathbf{5_{83}}$) originating the conflict.

in the presence of outliers, and the SDA becomes optional. The goal of this test is to validate this statement, stated in section 6.7.

These statements are proved using the following set of trajectories: without SDA (figure 7.10) and then, by switching-off only the *appearance test*, a part of SDA algorithm (figure 7.11). The trajectory obtained from *cog method with SDA* is already given in the analysis of different noise levels (figure 7.4).

Figure 7.10 indicates that, without SDA, translation computation using *cog method* is totally erroneous, whereas *WOCSC method* still functions precisely, implying the optimal estimation of both rotation and translation in the presence of outliers.

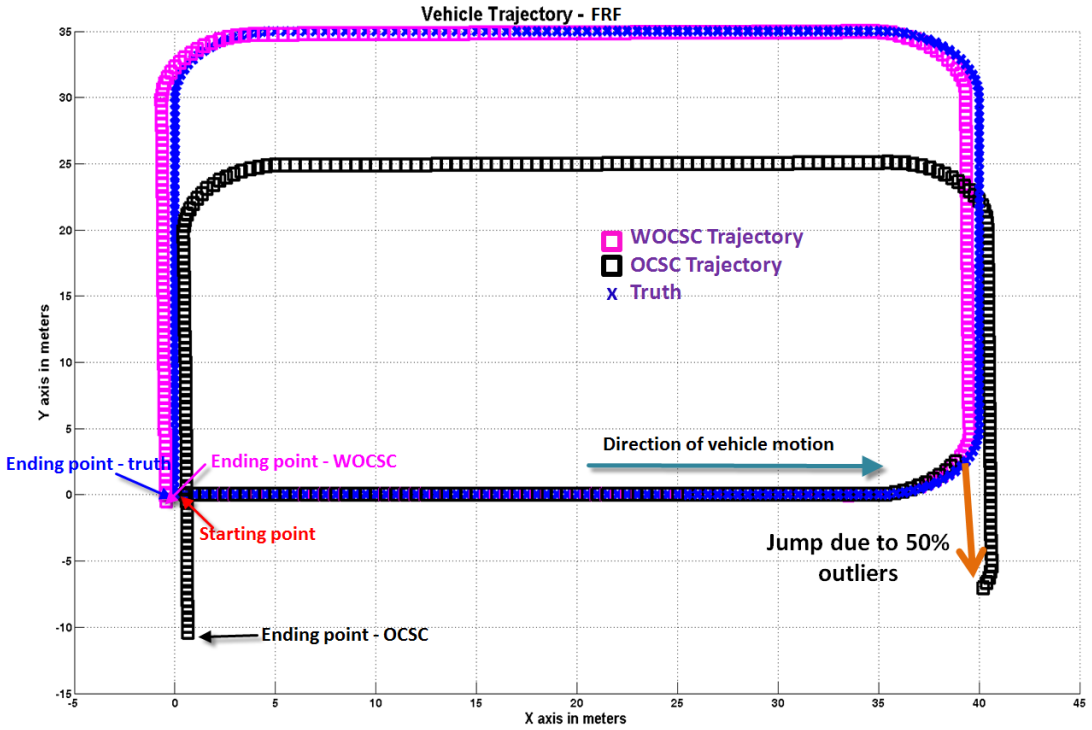

Figure 7.9: Generated trajectory comparison between OCSC and WOCSC methods, showing that WOCSC can handle 50% or more outliers. The scenario where OCSC fails is shown in figure 7.8. At epoch $\mathbf{k}+\delta = \mathbf{83}$, OCSC converges to an inaccurate optimal translation, resulting in a jump, and WOCSC overcomes this situation by using the confidence indicators **CPEF**.

Appearance test checks for the alignment between the two associated planes after compensating for the estimated rotation. Therefore, by turning it off, two planes located nearby (spatial neighbors), creating an equal angle with another plane, can result in a conflict, as shown in figure 7.11. Figure 7.11a shows such a scenario; at epoch $\mathbf{k} = \mathbf{262}$, planes **1** and **2** (tagged in green) represent the two facades of the building forming a corner, whereas at epoch $\mathbf{k}+\delta = \mathbf{263}$, the plane **1** (tagged in green) is not observed. The planes $\mathbf{1_{262}}$ and $\mathbf{2_{262}}$ are orthogonal, and therefore, have the same dihedral angle of $\mathbf{45}^\circ$ with the larger plane tagged as $\mathbf{3_{262}}$ (in green). This leads to an ambiguity for associating the plane **1** (tagged in red) observed at epoch **263**, with these two planes $\mathbf{1_{262}}$ and $\mathbf{2_{262}}$, when considered as a quadruple tuple with the plane $\mathbf{3_{262}}$ (or $\mathbf{2_{263}}$). Normally, this conflict is resolved by the *appearance test*, as it compares the angles between the associated pairs ($\mathbf{1_{262}}$, $\mathbf{1_{263}}$) and ($\mathbf{2_{262}}$, $\mathbf{1_{263}}$). The second combination has a better alignment ($\mathbf{0}^\circ$) compared to the first with $\mathbf{90}^\circ$. In the absence of this test, the conflict is retained and the ambiguity results in an outlier association, leading to a trajectory jump

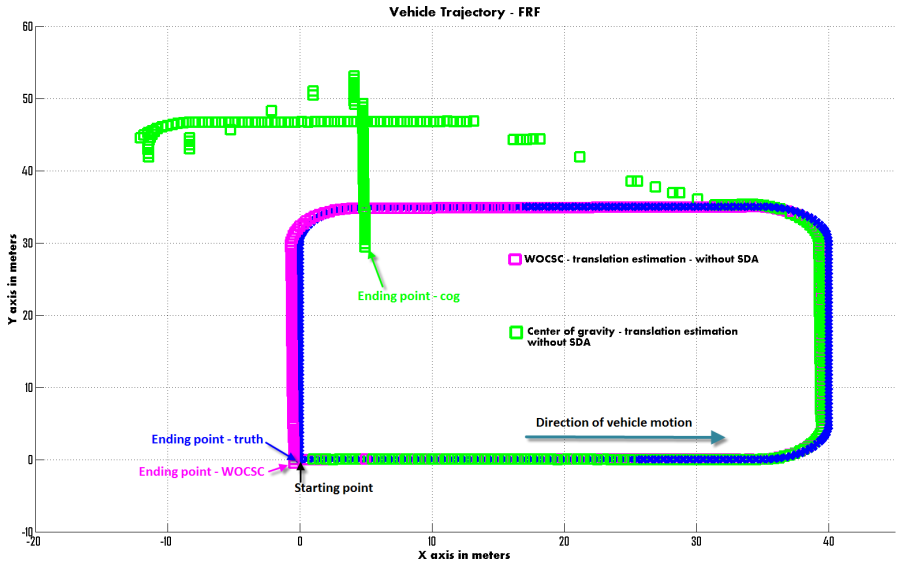

Figure 7.10: Figure demonstrates the importance of Strict Data Association (SDA) especially for the estimation of translation using center of gravity (cog) method. Trajectory generated from cog and WOCSC methods performed without SDA are given. As seen, cog method fails to close the loop, whereas WOCSC remains unaffected.

computed using the *cog method* (figure 7.11b). The result also proves that even a single ambiguous association is sufficient to affect the cog translation estimation, where as WOCSC remains unaffected.

These results demonstrate the importance of strict data association (SDA), and the sensitivity of the mean-based *cog method* to outliers. It also proves in all these scenarios the WOCSC algorithm performs satisfactorily, proving again its ability to cope with outliers.

- ***Scenario-02*: 10kmph run**
  The goal of this test is to validate the transformation estimation, when the data is acquired from a moving platform with a nominal mapping velocity of *LARA-3D*, without requiring a "'stop and go"' motion (stated in sections 5.2, 7.2.1).

  This dataset is generated using the *Scenario-02* described in section 7.3.2. The main difference with *Scenario-01* is that the laser scans are obtained continuously from the moving vehicle. Therefore, it is more closer to a real world situation, with both observation and motion noise affecting the measurement. Additionally, we use the forward and backward isoclinal pair of lasers to improve the observability of the scene (i.e., to see more planes).

  In this dataset, the vehicle is driven at $\sim$ **10** kmph with certain zones of accelera-

tion and deceleration. The dataset covers both *trajectory section-01* and *trajectory section-02*, as per figure 7.3. We chose to use a smaller time step $\delta = \mathbf{1}$, in order to retain the data associability with a relatively faster vehicle.

Figure 7.12 shows the results of the three proposed methods to estimate the trajectory. The offset between the trajectories estimated from two WOCSC methods (performed on associations with and without SDA) occurs in the zone of deceleration. This is because the order in which the ambiguity resolution algorithm (see in section 6.5.2) is applied, causing the removal of a valid association. The ambiguities are resolved by applying a row vote first, then the column one. If this order is reversed, at times, the converged injective associations can differ, removing some valid associations. As already mentioned, no ambiguity resolution algorithm can guarantee a perfect solution, as all the constraints cannot be applied simultaneously. However, our simple voting mechanisms can be improved further to tackle such a situation. Consequently, WOCSC without SDA managed to tackle this situation, despite the presence of several ambiguous associations, and produced a relatively better estimate of the true trajectory. The optimal candidate chosen by WOCSC is agreed by mutual consensus with all other candidate associations, therefore equivalent to applying a *simultaneous ambiguity resolution*.

In the rest of the section and figures, unless specified, WOCSC translation implies WOCSC translation method applied to the quadruple set $\hat{\mathbf{C}}^{\mathbf{3}}_{\mathbf{k},\mathbf{k}+\delta}$.

The error statistics are given in figures 7.13 and 7.14. From this, it can be concluded that the pitch rate is uniformly more noisier than the other two rotation rates, for the same reasons, as already explained while analyzing the effect of different noise levels. However, contrary to IMU, the yaw rate is less noisier, emphasizing that the solution is complementary to other localization senors. The translation errors are shown only for the methods of WOCSC without SDA and cog. The velocity error in the direction of motion (X translation error) is high in the zones of acceleration and deceleration (shown in figure 7.12), whereas the lateral velocity (Y translation error) is not much affected, having a σ half the magnitude compared to X translation.

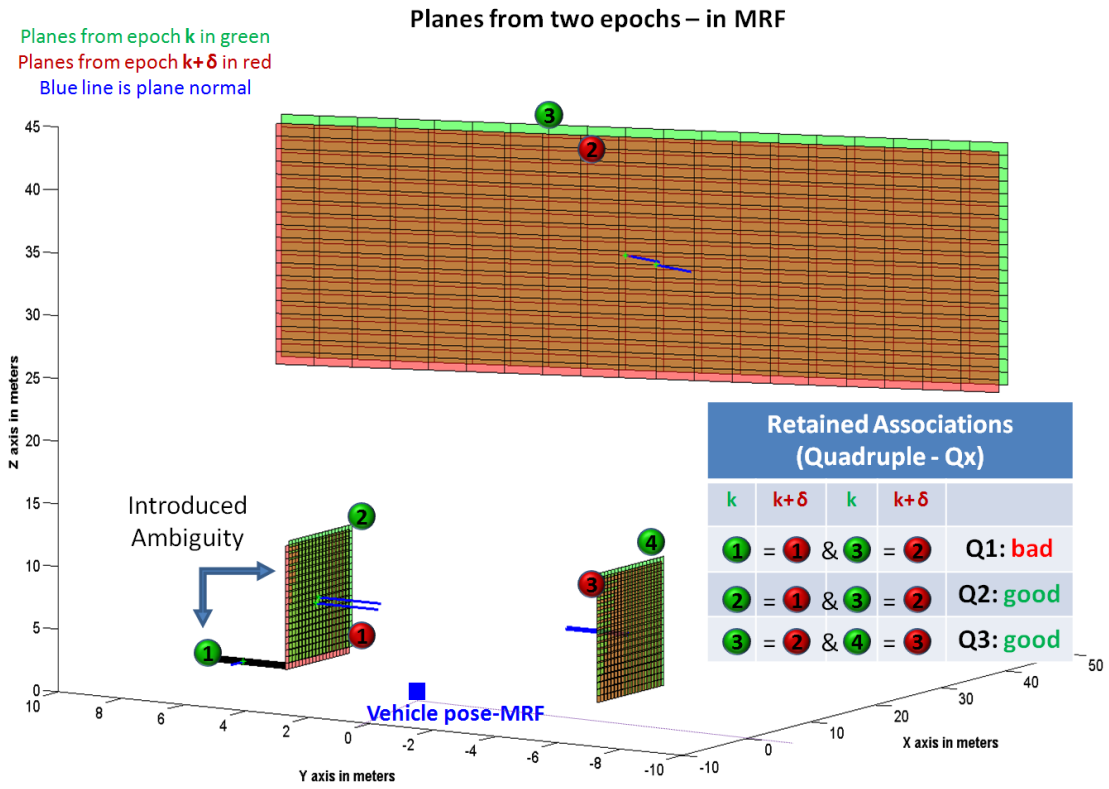

(a) Planes observed at epochs 262 and 263, and their retained associations

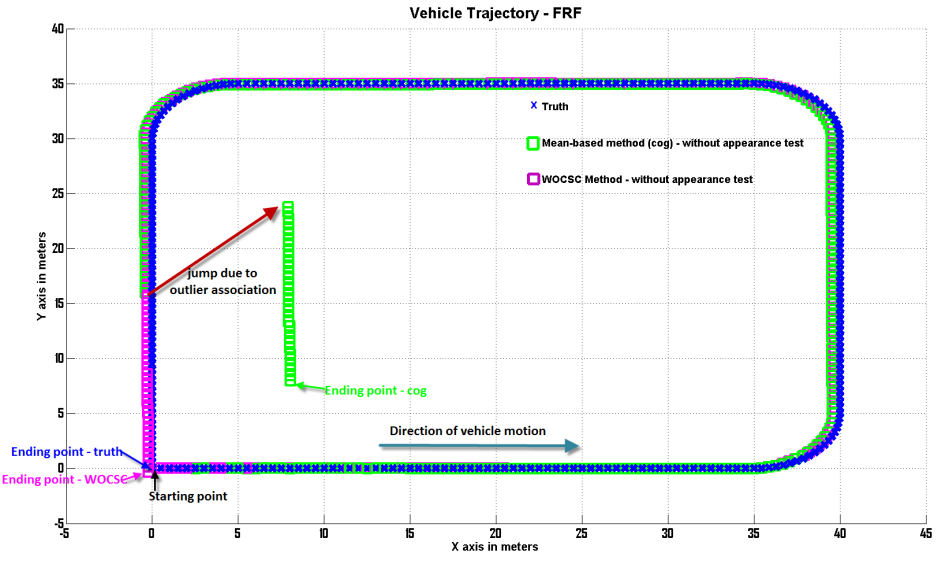

(b) Trajectories computed using cog and WOCSC translation methods

Figure 7.11: Figure demonstrates the importance of *appearance test* to resolve ambiguities, and also the sensitivity of cog method to even a single outlier. In the absence of appearance test, if two planes subtend an equal dihedral angle with a third plane, then the ambiguity to associate one of the two planes with the new set of observation still remains (an example is shown in figure 7.11a). The trajectory generated using cog method depicts this outlier (figure 7.11b).

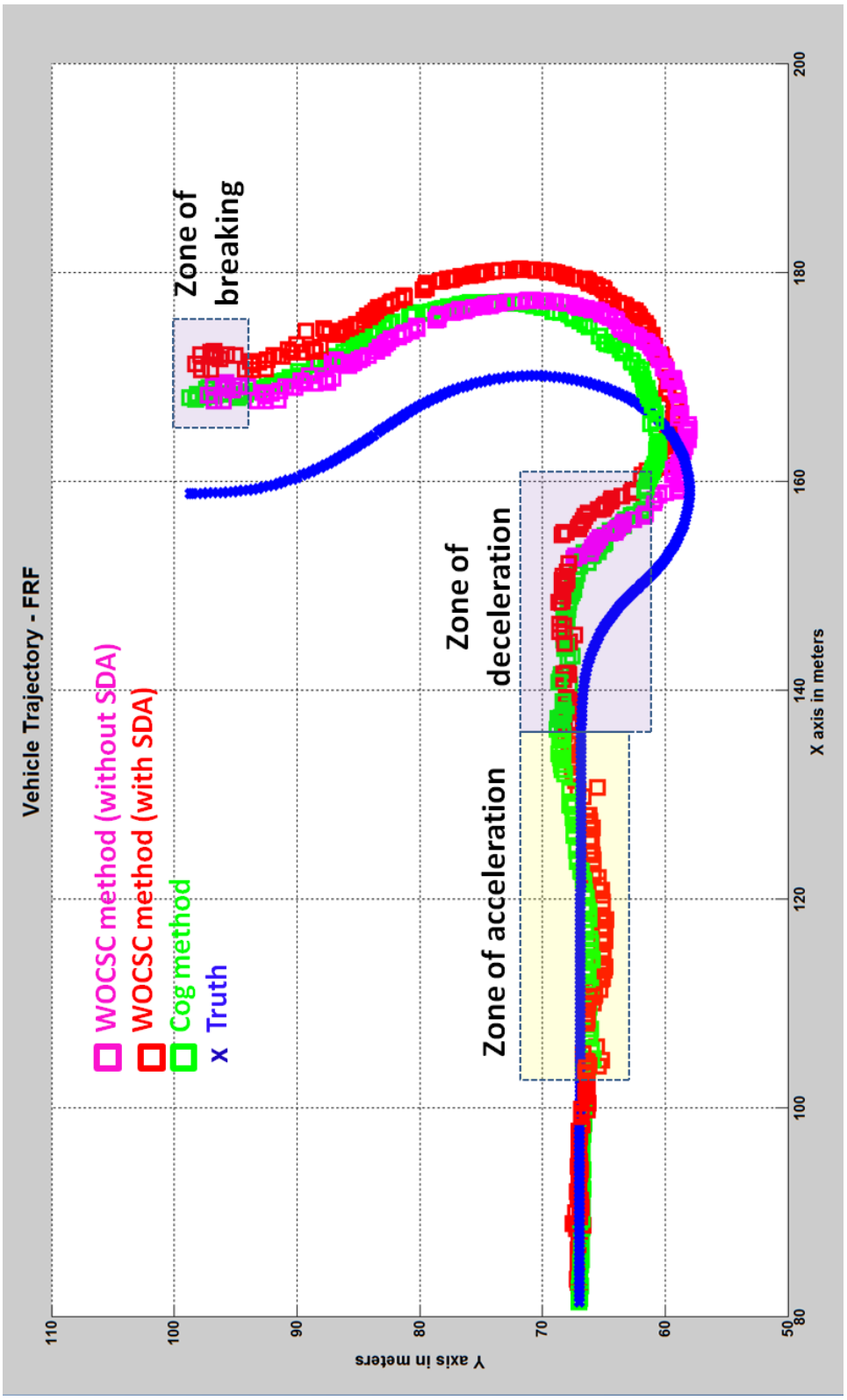

Figure 7.12: Three estimates of the trajectories for a vehicle driven at $\sim$ 10 kmph: (i) computed using WOCSC translation method without SDA (ii) WOCSC translation method with SDA ($\hat{\mathbf{C}}^{\mathbf{3}}_{\mathbf{k},\mathbf{k}+\delta}$ obtained after LDA, explained in section 6.5.1)(iii) cog method with SDA ($\hat{\mathbf{C}}^{\mathbf{5}}_{\mathbf{k},\mathbf{k}+\delta}$, refer to section 6.5.2).

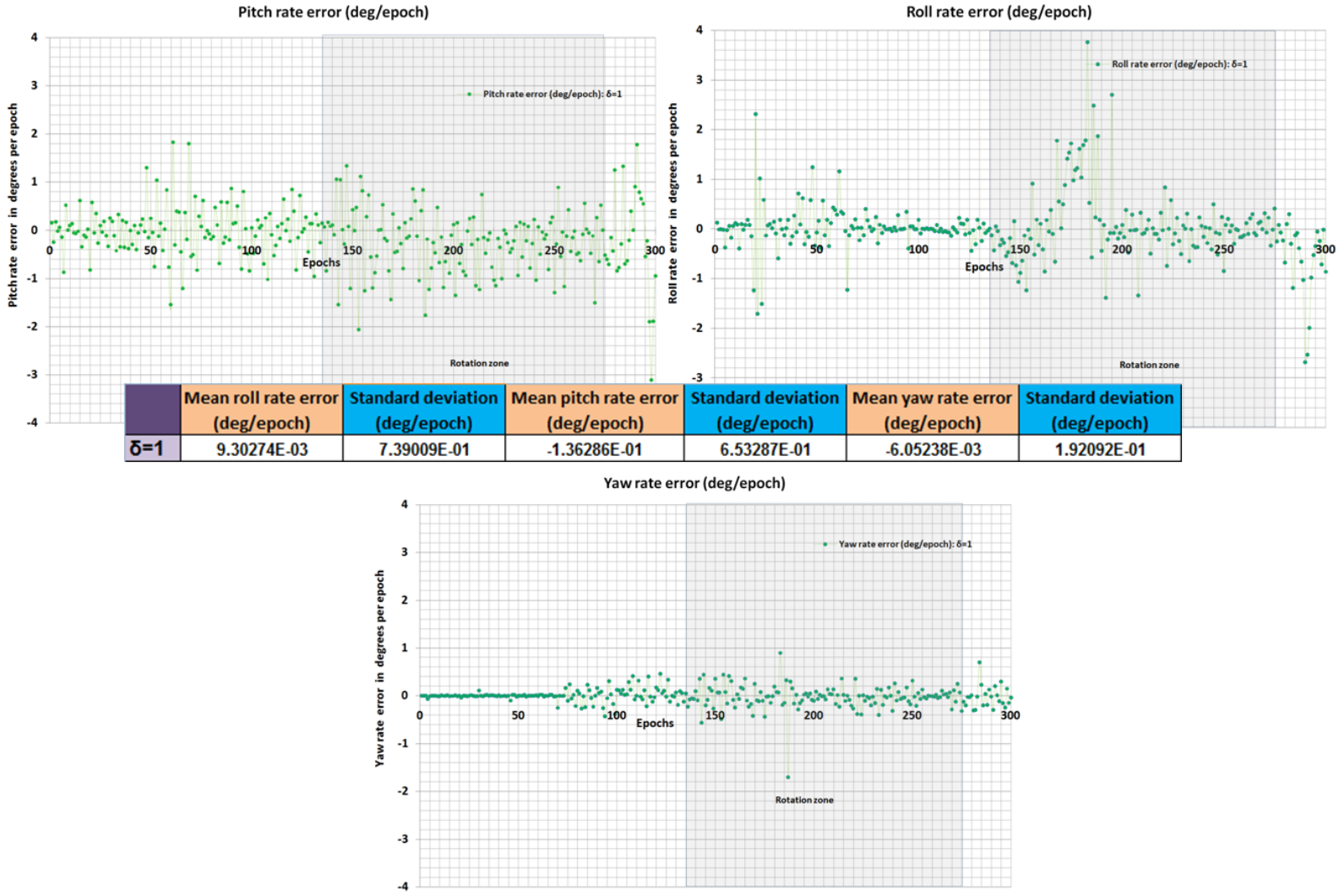

	Mean roll rate error (deg/epoch)	Standard deviation (deg/epoch)	Mean pitch rate error (deg/epoch)	Standard deviation (deg/epoch)	Mean yaw rate error (deg/epoch)	Standard deviation (deg/epoch)
δ=1	9.30274E-03	7.39009E-01	-1.36286E-01	6.53287E-01	-6.05238E-03	1.92092E-01

Figure 7.13: 3DOF rotation rate errors for the estimated trajectory (refer to figure 7.12), for a vehicle driven at $\sim$ 10 kmph. On each plot, the epochs corresponding to the rotation in the trajectory is highlighted. From the table of statistics given in this figure, as explained, the standard deviation for the pitch rate is expectedly higher. However, contrary to IMU, the yaw rate is less noisier, emphasizing that the solution is complementary to other localization senors.

This test demonstrates that the implemented algorithms indeed estimates the trajectory of a vehicle moving at $\sim$ **10** kmph, without the aid of any external pose sensors. The results ensure that the proposed method is capable of extracting the landmarks from the data acquired by a moving robot, not imposing the "stop and go" motion, as stated in sections 5.2, 7.2.1.

- ***Scenario-02*: comparison of a delayed association $\delta > 1$**

  The goal of this test is to validate that higher the association delay δ, better the estimation of the trajectory (refer to 5.3.3).

  This dataset is generated for the *trajectory section-02* of *Scenario-02*, where the vehicle turns in a roundabout (shown in figure 7.3), with a speed $\sim$ **5** kmph. We also use both the forward and backward isoclinal pair of lasers to improve the observability of the scene (i.e., to see more planes). We chose two time steps or epochs, $\delta = \mathbf{1}$ and $\delta = \mathbf{10}$, to compare the effects of delayed association on the estimated trajectory.

  In smaller time steps ($\delta = \mathbf{1}$), the effect of noise is higher compared to the actual signal (transformation), when moving at a lower speed (i.e., a lower signal to noise ratio). Therefore, by increasing δ, the signal to noise ratio can be improved, and the effect of noise on the trajectory can therefore be minimized.

  The transformation from pose at $\mathbf{k}$ to pose at $\mathbf{k+1}$, is the average transformation estimation between the two datasets $\mathbf{k}$ and $\mathbf{k}+\delta$, averaged by δ.

  As demonstrated in figure 7.15, the estimated trajectory improved significantly with $\delta = \mathbf{10}$.

  The improvement can be quantified from the error statistics given in figures 7.16 and 7.17. The delayed association with $\delta = \mathbf{10}$, reduces the standard deviation of all the 5DOF, by the factor of **10**.

  Therefore, delayed association is an excellent way to improve the quality of the resulting trajectory. It filters the noise and reduces the drift errors occurring due to the integration of the transformation estimation in a FRF (i.e., in the trajectory).

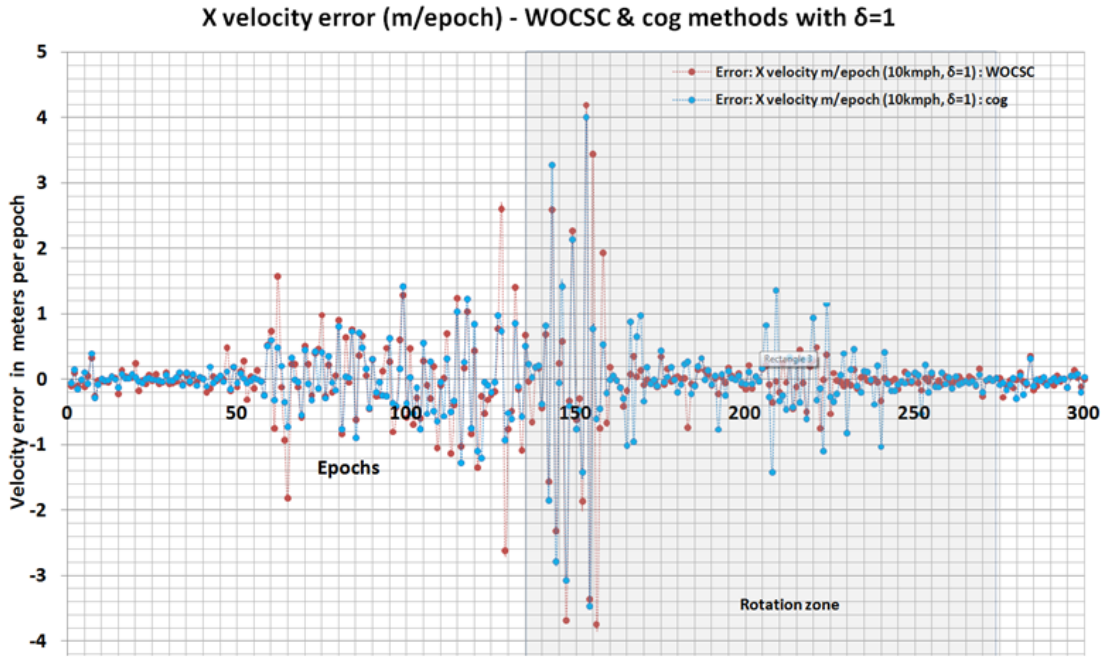

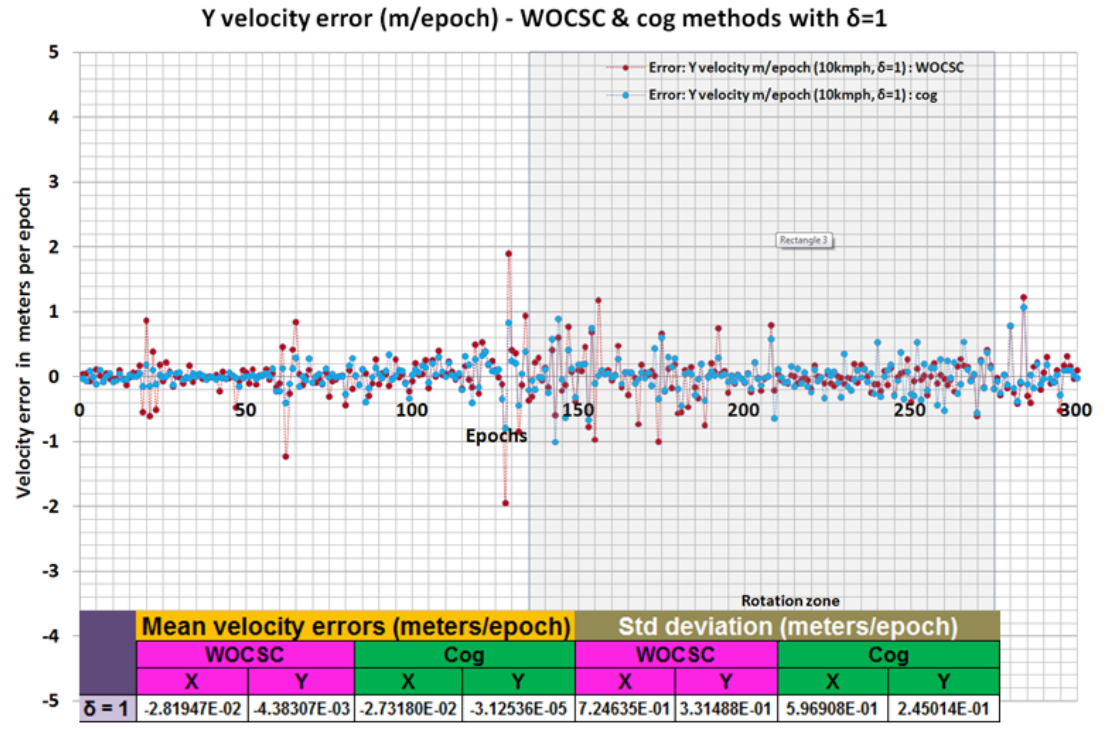

	Mean velocity errors (meters/epoch)				Std deviation (meters/epoch)			
	WOCSC		Cog		WOCSC		Cog	
	X	Y	X	Y	X	Y	X	Y
δ = 1	-2.81947E-02	-4.38307E-03	-2.73180E-02	-3.12536E-05	7.24635E-01	3.31488E-01	5.96908E-01	2.45014E-01

Figure 7.14: 2DOF (X and Y) translation errors for the estimated trajectory (refer to figure 7.12), for a vehicle driven at $\sim$ 10 kmph. The error statistics (refer to the table in this figure) for two alternative methods to compute translation: WOCSC without SDA and cog with SDA, are comparable. this demonstrates that in the absence of association outliers both the methods function equivalently. In each plot, the epochs corresponding to the rotation in the trajectory is highlighted.

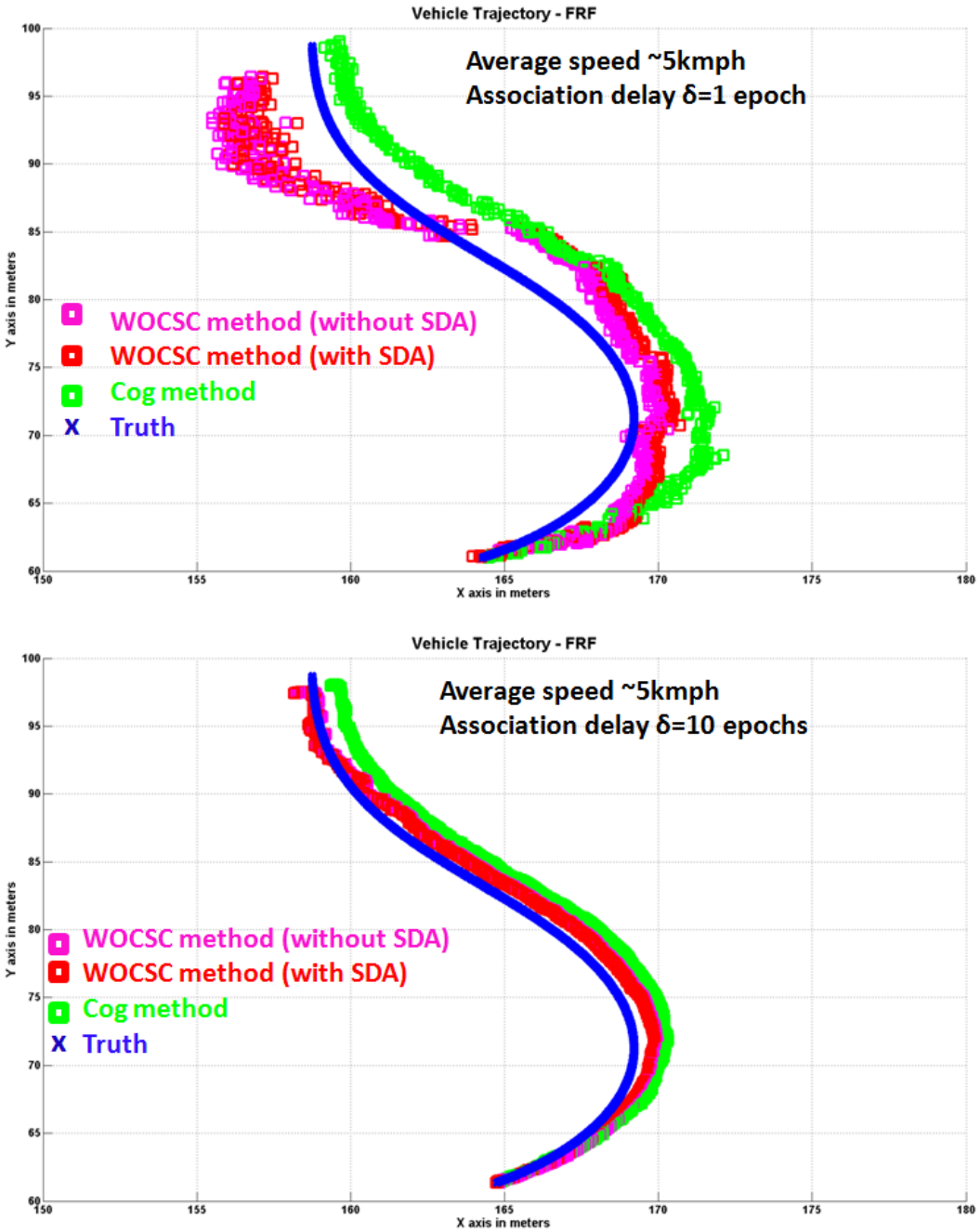

Figure 7.15: Trajectory estimation improvement using delayed data association. First figure is the trajectory estimation with association delay $\delta = \mathbf{1}$, and the second with $\delta = \mathbf{10}$. The association delay acts as a filter, and the obtained result is significantly improved.

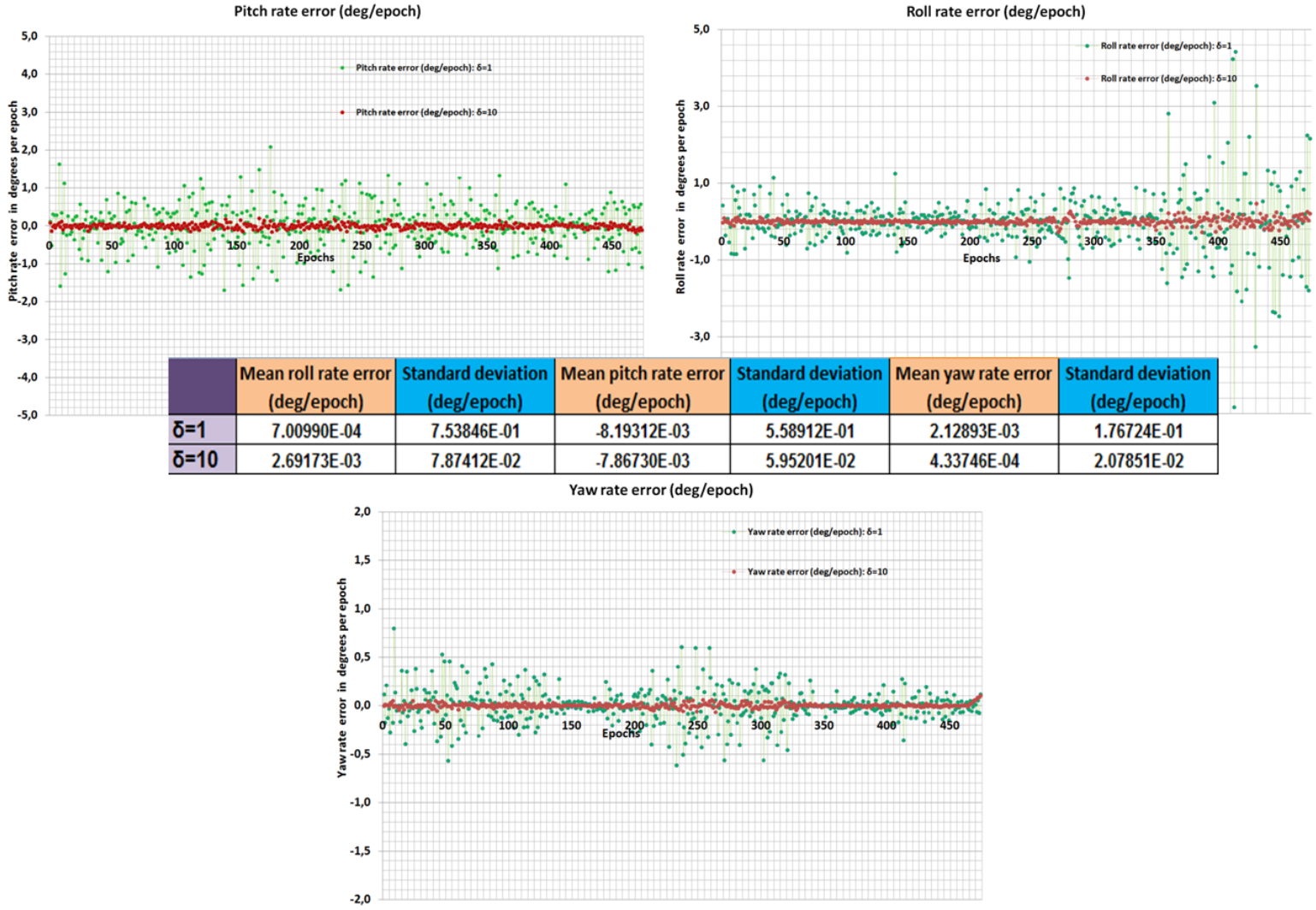

	Mean roll rate error (deg/epoch)	Standard deviation (deg/epoch)	Mean pitch rate error (deg/epoch)	Standard deviation (deg/epoch)	Mean yaw rate error (deg/epoch)	Standard deviation (deg/epoch)
δ=1	7.00990E-04	7.53846E-01	-8.19312E-03	5.58912E-01	2.12893E-03	1.76724E-01
δ=10	2.69173E-03	7.87412E-02	-7.86730E-03	5.95201E-02	4.33746E-04	2.07851E-02

Figure 7.16: Comparison of 3DOF rotation rates for the association delays of $\delta = \mathbf{1}$ and $\delta = \mathbf{10}$, for the trajectory given in figure 7.15. By referring to the error statistics given in this figure, the improvement in the obtained results is proportional to the delay δ (i.e. **10** in this case) for all the 3DOF.

7.4 A possible improvement

The experimental results signify that, by carefully choosing the value of δ, which separates the two associated data sets, one improves the trajectory estimation drastically. The same concept can be further enhanced by introducing a map in the laser odometry process. Maps retain history of all the past observations, and it gives visibility across multiple epochs. However, unlike the traditional SLAM approaches, where the map is updated whenever a new landmark is observed, we propose a delayed map update (similar to δ) to minimize the drift errors (occurring in the FRF). By constructing the map of landmarks with minimal pose errors, the drift, a common problem to SLAM approaches, can be minimized. As already mentioned, higher the association period (δ), better the estimation of pose. The usage of the forward and the backward isoclinal pairs of lasers permits to increase this update delay. For these reasons, we propose a method of delayed map update.

7.4.1 Delayed map update

As already introduced, the main purpose of delayed map update is to minimize the drift errors. We propose to construct a map of landmarks, and to associate a maturity status indicating the trust on their pose on the map. The landmarks with trusted pose on the map participate in the data association process, and therefore allow to compute the pose of the vehicle.

The proposed implementation updates the map in each measurement epoch with the new landmarks, similar to the traditional SLAM approach. However, by assigning a binary trust indicator (values *UNTRUSTED* and *TRUSTED*) to the landmarks, the concept of delayed update can be implemented. This also implies that the map evolves with two types of landmarks (planes in our case), *TRUSTED* and *UNTRUSTED*.

The newly observed landmarks are assigned with the *UNTRUSTED* status. The landmarks can transit only in one direction, from the *UNTRUSTED* to *TRUSTED*, and not in the other way. Using the properties of our specific laser arrangement, this transition can be done under two conditions:

- The planes $\rho_{\mathbf{k}}$ observed at epoch k by the forward laser scanner pair, becomes observable by the backward laser scanner pair at $\mathbf{k}+\delta$ as plane $\rho_{\mathbf{k}+\delta}$.
- Once a plane $\rho_{\mathbf{k}}$, is observed for more than a certain number of times. This is useful not only for building the initial map, but also when a vehicle is stationary or moving slowly.

These transitions are shown in figure 7.18.

The concept of *TRUSTED* and *UNTRUSTED* is analogical to the covariance in the general SLAM literatures, as it depicts the uncertainty in the observations, and therefore, the uncertainty on the derived vehicle pose. A diminishing gain filter (equivalent to Kalman filter) can be applied to correct the pose of the *UNTRUSTED* landmarks on the map, based on the generated corrections for the vehicle pose. Once all the landmarks attain a *TRUSTED* status, the mapping of the scene can be considered as finished.

Initially, at time $\mathbf{k} = \mathbf{0}$, the map is empty, and the first set of *TRUSTED* landmarks are built by keeping the vehicle in a stationary state. With repeated observation of the landmarks, they attain the status of *TRUSTED*, and then the robot can start its displacement.

As long as there is a continuity in the observation of associable landmarks (applicable even for scan correlation techniques), this technique can nullify the drift errors in the computed trajectory.

7.5 Conclusion

This chapter described the constructed algorithms and the implementation details of the methods presented in chapter 6. The results of different validation tests demonstrate the relevance of the concept, and the functioning, of the 5DOF laser odometry using vertical planar landmarks.

The optimal candidate selection algorithm (WOCSC) is proved as the critical step for simplifying the 3D transformation problem, by splitting the entire process (data association and transformation computation). The results prove that WOCSC handles even 50% of outliers, reduces noise (compared to mean-based cog, when exposed to noisy measurements) and handles outliers (works without strict data association).

The result from the simulations also shows that the transformation can be computed for a continuously moving vehicle. The trajectory can be further improved by using a larger delay between the two associated sets of data, permitting to have a better signal to noise ratio. Ideally, a higher association delay (meaning the landmarks remain observable for longer period), and a higher perception rate, can provide a continuous and better estimate of the trajectory. This is the advantage of using the forward and backward lasers, as it keeps the landmarks observable for a longer period of time, allowing a larger associable delays.

Motivated from this result, we propose a new delayed map update strategy for the typical SLAM approaches, to reduce the effect of the unavoidable drift errors.

This localization approach works well in the mapping environments with plenty of planar objects, where GPS (GNSS) receivers often fails. The experimental results also

proves that the yaw (heading) rate is less prone to noise, unlike the IMU. With the delayed association and map update methods, even the common localization problem of drift errors can be tackled. Therefore, the proposed solution is not only complementary to the common localization sensors but also addresses the pose in 3D space, meeting both objectives of this thesis.

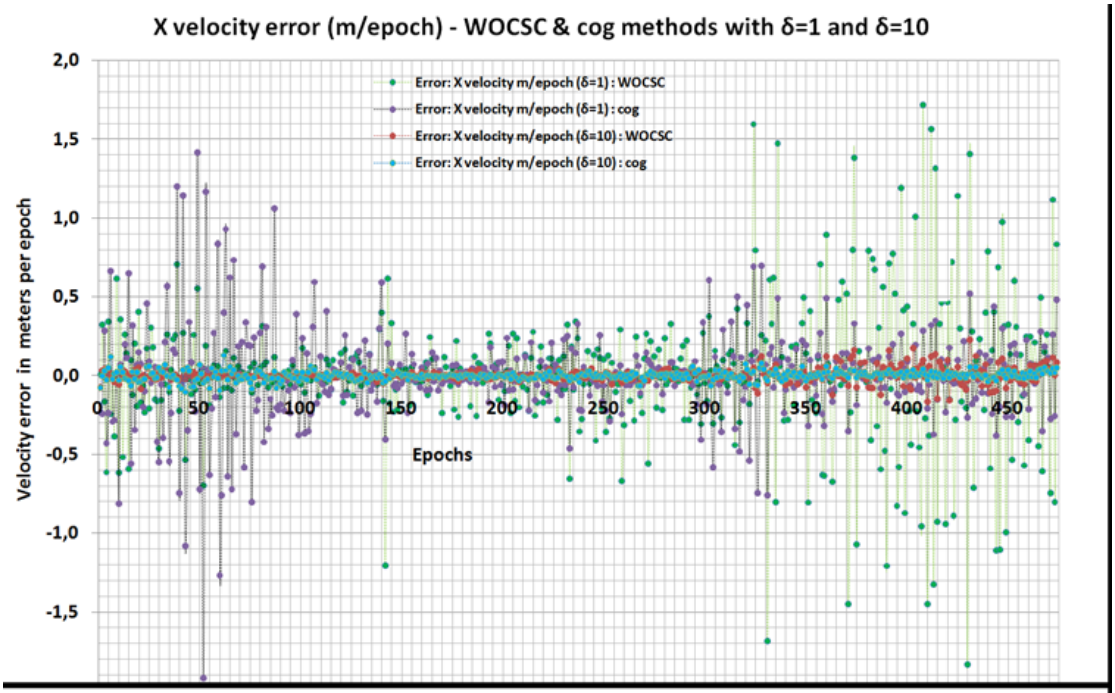

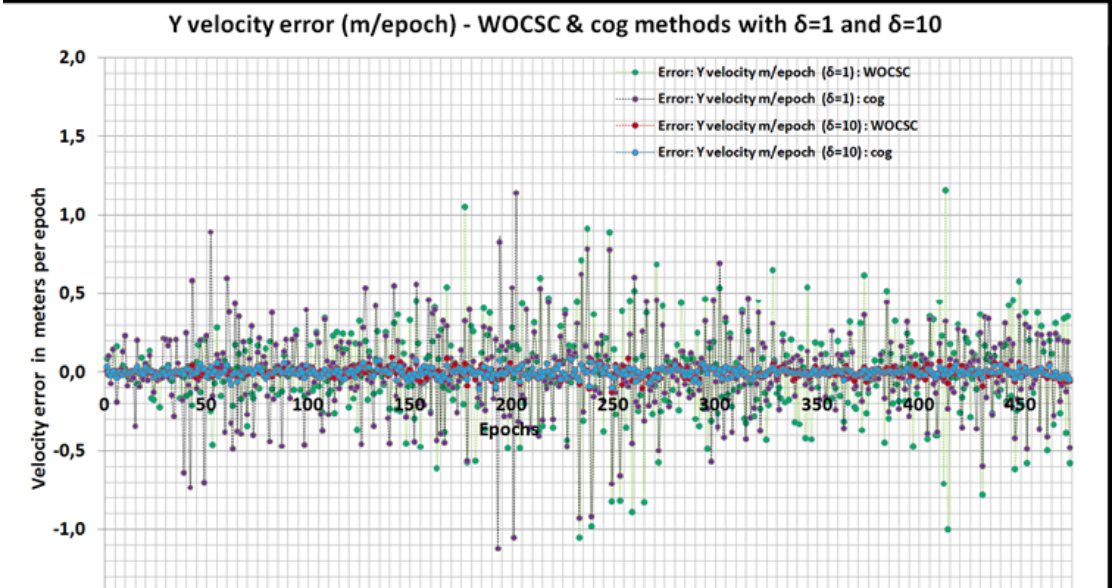

	Mean velocity errors (meters/epoch)				Std deviation (meters/epoch)			
	WOCSC		Cog		WOCSC		Cog	
	X	Y	X	Y	X	Y	X	Y
δ=1	5.95962E-03	-5.88643E-03	-8.71674E-04	-2.17604E-04	4.14635E-01	2.78114E-01	2.93114E-01	2.69400E-01
δ=10	1.57618E-03	-3.10892E-03	-7.27108E-04	-1.91178E-03	4.26523E-02	2.99742E-02	2.75920E-02	2.74808E-02

Figure 7.17: Comparison of 2DOF translation (X and Y) for the association delays of $\delta = \mathbf{1}$ and $\delta = \mathbf{10}$, for the trajectory given in figure 7.15. By referring to the error statistics given in this figure, the improvement in the obtained results is proportional to the delay δ (i.e. **10** in this case) for both the 2DOF.

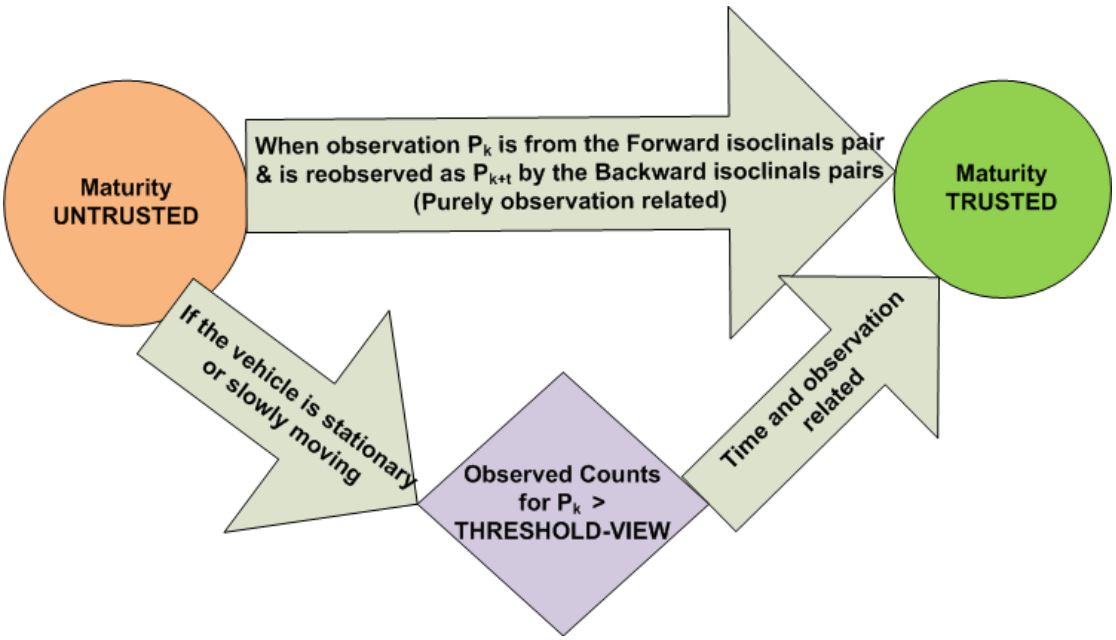

Figure 7.18: Proposed delayed map update method, and conditions for the transition of trust indicators (from *UNTRUSTED* to *TRUSTED*).

Chapitre 8

Conclusion

Ce chapitre conclut la thèse en proposant des pistes d'améliorations.

Après avoir résumé les deux solutions présentées, nous proposons des extensions envisageables pour chacune d'elle.

Cette thèse n'a fait que lever le voile sur la partie émergée de l'iceberg des possibilités offertes par l'utilisation des informations perceptives dans la localisation. Cet axe de recherche est très prometteur pour améliorer la localisation des systèmes de cartographie mobiles.

Chapter 8

Conclusion

Contents

8.1 Summary

This thesis, set its objective to develop methods to complement the existing 3D pose sensors to improve localization function of a land-based, laser Mobile Mapping Systems (MMS).

The research on the state of the art MMS, showed the shortcomings of the traditional localization techniques: dependency on GPS position fix, lack of 3D pose sensors, and high cost of a good quality IMU (supporting pose sensor for most MMS). Land-based MMS prototype platform, *LARA-3D*, too suffers from the known limitations of the localization sensors, similar to all MMS around the world. Some of the MMS minimize these errors by using high quality sensors, which are too expensive, and ill afforded by many applications.

The thesis presents a smoothing-based post mission processing method, to improve the 3D maps generated by MMS. Post mission implies, the trajectory is already estimated for the entire mapping period. This approach corrects any apparent errors (measured by pose signal discontinuities) in the trajectory by applying continuity constraints. Typical errors observed are in the altitude (least precise information in GPS position fix) and the azimuth or yaw (least precise information from IMU). The obtained results from this approach assures that the algorithms can improve appearance

of the generated point clouds. However, they are not suitable for precise localization, since they cannot handle slowly varying sensor/trajectory errors such as IMU bias, long period of GPS signal loss or degradation etc.

Then we explore the option of localization-based on perception sensors, which are integral part of the MMS for mapping purposes. We use 2D laser scanners, because they are precise, faster for data acquisition, and provide an easy way to capture the 3D information of the scene. In most cases they are cheaper compared to high end IMUs.

Perception-based localization techniques are used in the domain of Simultaneous Localization and Mapping (SLAM) for autonomous robot navigation in the indoor environments. Most of these approaches work in a 2D environment, since for indoor applications the assumption of a flat world holds good, and 2D pose computation is much easier to resolve. However, for an application like MMS, it is desirable to have a 3D pose. There are two main branches of SLAM approaches available in the literatures.

Feature based SLAM approaches often fail, as they associate the observed landmarks (identifiable features) on an absolute reference frame (a map), but due to growing uncertainties, the association of the already observed landmarks with the new observations (Data Association, DA) often fails. Scan matching SLAM approaches are based on optimization algorithms, attempts to resolve both transformation and DA in a single process (also in a relative reference frame), therefore exploding the time complexities to converge to an optimal solution.

We opt to take advantage of both these approaches, first, by using planar features as landmarks (to reduce the search space for the solution), and then computing the transformation in a relative reference frame (like scan matching). This can be categorized as a *laser odometer* approach, since we use laser scanners for the perception of landmarks. We present a novel plane extraction technique, using a pair of synchronized 2D laser scanners, for quick acquisition of the landmark data in such a short time that the properties of the landmarks are not deformed, even when scanned from a moving platform. The successful extraction process is demonstrated using both simulated and real data.

The next step in the *laser odometer* approach, is to exploit the time invariant properties of the landmarks (dihedral angles, intersection points etc.) to estimate the relative transformation between two sets of observations. However, to do so, a correct association between the two sets of landmarks (DA), needs to be performed. The aim of this thesis is also to address the complementary pose in a 3D space. To simplify the computation of complex 3D pose, we use a Divide and Conquer (D&C) approach, performing the DA and transformation estimations separately (contrary to scan matching) and also splitting both these operations in two. The sequence of operations are: A Lenient Data Association (LDA), 3DOF rotation estimation, a Strict Data Association (SDA), and a 3DOF translation estimation. However, since most of the manmade structures are

eruct, only 5DOF pose (3DOF rotation and 2DOF translation) is a feasible solution with planar landmarks. We foresee that, an image sensor added along with the laser scanner pair, can help to compute the 6^{th} DOF.

LDA is the first step in the sequence of algorithms, implying it has to be compensated for all the unknowns relating to the different degrees of freedom. The relaxed relationships for association can result in some ambiguities, and hence, some outliers. An algorithm is needed, which can identify the required minimal set of associations, even in the presence of outliers. This is a critical step for D&C approach. We present the Optimal Candidate Selection by Consensus (OCSC), and its Weighted variant (WOCSC), which not only performs this task, but also computes the optimal transformation by consulting (democratic) with all the set of observations. This approach therefore, works much better in comparison to a mean-based approach, which creates biased solutions in the presence of even a single outlier. Therefore, the rotation estimation is computed using WOCSC approach. Once the rotation is estimated, remaining ambiguities can be resolved by SDA, applying stringent constraints. Following that, the translation can be computed by either a mean-based method (averages noise, if Gaussian, then it reduces it to almost zero) or again by applying WOCSC.

These algorithms are validated using two experimental simulated data sets. The approach of WOCSC proves to be good alternative for transformation estimation: in the presence of noisy and outlier associations, as well as democratically resolve ambiguities. In comparison to simple OCSC, WOCSC has a slight advantage, it can even survive the presence of 50%of outliers, with a good weighting function. The results also demonstrate that the mean-based approach fails even in the presence of single erraneous association where as WOCSC has no effect of such situations. In these analysis, we observed that the pitch rate errors increase signifcantly compared to other DOF as the noise level increase. This is because, the planar landmarks in direction perpendicular to the vehicle motion (incidence angle 0°), gets the full magnitude of the laser measurement noise. However, the yaw rate is less affected, thus complementing the IMUs. Finally, by increasing the association delay δ, between the two observation sets, we improve significantly the estimated pose, minimizing the drift in the trajectory. This motivated us to present a design for a novel delayed map update method, which can prove to be a solution to the drift (in the absolute pose, w.r.t. a map) errors observed in all the odometry, IMU and SLAM approaches.

8.2 Future extensions

From the results obtained in this thesis, many research axis can be developed to improve localization. Some of these future improvements are listed below.

- Post processing improvements

  Presented post mission processing can be further improved by using Rational B-Splines, a variants of the Rational Bézier Curves. This interpolation technique provides a mean to quantify the quality of the control points or knots, used for interpolation. The quality can be determined by the quality of the sensor information. For e.g. a GPS receiver provides Dilution of precision (DOP) indicator as a quality parameter on it's estimated position fix.

- Perception-based solution : real data validation

  The current implementations of the algorithms is done in MATLAB and validated using simulated environments. These implementations can be integrated to environments such as ^{RT}Maps, and the real data acquired from *LARA-3D* can be used for algorithm validation.

- Extension to compute 6DOF transformation

  Algorithms given in chapter 6 computes 6DOF information in the ideal environments where always at least three linearly independent planar features are visible. However, such situations are very rare in the typical manmade environments, because most of the planar features are normally vertical. Due to this constraint, it becomes impossible to compute the vertical displacement parallel to the eruct planar features. Therefore, in many cases, in the ideal environments only 5 DOF information can be extracted. By using an additional sensor such as a camera, one can compute the missing vertical information (by using the 5 DOF transformation parameters already computed, this step is simplified). Moreover, the camera can help in merging the lines and planes for tackling occlusions.

  In the future extensions, multilayer laser scanners can be used instead of 2D laser scanners to extract the planar features. This avoids the scanner synchronization step explained in chapter 5.

- Additional feature extractions

  This first level of modeling only handles one of the most recurrent features of manmade environments - planar landmarks. In the future extensions, various other features can be extracted, such as ellipsoidal, cylindrical shapes, which can complement the planar features to compute the 3D pose. The final goal is to come up with a computationally effective algorithm, which can work both in the structured and unstructured environments.

- Generation of 3D point clouds from features

An approach to compute the 3D transformation is to use Iterative closest point(ICP) algorithm between two set of 3D points obtained using a 3D scanner.

If ICP needs to be used for scan registration purposes, a randomly sampled dense 3D points from the extracted planar landmarks can be easily obtained. In this way, without using any additional 3D sensors one can obtain 3D planar point clouds for generating test data for the ICP based approach. This is a faster approach to generate 3D points than using the servo motor based 3D scanning.

8.3 Epilogue

Perception-based localization is natural to humans, and is the most promising way of improving the localization functionality for a Mobile Mapping System. If this axis is combined with the algorithmic post-mission processing the localization can be significantly improved. This thesis just scratched the tip of a potential ice burg. The precision and perception abilities of the sensors such as laser scanners, digital cameras, are expected to improve, and this branch of research is likely to become popular in the time to come. Applications will open up not only in this planet, but much beyond our own planetary systems, and the feasible future homes of mankind.

Publications & conferences

International conferences with proceedings

K. Narayana, S-W. Choi & F. Goulette. Localization for mobile mapping systems, experimental results, analysis and post-processing improvements. Proceedings of the 6th International Symposium on Mobile Mapping Technology, Brazil, 2009.

K. Narayana, F. Goulette & B. Steux. Planar Landmark Detection Using A Specific Arrangement of LIDAR Scanners. Proceedings of the Position Location and Navigation Symposium 2010, USA, 2010.

Other communications

K. Narayana, F. Goulette. Localisation for Mobile Mapping Systems, experimental results and analysis on rural and urban environments, GDR Journée de Localisation, GDR robotique, Paris, January, 2009

K. Narayana, B. Steux & F. Goulette. A planar feature-based SLAM like approach to aid localization, Journée: Avancées en Traitement du Signal et en Fusion pour la Localisation, GDR robotique, Paris, June, 2010

Appendix A

GNSS receiver analysis in mid urban environment

Figure A.1 shows the trajectories obtained using a GNSS receiver, and the effects of the ULEE errors (refer section 2.8) in this trajectory. The tests are done near the laboratory (Mines ParisTech) in the 6th district of Paris. The GNSS receiver used for these tests is the PRO XRT receiver from Trimble. It has the ability to process both GPS and GLONASS satellite signals. It has the clear advantage to observe numerous satellites, and therefore, expected to increase availability and accuracy of the computed position fix. This receiver has 72 channels (thus capable of simultaneously tracking 72 satellites) with processing abilities for $L1$ PRN code, and $L1$ and $L2$ carrier phase signals. This receiver could attain a position fix accuracy of 10 cm under the open sky environments, with certain post processing. The data is available at 1 Hz ([Trimble 08]).

During the test the receiver is configured to process GPS, GLONASS and a differential corrections from SatInfo GNSS network (refer to Annex B). However, the main problem is the presence of ULEE (section 2.8.1), which can vary from user to user depending on its location and the time. As it can be seen in figure 2.8, the position fix has outages at several occasion. This is either due to the reduction in the number of visible satellites to less than 4 or due to a high DOP, meaning poor visibility to the clear sky. Multipath effects are observed in the street rue Gay-Lussac resulting in jumps up to 50 meters. The position fix outages occurred in the streets, rue Royer-Collard and rue St-Jacques. This is due to the bad DOP, a typical effect of urban canyon.

(a) Trimble Pro XRT receiver

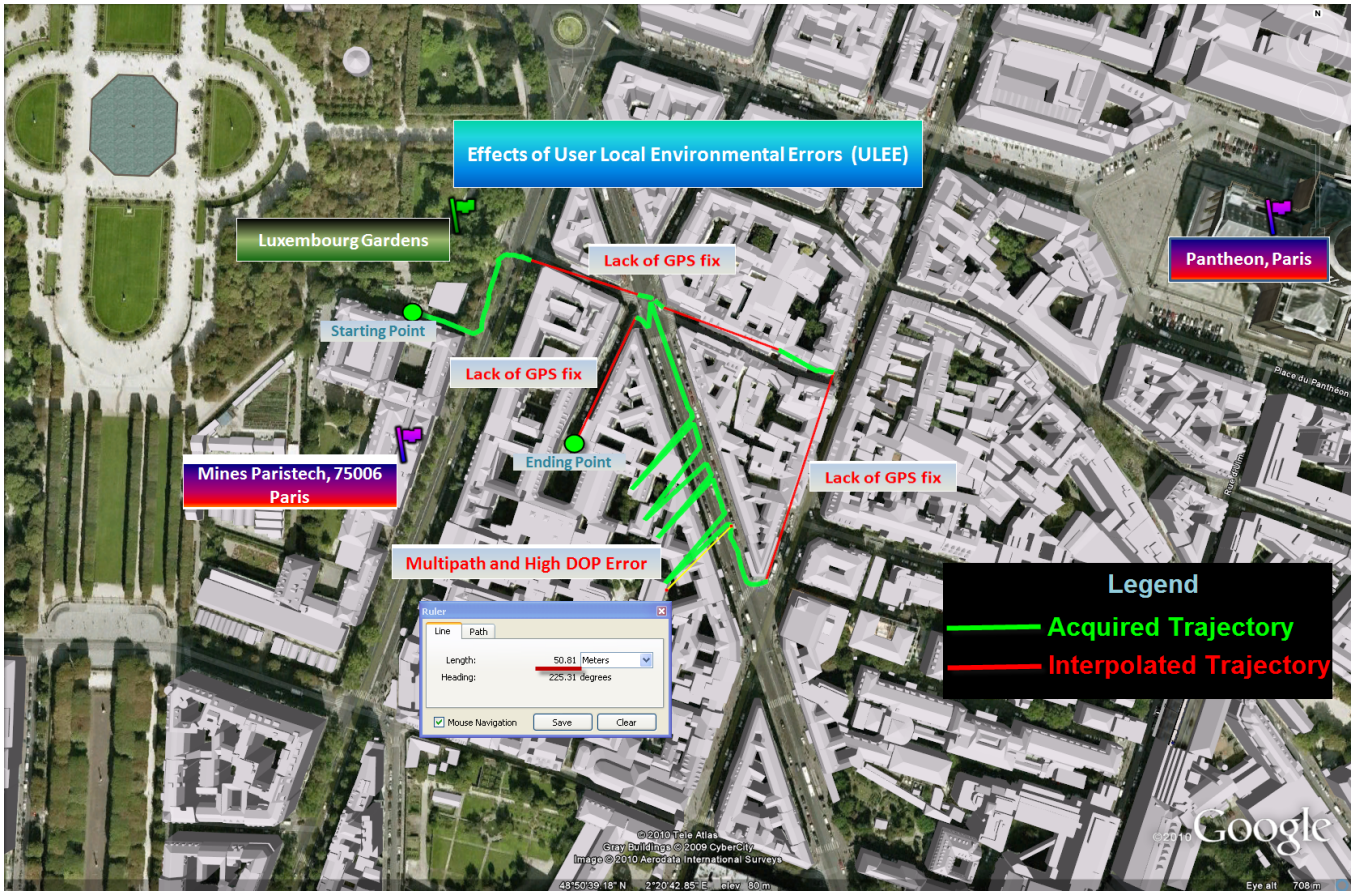

(b) ProXRT results - from Paris

Figure A.1: Test results in urban areas using a GNSS receiver (Trimble Pro XRT) showing the problems of ULEE errors (multipath, high DOP, lack of position fix etc.)

Appendix B

Differential GPS analysis

GPS fix augmentation systems

As already mentioned, GNSS position fix suffers from several systematic errors. Most of these errors are either corrected or mitigated using algorithms within the receiver or using different differential correction techniques. A short list of differential techniques are given, which not only help in reducing the systematic errors, but also provide some kind of trust measure on the position fix (integrity).

- *Differential GPS (DGPS)* DGPS is a system, whose goal is to improve the accuracy of the GPS position fix by providing correction information for the various error sources originating from the space segment (Satellite Orbital and Clock Errors) and from the environment (typically Ionosphere). DGPS uses a network of ground-based, fixed reference stations with known positions to compute the difference between these known positions and the one computed using GPS signals. This way it can determine the various error factors of the GPS fix.

  The present DGPS systems could be primarily categorized in two types: Ground Based Augmentation Systems (GBAS) and Space Based Augmentation Systems (SBAS). The primary difference is the service area over which the provided corrections are applicable. GBAS uses local beacon stations to transmit the corrections, and the SBAS uses the geostationary satellites. The primary corrections comprises the satellite orbit, the satellite clock corrections (slowly varying and fast varying parameters), and the ionospheric corrections over the local area. The corrections for the atmospheric errors (Ionosphere and Troposphere) are applicable only for the local area. Thus the accuracy of the corrections is closely related to the closeness of the fixed reference stations to the receiver, and the density of the fixed reference stations.

Some of the operational DGPS technologies over Europe are *Omnistar* which provides worldwide DGPS service using satellites, and *European Geo Stationary Navigation Overlay Service (EGNOS)*, the SBAS service available over the European region.

- *Real Time Kinematics* The accuracy of the resulting range measurement is generally a function of the ability of the receiver's electronics to accurately compare the signal transmitted by the satellite and the internally generated replica in the receiver. In general receivers are able to align the signals to about 1% of one bit-width. The receivers use the Coarse-Acquisition (C/A) code in the Pseudo Random Noise (PRN) signal (used for uniquely identifying the transmitting satellite) to perform this alignment to deduce the range measurement which has a bit width of 0.98μs, corresponding to ~ 3 m in terms of range.

  RTK follows the same general concept, but uses the satellite's carrier frequency as its signal, not the messages contained within. The possible improvement using this signal is potentially very high if one continues to assume a 1% accuracy in locking the signal. For instance, the GPS C/A code broadcast in the $L1$ signal changes phase at 1.023 MHz, but the $L1$ carrier itself at 1575.42 MHz. This frequency corresponds to a wavelength of 19 cm for the $L1$ signal. Thus a 1% error in the $L1$ carrier phase measurement corresponds to a $1.9mm$ error in the baseline estimation.

  The problem with RTK is that the carrier phase signals are not encoded like the PRN signals. Thus every cycle of the carrier phase appears the same. The alignment of the phase is easy within a cycle but matching the cycles is a complex problem known as *integer ambiguity*. The carrier phase signal, once locked, must be tracked continuously otherwise it takes certain time and algorithmic effort to resolve the problem of integer ambiguity. The loss of lock problem is called *cycle slips*. Normally a fixed base reference station is used whose antenna has a clear view to the sky. The moving sensing platforms, called rovers, are connected to this fixed base station to obtain the correction signals. The base station shall be geographically closely located to the user to estimate the correct atmospheric error parameters.

  Several companies have come up with the concept of Virtual Reference Station (VRS), where they make use of a network of base stations to provide service to a certain area. SatInfo, Teria and Orpheon are some examples for such systems operating in France.

- *Offline Corrections* For the applications suitable for offline processing, there are data centers such as European Space Operations Center (ESOC), which provide the correction parameters for the satellite orbit, satellite clock and ionosphere errors. They use the International GPS Service (IGS) network to obtain the data inputs to compute these corrections. These correction data are made available with different delays depending upon the accuracy needed. For example, ESOC provides ultra-rapid data twice a day (in the form of .sp3 files), daily data at two

different rates, daily rapid within 10 hours, and the daily final data within 11 days etc. (ref:http://nng.esoc.esa.de/gps/dat_ana.html).

These corrections can be integrated to the data acquired from the GPS raw range data, and the position fix could be recomputed offline. Thus it helps to reduce the space and control segment errors, and to tackle certain parameters of the ionospheric delays.

Test results with DGPS (EGNOS) using Trimble Ag332

Tests were performed by keeping the antenna of the single frequency GPS receiver Trimble Ag332 at a fixed location. The antenna was kept in an environment surrounded by buildings and trees, so ULEE like multipath are unavoidable. These tests are performed on two consecutive days at the same time (2^{nd} and 3^{rd} April 2009 at 20:05 hrs) to ensure that the satellite configurations were similar. Same receiver configurations are used, including the satellite mask angle (8°), accepted signal to noise ratio (10 to 60). There were 9 GPS satellites visible during the two test scenarios. Tests were conducted for a period of 12 minutes. GPS receiver was configured to provide output at the rate of 10 Hz. DGPS correction signal is provided by the EGNOS geostationary satellite AORE (PRN 120). Obtained results are compared in figure B.1.

In figure B.1a, the horizontal error (Latitude and Longitude) varies in diameter from 13.5 m without DGPS to 6.5 m with DGPS. This shows that the EGNOS signal reduced the horizontal position error by nearly 50%. Similarly from figure B.1b, the maximum altitude error in the observed period of 12 minutes is $\sim$ 30 m for the case without EGNOS, and $\sim$ 7 m with EGNOS, again a signifiant improvement.

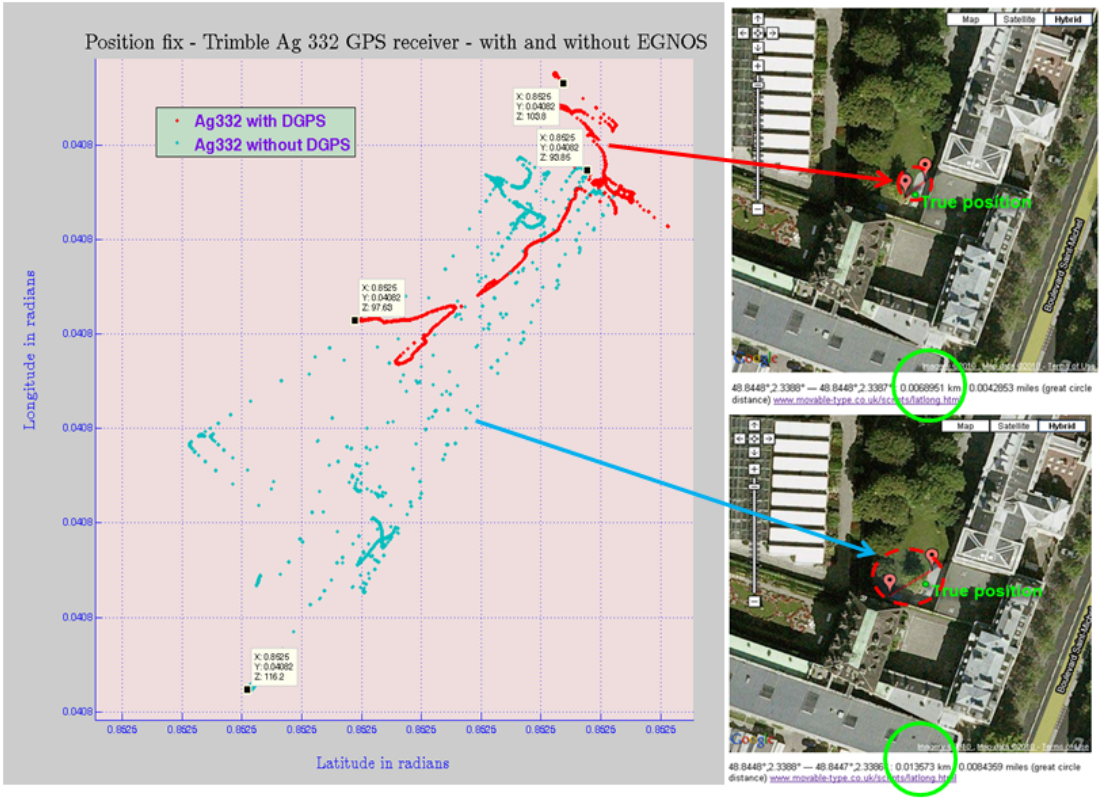

(a) Trimble Ag332 - with and without EGNOS - horizontal error

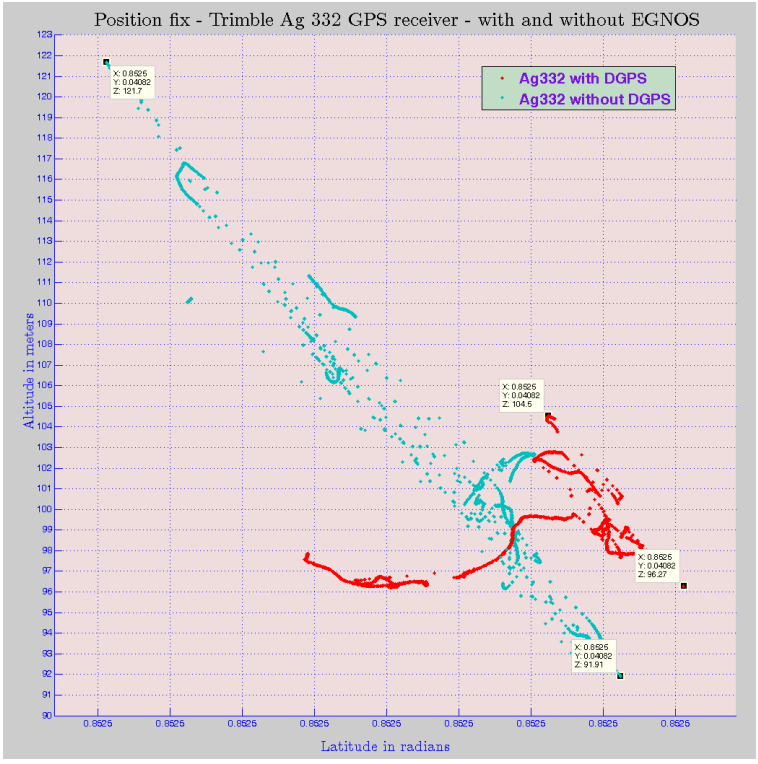

(b) Trimble Ag332 - with and without EGNOS - vertical error

Figure B.1: Improved GPS position fix by using a DGPS (EGNOS). Tests done using a single frequency GPS receiver (Trimble Ag332).

Appendix C

Effect of simulated GPS loss on pose

Using the acquired data from the *LARA-3D* platform around Panthéon in Paris, we performed some tests to measure the impact of the GPS position fix loss on the computed trajectory. The acquired GPS data is removed from input stream for a given period. Four different instrumentation of loss of GPS data are simulated: no loss, loss for 2 to 4 seconds, for 10 to 20 seconds and for 2 minutes. The results are shown by the plots with planimetric views (X and Y axis) and the altitude information. The planimetric plots represent the X and Y coordinates of the trajectory during the acquisition, and altitude plot shows the distance cruised on the horizontal axis and altitude on the vertical axis. All data losses in these simulations are instrumented to start after the initial 3 minutes of the data acquisition.

This test concludes that the present localization technique employed in the *LARA-3D* platform is very sensitive to the GPS fix outages. This behavior is a common problem for MMS relying on medium range localization sensors. Even when the signal outage period is 2 to 4 seconds there is an obvious dragging effect seen due to the drift errors in the INS observations, slowed by the EKF. The loss of 2 to 4 seconds is a very common phenomena in the mapping environments such as urban area.

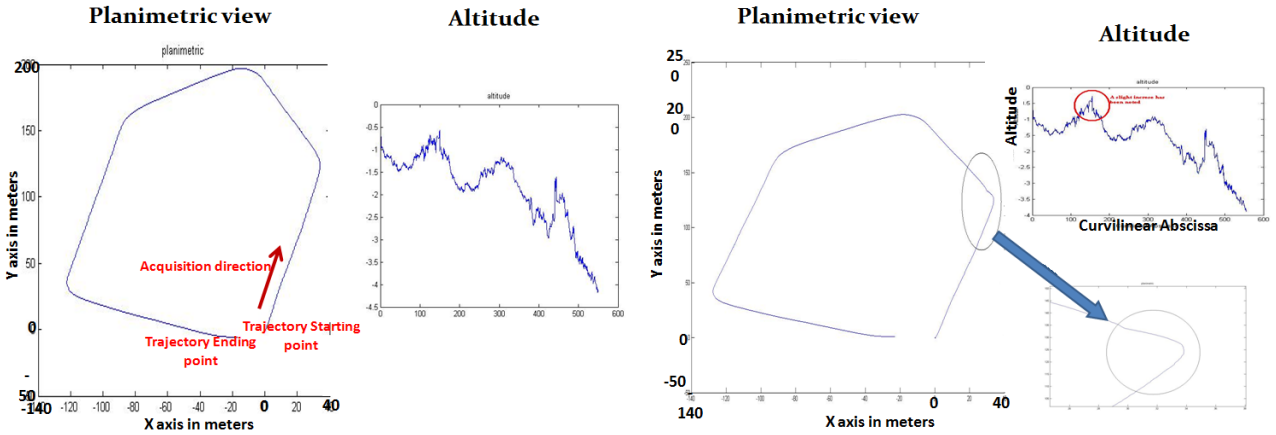

(a) Reference trajectory - No loss

(b) 2 to 4 seconds of GPS fix loss

(c) 10 to 20 seconds of GPS fix loss

(d) 2 minutes of GPS fix loss

Figure C.1: Results of simulated GPS data loss performed to analyze its effect on localization (tested with *LARA-3D*). Each subfigure for each of the four cases, contains a planimetric view or the top view of the trajectory, and an altitude plot or side view of the trajectory. As it can be seen, more the period of data loss, worst the degradation of localization, depicting a dragging effect due to the data fusion filter used (EKF).

Appendix D

Analysis of a low cost navigation sensor

A Micro Electro Mechanical System sensor - MTi-G

These are the newly developing sensor solutions for the navigation purposes, with advantage of low cost, tiny size, less power consumption and integration of several sensors in one small module. According to [Schmidt 04], by 2020 they expect to achieve the necessary accuracy to even be used in military applications. We analyzed the performance of a specific model called MTi-G Xens Technologies (figure D.1).

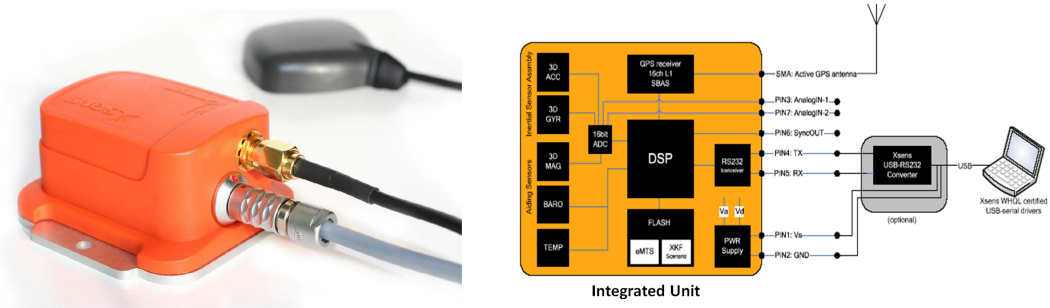

(a) Integrated miniature sensor MTi-G

(b) MTi-G sensor architecture

Figure D.1: Low-cost integrated MEMS sensor - MTi-G [Technologies 07]

MTi-G sensor is a miniature Navigation and Attitude and Heading Reference System (AHRS) with integrated data processor, a GPS receiver, Micro Electro Mechanical System (MEMS) Inertial Measurement Unit (IMU) and additional aiding sensors such as a

3D magnetometer and a static pressure sensor. It uses a loosely coupled Kalman Filter (XKF, Xens Kalman Filter) for sensor data integration. The primary sensor is a MEMS based IMU/INS. The integrated GPS receiver corrects the IMU measurement biases. Additionally, a pressure sensor (barometer) is used for correcting the altitude errors, and optional magnetometers are used for correcting the orientation. Magnetometers are highly sensitivity to electromagnetic fields, thus less reliable.

The sensor documentation says that it can provide output updates at 120 Hz, and if only IMU is used then the update rate is 512 Hz. The GPS receiver is capable of tracking 16 satellites simultaneously, and even has the capability of using SBAS corrections ([Technologies 07]).

Experimental results

The accuracy of a miniature MEMS device like MTi-G is still not comparable to larger specific purpose sensors. The documentation of MTi-G [Technologies 07], states that the accuracy of MEMS inertial sensors is still limited, and errors can grow to significant levels if integrated for more than a few seconds. Orders of magnitude of the drift errors for orientation is approximately 1° to 2° over 10 seconds.

We performed two tests: first, to observe the stationary error characteristics of the system, and the second, for the motion. For the first test, we placed the sensor on a stable platform with the GPS antenna placed outdoors. The obtained results are given in figure D.2a. It can be seen that the altitude varied up to 30 m within 2 minutes (data collected for 10 minutes after a long initialization period of more than 10 minutes). Even longitude and latitude are error prone, and these errors are attributed to ULEE including multipath. Regarding the attitude, the pitch and roll measurements are almost have a zero mean but the yaw seems to have a continuous drift (change in yaw of nearly 40°, in less than 2 minutes). However, this can be attributed to the incorrect alignment of the vertical axis.

Seondly, we conducted a set of acquisitions around the Panthéon area in Paris (results in figure D.3), with the vehicle driven at $\sim$ 10 kmph. During the acquisition the number of satellites observed by each sensor is noted (figure D.3a). The difference in number of satellites can be due to the sensitivity of the receiver to the multipath, and the configured mask angles.

As it can be seen the results obtained by *LARA-3D* is much better than the MTi-G. For this reason the idea of introducing this sensor to the *LARA-3D* platform is put on hold.

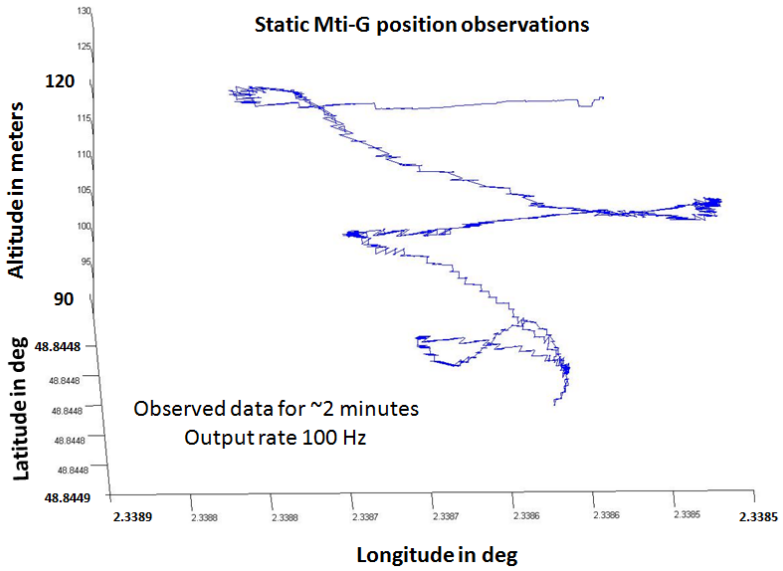

(a) MTi-G observed position error

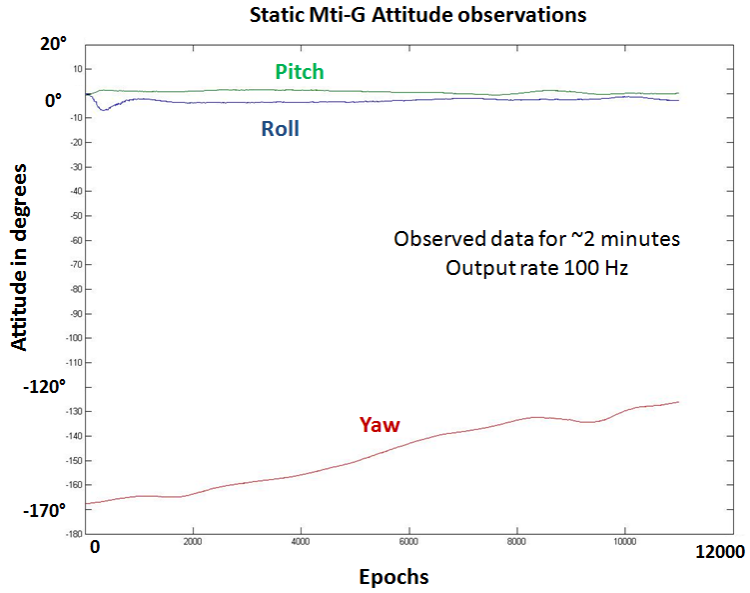

(b) MTi-G observed orientation (attitude) error

Figure D.2: MEMS sensor MTi-G is retained in a stationary position to observe the precision of its measurements and its pose estimation for a short duration.

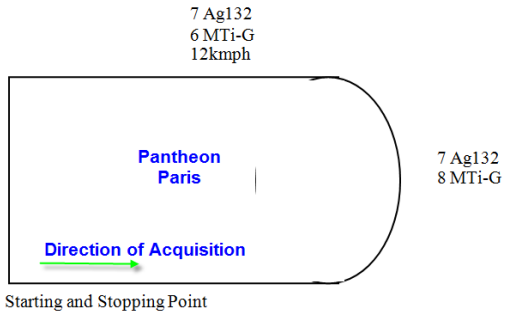

(a) Number of visible satellites - Trimble Ag132 vs MTi-G

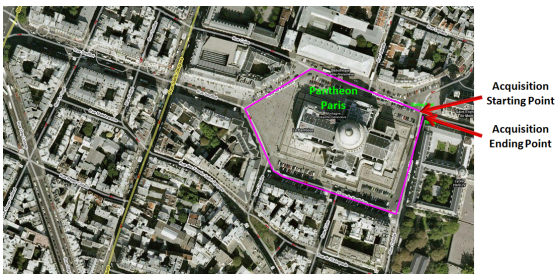

(b) Test itinerary around Panthéon, Paris

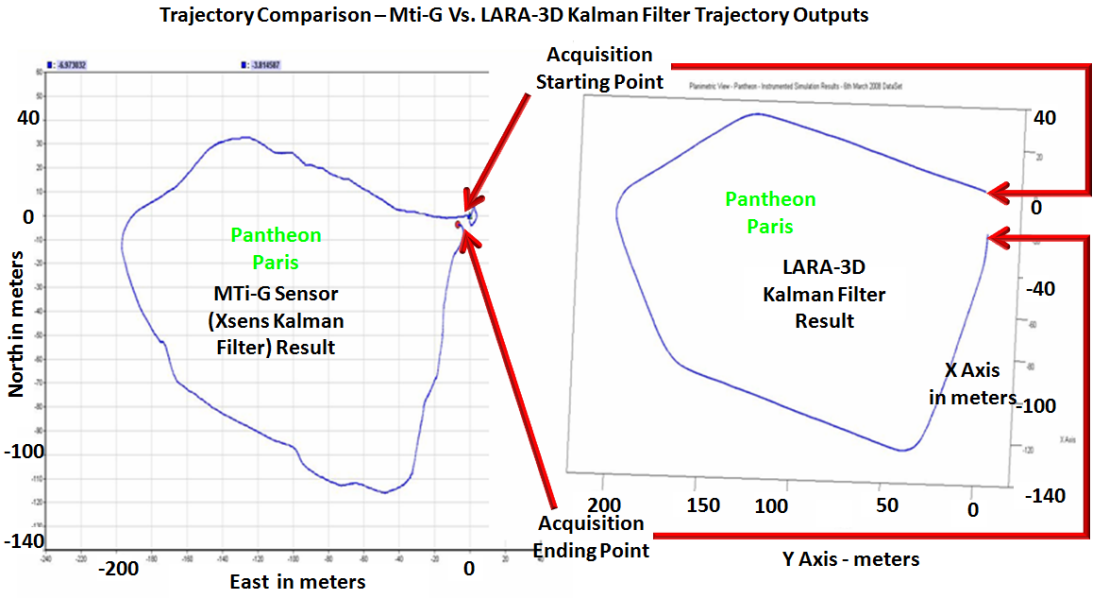

(c) Obtained results - MTi-G and LARA-3D trajectory outputs

Figure D.3: MTi-G is fitted on to the *LARA-3D* vehicle and tested around Panthéon in Paris. In the figure D.3c, the trajectory on the left is obtained by MTi-G, and on the right by *LARA-3D* system alone. The MTi-G results seem to suffer from inconsistent yaw problems in comparison to the current *LARA-3D* platform.

Appendix E

Gyro bias identification in real time

The ability to extract planar landmarks from batch data acquisitions (explained in chapter 5), bring in added advantages to determine the IMU gyro's biases. Under normal conditions, this bias is identified by keeping the vehicle at rest. However, these biases can also tend to drift due to temperature changes (mentioned in section 2.8.2. Therefore, the ability to measure them in real time is a desirable feature.

The gyros provide the measure $\hat{\omega}$, of the instantaneous angular velocity vector ω. Ignoring the white noise (with mean over time= 0) the measurement can be expressed as:

$$\hat{\omega} = \omega + \mathbf{b} \tag{E.1}$$

where, $\mathbf{b}$ is the bias, the significant error in IMU measurements.

From the kinematics equations, the evolution of a static direction expressed in the body frame (by a vector $\mathbf{N}$) over a small time δ is given by the relation:

$$\mathbf{N_{k+\delta}} = \mathbf{N_k} + \delta\omega \otimes \mathbf{N_k} \tag{E.2}$$

up to the second order term in δ, where, $\otimes$ is the vector cross product. The vector $\mathbf{N}$ is assumed to have correctly data associated across the epochs $\mathbf{k}$ and $\mathbf{k} + \delta$.

Applying equation E.2, for two vectors $\mathbf{N^1}$ and $\mathbf{N^2}$ we get

$$\mathbf{N^1_{k+\delta}} = \mathbf{N^1_k} + \delta\omega \otimes \mathbf{N^1_k N^2_{k+\delta}} = \mathbf{N^2_k} + \delta\omega \otimes \mathbf{N^2_k} \tag{E.3}$$

The vectors $\mathbf{N^1}$ and $\mathbf{N^2}$, are obtained from the normals of extracted two non parallel planar patches, which can further deduced as shown in equation E.4.

$$\hat{\omega} \otimes \mathbf{N^1_k} - \omega \otimes \mathbf{N^1_k} + \mathbf{b} \otimes \mathbf{N^1_k}\hat{\omega} \otimes \mathbf{N^2_k} - \omega \otimes \mathbf{N^2_k} + \mathbf{b} \otimes \mathbf{N^2_k} \tag{E.4}$$

In equation E.4, except $\mathbf{b}$ all other terms are known and therefore, the bias can be deduced.

Proof:

Calculate $(\mathbf{b} \otimes \mathbf{N^1_k}) \otimes (\mathbf{b} \otimes \mathbf{N^2_k})$. This vector is collinear to $\mathbf{b}$, since, $\mathbf{b} \otimes \mathbf{N^1_k}$ and $\mathbf{b} \otimes \mathbf{N^2_k}$ are orthogonal to $\mathbf{b}$ and their cross product is orthogonal to the plane which is orthogonal to $\mathbf{b}$ i.e., the resulting vector is collinear to $\mathbf{b}$. By applying the mixed product rule we get:

$$[(\mathbf{b} \otimes \mathbf{N^1_k}) \otimes (\mathbf{b} \otimes \mathbf{N^2_k})] \odot \mathbf{b} = [\mathbf{b} \otimes (\mathbf{b} \otimes \mathbf{N^1_k})] \odot (\mathbf{b} \otimes \mathbf{N^2_k}) \tag{E.5}$$

where $\odot$ is the vector dot product. This can further deduced as:

$$[\mathbf{b} \otimes (\mathbf{b} \otimes \mathbf{N^1_k})] \odot (\mathbf{b} \otimes \mathbf{N^2_k}) = [(\mathbf{b} \odot \mathbf{N^1_k})\mathbf{b} - \mathbf{b} \odot \mathbf{b}\mathbf{N^1_k}] \odot (\mathbf{b} \otimes \mathbf{N^2_k}) \tag{E.6}$$

However, $(\mathbf{b} \otimes \mathbf{N^2_k})$ is orthogonal to $\mathbf{b}$. Therefore, we have:

$$[\mathbf{b} \otimes (\mathbf{b} \otimes \mathbf{N^1_k})] \odot (\mathbf{b} \otimes \mathbf{N^2_k}) = -(\mathbf{b} \odot \mathbf{b}\mathbf{N^1_k}) \odot (\mathbf{b} \otimes \mathbf{N^2_k}) = -(\mathbf{b} \odot \mathbf{b})\mathbf{b} \odot (\mathbf{N^1_k} \otimes \mathbf{N^2_k}) \tag{E.7}$$

This implies that $\frac{\mathbf{b}}{||\mathbf{b}||}$ is known, or in other words the direction of the bias is known. The magnitude of the bias can therefore obtained by first computing the term $\frac{-(\mathbf{b}\odot\mathbf{b})(\mathbf{N^1_k}\otimes\mathbf{N^2_k})\odot\mathbf{b}}{||\mathbf{b}||}$, and then deducing the term $\frac{(\mathbf{N^1_k}\otimes\mathbf{N^2_k})\odot\mathbf{b}}{||\mathbf{b}||}$.

Bibliography

[Abuhadrous 03a] I. Abuhadrous, F. Nashashibi & C. Laurgeau. *3-D Land Vehicle Localization: a Real-time Multi-Sensor Data Fusion Approach using RTMAPS.* In Proc. of the 11th International Conference on Advanced Robotics. June 30th-July, 3rd, 2003.

[Abuhadrous 03b] I. Abuhadrous, F. Nashashibi, C. Laurgeau & F. Goulette. *Onboard Real-time System for Digitizing and Geo-referencing of 3D Urban Environments.* In Proc. of the 11th International Conference on Advanced Robotics. June 30th-July 3rd, 2003.

[Abuhadrous 05] I. Abuhadrous. *Système embarqué temps réel de localisation et de modélisation 3D par fusion multi-capteur.* PhD thesis, Ecole des Mines de Paris, 2005.

[Andersson 03] F. Andersson & B. Kvernes. *Bezier and B-spline Technology.* 2003.

[Bailey 01] T. Bailey & E. Nebot. *Localisation in large-scale environments.* Robotics and Autonomous Systems, vol. 37, no. 4, pages 261–281, 2001.

[Bailey 02] T. Bailey. *Mobile robot localisation and mapping in extensive outdoor environments.* PhD thesis, Australian Center for Field Robotics, University of Sydney, 2002.

[Bailey 06] T. Bailey & H. Durrant-Whyte. *Simultaneous localization and mapping (SLAM): Part II.* IEEE Robotics & Automation Magazine, vol. 13, no. 3, pages 108–117, 2006.

[Barber 08] D. Barber, J. Mills & S. Smith-Voysey. *Geometric validation of a ground-based mobile laser scanning system.* ISPRS Journal of Photogrammetry and Remote Sensing, vol. 63, no. 1, pages 128–141, 2008.

[Bengtsson 03] O. Bengtsson & A.J. Baerveldt. *Robot localization based on scan-matching–estimating the covariance matrix for the IDC algorithm.* Robotics and Autonomous Systems, vol. 44, no. 1, pages 29–40, 2003.

[Besl 92] P.J. Besl & N.D. McKay. *A method for registration of 3-D shapes.* IEEE Transactions on pattern analysis and machine intelligence, pages 239–256, 1992.

[Borenstein 02] J. Borenstein & L. Feng. *Measurement and correction of systematic odometry errors in mobile robots.* Robotics and Automation, IEEE Transactions on, vol. 12, no. 6, pages 869–880, 2002.

[Borges 04] G.A. Borges & M.J. Aldon. *Line extraction in 2D range images for mobile robotics.* Journal of Intelligent and Robotic Systems, vol. 40, no. 3, pages 267–297, 2004.

[Bourke 05] T. Bourke. *A Positon and Orientation Post-Processing Software Package for Land Applications - New Technology.* Applanix Corporation, 2005.

[Charbonnier 97] P. Charbonnier, L. Blanc-Feraud, G. Aubert & M. Barlaud. *Deterministic edge-preserving regularization in computed imaging.* IEEE Transactions on image processing, vol. 6, no. 2, pages 298–311, 1997.

[Charbonnier 09] P. Charbonnier, J-P. Tarel & S-S. Ieng. *Theorie semi-quadratique, regularisation et estimation robuste.* Problemes inverses en genie civil, Etudes et Recherches des Laboratoires des Ponts et Chaussees, 2009.

[Chen 02] Y. Chen & G. Medioni. *Object modeling by registration of multiple range images.* In Robotics and Automation, 1991. Proceedings., 1991 IEEE International Conference on, pages 2724–2729. IEEE, 2002.

[Chiang 05] K-W. Chiang & N. El-Sheimy. *An Alternative Low Cost MEMS IMU/GPS Integration Scheme.* Coordinates, vol. 1, 2005.

[Choi 07] S. Choi. *Geo-localisation precise et robuste pour la modelisation deenvironments 3D avec la plateforme LARA-3D.* Rapport technique, Ecole des Mines, Paris, 2007.

[Cramer 97] M. Cramer. *Gps/ins integration.* In Photogrammetric Week, volume 97, pages 3–12. Citeseer, 1997.

[Crossbow 01] Crossbow. *Crossbow DMU Users Manual VG600CA-200, Doc No: 6001-0002, Revision B*, 2001.

[Davison 07] A.J. Davison, I.D. Reid, N.D. Molton & O. Stasse. *MonoSLAM: Real-time single camera SLAM.* IEEE Transactions on Pattern Analysis and Machine Intelligence, pages 1052–1067, 2007.

[Dempster 77] A.P. Dempster, N.M. Laird, D.B. Rubin*et al. Maximum likelihood from incomplete data via the EM algorithm.* Journal of the Royal Statistical Society. Series B (Methodological), vol. 39, no. 1, pages 1–38, 1977.

[Dissanayake 01] M.W.M.G. Dissanayake, P. Newman, S. Clark, H.F. Durrant-Whyte & M. Csorba. *A solution to the simultaneous localization and map building (SLAM) problem.* IEEE Transactions on Robotics and Automation, vol. 17, no. 3, pages 229–241, 2001.

[Dold 04] C. Dold & C. Brenner. *Automatic matching of terrestrial scan data as a basis for the generation of detailed 3D city models.* International Archives of Photogrammetry and Remote Sensing, vol. 35, pages 1091–1096, 2004.

[Dold 06] C. Dold & C. Brenner. *Registration of terrestrial laser scanning data using planar patches and image data.* In ISPRS Comm. V Symposium Iamge Engineering and Vision Metrology, IAPRS, volume 36, pages 25–27. Citeseer, 2006.

[Douglas 73] D.H. Douglas & T.K. Peucker. *Algorithms for the reduction of the number of points required to represent a digitized line or its caricature.* Cartographica: The International Journal for Geographic Information and Geovisualization, vol. 10, no. 2, pages 112–122, 1973.

[Durrant-Whyte 06] H. Durrant-Whyte & T. Bailey. *Simultaneous localization and mapping: part I.* IEEE Robotics & Automation Magazine, vol. 13, no. 2, pages 99–110, 2006.

[El-Sheimy 96] N. El-Sheimy. *The development of VISAT-a mobile survey system for GIS applications.* PhD thesis, University of Calgary, 1996.

[El-Sheimy 04] N. El-Sheimy. *Emerging land-based mobile mapping system.* GIS development, November 2004, 2004.

[El-Sheimy 06] N. El-Sheimy, E-H. Shin & X. Niu. *Kalman Filter Face-Off Extended vs. Unscented Kalman Filters for Integrated GPS and MEMS Inertial.* Inside GNSS, March 2006, 2006.

[El-Sheimy 07] N. El-Sheimy, T. Hassan & M. Lavigne. *VISAT: Mapping what you see.* Coordinates Mazine, May 2007, 2007.

[Ellum 02] C. Ellum & N. El-Sheimy. *Land-based mobile mapping systems.* Photogrammetric Engineering and Remote Sensing, vol. 68, no. 1, pages 13–17, 2002.

[en Gutmann 97] J.S. en Gutmann & B. Nebel. *Navigation mobiler Roboter mit Laserscans.* In In Autonome Mobile Systeme. Springer Verlag, Berlin, 1997.

[Farrell 99] J. Farrell & M. Barth. The global positioning system and inertial navigation. McGraw-Hill Professional, 1999.

[Feynman 06] R.P. Feynman, M.A. Gottlieb, R. Leighton, M. Sands, R.B. Leighton, R.E. Vogt & A. Black. *Feynman's tips on physics: a problem-solving supplement to the Feynman lectures on physics.* 2006.

[Fischler 81] M.A. Fischler & R.C. Bolles. *Random sample consensus: A paradigm for model fitting with applications to image analysis and automated cartography.* Communications of the ACM, vol. 24, no. 6, pages 381–395, 1981.

[Flenniken 05] W. Flenniken, J. Wall & D. Bevly. *Characterization of various IMU error sources and the effect on navigation performance.* In ION GNSS, pages 13–16, 2005.

[Fraser 02] D. Fraser & J. Potter. *The optimum linear smoother as a combination of two optimum linear filters.* Automatic Control, IEEE Transactions on, vol. 14, no. 4, pages 387–390, 2002.

[Früh 04] C. Früh & A. Zakhor. *An automated method for large-scale, ground-based city model acquisition.* International Journal of Computer Vision, vol. 60, no. 1, pages 5–24, 2004.

[Gee 07] A.P. Gee, D. Chekhlov, W. Mayol & A. Calway. *Discovering planes and collapsing the state space in visual slam.* In British Machine Vision Conference (BMVC). Citeseer, 2007.

[Giebner 03] M.G. Giebner. *Tightly-coupled image-aided inertial navigation system via a kalman filter.* 2003.

[Gilliéron 01] P.Y. Gilliéron, J. Skaloud, Y. Levet & B. Merminod. *A mobile mapping system for automating road data capture in real time.* Swiss Federal Institute of Technology, Institute of Geomatics, vol. 1015, 2001.

[Google. 10] Google. *Google Trike*, October 2010.

[Goulette 06] F. Goulette, F. Nashashibi, I. Abuhadrous, S. Ammoun & C. Laurgeau. *An Integrated On-board Laser Range Sensing System for On-the-way City and Road Modelling.* In Proceedings of the ISPRS Commission I Symposium, From Sensors to Imagery, Paris, pages 3–5, 2006.

[Graefe 01] G. Graefe, W. Caspary, H. Heister, J. Klemm & M. Sever. *The road data acquisition system MoSES–determination and accuracy of trajectory data gained with the Applanix POS/LV.* In Proceedings, The Third International Mobile Mapping Symposium, Cairo, Egypt, January, pages 3–5, 2001.

[Grejner-Brzezinska 02] D.A. Grejner-Brzezinska. *Direct Georeferencing at The Ohio State University: A Historical Perspective.* ASPRS Journal of the American Society for Photogrammetry and Remote Sensing, vol. 68, no. 6, 2002.

[Grewal 01] M.S. Grewal, L.R. Weill, L.R. Weill & A.P. Andrews. Global positioning systems, inertial navigation, and integration. Wiley-Blackwell, 2001.

[Grinstead 05] B. Grinstead, A.F. Koschan, D. Page, A. Gribok & M.A. Abidi. *Vehicle-Borne Scanning for Detailed 3 d Terrain Model Generation.* 2005.

[Gruyer 06] D. Gruyer, C. Royere, N. du Lac, G. Michel & JM Blosseville. *Sivic and rtmaps, interconnected platforms for the conception and the evaluation of driving assistance systems.* In ITS World Congress, London, United Kingdom, 2006.

[Hassan 07] T. Hassan, K. Ellum, S. Nassar, W. Cheng & N. El-Sheimy. *Innovation: Photogrammetry for Mobile Mapping.* GPS World, March 2007, 2007.

[Hellström 06] T. Hellström, O. Ringdahl & A. Siddiqui. *Path tracking and localization in forest environment.* In Proceedings of the Israel Conference on Robotics (ICR06). Citeseer, 2006.

[Hofmann-Wellenhof 08] B. Hofmann-Wellenhof, H. Lichtenegger & E. Wasle. GNSS–global Navigation Satellite Systems: GPS, GLONASS, Galileo, and More. Springer, 2008.

[Hou 04] H. Hou. *Modeling inertial sensors errors using Allan variance.* UCGE Report, vol. 20201, 2004.

[Hunter 06] G. Hunter, C. Cox & J. Kremer. *Development of a commercial laser scanning mobile mapping system–Streetmapper.* In Second International Workshop The Future of Remote Sensing, Antwerp, 2006.

[Hutton 97] J. Hutton, T. Savina & L. Lithopoulos. *Photogrammetric applications of applanixs position and orientation system (POS).* In ASPRS/MAPPS Softcopy Conference, Arlington, Virginia, July, pages 27–30, 1997.

[Hwang 03] T-H. Hwang, Choi K-H., Joo I-H. & Lee J-H. *MPEG-7 Metadata for Video-Based GIS Applications.* In Geoscience and Remote Sensing Symposium. Proceedings. IGARSS 2003, 2003.

[IBEO 09] IBEO. *IBEO LD Automotive.* http://www.ibeo.de, 2009.

[Intempora 07] Intempora. *RT MAPS User's Manual*, 2007.

[Jekeli 00] C. Jekeli. Inertial navigation systems with geodetic applications. Walter De Gruyter Inc, 2000.

[Julier 97] S.J. Julier & J.K. Uhlmann. *A new extension of the Kalman filter to nonlinear systems.* In Int. Symp. Aerospace/Defense Sensing, Simul. and Controls, volume 3, page 26. Citeseer, 1997.

[Kaplan 06] E. Kaplan & C. Hegarty. Understanding GPS: Principles and Applications Second Edition. Artech House, 2006.

[Kapp 06] A. Kapp. *Quality Measures for lidar signal Processing.* Intelligent Vehicles Symposium, Tokyo, pages 163–168, 2006.

[Kiriy 02] E. Kiriy & M. Buehler. *Three-state extended kalman filter for mobile robot localization.* McGill University., Montreal, Canada, Tech. Rep. TR-CIM, vol. 5, 2002.

[Knight 02] D.T. Knight. *Rapid development of tightly-coupled gps/ins systems.* In Position Location and Navigation Symposium, 1996., IEEE 1996, pages 300–305. IEEE, 2002.

[Leonard 91] J.J. Leonard & H.F. Durrant-Whyte. *Simultaneous map building and localization for an autonomous mobile robot.* In IEEE/RSJ International Workshop on Intelligent Robots and Systems, volume 3, pages 1442–1447, 1991.

[Leonard 92] J.J. Leonard & H.F. Durrant-Whyte. Directed sonar sensing for mobile robot navigation. Springer, 1992.

[Li 97] R. Li. *Mobile mapping: An emerging technology for spatial data acquisition.* Photogrammetric Engineering and Remote Sensing, vol. 63, no. 9, pages 1085–1092, 1997.

[Lu 97] F. Lu & E. Milios. *Robot pose estimation in unknown environments by matching 2d range scans.* Journal of Intelligent and Robotic Systems, vol. 18, no. 3, pages 249–275, 1997.

[Mallios 09] A. Mallios, P. Ridao, E. Hernández, D. Ribas, F. Maurelli & Y. Petillot. *Pose-based slam with probabilistic scan matching algorithm using a mechanical scanned imaging sonar.* In OCEANS 2009-EUROPE, 2009. OCEANS'09., pages 1–6. IEEE, 2009.

[Manandhar 00] D. Manandhar & R. Shibasaki. *Geo-Referencing of Multi-Sensor Range Data for Vehicle-borne Laser Mapping System (VLMS).* In International Symposium on Remote Sensing, volume 16, pages 567–573, 2000.

[Manandhar 01] D. Manandhar & R. Shibasaki. *Feature extraction from range data.* In Paper presented at the 22nd Asian Conference on Remote Sensing, volume 5, page 9, 2001.

[Manandhar 03] D. Manandhar & R. Shibasaki. *Accuracy Assessment of Mobile Mapping System.* In Asian Conference on Remote Sensing, 2003. Proceedings. 2003, 2003.

[Martínez 06a] JL Martínez, J. González, J. Morales, A. Mandow & A. García-Cerezo. *Genetic and ICP laser point matching for 2D mobile robot motion estimation.* Journal of Field Robotics. John Wiley & Sons Ltd, vol. 23, no. 1, 2006.

[Martínez 06b] J.L. Martínez, J. González, J. Morales, A. Mandow & A.J. García-Cerezo. *Mobile robot motion estimation by 2D scan matching with genetic and iterative closest point algorithms.* Journal of Field Robotics, vol. 23, no. 1, pages 21–34, 2006.

[McLoughlin 08] S. McLoughlin, C. Deegan, C. Mulvihill, C. Fitzgerald & C. Markham. *Mobile mapping for the automated analysis of road signage and delineation.* IET, 2008.

[Misra 01] P. Misra & P. Enge. Global Positioning System: Signals, Measurements and Performance. Ganga Jamuna, USA, 2001.

[Montemerlo 02] M. Montemerlo, S. Thrun, D. Koller & B. Wegbreit. *FastSLAM: A factored solution to the simultaneous localization and mapping problem.* In Proceedings of the National conference on Artificial Intelligence, pages 593–598. Menlo Park, CA; Cambridge, MA; London; AAAI Press; MIT Press; 1999, 2002.

[Montemerlo 03a] M. Montemerlo. *FastSLAM: A Factored Solution to the Simultaneous Localization and Mapping Problem With Unknown Data Association.* PhD thesis, School of Computer Science Carnegie Mellon University, 2003.

[Montemerlo 03b] M. Montemerlo & S. Thrun. *Simultaneous localization and mapping with unknown data association using FastSLAM.* In IEEE International Conference on Robotics and Automation, 2003. Proceedings. ICRA'03, volume 2, 2003.

[Moon 96] T.K. Moon. *The expectation-maximization algorithm.* IEEE Signal processing magazine, vol. 13, no. 6, pages 47–60, 1996.

[Moon 99] S.W. Moon, J.H. Kim, D. Hwang, S. Ra & S.J. Lee. *Implementation of a Loosely-Coupled GPS/INS Integration System.* In Proc. of The 4th International Symposium on Satellite Navigation Technology and Applications, Brisbane, Queensland, Australia, 1999.

[Narayana 09] K. Narayana, S-W. Choi & F. Goulette. *Localization for mobile mapping systems, experimental results, analysis and post-processing improvements.* Proceedings of the 6th International Symposium on Mobile Mapping Technology, Brazil, 2009.

[Narayana 10] K. Narayana, F. Goulette & B. Steux. *Planar Landmark Detection Using A Specific Arrangement of LIDAR Scanners.* Proceedings of the Position Location and Navigation Symposium 2010, USA, 2010.

[Nguyen 07] V. Nguyen, S. Gächter, A. Martinelli, N. Tomatis & R. Siegwart. *A comparison of line extraction algorithms using 2D range data for indoor mobile robotics.* Autonomous Robots, vol. 23, no. 2, pages 97–111, 2007.

[Nieto 06] J. Nieto, T. Bailey & E. Nebot. *Scan-slam: Combining ekf-slam and scan correlation.* In Field and Service Robotics, pages 167–178. Springer, 2006.

[Nistér 06] D. Nistér, O. Naroditsky & J. Bergen. *Visual odometry for ground vehicle applications.* Journal of Field Robotics, vol. 23, no. 1, pages 3–20, 2006.

[Nuchter 05a] A. Nuchter, K. Lingemann, J. Hertzberg & H. Surmann. *6d SLAM with approximate data association.* In 12th International Conference on Advanced Robotics, 2005. ICAR'05. Proceedings., pages 242–249, 2005.

[Nüchter 05b] A. Nüchter, K. Lingemann, J. Hertzberg & H. Surmann. *Heuristic-based laser scan matching for outdoor 6D SLAM.* KI 2005: Advances in Artificial Intelligence, pages 304–319, 2005.

[Nüchter 07] A. Nüchter, K. Lingemann, J. Hertzberg & H. Surmann. *6D SLAM-3D mapping outdoor environments.* Journal of Field Robotics, vol. 24, no. 8-9, pages 699–722, 2007.

[Nüchter 09] A. Nüchter. 3D Robotic Mapping: The Simultaneous Localization and Mapping Problem with Six Degrees of Freedom. Springer Verlag, 2009.

[Ohno 04] K. Ohno, T. Tsubouchi & S. Yuta. *Outdoor map building based on odometry and RTK-GPS positioning fusion.* In 2004 IEEE International Conference on Robotics and Automation, 2004. Proceedings. ICRA'04, volume 1, 2004.

[Ooishi 04] T. Ooishi, K. Yamada, H. Takeda & T. Kawai. *Development of simple mobile mapping system for the construction of road foundation data.* Vol. XXXV, part B, vol. 2, pages 67–72, 2004.

[Optech. 10] Optech. *LYNX Mobile Mapper Data Sheet*, December 2010.

[Povazan 95] I. Povazan, D. Janglová & L. Uher. *Odometry in Determination of the Position of an Autonomous Mobile Vehicle.* Proceedings of ISMCR'95, pages 425–429, 1995.

[Reid 02] D. Reid. *An algorithm for tracking multiple targets.* Automatic Control, IEEE Transactions on, vol. 24, no. 6, pages 843–854, 2002.

[Reinsch 67] C.H. Reinsch. *Smoothing by spline functions.* Numerische Mathematik, vol. 10, no. 3, pages 177–183, 1967.

[Reshetyuk 09] Y. Reshetyuk. Self-calibration and direct georeferencing in terrestrial laser scanning. Arkitektur och samh
"allsbyggnad, Kungliga Tekniska h
"ogskolan, 2009.

[Ribeiro 02] M.I. Ribeiro & P. Lima. *Kinematics Models of Mobile Robots.* Mobile Robotics course. Apr, 2002.

[SARI. 10] SARI. *Surveillance Automatisée des Routes pour lÍnformation des conducteurs et des gestionnaires*, October 2010.

[Scherzinger 00] B. Scherzinger. *Precise robust positioning with inertial/GPS RTK.* Proceedings of the Institute of Navigations ION-GPS, pages 20–23, 2000.

[Schmidt 04] G.T. Schmidt. *INS/GPS technology trends.* Advances in Navigation Sensors and Integration Technology. RTO Lecture series, vol. 232, pages 1–1, 2004.

[Schultz 06] C.E. Schultz. INS and GPS integration. Informatik og Matematisk Modellering, Danmarks Tekniske Universitet, 2006.

[Schwarz 04] K.P. Schwarz & N. El-Sheimy. *Mobile mapping systems-state of the art and future trends.* International Archives of Photogrammetry, Remote Sensing and Spatial Information Sciences, vol. 35, no. Part B, page 10, 2004.

[Schwarz 07] KP Schwarz & N. El-Sheimy. *Digital mobile mapping systems–state of the art and future trends.* Advances in mobile mapping technology, page 3, 2007.

[Sedlak 94] J. Sedlak. *Comparison of Kalman filter and optimal smoother estimates of spacecraft attitude.* In Flight Mechanics/Estimation Theory Symposium, pages 431–445, 1994.

[Selkainaho 01] J. Selkainaho, A. Halme & J. Paanajarvi. *Navigation system of an outdoor service robot with hybrid locomotion system.* In International Conference on Field and Service Robotics (FSR), Finland, 2001.

[Selkainaho 02] J. Selkainaho. Adaptive autonomous navigation of mobile robots in unknown environments. Citeseer, 2002.

[Sever 04] M.D.M. Sever, F.A. Artés & R. Hill. *Using Inertially-Aided Real-Time Kinematic Technology as a land-based mapping tool.* 2004.

[Shaikh 03] K-N. Shaikh, A-R-M. Shariff, H. Jamaluddin & S. Mansoor. *GPS-Aided-INS for Mobile Mapping in Precision Agriculture.* GIS Development Magazine, 2003.

[Shi 08] Y. Shi, R. Shibasaki & Z.C. Shi. *Towards automatic road mapping by fusing vehicle-borne multi-sensor data.* The International Archives of the Photogrammetry, Remote Sensing and Spatial Information Sciences, vol. 37, 2008.

[SICK 06] SICK. *LMS200/211/221/291 Laser Measurement Systems, Technical description.* http://www.sick.com, 2006.

[Skaloud 99] J. Skaloud, AM Bruton & KP Schwarz. *Detection and filtering of short-term (1/fγ) noise in inertial sensors.* Navigation, vol. 46, no. 2, pages 97–107, 1999.

[Skaloud 05] J. Skaloud, J. Vallet, K. Keller, G. Veyssière & O. Kölbl. *HELIMAP: Rapid Large Scale Mapping Using Handheld LiDAR/CCD/GPS/INS Sensors on Helicopters.* 2005.

[Skolnik 80] M.I. Skolnik. *Introduction to radar systems.* 1980.

[Smith 86] R.C. Smith & P. Cheeseman. *On the representation and estimation of spatial uncertainty.* The international journal of Robotics Research, vol. 5, no. 4, page 56, 1986.

[Smith 90] R. Smith, M. Self & P. Cheeseman. *Estimating uncertain spatial relationships in robotics.* Autonomous robot vehicles, vol. 1, pages 167–193, 1990.

[Sola 07] J. Sola, A. Monin & M. Devy. *BiCamSLAM: Two times mono is more than stereo.* In Robotics and Automation, 2007 IEEE International Conference on, pages 4795–4800. IEEE, 2007.

[Sola 08] J. Sola, A. Monin, M. Devy & T. Vidal-Calleja. *Fusing monocular information in multicamera SLAM.* Robotics, IEEE Transactions on, vol. 24, no. 5, pages 958–968, 2008.

[Steux 10] B. Steux & O. El Hamzaoui. *CoreSLAM: a SLAM Algorithm in less than 200 lines of C code.* Proceedings of the 11th Control Automation Robotics & Vision (ICARCV), pages 1975–1979, 2010.

[Surmann 04] H. Surmann, A. Nüchter, K. Lingemann, J. Hertzberg & F. Publica. *6D SLAM-preliminary report on closing the loop in six dimensions.* In Proceedings of the 5th IFAC Symposium on Intelligent Autonomous Vehicles (IAV04), Lisabon. Citeseer, 2004.

[Technologies 07] Xsens Technologies. *MTi-G User Manual and Technical Documentation*, 2007.

[TerraNumerica. 10] TerraNumerica. *Terra Numerica*, October 2010.

[Thrun 98] S. Thrun, W. Burgard & D. Fox. *A probabilistic approach to concurrent mapping and localization for mobile robots.* Autonomous Robots, vol. 5, no. 3, pages 253–271, 1998.

[Thrun 00a] S. Thrun. *Probabilistic algorithms in robotics.* AI Magazine, vol. 21, no. 4, page 93, 2000.

[Thrun 00b] S. Thrun, W. Burgard & D. Fox. *A real-time algorithm for mobile robot mapping with applications to multi-robot and 3D mapping.* In IEEE international conference on robotics and automation, volume 1, pages 321–328. Citeseer, 2000.

[Trimble 99] Trimble. *Trimble; AgGPS 124 / 132 Operation Manual, Revision A*, 1999.

[Trimble 08] Trimble. *DATASHEET GPS Pathfinder ProXRT receiver.* http://www.trimble.com, 2008.

[Trimble. 10] Trimble. *Datasheet Trmble GS200 series*, December 2010.

[Tully 10] S. Tully, G. Kantor & H. Choset. *A Single-Step Maximum A Posteriori Update for Bearing-Only SLAM.* 2010.

[Velodyne. 10] Velodyne. *High Definition 3D LiDAR scannerVelodyne HDL-64E*, December 2010.

[Wang 04] C.C. Wang. *Simultaneous localization, mapping and moving object tracking [PhD thesis].* PhD thesis, Robotics Institute, Carnegie Mellon University, 2004.

[Weingarten 04] J.W. Weingarten, G. Gruener & R. Siegwart. *Probabilistic plane fitting in 3d and an application to robotic mapping.* In 2004 IEEE International Conference on Robotics and Automation, 2004. Proceedings. ICRA'04, pages 927–932, 2004.

[Weingarten 05] J. Weingarten & R. Siegwart. *EKF-based 3D SLAM for structured environment reconstruction.* In IEEE/RSJ International Conference on Intelligent Robots and Systems (IROS 2005). Proceedings, page 2089 2094, 2005.

[Weiss 95] JD Weiss & DS Kee. *A direct performance comparison between loosely coupled and tightly coupled GPS/INS integration techniques.* In Institute of Navigation, Annual Meeting, 51 st, Colorado Springs, CO, pages 537–544, 1995.

[Wendel 04] J. Wendel & G.F. Trommer. *Tightly coupled GPS/INS integration for missile applications.* Aerospace Science and Technology, vol. 8, no. 7, pages 627–634, 2004.

[Works. 10] How Stuff Works. *Mechanical odometer*, June 2010.

[Yoo 09] H-J. Yoo, F. Goulette, J. Senparoca & G. Lepère. *Simulation based comparitive analysis for the design of laser terrestrial mobile mapping systems.* Boletim de Ciências Geodésicas, vol. 15, no. 5, 2009.

[Yu 07] S.J. Yu, S.R. Sukumar, A.F. Koschan, D.L. Page & M.A. Abidi. *3D reconstruction of road surfaces using an integrated multi-sensory approach.* Optics and Lasers in Engineering, vol. 45, no. 7, pages 808–818, 2007.

[Zhang 03] K. Zhang & B. Xiao. *Current status of low-cost GPS and mobile mapping systems.* In Proceedings of the Malaysia Geoinformation and Surveying conference, Kuching, Malaysia, 2003.

SOLUTIONS DE LOCALISATION DES SYSTEMES MOBILES DE CARTOGRAPHIE EN ENVIRONNEMENTS STRUCTURES

RESUME : La localisation automatique est une fonctionnalité importante des systèmes de cartographie mobiles (*Mobile Mapping Systems*, MMS). La présente thèse présente des solutions complémentaires aux méthodes de localisation utilisées actuellement dans un système MMS terrestre, qui utilise des récepteurs GPS et des centrales à inertie (*Inertial Measurement Units*, IMU).

Un post-traitement, par lissage des données, permet d'améliorer les cartes 3D générées par un MMS. Cette approche est cependant insuffisante pour corriger les erreurs à variations lentes des capteurs. La présente thèse propose une technique de localisation alternative, fondée sur des scanners 2D à lasers. La méthode présentée ici, d'odométrie par laser, utilise des repères plans, qui sont fréquents dans les environnements créés par l'Homme : ces repères fixes permettent de déterminer le déplacement opéré par la plateforme mobile. Contrairement à la technique du SLAM (*Simultaneous Localization and Mapping*), utilisée pour la navigation des robots à l'intérieur d'un bâtiment, la transformation 3D est calculée sans avoir recours à une carte préétablie, mais en exploitant des propriétés invariantes des caractéristiques extraites de l'environnement. Nous proposons une approche par “division pour régner” (*divide and conquer*, D&C) qui simplifie les tâches d'association des repères (*data association*, DA) et de reconstruction du mouvement.

Mots clés : Localisation, Systèmes de cartographie mobiles (MMS), SLAM, Récepteurs GPS, Centrales à inertie (IMU), Scanners laser, Post-traitement, Odométrie laser, Repères plans, Association de données.

SOLUTIONS FOR THE LOCALIZATION OF MOBILE MAPPING SYSTEMS IN STRUCTURED ENVIRONMENTS

ABSTRACT : Automated localization is an important functionality for *Mobile Mapping Systems* (MMS). This thesis presents complimentary solutions to the current localization methods used in a terrestrial MMS, using GPS receivers and *Inertial Measurement Units* (IMU).

A smoothing-based post-mission processing improves the 3D maps generated by MMS. However, this approach is still insufficient, when exposed to slowly varying input sensor errors. The thesis proposes an alternative localization method using 2D laser scanners. The proposed laser odometry approach uses planar landmarks in manmade environments, to detect and compute the transformation of the mobile platform. Unlike *Simultaneous Localization and Mapping* (SLAM) technique, used in indoor robotic navigation, the relative 3D transformation is computed without using a map, but by exploiting the time invariant properties of the extracted features. A new Divide & Conquer (D&C) approach is proposed to simplify the computation, involving both transformation and *Data Association*.

Keywords : Localization, Mobile Mapping Systems (MMS), SLAM, GPS receivers, Inertial Measurement Units (IMU), Laser scanners, Post-Mission processing, Laser odometry, Planar landmarks, Data Association (DA).

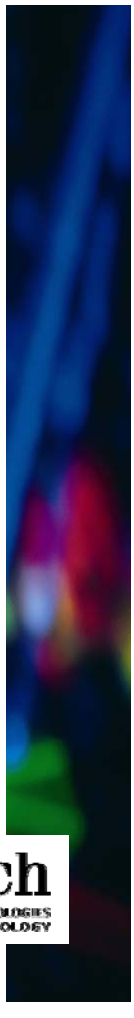

MINES ParisTech

ParisTech
INSTITUT DES SCIENCES ET TECHNOLOGIES
PARIS INSTITUTE OF TECHNOLOGY